Imaging fast neural activity in the brain with Electrical Impedance Tomography

Brett Conrad Packham

Submitted for the degree of Doctor of Philosophy

Department of Medical Physics & Bioengineering

University College London

2013

Declaration

I, Brett Conrad Packham, confirm that the work presented in this thesis is my own. Where information has been derived from other sources, I confirm that this has been indicated in the thesis.

Signature	Date

Acknowledgements

This thesis was only possible through the support of a number of people. First, I am grateful to my supervisors: Professor David Holder, for the opportunity to work on such a stimulating project, Mr. Andy McEvoy for his realism and advice, and Professor Jem Hebden for his support, constructive criticism and foresight.

I am especially grateful to, and cannot thank enough, Mr. Hwan Koo and Dr. Kirill Aristovich, who were both a great support to me throughout my years of study. Their assistance, both through friendship and during the animal studies, kept the work moving forward as without their contributions in the engineering and modelling components of these studies none of the work would have been possible. Dr. Gustavo Sato dos Santos provided me with much sound advice on coding, statistics and inverse solutions, and I thank you for being such a great sounding boarding for ideas. Dr. Anna Vongerichten and Dr. Anthony Ghosh provided me with support and guidance on the animal preparation I undertook. Mr. James Avery was a great support to me on too many tasks to mention, but his advice on my thesis, plans and help with the piezoelectric stimulator were greatly appreciated. I must thank all of the past and present members of the UCL electrical impedance tomography (EIT) group, it is because of their work and advice that the work presented in this thesis was possible.

This work would not have been possible without the support of a multitude of people. Dr. Gareth Barnes who gave me statistical advice, Professor Matteo Carandini and Mr Andrea Pisauro who advised me on the use of optical imaging, Dr. Jason Berwick for his advice on whisker stimulation, and, Professor Roger Lemon and Dr. Alexander Kraskov who gave me guidance on the use of depth electrodes for local field potential measurement.

Finally, I am grateful to my partner, Alžběta Zuzíková, and my parents and brother: without their support none of this would have been possible.

Abstract

Electrical impedance tomography (EIT) is an emerging medical imaging technique that can be employed to reconstruct the internal conductivity of an object from measurements made on the boundary. One proposed application for EIT is in head imaging, including imaging of impedance changes that occur with neuronal depolarisation and the imaging of acute stroke. The work of this thesis was aimed at advancing the imaging of brain pathology and function, with particular focus on the imaging of fast neural activity. Chapter 1 is a review of other brain imaging techniques, the principles of bioimpedance and EIT, and of previous impedance recordings of fast neural activity. Chapter 2 was a comparison of reconstruction algorithms for the detection of acute stroke using EIT in a realistic head-shaped tank, which entailed assessing boundary voltage rejection methods and quantitative analysis of image quality to determine the best reconstruction algorithms for the detection of acute stroke. In chapter 3, an EIT imaging dataset of fast neural activity, previously collected in a rat model, was assessed using second-level statistical parametric mapping (SPM) and the spatio-temporal propagation of the activity assessed and compared to the neurophysiological literature, which was reviewed in chapter 1. The analysis undertaken in chapter 3 illustrated some key methodological issues, which were addressed in chapter 4: new high resolution meshes and better optimised matrix inversion were employed, a new algorithm for electrode alignment was developed, also the use of SPM was validated by applying it to control datasets and through the use of statistical non-parametric mapping. Chapters 5 and 6 detail work attempting to cross-validate the use of EIT to image fast neural activity by employing a physiological stimulus, mechanical whisker displacement, and comparing the findings to other neurophysiological techniques recorded in the same model. Chapter 5 details work to validate the model and the impedance findings in this model as compared to previously published neurophysiological results, while chapter 6 details the use of other neurophysiological techniques for cross-validation.

Publications and Presentations

Refereed Papers

B. Packham, H. Koo, A. Romsauerova, S. Ahn, A. McEwan, S.C. Jun and D.S. Holder. Comparison of frequency difference reconstruction algorithms for the detection of acute stroke using EIT in a realistic head-shaped tank. *Physiological Measurement*, 33(5):767-86, May 2012.

Conference Talks

B. Packham, H. Koo, K. Aristovich, G. Sato dos Santos and D.S. Holder. Cross-validation of electrical impedance tomography of epicortically recorded evoked neural activity in the anaesthetised rat barrel cortex. *XVth International Conference of Electrical Bioimpedance and XIVth Conference on Electrical Impedance Tomography*, Heiligenstadt, Germany, April 2013.

M. Koronfel, J. Avery, A. Vongerichten, **B. Packham** and D.S. Holder. A flexible polyimide epicortical electrode array for imaging fast neural activity in the rat cortex using EIT. *XVth International Conference of Electrical Bioimpedance and XIVth Conference on Electrical Impedance Tomography*, Heiligenstadt, Germany, April 2013.

E. Magee, A. Vongericthen, **B. Packham**, K. Aristovich, A. Vanhoestenberghe and D.S. Holder. Design, production and use of stainless steel microelectrode arrays for the collection of epicortical fast neural electrical impedance tomography data. *IMAPS-UK Annual Conference "MicroTech"*, Cambridge, United Kingdom, March 2013.

B. Packham, G. Sato dos Santos, K. Aristovich, O. Gilad, T. Oh, A. Ghosh, G. Barnes and D.S. Holder. Statistical analysis of electrical impedance tomography image sets of epicortically recorded evoked neural activity in the anaesthetised rat. *XIIIth International Conference on Biomedical Applications of Electrical Impedance Tomography*, Tianjin, China, May 2012.

T. Doru, **B. Packham**, H. Koo and D.S. Holder. Evaluation of reconstruction algorithms and imaging acute stroke with multi-frequency electrical impedance tomography in a head-shaped tank with a real human skull. *XIIIth International Conference on Biomedical Applications of Electrical Impedance Tomography*, Tianjin, China, May 2012.

B. Packham, G. Sato dos Santos, K. Aristovich, O. Gilad, T. Oh, A. Ghosh, G. Barnes and D.S. Holder. Statistical analysis of electrical impedance tomography image sets of epicortically recorded evoked neural activity in the anaesthetised rat. *World Congress on Medical Physics and Biomedical Engineering*, Beijing, China, May 2012.

T. Doru, **B. Packham**, H. Koo and D.S. Holder. Evaluation of reconstruction algorithms and imaging acute stroke with multi-frequency electrical impedance tomography in a head-shaped tank with a real human skull. *World Congress on Medical Physics and Biomedical Engineering*, Beijing, China, May 2012.

B. Packham, H. Koo, S. Ahn, S.C. Jun and D.S.Holder. Evaluation of the UCH Mk2.5 MFEIT system for imaging stroke in liquid filled anatomically realistic tanks. *XIIth International Conference on Biomedical Applications of Electrical Impedance Tomography*, Bath, United Kingdom, April 2011.

T. Doru, **B. Packham**, H. Koo and D.S.Holder. Is the 16 channel Spiral16 or 32 channel EEG31 electrode protocol better for stroke MF imaging in the head shaped tank? *XIIth International Conference on Biomedical Applications of Electrical Impedance Tomography*, Bath, United Kingdom, April 2011.

H. Koo, **B. Packham** and D.S.Holder. Optimization of calibration method to enable imaging acute stroke using the portable serial UCH Mk2.5 Multi-frequency Electrical Impedance Tomography (MFEIT) system. *XIIth International Conference on Biomedical Applications of Electrical Impedance Tomography*, Bath, United Kingdom, April 2011.

D.S. Holder, A. Romsauerova, J. Luis, J. Cornell, **B. Packham**, E. Smith, K. Wloch, D. Parvin, S. Ahn and S.C Jun. A method for recording Electrical Impedance Tomography images in human acute stroke subjects. *XIIth International Conference on Biomedical Applications of Electrical Impedance Tomography*, Bath, United Kingdom, April 2011.

A. Ghosh, O. Gilad, T. Oh, M. Schuettler, **B. Packham** and D.S. Holder. Imaging fast neural activity in the brain with Electrical Impedance Tomography using a low frequency sinusoidal applied current: single channel measurements during somatosensory evoked potentials with epicortical electrodes in the rat brain. *XIth International Conference on Biomedical Applications of Electrical Impedance Tomography*, Florida, USA, April 2011.

Poster Presentations

B. Packham and D.S Holder. Statistical analysis of electrical impedance tomography image sets of fast neural activity. *Graduate School Poster Competition, University College London*, London, United Kingdom, June 2012.

B. Packham, H. Koo, A. McEvoy, D.S. Holder. Electrical impedance tomography of fast neural activity in the brain: improvements to the method for imaging during visual evoked responses in the cerebral cortex of the anaesthetised rat. *Graduate School Poster Competition, University College London*, London, United Kingdom, June 2011.

Contents

List of Figures

List of Tables

Acronyms

V_c	trigeminal nucleus caudalis
V_i	trigeminal nucleus interpolaris
V_o	trigeminal nucleus oralis
V_P	trigeminal nucleus principalis
ABG	arterial blood gas
AC	alternating current
ADC	analogue-to-digital converter
ADP	adenosine diphosphate
Ag-AgCl	silver-silver chloride
ALBSF	anterior lateral barrel subfield
ANOVA	analysis of variance
ATP	adenosine triphosphate
BOLD	blood-oxygen-level dependant
Ca^{2+}	calcium
CAP	compound action potential
CaSD	calcium sensitive dye
CI	confidence interval
CIR	calbindin-immunoreactive
Cl^-	chloride
CNS	central nervous system
CSDA	current source and sink density analysis
CT	X-ray computed tomography
DC	direct current
DCM	dynamic causal modelling
dLGN	dorsal part of lateral geniculate thalamic nucleus
DOI	diffuse optical imaging
ECG	electrocardiography
ECoG	electrocorticography
EEG	electroencephalography
EIDORS	electrical impedance tomography and diffuse optical tomography reconstruction software
EIT	electrical impedance tomography
EP	evoked potential
EPSP	excitatory postsynaptic potential
FD	frequency difference
FDA	frequency difference adjacent
FEM	finite element method
fMRI	functional magnetic resonance imaging
F-SEP	forepaw somatosensory evoked potential
FSL	functional magnetic resonance imaging of the brain software library
FWE	family-wise error
FWHM	full width at half maximum
GABA	γ-aminobutyric acid
GLM	general linear model
H-SEP	hindpaw somatosensory evoked potential
iCSDA	inverse current source and sink density analysis
IGL	intrageniculate leafle
IPSP	inhibitory postsynaptic potential
ISOI	intrinsic signal optical imaging

K^+	potassium
LED	light-emitting diode
LFP	local field potential
LOT	laminar optical tomography
LP	lateral posterior thalamic nucleus
LPA	laminar population analysis
M1	primary motor cortex
M2	secondary motor cortex
MAP	mean arterial pressure
MEG	magnetoencephalography
MFEIT	multi-frequency electrical impedance tomography
MRI	magnetic resonance imaging
MUA	multi-unit activity
N1	first negative-going evoked potential component
N2	second negative-going evoked potential component
Na^+	sodium
NaCl	sodium chloride
NaN	not-a-number
nc-MRI	neuronal current-magnetic resonance imaging
NIR	near infrared
NMDA	*N*-methyl-d-aspartic acid
OCT	optical coherence tomography
P1	first positive-going evoked potential component
P2	second positive-going evoked potential component
PCA	principal component analysis
PET	positron emission tomography
PIR	parvalbumin immunoreactive
PM	parietal-medial cortical area
PMBSF	posteromedial barrel subfield
PNS	peripheral nervous system
Po	posterior thalamic complex
POC	posterior caudal thalamic nucleus
POM	posterior medial thalamic nucleus
PR	parietal-rostral cortical area
PSTH	peristimulus time histogram
PV	parietal-ventral cortical area
RFT	random field theory
RMS	root-mean-square
RtN	reticular thalamic nucleus
ROI	region of interest
S1	primary somatosensory cortex
S1FL	primary somatosensory forelimb region
S1HL	primary somatosensory hindlimb region
S2	secondary somatosensory cortex
SC	superior colliculus
SD	standard deviation
SEM	standard error of the mean
SEP	somatosensory evoked potential
SnPM	statistical non-parametric mapping
SNR	signal-to-noise ratio
SPECT	single photon emission computed tomography
SPM	statistical parametric mapping
SQUID	superconducting quantum interference device
TD	time difference
tPA	tissue plasminogen activator
tSVD	truncated singular value decomposition
V1	primary visual cortex
V2	secondary visual cortex
V2L	lateral area of secondary visual cortex

V2M	medial area of secondary visual cortex
VEP	visual evoked potential
vLGN	ventral part of lateral geniculate thalamic nucleus
VP	ventral posterior thalamic complex
VPL	ventral posterolateral thalamic nucleus
VPM	ventral posteromedial thalamic nucleus
VSD	voltage sensitive dye
V-SEP	vibrissae somatosensory evoked potential
WFD	weighted frequency difference
WFDA	weighted frequency difference adjacent

Chapter 1

Introduction and Review

The work within this thesis is aimed at examining the possibility of measuring fast neural activity using EIT. EIT is a tomographic medical imaging technique in which the internal impedance of an object is imaged using boundary voltage measurements from surface electrodes. EIT has been proposed for a multitude of imaging applications, including imaging of acute stroke and for imaging fast neural activity in nerves and the brain, the latter is the primary focus of this thesis. This chapter details the concepts and reviews the relevant literature which are fundamental to all the subsequent chapters.

1.1 Nerve physiology

The activity of the brain is best understood through consideration of its constituent structures, the structures of nerves, and of the physiological processes underlying this activity, the transmission of signalling through nerves. The neurophysiological principles that underpin nerve signal transmission are routed in the structure of neurons, so these are considered first, after which the underlying physiology of neuronal signalling is considered.

1.1.1 The neuron

The neuron is the basic functional unit of the nervous system, as conclusively described by Cajal, for which he and Golgi, ironically an opponent of the neuron doctrine, won the 1906 Nobel Prize for Physiology or Medicine[1]. The neuron comprises three components: the cell body, or soma, axon and terminal branches, although variants of this template exist for varying roles (Figure 1.1). In the archetypal neuron, the cell body and the associated dendritic projections receive a chemical signal that leads to further transmission of signals, as shown, in spite of experimental difficulties, by Araki and Terzuolo using the voltage clamp technique on spinal motor neurons[2]. The axon then transmits the signal and at its terminal conveys the signal either to another nerve or to another target structure.

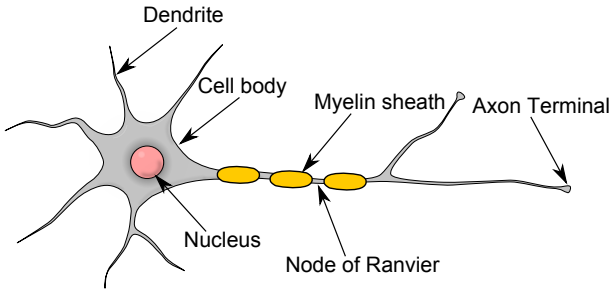

Figure 1.1: *A representation of a mulitpolar motor neuron demonstrating the basic structure of the neuronal unit.*

However, there are certain differences between the neurons of the central nervous system (CNS), the spinal cord and brain, and those of the peripheral nervous system (PNS), which makes up the remainder of the body's innervations.

Most importantly, the CNS's neurons' axonal myelin sheath, if at all present, is formed by oligodendrocytes, originally stained at the turn of the century and clearly visualised by the mid-20$^{\text{th}}$ century [1], as opposed to the myelination of the PNS which is due to the presence of Schwann cells. Myelination underlies some of the rapidity of neuronal transmission along the axon and so is discussed further below (section 1.1.3). Additionally dendrites are the most prevalent neuronal process in the cerebral cortex and glial cells, an increasingly important focus in neuroscientific research, make up a large proportion of the cortical volume.

1.1.2 The action potential

In overview an action potentials' production is initially dependent on an inward flux of sodium (Na^+) into an axon via voltage-gated sodium channels, causing depolarisation, which causes more channels to open allowing further inward movement of Na^+ and depolarisation. This process continues along the axon so that the action potential proceeds until it arrives at its target neuron or other structure. Essentially this process has two components: creation of the signal and the signal's propagation.

It was as early as the 18$^{\text{th}}$ century, with Galvani's famous experiments with frog musculature, that it was known that electrophysiology plays a role in the nervous systems' control. It was an anonymous article in 1794 by Galvani that confirmed the concept of innate animal electricity*. Nearly 150 years later Hodgkin and Huxley published a study in which they placed an electrode inside a squid giant axon and measured a transmembrane potential of around $-60\,\text{m V}$ inside the axon, relative to the outside, under resting conditions: the resting membrane potential [3]. This provided the first

*Dell'uso e Dell'attività Dell'arco Conduttore Nella Contrazione dei Muscoli (On the Use and Activity of the Conductive Arch in the Contraction of Muscles)

direct recording of the electrical changes across the neuronal membrane that result in the transmission of a signal: an action potential.

A range of properties of action potentials were also discovered, including that a threshold must be met if an action potential is to be transmitted. If a stimulus does not surpass this minimum level it fails to produce an action potential (subthreshold), while if the stimulus surpasses the threshold (suprathreshold) the magnitude and duration of the action potential, irrespective of stimulus amplitude, is unchanged. These properties were shown to be present, in experiments using cardiac muscle, by Bowditch in 1871, who described them as the 'all-or-nothing' law[4]. However, there are temporary depolarisations of the postsynaptic membrane, due to the flow of positively charged ions into the postsynaptic cell, known as an excitatory postsynaptic potential (EPSP) and enough of these can summate to result in an action potential, and similarly the opposite can occur to make a postsynaptic neuron less likely to generate an action potential and this is known as an inhibitory postsynaptic potential (IPSP). Essentially, both EPSPs and IPSPs both cause an offset in the baseline potential altering the ease with action potentials can be elicited. As a result of the 'all-or-nothing' law the action potential cannot carry stimulus/signal amplitude information and so addresses this by other means, for example with some sensory information being frequency coded: a stronger stimulus coded with a higher action potential frequency.

Additionally, Bowditch showed that a second action potential cannot occur until a period of time, known as the absolute refractory period, has been completed-determining the upper limit of the number of action potentials that an axon can transmit in a given time period. After the absolute refractory period a stronger stimulus is required for the second action potential than was required for the first; this is known as the relative refractory period. The phenomena of the 'all-or-nothing law' and the refractory periods are due to the physiology underlying action potential conduction.

The human resting potential is $-70\,\mathrm{m\,V}$, due to an outward potassium (K^+) current, because the neuronal membrane is permeable to K^+ and the concentration is higher, by about 20 times, inside the cell[5]. This membrane potential changes to 40 to $50\,\mathrm{m\,V}$ during the action potential, comparable to the equilibrium potential of Na^+, and then returns back to $-70\,\mathrm{m\,V}$. The mechanism underlying this change during action potentials was first explained by Hodgkin and Katz to be due to an increase in the permeability of the axon to Na^+ and a concurrent influx. This mechanism was confirmed by the fact that action potentials do not occur if Na^+ is removed, and action potentials are slower and smaller if Na^+ concentration is reduced[6].

The process, much of which was shown by Hodgkin and Katz, can be summarised as follows: a stimulus occurs, the membrane depolarises and axonal voltage-gated sodium channels open and Na^+ moves inward, down the electrochemical gradient. This depo-

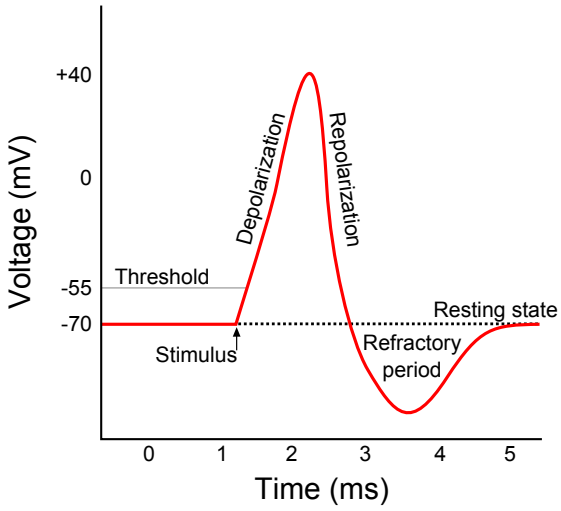

Figure 1.2: *A simplified representation of an action potential and its associated phenomena (Modified under the GNU Free Documentation License).*

larises the membrane further, causing the opening of more voltage-gated sodium channels and leading to further Na^+ influx. At the peak of this process the axonal membrane is more permeable to Na^+ than K^+ and the positive peak of the action potential occurs.

The open state of the sodium channels is unstable and soon becomes inactive: the sodium channels starts to become inactive after the action potential has peaked. It was not until the mid 1970s that this rapid reduction in permeability was experimentally shown[7]. Although it was hypothesised by Hodgkin and Huxley in their earlier work[3]. While the sodium channels are becoming inactive potassium channels are opening, as a result of the depolarisation, allowing K^+ to exit the axon down the electrochemical gradient (figure 1.2).

The Na^+ and K^+ gradients of the resting neuronal membrane that result in the resting membrane potential are maintained by an ion pump, the Na^+/K^+ ATPase pump. The nature of this pump was elucidated first by showing that Na^+ outflow and therefore action potentials are diminished by the application of cyanide, or dinitrophenol, known to be involved in the catabolism of adenosine triphosphate (ATP)[8], and then by demonstrating that this effect is reversed by ATP injections[9]. This Na^+/K^+ ATPase pump acts to pump out three Na^+ from the cell in exchange for two K^+ back into the cell: this net outward positive ionic current contributes to the resting potential. This movement of ions is opposed to the electrochemical gradient, hence the requirement for energy within this mechanism in the form of the catabolism of the phosphate bonds of ATP to produce adenosine diphosphate (ADP) and inorganic phosphate. This has the added importance of contributing to cell swelling, due to the increase in osmolarity from the replacement of one molecule of ATP with two other molecules. The same Na^+/K^+ ATPase pump is

responsible for the restoration of the resting potential following neuronal depolarisation.

In summary, during repolarisation, the membrane permeability to K^+ increases while Na^+ permeability decreases and with the aid of the Na^+/K^+ ATPase pump the membrane potential now returns towards its negative value: the equilibrium potential of K^+. As the membrane returns to its resting value the voltage-gated potassium channels close and the inactivated voltage-gated sodium channels return to their closed state. The above ionic theories presented by Hodgkin and Huxley and Hodgkin and Katz offered an explanation for the phenomena of the 'all-or-nothing law' and refractory periods.

The concept of there being a threshold can be understood by realising that a weak stimulus does not open enough voltage-gated sodium channels to allow propagation of the action potential and so is a subthreshold stimulus. When the threshold is met a sufficient number of channels open to allow the propagation of an action potential. Similarly, the fact that a suprathreshold stimulus does not produce any greater effect is understandable as either the channels are open and an action potential occurs, or it does not. There is a clear dependency of the threshold on the membrane potential: if a constant subthreshold stimulus is applied then the threshold rises and conversely hyperpolarisation results in a threshold decrease. If hyperpolarising currents are sufficiently strong then the threshold may even fall below the resting potential so that after it is removed the membrane potential is above threshold and an action potential occurs-this is anode break excitation.

With regard to the refractory periods, it is clear that voltage-gated sodium channels cannot open after an action potential, as they must close after entering the inactivated state that they assume after the action potential, thus explaining the absolute refractory period. Moreover, the relative refractory period is explained by the fact that when enough voltage-sodium channels have returned to their closed state, an action potential can only occur if all of them are activated at the same time, which would require a greater stimulus. In a similar manner this explains the reduction in latency with increasing current strength and the phenomenon of latent addition in which for a short time following a subthreshold stimulus the membrane potential is closer to threshold, with some voltage gated channels open, and so a smaller stimulus is required to elicit an action potential. Equally the opposite is true with an anodal shock resulting in a state in which a suprathreshold stimulus will be required to elicit a normal action potential.

1.1.3 Propagation of the action potential

As detailed above, when an action potential occurs a region of the axon is positive, at $50\,\mathrm{m\,V}$, and the surrounding inactive membrane is negative, at $-70\,\mathrm{m\,V}$, resulting in the formation of an electrical current between the two regions. This current causes the surrounding area to depolarise, as the change in voltage opens voltage-gated sodium channels and, when sufficient channels have opened, the action potential invades the resting area,

spreading the action potential further along the axon. However, the propagation of the action potential can only be in one direction from the point of origin (orthodromic). This is a result of the refractory period: the voltage-gated sodium channels in the area preceding the currently active part of the membrane are in an inactivated state, which prevents backward propagation of the action potential.

Action potentials are propagated in different ways depending on whether the axon is myelinated or demyelinated. In demyelinated axons the action potential is propagated in a continuous manner as the active region depolarises the region immediately adjacent to that which is currently active and this process continues along the axon in a contiguous fashion. In myelinated axons the process is somewhat different as the myelinated regions are insulated from the extracellular fluid, except for areas adjacent to what are termed the nodes of Ranvier.

Lillie in 1925 observed that in a passive iron wire covered with a glass tube broken at regular intervals, the current does not spread over the whole wire, but rather jumps from one break to another. This observation led to him suggesting that 'electro-saltatory' transmission may occur in myelinated nerve fibres with an action potential jumping from one node of Ranvier to another [10]. It was later shown that the action potential completes its electrical circuit between adjacent nodes of Ranvier, and so the action potential jumps from one node to the next: saltatory conduction [11]. Essentially the high resistance and capacitance of the myelin increases the longitudinal spread of current and this saltatory conduction increases the rate that action potentials are propagated along axons and towards their eventual synaptic target.

The changes that occur during action potentials, often termed fast changes, are difficult to measure. This is because they are very low amplitude electrical changes that occur over a very brief period of time (milliseconds) in a localised region (sub-millimetre). Therefore, their measurement requires low noise and high spatial and temporal resolution hardware. The somewhat technically easier task is the measurement of slow changes, which are blood flow and volume changes associated with the increased metabolic demands of neuronal activity. These changes have a larger signal amplitude, occur in a less localised region and over a much longer time frame of seconds.

1.2 Functional brain imaging modalities

Effective imaging techniques have underlain an array of biomedical and scientific advances over the centuries, with imaging allowing a non-invasive anatomical insight and more recently the ability to image functional physiological or pathological processes such as with the modality of echocardiography. Arguably in no other area could the prospect of effective functional imaging potentially revolutionise its associated scientific fields than in

the brain. Consequently an array of modalities have been investigated as potential tools for imaging brain activity. This imaging can be of the sequelae of brain activity, such as the influx of blood to an active region of the brain, which typically evolves over seconds, to meet increased metabolic demands, which is referred to as imaging of slow changes. Alternatively, brain imaging can be the direct imaging of the underlying physiological activity of neuronal functional, such as the ionic movements or resultant voltage changes in depolarisation.

1.2.1 Imaging slow changes

1.2.1.1 Available techniques

The commonly used imaging modalities of X-ray computed tomography (CT) and magnetic resonance imaging (MRI) are seen as the gold standard of neuroanatomical imaging and also have a role to play in functional brain imaging. In the imaging of slow changes, both implement systems based upon imaging haemodynamic changes which occur as a response to increased activity, to localise regions of brain activity. Tracer or perfusion CT is still a relatively new technique, first proposed in 1979 [12], which enhances the standard 3D X-ray imaging technology of CT by the administration of a contrast agent. Perfusion CT has mainly been implemented in imaging of acute stroke and oncological imaging and has stimulated new treatments in both fields: thrombolysis and anti-angiogenic treatment respectively [13]. However, despite a high spatial resolution of 1 mm, it suffers from a limited temporal resolution (1 s) and poor sampling volume (20 mm) [13;14].

A variant of the MRI technique, known as functional magnetic resonance imaging (fMRI) has been employed to image the slow neurovascular changes associated with neuronal activity. fMRI is centred upon the implementation of a contrast referred to as blood-oxygen-level dependant (BOLD), which utilises the differing magnetic properties of haemoglobin when it is oxygenated or deoxygenated [15]. While oxyhaemoglobin exhibits diamagnetism, deoxyhaemoglobin is paramagnetic and is attracted to external magnetic fields [16]. Therefore changes in haemoglobin oxygenation result in changes in the BOLD signal intensity, although interpretation must be made with consideration that changes in the BOLD signal intensity are coupled to both cerebral blood flow and oxygen consumption and both will alter the local concentrations of haemoglobin. fMRI has a temporal resolution in the region of more than one second, while it has a high spatial resolution of below 1 mm [17].

Another modality is positron emission tomography (PET), which is a form of nuclear imaging, based upon the detection of photon pairs. In PET a radioactive isotope, which emit positrons due to beta radiation, is used to label a biologically active molecule. The emitted positrons will, subsequent to anti-particle collision with electrons, produce

gamma decay photons. For each such interaction two photons are produced at 180° from each other allowing, after their detection by a scanning device, for backwards projection to localise their point of origin[18]. One of the most commonly used tracers is fluorodeoxyglucose, a glucose analogue, so that glucose uptake and metabolic activity can be imaged by recording the decay of fluorodeoxyglucose concentration. This is comparable to monitoring the haemodynamic changes secondary to neuronal activity, as in perfusion CT and fMRI, and in fact a more complex and technically difficult option is to use oxygen-15 to indirectly measure cerebral blood flow, and additional more specific labels have become available. PET has spatial and temporal resolutions of 4 mm and 30 s respectively[19].

An additional nuclear imaging technique is single photon emission computed tomography (SPECT) in which a radioactive isotope is imaged. However, in SPECT gamma ray emitting compounds are used, which may be bound to substances preferentially taken up by a certain tissue type. In the case of functional brain imaging hexamethylpropylene amine oxime is labelled with a radioisotope of technetium and the compound is taken into the brain, so that intensity is proportional to cerebral blood flow and this in turn is assumed to reflect haemodynamic changes secondary to changes in brain activity. SPECT has a spatial resolution of 7 mm and a temporal resolution of 15 min[20].

Optical imaging is another modality for imaging the slow changes associated with brain activity, a technique based upon the phenomena associated with the interactions between visible and near infrared (NIR) light with biological tissue: absorption, for haemoglobin characterisation, and scatter, for cell morphological characterisation. An often implemented optical technique is diffuse optical imaging (DOI), which is typically described as topographic or tomographic, typically taken to mean the reconstruction of two-dimensional and three dimensional images respectively. DOI, as with fMRI, relies upon the differing absorbing properties of oxyhaemoglobin and deoxyhaemoglobin, as a function of optical wavelength, to image the haemodynamic changes that occur during brain activity[21]. The technique has a temporal resolution of up to 0.1 s and a spatial resolution of about 10 mm[22]. This BOLD-like response can also be imaged by visualising the cortex and measuring the absorption spectra of blood, this is known as intrinsic signal optical imaging (ISOI). Although this technique has good lateral spatial resolution, 50 µm, and a temporal resolution of <1 s, it suffers from a poor sampling depth and from being invasive. Other techniques have been developed which can partially overcome the limitations of ISOI, these include optical coherence tomography (OCT) and laminar optical tomography (LOT). OCT allows for depth imaging by using NIR wavelengths to find backscattering. OCT can be matched to intrinsic signals and give three frames a second to a depth of 2.8 mm with a spatial resolution down to 2 µm[23]. Another optical imaging method is laser speckle flow imaging which provides spatially resolved images of

flow throughout vasculature by implementing a divergent laser diode. The principle is that speckle is caused by scattering in the brain and that this varies over time as a result of blood flow. This technique allows for measurements of cerebral metabolic rate of oxygen consumption, which correlates better with neuronal activity than BOLD or BOLD-like responses[24].

EIT (the details of which are given in section 1.4), has also been used to image the slow changes associated with brain activity, the principle being, as with other modalities, based upon haemodynamic changes, which would decrease the impedance of the active region as blood allows current to more freely pass through it. Holder et al. published a report of the first recordings of cerebral impedance during visual and somatosensory evoked responses in anaesthetised rabbits using an epicortically placed ring of 16 electrodes[25]. An impedance decrease of $4.5 \pm 2.7\,\%$ and $2.7 \pm 2.4\,\%$ were recorded for the respective paradigms, attributed to increased regional blood flow, and some adjacent smaller impedance increases, attributed to errors in reconstruction or neuronal swelling, as a result of ionic movement following sustained activity, reducing the extracellular volume and increasing the impedance. Later, Tidswell et al. undertook the first EIT recordings of the impedance changes associated with evoked responses in humans. Thirty nine healthy adults were enrolled, with a total of 52 recordings being made of visual, motor and somatosensory paradigms. The measurements were made using 31 silver-silver chloride (Ag-AgCl) electroencephalography (EEG) cup electrodes and assessed by comparison to baseline impedances during rest/no stimulation. Current was injected into two diametrically opposed electrodes at an amplitude between 1 to 2.5 m A and a frequency of 50 kHz, with each image consisting of 258 measurements with 15 such images in each experiment with experiments repeated six to 12 times. Impedance changes were found to be reproducible in 51 of the 52 recordings, with a mean impedance change of $0.19 \pm 0.02\,\%$, $0.43 \pm 0.05\,\%$ and $0.34 \pm 0.05\,\%$ for the somatosensory, visual and motor experiments, respectively. The most disappointing aspect of this study was that reconstructed images did not show consistent localisation of the impedance changes, largely due to a poor signal-to-noise ratio (SNR) and errors in head modelling, which consisted of a homogeneous sphere, without realistic layering or anisotropy, and possibly also inaccurate electrode localisation. In addition to this, the presence of impedance increases and decreases occurred and their cause was undetermined, although reduction in the extracellular volume was again a suggested cause. Twinned with the low resolution of EIT, this could have compounded the failure of localisation. However, this study highlighted some of the important areas for future work and improvements applicable to all applications of EIT in the head. Nonetheless, EIT offers portability, inexpensiveness and a high temporal resolution, in spite of a poor spatial resolution[26].

1.2.1.2 Advantages and disadvantages of techniques

CT carries the drawback of high levels of x-ray radiation exposure associated with each scan. Nonetheless, the rapidity of clinical scans, relative low cost and high spatial resolution means that CT is in widespread use in both clinical and research applications. In contrast to this, fMRI is an expensive technique, although this has not limited its widespread use because it is a technique with an excellent spatial resolution and unlike CT it is not associated with radiation exposure. However, the assumed simplistic relationship between the BOLD signal and brain activity has been shown to be complex and this signal shown to be easily misinterpreted [27]. In contrast to both CT and fMRI, PET includes both the risks of an exposure to a radioactive material and is associated with high purchasing and maintenance costs and has lower spatial and temporal resolutions. While SPECT suffers from a lower spatial and temporal resolution than fMRI, PET and CT, unlike these techniques SPECT has the unique advantage of not requiring the patient/subject to remain inside a scanner for the duration of the experiment allowing cognitive studies to be more readily undertaken [20]. With respect to imaging slow changes optical studies and EIT suffer from similarly poor spatial resolutions and benefit from the highest temporal resolution and lowest costs. Nonetheless, both techniques have yet to achieve widespread use as they need further study to prove their efficacy. This is more true of EIT than optical imaging, which, with the implementation of OCT as a supplement to ISOI, has a greatly improved spatial resolution, especially in the axial plane, although this is still limited and suffers from being an invasive technique.

From the comparative values of the array of modalities it is clear that each has different advantages and disadvantages (table 1.1), which some have attempted to address with the fusion of different modalities. However, at present for clinically imaging the slow changes associated with brain function fMRI is most commonly used and seen as somewhat of a gold standard, although its limitations in given situations are clear, as is the imaging of slow changes as it is the imaging of changes associated with activity as opposed to the desired goal of actually imaging the change itself.

1.2.2 Imaging fast changes

1.2.2.1 Available techniques

The alternative to imaging the sequelae of neuronal activity, as detailed above, is to image the neuronal activity itself. This task requires an imaging modality that has both a high spatial and temporal resolution of 1 mm and 1 ms, respectively, as action potentials can propagate at speeds up to $100\,\mathrm{m\,s^{-1}}$ [28]. A modality that can reliably achieve this does not yet exist, although several modalities have been employed in an attempt to achieve this, including EIT. Invasive methods that have high temporal and spatial resolution

Method	Spatial Resolution	Temporal Resolution	Limitations
Perfusion CT [13;14]	1 mm	1 s	Sampling volume, radiation exposure
fMRI [17]	1 mm	1 s	Expensive
PET [19]	4 mm	30 s	Expensive, radiation exposure
SPECT [20]	7 mm	15 min	Radioactive materials
DOI [21;22]	10 mm	100 ms	Poor depth penetration, image reconstruction requires improvement
ISOI [24]	50 µm	100 ms	Invasive
EIT [25;26]	10 to 20 mm	300 ms	Imaging has not yet been possible

Table 1.1: *Summary of the imaging modalities for detecting slow changes that occur during/as a result of neural activity.*

do exist, such as subdural electrocorticography (ECoG), an invasive variant of the EEG modality, and the application of voltage sensitive dyes (VSDs) to the cortex. However such techniques are undesirable clinically for the need to expose the cortex and its associated risks, but also for other reasons detailed below.

EEG was a technique first implemented over 90 years ago by the German physician Hans Berger and uses measurement of potential differences between scalp electrode pairs to produce traces of the brain's electrical activity: the voltages represent the synchronous activation of macrocolumns of many cortical neurons, with magnitude being proportional to the number, location and geometry of these neurons [29]. The technique is widely used in research and clinical settings for obtaining information regarding normal activity, epilepsy, encephalitis, monitoring sleep stages and response to stimuli. EEG has allowed for the characterisation of normal activity into a set of frequency bands, the first three, delta, theta and alpha, existing in bands increasing by approximately 4 Hz, the fourth band, beta, is in the region of 12 to 30 Hz and the final frequency band, gamma, that exists up to around 100 Hz. Extensive work has been undertaken to reconstruct images from EEG activity, based upon estimation of the current sources within the brain that have produced the EEG signals [30]. One such technique for achieving this is inverse dipole modelling, which assumes cortical activity can be represented by dipole sources, however, the number, location, magnitude and orientation are iteratively estimated until the calculated distribution best matches the recorded findings, which, due to the non-uniqueness of the problem, can result in non-physical solutions. EEG has a high temporal resolution of approximately 1 ms and spatial resolution of about 10 mm; the spatial resolution, with sufficient priori information, such as from MRI or fMRI data, can be reduced to less than 10 mm [31;32].

A variant of EEG is the magnetoencephalography (MEG) technique which is based

upon the detection of the magnetic induction produced by neural currents, which are extremely weak, in the tens to hundreds of femtoTeslas, and so requires advanced equipment to undertake recordings. These fields are detected using a highly sensitive amplifier invented in the late 1960s, known as a superconducting quantum interference device (SQUID) that possesses magnometer coils maintained in a superconducting environment[33]. MEG has similar temporal and spatial sensitivities to EEG.

With the underlying technology of MRI being based upon magnetic field measurement it would seem that this high spatial resolution imaging modality might be used to detect neuronal activity directly, by measuring changes in magnitude and phase of the nuclear magnetic resonance signal resulting from neuronal activity[34;35]. However, the underlying challenges for neuronal current-magnetic resonance imaging (nc-MRI) are that these changes are exceptionally small and that such changes, which occur over a small time scale, must be accurately separated from more delayed and persistent changes associated with neuronal activity such as the BOLD response underlying the implementation of fMRI[36]. The technique has borne mixed results in the studies undertaken. In an *in vivo* study with six human volunteers changes of $-1\,\%$ were recorded with visual evoked responses[37], while in another study including eight volunteers, also using visual stimuli, but with the addition of MEG and filtering of cardiac and respiratory signal, no changes were detected[38]. Similarly, Parkes et al., in trying to replicate these results, found no detectable changes[39]. Combination of nc-MRI with the fast imaging of fMRI allows nc-MRI to have a temporal resolution of 20 ms.

Another imaging modality that has been used in order to image fast neural activity is optical imaging of the fast scattering signal, with effects being noted within 1 ms or less of neuronal activation and therefore believed to be a direct result of neural activity rather than one of its sequelae[40]. Franceschini and Boas reported a fast signal change in 23 to 60 % of measurements, depending on the stimuli, in recordings taken from 10 healthy volunteers. The experiments allowed for a temporal resolution of 25 ms per image and a SNR of 10[41]. Although similar findings have been made by other groups and with other stimuli, Syre et al. called into question such findings by citing a prior failure to replicate such findings[42]. Steinbrink et al., by presenting a prediction of the signal that might be detected, which was close to or below the noise level of previously implemented systems, faced problems in replicating both sensory and visually evoked responses that had been detected[43].

The use of extrinsic VSDs is an optical imaging technique that has been used for imaging fast neural activity. VSDs were first used in 1968 but were then revitalised in 1986 with the first use of VSDs in mammalian brains[24]. VSDs bond across the membrane of cells and change their fluorescence with changes in membrane potential, with the amount of light released being a function of changes in the membrane potential, and so

VSDs are sensitive to spiking and synaptic activity. Due to the low contrast of VSDs, approximately 0.5 % change in signal, this means they can be masked by haemodynamic changes, so new dyes have been developed that are active at higher wavelengths away from haemoglobin absorption. A similar technique is the use of calcium sensitive dyes (CaSDs), which have a higher contrast and fluorescence change in response to increased calcium concentration and so allows imaging of firing, as calcium influx occurs during neural activity [24]. These techniques allow for imaging with a spatial resolution of 20 to 50 µm and temporal resolutions of around 1 ms [44]. The depth penetration is around 400 to 800 µm, which corresponds to the superficial layers of the neocortex. This depth can be improved through the use of OCT, two photon microscopy and, it has been suggested, LOT [24].

Two photon microscopy allows for imaging to depths greater than 600 µm, but requires the use of fluorescent contrasts. By using wavelengths twice that in confocal microscopy many of the disadvantages, including scatter, are overcome. Flurophores, activated when struck by two successive photons, release a photon at the flurophores' emission wavelength. As this emission can only be from the focus of the scanning beam scatter rejection is not required. Two photon microscopy has been used for perfusion mapping and to improve the sampling depth in CaSD mapping [24].

EIT has the theoretical potential to allow for non-invasive direct imaging of the changes in neuronal membrane impedance that underlie neural activity. The allure of the technique is that it has a high temporal resolution, comparable to EEG and MEG, and reasonable spatial resolution. Based upon the findings of previous work, Barber and Brown predicted a spatial resolution of approximately 1 % of the array diameter, which in the adult human head would equate to approximately 2 mm, with a data collection time of 57 ms using a 128 electrode system, although such a high spatial resolution has so far been elusive, and has been limited to around 10 mm [45]. The evidence for the potential of EIT in imaging fast changes associated with brain activity and experimental attempts to continue work aimed at accomplishing this feat are the subject of this thesis.

1.2.2.2 Advantages and disadvantages of techniques

Whilst EEG has a high temporal resolution and is an established, portable, non-invasive, low cost technique, it is mainly sensitive to superficial gyral activity. In contrast, MEG is more sensitive to sulcal sources as it is sensitive to radial fields. In addition to this, the requirement for SQUIDs means the modality is expensive to purchase and maintain, immobile and requires a dedicated magnetically shielded room. The key advantages of MEG are that signals are not attenuated by the skull and it can provide several hundred channels of signal instantly without the need for contacting electrodes as in EEG [46]. However, for both EEG and MEG, the inverse solution is non-unique, that is there are multiple possible

solutions. While this may be overcome by employing simplifying assumptions, the limits of accuracy are unknown in any given recording situation as it is not known to what extent the assumptions are violated. While fMRI is an established research field with a lot of interest, nc-MRI has not yet reached the same level of intense interest, with one of the key reasons being the conflicting findings of nc-MRI studies, suggesting further study is required. Similarly, an inconsistency of findings with optical imaging of scattering during fast neural activity mars the modality, however, it also suffers from an inherently limited maximum penetration of 15 mm, preventing imaging of deep structures [21]. VSD and CaSD imaging offer some of the best temporal and spatial resolutions of the fast neural imaging techniques, but there are limitations in these techniques beyond their invasiveness and lack of depth sensitivity. First, VSDs must be applied 1 to 2 h before recordings and some have photobleaching and phototoxic effects. Similarly CaSDs are difficult to administer, requiring dimethyl-sulfoxide and pluronic acid and direct pressure injection. Secondly, the VSD signal is hard to interpret, as the dyes are sensitive to all elements, neurons and glia, and to both excitatory and inhibitory signals, with the contributing origins of the signal being uncertain [44] (table 1.2).

In addition to this, whilst the sampling is mainly from layer II/III of the neocortex, this will also include the arborisations of layer V which extend up into the superficial layers. Two photon microscopy has promise in extending the depth sensitivity of VSD and CaSD imaging. However, cost and lack of purpose built commercial systems are significant considerations in its implementation [24]. Despite these limitations and the invasiveness of these optical dye imaging techniques they are perhaps one of the most useful imaging techniques in neuroscience research. EIT has the inherent advantage of high temporal resolution, but the disadvantages of low spatial resolution and a limited number of studies (further details are given in section 1.4).

1.2.3 Neurophysiological recording techniques

While there are multiple methods of imaging neural activity and its related phenomenon, there are other techniques which utilise more invasive non-imaging methods to measure fast neural activity. The following is a brief introduction and explanation of the key neurophysiological techniques employed in the literature to directly measure electroneurophysiology.

The patch clamp technique relies upon the use of micropipettes that have a tip-diameter of around 1 µm which is approximating the size of a single, or a few, ion channels, hence the term patch, and these are used to make surface membrane measurements. The micropipette contains a solution matching the sample's bathing solution and a wire recording electrode, and typically the pipette's tip is sealed against the membrane with pressure or suction. The patch clamp technique detailed thus far is sometimes referred

Method	Spatial Resolution	Temporal Resolution	Limitations
EEG [31;32]	10 mm	1 ms	Signal is summation of sources, so limited to surface
MEG [30;46]	10 mm	1 ms	Signal largely sulcal, expensive setup and maintenance
nc-MRI [36;37]	3 mm	20 ms	Requires further study
Optical fast scatter signal imaging [22;43]	10 mm	25 ms	Sampling limited to surface, requires further study
Optical extrinsic dye imaging [24;44]	20 µm	1 ms	Invasive, limited sampling, complex signals
EIT	10 mm	1 ms	Requires further study

Table 1.2: *Summary of the imaging modalities for detecting fast changes that occur during/as a result of neural activity.*

to as cell-attached or on-cell patch clamp recordings in order to differentiate it from other variants. If the micropipette is withdrawn after it has been sealed against the cell under study, the membrane patch will be removed and the cell interior exposed to the bathing solution, and this is termed inside-out patch clamp recording. A second branch of patch-clamp recordings is whole-cell recording, which involves recording from multiple sites to acquire data from the whole cell, and also the membrane of the cell is ruptured, by applying greater suction, in order to allow for study of the cell's interior. However, as the cell's interior is exposed to the solution in the pipettes, recordings can only be made in a short window of opportunity prior to the solution dialysing the intracellular contents. Alternatively, the cell membrane can be perforated by the use of antifungal or antibiotic agents that generate perforations in the cell's membrane. A variant of whole-cell recordings, termed outside-out patch recording, is similar to inside-out patch clamp recording, in that the pipette is withdrawn from the cell's membrane; however in outside-out patch recording a section of membrane is kept on the tip of the pipette [47].

A comparatively larger recording technique is single-unit recording, which involves the insertion of microelectrodes, with a tip of approximately 3 to 10 µm, into neural tissue. A single-unit is determined by isolating the the activity of a single, firing neuron, by recording its voltage changes over time. Recordings of single-unit activity can be made intracellularly, in which case information regarding the resting potential, postsynaptic potentials, and spikes of a neural tissue is measured, or extracellularly, in which case only spike activity is measured. Although the information obtain extracellularly is less than that which can be obtained from intracellular recordings, extracellular recordings carry a reduced risk of cellular damage allowing for longer recordings and are more suitable in awake, freely-moving animals. Single-unit recording electrodes are typically fine-tipped

glass micropipettes or metal microelectrodes, with the prior being more common in intracellular recordings. If the configuration is such that the activity of multiple, active cells is simultaneously recorded, then this is recording of multi-unit activity (MUA)[48].

On a larger scale than single and multi-unit recordings is the recording of LFPs, which is undertaken with larger electrodes and therefore at a lower spatial resolution. The measurement of LFPs reveals the net activity of multiple cells by measuring the voltage changes in the extracellular space that results from dendritic synaptic activity. These measurements are ideally a net effect measurement, and so not dominated by the activity of any single-unit, with the voltage being measured between a microelectrode within the neural tissue and a reference electrode. Unlike the spike activity recorded in single and multi-unit recordings, LFPs reflect postsynaptic events, and not action potentials, in cells with dendrites arranged so as to produce a net effect, rather than cancel one another's fields out[49;50]. In a study comparing the recording of LFPs, MUA, and a third technique called current source and sink density analysis (CSDA), Kajikawa and Schroeder explored the volume sensitivity of these techniques in the macaque auditory cortex. While the activity in MUA recordings and CSDA diminished as the stimulus was changed the LFP amplitude only mildly reduced. The conclusion was that despite the use of the word local, LFPs are generated from both local and non-local electrophysiology as a result of volume conduction, with amplitude being inversely proportional to distance[51].

The technique of CSDA is comparable to the measurement of LFPs, however it to some extent eliminates volume conduction in the spatial domain of interest in LFP recordings and has a more direct relationship with the neurophysiology. The relationship between LFPs and synaptic activity is complicated by the slowing and nonlinear effects of membrane capacitance and dynamics of ionic conductance states on membrane potential dynamics, whereas the transmembrane currents that are directly related to the extracellular potential are incorporated in CSDA[51]. Although first introduced in the 1950s, the particulars of CSDA were elucidated by Nicholson and Freeman and Mitzdorf in 1975 and 1985, respectively[49;52]. The current source density, C, is the macroscopic, volume-averaged, derivation of current sources and sinks from a three-dimensional current flow, J, related via the divergence of this field:

$$\nabla J = C. \tag{1.1}$$

From Ohm's law, J is the product of the electric field, E, and a conductivity tensor, $\boldsymbol{\sigma}$

$$\nabla J = \boldsymbol{\sigma} E. \tag{1.2}$$

If magnetic effects are neglected then E can be substituted for the gradient of the field potential, ϕ

$$E = -\nabla\phi, \tag{1.3}$$

so substituting equation 1.3 into equation 1.2 gives

$$J = -\boldsymbol{\sigma}\nabla\phi, \tag{1.4}$$

which from equation 1.1 means C can be calculated from

$$\nabla(\boldsymbol{\sigma}\nabla\phi) = -C. \tag{1.5}$$

Often the assumption is made that the conductivity tensor, $\boldsymbol{\sigma}$, is in fact a stationary scalar, and therefore an assumption of isotropy is made. This assumption is partially valid for a number of reasons, first, Nicholson and Freeman found that along each axis the conductivity in the brain is effectively constant, second, while a conductivity change does occur during neural activity for the purposes of CSDA this is negligible[52], and lastly, CSDA is often only performed in a single dimension, along the z-axis, perpendicular to the pial surface. If only the z-axis is considered and its conductivity is assumed isotropic then equation 1.5 simplifies to:

$$\boldsymbol{\sigma}\frac{\partial^2\phi}{\partial z^2} = -C(z), \tag{1.6}$$

which reveals that C in the z-axis is the second spatial derivative of the field potential in the same axis.

However, experimentally, the field potential is measured at a series of discrete points, typically equidistant from one another and this results in the second spatial derivative being calculated as the finite difference, which is a discrete analogue of the derivative and gives:

$$-C(z) = \boldsymbol{\sigma}\frac{\partial^2\phi}{\partial z^2} \approx \boldsymbol{\sigma}\frac{\phi(z+h) - 2\phi(z) + \phi(z-h)}{h^2}. \tag{1.7}$$

Where h is the fixed spacing between measurements of ϕ, or, in other words, the inter-electrode spacing. Although ϕ is measured at N electrodes, given that CSDA requires the calculation of the difference between these, as shown in equation 1.7, the resultant CSDA is actually at $N-2$ points. Some approaches to handling this are to make assumptions about the current flow above and below the first and last electrodes, for example, if oil is placed epicortically, then zero current is assumed to be flowing above the top electrode.

In simple terms, assuming a purely ohmic medium, CSDA indicates that, with a steeper potential gradient, more current flows, with increases and decreases being the respective result of membrane currents entering or leaving the extracellular space. Therefore post-synaptic potential activity is indicated by the presence of sinks, which are associated with

net local inward transmembrane current flow, and are coupled to concordant sources that show outward flow[49–52].

Relatively more recent approaches to CSDA include the application of principal component analysis (PCA) to CSDA and an inverse method of CSDA, termed inverse current source and sink density analysis (iCSDA). While direct interpretation of the principal components of CSDA is complex it is a valid means of determining the effective dimensionality of the CSDA and so hinting at the complexity of the underlying model[53;54]. The aim of iCSDA is to better describe the spatial extent of the current sources by inverting the electrostatic forward solution, as opposed to the standard assumption that the current sources are evenly distributed infinite planes. The crux of iCSDA is the formulation of a matrix, F, relating the field potential and current source density, which once inverted can be multiplied against the measured field potential to give the estimate of the current source density. Pettersen et al. in developing the technique, examined three methods of matrix formulation and determined that a continuous and smoothly cubic spline method, while more computationally demanding and more sensitive to spatial noise, was the method of choice, as confirmed in simulation and in the rat barrel cortex[55;56].

1.3 Bioimpedance

EIT is based upon the concept of bioimpedance, which describes the electrical property of a tissue in response to an externally applied current or voltage. This characteristic varies with frequency, tissue and histology, which allows for the distinction between tissue types and theoretically for the distinction between histological variants of tissue types, whether they be physiological or pathological variants. In order to fully understand bioimpedance it is important to understand the concept of electrical impedance, which in a direct current circuit is referred to as resistance, or the opposition to flow of electrons in circuits or among cells, which is directly related to current and voltage.

Electric current, I, which is expressed in amperes, is equivalent to the movement of one coulomb of electric charge, Q, per second: electric current describes the rate of flow of electric charge carried across a series of electrons and/or ions. So that current can be defined as,

$$I = \frac{\delta Q}{\delta t}. \tag{1.8}$$

While the potential difference or voltage, V, is the difference in voltage between two positions in an electrical conductor,

$$V = V_a - V_b, \tag{1.9}$$

with the voltage being the force driving the current and so it can be calculated from a rearrangement of Ohm's Law:

$$I = \frac{V}{R}. \tag{1.10}$$

However, with the possibility of phase variance within alternating current (AC) circuits the equation becomes:

$$V = \frac{IR}{\cos\phi}, \tag{1.11}$$

where ϕ is the phase difference between I and V. Phase and capacitance are both concepts that must be introduced when considering alternating currents. Capacitance describes the ability of a component or tissue constituent to store charge which with each cycle accumulates and discharges. This occurs more readily with increasing frequency. The storage of charge that capacitors induce can lead to a phase lag, where the phase of the voltage will lag behind the current's phase by 90°, as the current must charge up and discharge for a potential difference to form. This is opposed to the situation that exists in a purely resistive circuit where voltage and current are in phase, while a value between these absolutes exists when a mixture of resistance and capacitance exists in a circuit.

This phase variance and frequency dependence is also centred upon reactance, X, which is a component's opposition to an AC due to opposing electromagnetic field generation. In a capacitive circuit, as is the case in the bioimpedance circuit, capacitive reactance, X_c, is:

$$X_c = -\frac{1}{\omega C} = -\frac{1}{2\pi f C}, \tag{1.12}$$

where ω is the natural frequency, related to frequency, f, by $\omega = 2\pi f$. Obviously if the capacitance is fixed, and becomes a constant, reactance is simply inversely proportional to frequency. Reactance is often referred to as the imaginary component of impedance, Z, as impedance is a product of both resistance and the frequency dependant reactance:

$$Z = R + jX, \tag{1.13}$$

where j is the imaginary unit. The complex impedance plane, including the total amplitude and phase angle, or its modulus, $|Z|$, can be graphically depicted (figure 1.3) [57].

1.3.1 Bioimpedance principles

When considering bioimpedance, or impedance in tissue, it is valuable to consider circuit representation of a cell or tissue. The ionic fluids that make up the extracellular and

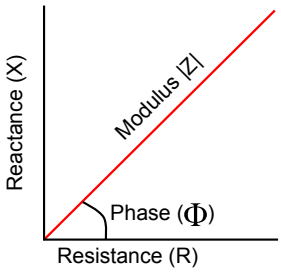

Figure 1.3: *Impedance in the complex plane: a representation of the impedance as a combination of its amplitude and phase angle.*

the intracellular spaces are resistive, while the membrane is an electrical insulator and has capacitive properties. An extension of this circuit representation can be applied to the neuron and its basis is termed Cable Theory. Therefore, as detailed above regarding the capacitor-frequency relationship, at low frequencies (less than 100 Hz) current will not pass across the capacitive membrane and so flows through the extracellular space, resulting in a largely resistive impedance. While at higher frequencies the current crosses the membrane and so the phase angle increases. At the highest frequencies this capacitive involvement diminishes and the phase angle returns to zero [57].

This variance of impedance, frequency, and phase angle within tissue can be divided into different dispersion bands. Alpha dispersion, around 100 Hz, describes a situation where phase increases and there is a greater decrease in resistance against frequency. Beta dispersion, between 10 kHz and 10 MHz, is more sensitive to intracellular changes as more current passes through the membrane. Gamma dispersion, at extremely high frequencies around 10 GHz, there is alteration of cell constituents through an effect upon water molecules [57].

1.3.2 Bioimpedance measurements and sources of error

In order to measure these impedances a constant current (or voltage) must be applied across a tissue and the voltage (or current) across this tissue is measured. From this, applying Ohm's law with one of the two variables being constant, normally an applied current, the resistance or impedance can be calculated. However this is complicated by artefacts that are recorded within an impedance measurement.

When measuring the voltage during an impedance measurement it does not truly reflect the impedance of the tissue through which the current is being injected into, as there will also be an addition to this impedance by the impedance of the electrodes. This can be mitigated by calibrating for the electrode impedance, or by using a four electrode system as the constant current will be independent of the electrode impedances.

There is also a contact impedance that exists due to the electrode-tissue interface and

will result in a reduction in the voltage measured and subsequently an incorrectly low impedance. As the applied current frequency increases the contact impedance is lowered, so that at 1 MHz it falls to about 200 Ω for an EEG type electrode, while in the ranges typical to EIT the typical contact impedance is 100 Ω to 1 kΩ[58]. A common way to try and minimise the level of contact impedance is to abrade the skin where the electrodes will be placed. However, this can induce another problem as the amount by which the contact impedance has been reduced can be variable from site to site, which can result in the noise on different electrodes being uncorrelated.

In addition, electrodes will possess an electrode-electrolyte potential, as the metal electrode, being in contact with a salt solution, will have ions move in and out of it, until an equilibrium is reached. However these electrode potentials do not cancel out perfectly due to differences in the tissue underlying electrodes and as the potentials will change with time. A means of overcoming this is to use slow electrolysis, as rapidity leads to a brittle coating, to stabilise this interaction, such as the formation of a Ag-AgCl electrode. An Ag-AgCl electrode is stable and has a combined electrode potential less than 5 mV, as compared to approximately 8 mV for a silver electrode[58].

Another key source of electronic artefact can be due to stray capacitance, in which two adjacent conductors will act like a small capacitor, leaking signals into undesired routes. However as the capacitance of the leads and electronics are out of phase, only recording the in phase impedance component can be used to circumvent these errors. A range of other methods of error reduction including reciprocity, averaging, subtraction and filtering can be implemented and are discussed later where relevant. A review of these topics can be found in a 2006 review by Bayford[59].

1.3.3 Bioimpedance measurements of fast neural activity

There is a long history of measuring impedance changes during neuronal activity, dating back to the 1930s, with decreases in impedance being recorded in frog's nerves and squid giant axons[60]. The basis of such recordings is that if current of a sufficiently low enough frequency is applied it will not pass across the capacitive membrane, yet when the voltage-gated sodium channels, associated with activity open, the current can more readily move through the cell and so the bioimpedance of the neuron reduces. Despite the simple basis of impedance changes during neural activity, concerns regarding artefact were a consideration during these early experiments, such as the change in impedance being due to the stimulus. This potential artefact was excluded by showing that the change in impedance was directly proportional to the applied voltage while the action potential was unaffected[61], a technique that is still effective.

A number of repeated experiments have been undertaken on crab nerves: Boone produced a compound action potential (CAP) using a stimulator and applied a direct

current (DC) driven between two electrodes 1 mm apart and measured the resultant voltage from two electrodes: one proximal to the driving electrodes and the other several centimetres more distal[62]. Following this a DC was applied in the opposite direction therefore making a square wave allowing for subtraction to isolate the impedance change, which was a decrease of approximately 0.5 to 1 %. Similar studies have been undertaken in the same group using stimulation of the walking leg nerve of the crab *Cancer pagurus* to evoke CAPs for impedance measurement. Current injection at 1 Hz with an amplitude from 1 to 10 µA produced impedance decreases of 0.85 ± 0.40 % (mean ± standard deviation (SD)). The results were confirmed to be real and not artefactual by showing a correlation between increasing injected current and recorded voltage, while the CAP was unaffected, and also that the impedance decreased with increasing current injection electrode spacing[63]. Later work on the same experimental setup looked at the effectiveness of different frequencies of the injected current, 1, 225 and 825 Hz, which produced decreases in impedance of 1.00 ± 0.13, 0.19 ± 0.03 and 0.060 ± 0.004 % (mean ± standard error of the mean (SEM)), respectively[64].

Impedance measurements have also been undertaken on cortical activity. Freygang and Landau used a four electrode arrangement with 0.3 to 0.7 ms applied DC pulses to measure impedance decreases of 3.1 ± 0.8 % (mean ± SD) from cat cortex following cortical stimulation[65]. In a series of studies looking at seizure activity and normal neuronal activity, via evoked responses, Van Harreveld and Schade measured the impedance change in cat and rabbit visual cortices following visual stimulation, but commented that impedance changes could not be recognised with certainty[66]. Adey et al. were able to record impedance decreases of 1.4 to 1.8 %, in cat cortices following a range of visual stimuli: a person in the room, exposure of a female cat to a male cat and presentation of milk. It was also noted that these changes had an onset of 2 to 5 s and decayed to baseline after 20 to 30 s[67]. Aladjolova undertook experiments in which the cortex of rabbits' was stimulated to produce a forepaw twitch. This stimulus was reduced until there was no motor response, and at this point an average impedance decrease of 1.5 % could still be recorded[68]. In contrast to the findings detailed above much smaller changes were found by Klivington and Galambos who in 42 cats used an intracranial wire and epicortical platinum plate electrodes to measure auditory evoked responses in cats and recorded an impedance change of −0.003 % with an injected current of 10 kHz, which is at such a high frequency as to readily pass through the neuron membrane even during its resting state[69]. Boone undertook a series of epicortical recordings on rabbits, which had their median nerve stimulated, with a square wave current source and electrodes 1 to 3 mm apart and measured at 9 mm apart. Impedance changes of −0.01 to 0.03 % were reported, with a noise of 0.03 % after 800 to 2000 stimulations[62] (see table 1.3 for a summary of the above detailed studies). The next step from making measurements of the impedance

change that occurs during neuronal activity is to attempt to make current injections at multiple points and record these changes at multiple sites around the active tissue in order to allow tomographic reconstruction; this is the aim of EIT of fast neural activity.

Source	Experimental Model	Impedance Change	Comments
Boone (1995)[62]	Crab Nerve	-0.5 to $-1\,\%$	
Gilad et al. (2009)[63]	Crab Nerve	$-0.85 \pm 0.40\,\%$	
Oh et al. (2011)[64]	Crab Nerve	$-1.00 \pm 0.13\,\%$	1 Hz
		$-0.19 \pm 0.03\,\%$	225 Hz
		$-0.060 \pm 0.004\,\%$	825 Hz
Freygang and Landau (1955)[65]	Cat Cortex	$-3.1 \pm 0.8\,\%$	Direct cortical stimulation
Van Harreveld and Schade (1962)[66]	Cat & Rabbit Cortex	No identifiable changes	
Adey et al. (1962)[67]	Cat Cortex	-1.4 to $-1.8\,\%$	Varied visual stimuli
Aladjolova (1964)[68]	Rabbit Cortex	$-1.5\,\%$	Subthreshold cortical stimulation
Klivington and Galambos (1968)[69]	Cat Cortex	$-0.003\,\%$	10 kHz
Boone (1995)[62]	Rabbit Cortex	-0.01 to $-0.03\,\%$	

Table 1.3: *Summary of single channel impedance measurements made of fast changes that occur during/as a result of neural activity.*

1.4 Electrical impedance tomography

The first published impedance images were produced by Henderson and Webster, using a rectangular array with 100 electrodes on one side of the chest and a single large earth on the contralateral side and the areas found to have low conductivity were deemed to represent the lungs[70]. It was in the same year that Benabid et al. suggested an EIT system for imaging the brain, with a prototype with two parallel arrays immersed in a saline tank able to detect impedance change due to an object inserted between the electrode arrays[71].

The instrumentation of EIT systems usually consists of a collection of electronics to supply a constant current, and record and relay the measured voltages, from a series of electrodes; the most notable and widely used of such systems being the Sheffield Mark 1[72]. The experimental setup also requires a computer to store and later process the data.

In addition to the impact that technical improvements can make to this fundamental set-up, in theory a higher spatial resolution can be achieved by injecting from many electrodes at once. Groups have suggested that different combinations may be used to give fixed patterns of increasing spatial frequency [73–75], and that these patterns may be automatically adjusted to give the best image resolution [76], however, the benefits of these are largely outweighed by the greater precision and subsequent technical complexity required.

There are also different options for the over-arching data collection strategy: dynamic and absolute imaging. In dynamic imaging the impedance change is compared to baseline, which offers the best means of eliminating a range of error sources as over the short term the only contributors to impedance change should be physiologically based. Absolute imaging in contrast is more sensitive to instrumentation error and this is often dealt with by making the dynamic aspect frequency rather than time. This imaging of difference between frequencies is often termed electrical impedance spectroscopy or multi-frequency electrical impedance tomography (MFEIT). MFEIT works on the basis that different tissues have different impedance characteristics at different frequencies [77].

1.5 Image reconstruction

Back projection can be used to reconstruct tomographic images of changes in EIT, by assessing the change in impedance for each combination and defining the recording pairs volume of sensitivity, followed by using filters to sharpen the image. This method of image reconstruction requires an assumption of uniform resistivity and is applicable to two dimensional imaging only. An alternative and more commonly used reconstruction is based upon the production of a 'sensitivity matrix' [78]. The 'forward solution' of this reconstruction is based upon a calculation of the expected voltages for each combination from the expected resistivity for a voxel, the accuracy of which is iteratively improved, which results in the generation of a sensitivity matrix. Obviously, each voxel contributes a different amount to the voltage measured by a given electrode pair and so images can only be produced if a sufficient number of independent measurements have been made. An inversion of the sensitivity matrix, which contains the voltages for each combination and the factor by which these are related to their respective resistivities, yields the resistivity for each combination. The data within this inverted matrix are also regularised through a range of mathematical procedures (where different regularisation procedures are employed within the thesis further explanation is given). One of the limitations with this reconstruction is the assumption of linearity in a non-linear model, as the assumption that the relationship between voxel resistance and its effect upon the recorded voltage is linear must be made [45;59]. Non-linear methods have been employed; however,

historically these have been eschewed due to increased computational complexity and therefore computational time. Moreover, the non-linearity of EIT is most apparent for larger conductivity changes of approximately 10 to 20 %[79] and so can often be ignored, nonetheless work continues to optimise non-linear approaches[80].

1.6 Applications of EIT of the head

Potentially, EIT might be applied clinically to the imaging of a range of body systems, but it is not of ubiquitous use for all associated imaging needs. In fact as can be seen in section 1.2 imaging modalities always offer a balance between different advantages and disadvantages and as such the applications of EIT should play to its strengths: low cost, portability, no risk/radiation exposure and high temporal resolution. The main areas of EIT imaging are lung ventilation, with current work looking at its use in long term ventilation, cardiac function, gastric structure and emptying, brain function and pathology and breast cancer[59;78;81].

In addition to the imaging of brain function, both slow and fast, work has been undertaken to assess the role of EIT in imaging acute cerebral stroke and epileptic activity in the brain. Stroke is a major cause of morbidity and mortality, and is due to an interruption in the brain's blood supply, and therefore oxygen and metabolite delivery, due to either obstruction of the blood supply by means of thromboembolism or due to haemorrhage following the rupture of vasculature. The potential role of EIT in stoke is earlier diagnosis of the subtype of stroke, which has implications on its treatment. Pharmacological thrombolysis in thromboembolic stroke offers the chance to avoid potentially irreversible brain damage, but must be given within 3 h of the onset and is potentially fatal if given in a haemorrhagic incident. Therefore EIT could potentially allow for first responders to diagnose the type of stroke and administer thrombolytics before their window of administration has passed. For epilepsy EIT offers depth advantages over the commonly used modality of EEG, as detailed in section 1.2, and has the advantages of being inexpensive and portable enough to allow for continuous recording[59;78;81].

1.7 Electrical impedance tomography of fast neural activity

From an understanding of the changes in electrical properties that occur to a neuron during electrical activity and from previous work showing that impedance changes occur during neuronal activity, it is clear that it is not unreasonable to imagine that EIT might allow for the production of tomographic images with a high enough temporal resolution to show the fast changes of neuronal activity. Therefore there has been a recent surge in

interest and research aimed at achieving this goal.

Liston et al. undertook extensive modelling in an attempt to show what order of magnitude of impedance changes might be theoretically expected during fast neural activity[82]. First, the changes of a peripheral nerve, being a simpler model, were predicted, then cortical nerves and bulk cortical tissue and finally the changes that might be measured on the scalp were modelled. As with much of the work associated with EIT certain shortcomings existed, highlighted by the authors, as a result of assumptions that had to be made. In particular the more complex model of the cortical neurons was only based upon figures obtained on cat spinal motor neurons, and the modelling of dendrites was not ideal, although evidence to show the excitable nature of dendrites[83;84] suggests that this might not necessarily have been a problem.

Liston et al. predictions for peripheral nerves for direct current injection, once the effect of capacitance and incomplete depolarisation was taken into account, was 2.8 %, which is somewhat larger than those found in previous impedance recordings (table 1.3). It was suggested that this disparity in results may have been due to experimental problems causing the peripheral nerve impedance changes to be underestimated. Liston et al. predicted a cortical decrease, with the same considerations as above, of 0.6 to 1.7 %, which with the attenuation of a highly resistive skull, would be between 0.006 to 0.17 % with an attenuation between 10 and 100 times. Again these predictions are in broad agreement with prior findings. Citing the impedance decreases noted by Boone (1995)[62], Liston et al. commented that with the noise levels Boone reported and their smallest predictions for scalp changes, the SNR would be two and so at the limit of detection. Liston et al. suggested the use of a better anatomical model might improve the localisation of such changes, as electrode mislocalisation is an importance source of error, something others have since addressed[82].

Gilad et al. examined a range of means of optimisation, an exceptionally important topic if such small changes are to be accurately reconstructed, and the calculation and limits of current density in the head. Gilad et al. commented on the importance of accurate meshes for reconstruction, and describe the use of a finite element method (FEM) mesh with 53 336 tetrahedra and realistic layering far more realistic than the homogeneous sphere often used in other reconstructions[85]. Using a similar FEM mesh produced from high resolution MRI scans, modelling was undertaken by Gilad et al. to predict the impedance changes that might occur as a result of visual evoked responses. Peak changes of 0.004 % with an SNR of about 4 were predicted with the conclusion that *in vivo* recordings would find reproducible changes, but that the low SNR would be prohibitive to image reconstruction[86].

Tidswell et al. reflected upon the importance and difference in results produced by different head electrodes and scalp preparation. A difference in SNR of 3.1 $\pm$ 0.4 and

1.4 ± 0.1 was shown for the best and worst setup, respectively [87], which once again highlights the importance of optimisation of all aspects of EIT recordings if the aim of accurately imaging such small and transient changes is to be achieved, although in this study fast changes were not being recorded.

The first imaging of physiological evoked activity was undertaken by Holder et al., and offered hope that image reconstruction of such small changes might be possible, although these changes were largely due to slower changes, such as increased regional blood flow [25]. More recently, the first successful images have been produced from rat cortices, which are discussed after consideration of human single channel recordings due to the significance of these first images of neural activity.

Earlier work by Holder had been undertaken to attempt to produce similar recordings that might later allow for recording in humans that might be reconstructed, but as with similar work since these attempts were unsuccessful. Although not strictly EIT recordings, as a four electrode method was used, it did involve attempts to measure short latency responses to visual and somatosensory stimuli using scalp electrodes. Unfortunately, the peak impedance changes were only about 0.001 %, and these were not consistent and none of the short latency changes were significantly different to baseline [88].

A more successful set of fast neural activity recordings were more recently undertaken by Gilad and Holder. Although again single channel recordings, they produced more promising results regarding the feasibility of recording fast impedance changes. Using scalp electrodes and a visual stimulus of a checkerboard pattern changing twice a second, visual evoked responses were recorded with a current injection of a 1 Hz square wave of 0.1 to 1 mA at one of two injection sites over 10 min. These recordings were performed 16 times in six subjects and an average impedance decrease of 0.0010 ± 0.0005 % (mean ± SEM) was recorded. This was in broad agreement with the suggested size of such changes from prior modelling studies, but, as suggested in Gilad's prior modelling study, Gilad et al. (2009) [86], the SNR was too low, at 2:1, for imaging to have been possible if multiple injection had been undertaken. Again the concern of artefactual impedance changes due to the injected current affecting neuronal activity was addressed, but Gilad and Holder claimed that this could largely be dismissed due to the amplitude of the injected current being insufficient to alter neuronal activity and also citing the similarity with modelling changes. This study, although only a single channel recording, showed, for the first time, that such impedance changes could be measured in humans and also highlighted that if the ultimate aim of image reconstruction was to be met then further work would be required to improve the SNR, such as technical improvement, multiple injection sites, lengthened averaging times and the implementation of other means of noise reduction [89].

In a methods paper Oh et al. detailed the principles underpinning the success of

imaging fast activity with EIT. The authors aimed to develop a means of recording the impedance changes associated with neuronal depolarisation with a low-frequency EIT system[64]. This system was first validated in the crab nerve studies detailed above[63]. One of the key realisations was that whilst bioimpedance theory suggests that the maximum signal occurs near DC, the maximum SNR occurs at higher frequencies than this. This is because the ECoG, which is the main source of noise and is 100 to 1000 times larger than the signal, has a frequency spectra of <100 Hz. Therefore by injecting a sine wave current of >100 Hz Oh et al. could reduce the noise by a greater amount than the attenuation of the signal and so improve the SNR. Therefore using a rat model and a platinum silicone electrode with 29 contacts they made epicortical single channel recordings. The recordings were made of somatosensory evoked potentials (SEPs) produced by stimulation of the contralateral forepaw with pulses 100 µs in duration and 5 to 10 mA at 2 Hz. Current was applied at a series of frequencies, 125, 225, 325, 625 and 1225 Hz, and a range of current amplitudes, 2, 5, 10, 20, 50 and 100 µA. A signal of -0.074 ± 0.010 % and -0.07 ± 0.01 % was found at 125 and 225 Hz, respectively, and this decreased with increasing frequency, with 225 Hz appearing as the optimal frequency as the bandpass filter, ±125Hz, allowed for better exclusion of ECoG noise and an SNR of 50. It was reported that there was no effect from increasing current up to 50 µA and a non-significant decrease at 100 µA, this, in addition to the changes being in agreement with modelling studies, was suggested as evidence that the current injection was not affecting normal neuronal activity. These findings were impressive and led to multi-channel imaging studies. However, one of the key limitations and future aims of this study was the limited temporal resolution, which was 8 ms, as a result of the demodulation bandwidth.

The experimental set-up and data collected by Oh et al. was then expanded into a multi-channel imaging study. In these experiments the same electrode design was used to place electrodes intracranially in an anaesthetised rat model, from which both the evoked potentials (EPs) and impedance changes were extracted. In these experiments current was injected at 50 µA and at 225 Hz. The current amplitude of 50 µA was used as it gave the maximum SNR in pilot studies without attenuating the EPs or impedance change. Although it was noted that this was a higher current than modelled, the acceptability of this higher current level was attributed to a partial volume effect. The carrier frequency of 225 Hz, with a bandwidth of ±125Hz, was used as it was found in the group's prior work[64] to be the optimal carrier frequency, given the limitations of their hardware. Overall, 57 technically valid recordings were made in four stimulation modalities: forepaw, whisker and hindpaw somatosensory stimuli and visual evoked responses and from this data images were reconstructed (this study is the focus of chapters 3 and 4 and discussed in further detail in section 3.1.1). Identified areas for future work were the use of specific meshes, exact electrode localisation, and, as previously noted by Oh et al.,

improvements in temporal resolution. The final point might be addressed by finding a balance between SNR and temporal resolution somewhere between 200 and 2000 Hz for a resolution of around 1 ms[90].

Experimental Model	Source	Experimental Paradigm	Impedance Change	Comments
Modelling	Liston et al. (2012) [82]	Peripheral Nerve	−2.8 %	DC injection
		Cortical bulk/with skull	−0.6 to −1.7 %/−0.006 to −0.1 %	Predicted SNR of 2
	Gilad et al. (2009) [86]	Scalp Recordings	−0.004 %	Predicted SNR of 4
Peripheral Nerve Studies	Boone (1995) [62]	Crab Nerve	−0.5 to −1 %	
	Gilad et al. (2009) [63]	Crab Nerve	-0.85 ± 0.40 %	
	Oh et al. (2011) [64]	Crab Nerve	−1 to −0.06 %	1 to 825 Hz
Animal Cortical Studies	Freygang and Landau (1955) [65]	Cat Cortex	-3.1 ± 0.8 %	Direct cortical stimulation
	Van Harreveld and Schade (1962) [66]	Cat and Rabbit Cortex	No identifiable changes	
	Adey et al. (1962) [67]	Cat Cortex	−1.4 to −1.8 %	Varied visual stimuli
	Aladjolova (1964) [68]	Rabbit Cortex	−1.5 %	Subthreshold cortical stimulation
	Klivington and Galambos (1968) [69]	Cat Cortex	−0.003 %	10 kHz
	Boone (1995) [62]	Rabbit Cortex	−0.01 to −0.03 %	
	Oh et al. (2011) [64] and Gilad et al. (2010) [90]	Rat Cortex	-0.07 ± 0.01 %	Limited temporal resolution, imaging study
Human Studies	Holder (1989) [88]	Scalp recordings	−0.001 %	Non significant changes
	Gilad and Holder (2009) [89]	Scalp recordings	-0.0010 ± 0.0005 %	SNR of 2

Table 1.4: *Summary of single channel impedance measurements and EIT measurements made of fast changes that occur during/as a result of neural activity*

1.8 The rat sensory nervous system

The sensory neurophysiology of rat's cortex is the key model employed in this thesis, and examination of the processing of sensory stimuli of the forepaw, hindpaw, vibrissal and visual systems will be undertaken. Therefore the key aim of this section is to cover ascending pathways, that is transmission of information from receptor to brain, topographical discretisation within the cortex, cortical lamination, and columnar organisation, and then examine the specifics of these for the different evoked responses that will be examined within this thesis.

1.8.1 Hierarchy of transmission: receptor to cortex

The sensory system supplies information from peripheral receptors to the brain, which processes the data at a variety of levels of complexity. The peripheral receptors are analogous to analogue-to-digital converters (ADCs), in that data from the external world, being generally grouped as visual, auditory, somatosensory, gustatory and olfactory, must be collected and then converted into a signal that can be processed within the brain. Often each receptor organ responds to an aspect of the input, such as a colour of the light spectrum or modality of touch, such as temperature, and also have an area of sensitivity, known as a receptive field, within which an appropriate stimulus will result in activation of neurons.

The neurons carrying signals from sensory receptors are afferent neurons of the PNS. These neurons project to the CNS, typically either to spinal cord ganglia or nuclei, brainstem nuclei, or other subcortical targets, such as thalamic nuclei, and often via a series of targets. At some point along a neuron's final projection to the cortex it is common for the neurons to cross over, or decussate, to the contralateral side of the cortex, although this is not a ubiquitous behaviour.

The final target of ascending sensory neurons are to, varyingly discretised, often topographical, areas of the cerebral cortex. For example, the rat's somatosensory area lies in the parietal region of the cortex, while the visual cortex lies in a separate area in the occipital region of the cortex. The topography of the human cortex is most often associated with work of the neurosurgeon Wilder Penfield, who identified and mapped the primary motor cortex, which, similar to the primary somatosensory cortex, also has a topographical map. In the mid-20$^{\text{th}}$ century, Penfield and Boldrey, while undertaking operations in order to alleviate patients' epileptic symptoms, were stimulating various areas of the cortex to identify vital ones that should not be removed. During this process, Penfield and Boldrey discovered that stimulations applied to the precentral gyrus, also known as the motor strip, resulted in highly localised muscle contractions on the contralateral side of the body, and in addition to this that there was a somatotopic representation of the

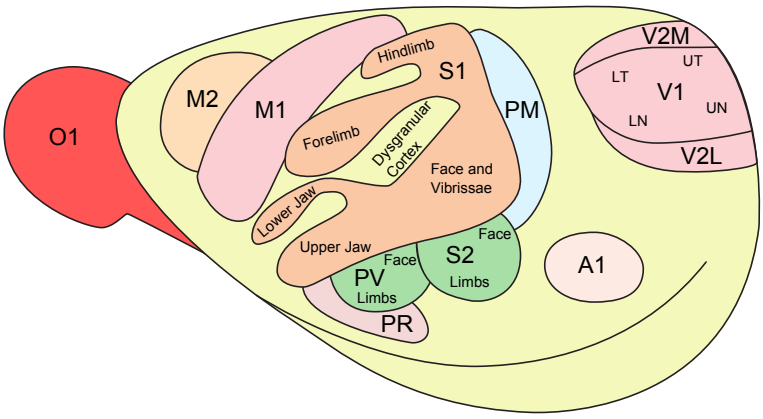

Figure 1.4: *Lateral view of the rat's cortical areas and their topography. The primary somatosensory cortex (S1) has a body representation, the ratunculus, which has finer representations for the paw digits and the large vibrissae. S1 is surrounded by association cortices: the secondary somatosensory cortex (S2), dysgranular cortex, and the parietal-ventral (PV), parietal-medial (PM), and parietal-rostral (PR) areas. The S2 and PV regions have additional body maps. The primary visual cortex (V1), and medial and lateral secondary visual cortices (V2M and V2L) also have a topography. Only a coarse retinotopic map of the visual field is shown for V1: upper and lower temporal (UT and LT), and upper and lower nasal (UN and LN). Also shown are the primary motor cortex (M1), secondary motor cortex (M2), auditory cortex (A1), and olfactory cortex (O1). Modified from Kaas (2009)[93], with permission from Elsevier.*

corresponding parts of the body[91]. The same topography has been found in the rat somatosensory cortex, and whilst the discovery of Penfield and Boldrey was termed the motor homunculus, the rat's equivalent is the ratunculus (Figure 1.4). Such topography has also been identified in the visual cortex and this is referred to as retinotopy; the retinotopic map reveals different neuronal populations responding to different portions of the visual field. The afferents supplying these areas typically arise from topographically organised sources, although there are also non-topographical areas: noradrenergic cells of the locus coeruleus, serotoninergic cells of the midbrain, cholinergic cells of the basal forebrain, and in dopaminergic cells of the midbrain. The non-topographically arranged areas projecting to the cortex may have a role in controlling cortical excitability, arousal and consciousness[92].

Despite the elegant simplicity of the topographical maps, they are not fixed in their layout, with the ability of the cortex to rearrange, known as plasticity, being an important consideration. Although the main topographic features are found to be common to all animals, cutaneous map configuration and areal extent vary substantially across individuals; early developmental experience refines and consolidates cortical functional organization. However, such reorganisation can also occur in later life; in a study by Coq and Xerri it was highlighted how, in the rat forepaw cortical region, cortical maps are con-

tinuously in use-dependent flux, with environmental enrichment refining the topography, but also increasing sensitivity [94]. There have been similar findings of inter-individual topographical variation in other cortical areas, such as the whisker representation [95], and in other species.

The traditional view is that these primary areas, such as primary somatosensory cortex (S1) and primary visual cortex (V1), then send projections to association cortices, such as secondary somatosensory cortex (S2) and secondary visual cortex (V2), which are typically numbered in an ascending fashion. This has led to a view of the nervous system and cortical processing as a hierarchical, or feed-forward, system, but, although this is in part true, the system has more complex connections. For example, often different systems integrate in a more lateral, rather than hierarchical, fashion, and connections from the cortex to subcortical areas, via feedback projections, occur. The importance of this is clear from a series experiments by Kulics et al. where monkeys were trained to report the intensity of a stimulus through the use of a button press. It was determined that the first negative-going evoked potential component (N1), which reflects signalling between S1 and S2, correlated best with behavioural reports of the sensation, that is belief of a weak stimulus resulted in a smaller N1 signal, and vice versa, and this correlated to the chosen action [96]. This reflects the situation that cortical hierarchy is not strictly serial, and rather primary areas depend on higher areas as secondary input for priming and predictive mechanisms.

The reality is that both serial labelled-line processing, where each receptor signal is transmitted through a chain of relays without cross-talk, and integrative parallel processing occur. Labelled-line processing provides the advantage in the somatosensory system of a stimulus conveying information of the exact location of the input [97]. Nonetheless, around 70 % of cortical synapses result from intracortical connections between cortical cells. This high level of integrative, self-connectivity is almost certainly responsible for the high level of sensory processing and plasticity possible in the cortex [98]. Similarly, feedback has an important role in the sensory system; the ability to make fine tactile discriminations or to ignore somesthetic information in certain situations is facilitated by cortical feedback projections, these modulate the feed-forward transmission of tactile information at each level of the somatosensory system [99].

1.8.2 Neocortical lamination

The neocortex is the outermost aspect of the cerebral cortex and is subclassified into several types: homotypical, found in frontal, temporal and parietal lobes, and heterotypical, which is subdivided into granular, also known as koniocortex, and agranular cortex, which are found in sensory and motor cortical areas, respectively. The neocortex is noted for its horizontal layers or laminae, of which there are six in the granular cortex of the

somatosensory and visual cortical areas. This lamination originates in the embryological development of the neocortex; new cells migrate radially, outward from proliferative areas and invade the previously laid down waves of cells, and push through these to lie superficial to them. The resultant layers are numbered from I, closest to the pial surface, down to layer VI, adjacent to the white matter, with subdivisions of a, b and c, from superficial to deep, sometimes also being used. This lamination was first identified based upon histological differences in cell distribution and is also evident in afferent and intrinsic axon distribution, which in turn underlies the functional lamination of the cortex [92].

The neuronal cells of the neocortex can be subdivided in multiple different ways: division being excitatory and inhibitory, and division based upon cell morphology, with cells described as pyramidal or non-pyramidal, and spiny or non-spiny cells. The division of spiny and non-spiny regards those cells possessing substantial populations of dendritic spines and those that do not, respectively, but also a difference in neurotransmitter: spiny neurons produce the excitatory transmitter glutamate, while non-spiny neurons produce the inhibitory neurotransmitter γ-aminobutyric acid (GABA) [92]. The term pyramidal refers to the triangular shape of the soma of these cells, with the pyramid's apex, usually oriented toward the pial surface and possessing a dendrite that is typically oriented upwards, although some in layer II run horizontally. A pyramidal cell's apical dendrite is typically its thickest and is not branched [100]. Noting whether a cell is pyramidal or not reflects a difference between extrinsically and intrinsically projecting neurons: both cells have dendrites and axons that can extend into or through other layers, but the majority of pyramidal cells, with somata in any layer, send their apical dendrites through all superficial layers into layer I, and are also a main output cell of the cortex, projecting to subcortical, and ipsilateral and contralateral cortical targets. The majority of non-pyramidal neurons are non-spiny and so inhibitory cells, and account for up to 30 % of the total population of cortical neurons [92].

There are three main types of excitatory cell in the neocortex: the pyramidal cell, the spiny stellate, and the star pyramid, with the latter being intermediate between the former two. Spiny stellate cells have a star-shaped, anisotropic dendritic pattern and are mainly vertically oriented with connections to layers II, III, and IV, and sparsely to layers V, and VI [100]. Star pyramid cells have an ascending apical dendrite as found in pyramidal cells in general, but their somata are not as overtly pyramidal as pyramidal cells, nor the apical dendrite as long, and have apical basal dendrites, unlike spiny stellate cells. Star pyramid cells are mostly located in layer IV and like spiny stellate cells connect to layers II, III, and IV, and sparingly to II, and VI. Although most of the connections of star pyramid cells are vertical, some are horizontal connections and some more diagonal and rambling than those of spiny stellate cells. It is important to note that such broad categorisation can give an incomplete view of cortical cellular diversity, for example, there

are numerous subtypes of inhibitory cell in the cortex, and full diversity almost defies any summary [100].

1.8.3 Connectivity of the laminae

The cells and connectivity of the neocortical laminae vary between the different cortical areas, nonetheless there is some archetypal circuitry and cell distribution, and so each layer is described in turn as well as the canonical circuit.

Layer I possesses few cell bodies, with those present being mainly neuroglia and non-pyramidal cells, for this reason it is often termed the molecular layer, although it has also been referred to as the the plexiform layer due to the presence of a tangential fibre plexus. In addition to this plexus, in the deepest aspects of layer I there is a condensation of fibres termed the stria of Kaes or Becheterew [92]. In rats, feedback projection from S2 to S1 terminate heavily in layer I, avoiding layer IV, and can branch horizontally over several millimetres within layer I [101]. It is typically held that the majority of terminations in layer I are apical tufts of pyramidal neurons from deeper layers and cortical projections, however Rubio-Garrido et al. determined there is also substantial thalamic input to layer I. Rubio-Garrido et al. examined, through the used of labelled tracer, thalamocortical connectivity in 75 adult, female Sprague-Dawley rats, and determined that many thalamic nuclei contain large numbers of layer I projecting neurons, which arose from matrix, or M type cells, which have also been termed calbindin-immunoreactive (CIR) neurons. These neurons were found to be numerous in many thalamic nuclei, and to have both diffuse projections, covering large areas of the cortex, and also highly convergent projections into single cortical areas. Although there is increasing interest in the CIR neuronal pathway, which also project to layer II and the upper part of layer III, most functional hypothesis are currently confined to inferences from structural studies [102;103].

Layer II contains small, tightly packed cell bodies, which are mostly small pyramidal neurons and also stellate neurons, and is referred to as the external granular layer [92]. Deep to layer II is layer III, which is a thick layer mainly possessing small to medium-sized pyramidal cells, whose somata increase progressively with depth, hence it being referred to as the external pyramidal layer, and also non-pyramidal neurons that have vertically-oriented intracortical axons. Layers I, II and III, which when considered together are often referred to as the supragranular layers, are a key target of interhemispheric and intrahemispheric corticocortical afferents, and layer III itself is the primary source of corticocortical efferents, although both occur in other layers as well [92].

Layer IV, also known as the internal granular layer, is thin, but is densely packed with small pyramidal, and non-pyramidal cells [100], and possess a horizontal plexus known as the 'outer band of Ballinger', formed by thalamocortical terminals [92]. The glutamatergic, spiny, non-pyramidal, stellate cells that dominate layer IV, are the major recipients of

thalamic synapses and their axons provide the main route for transmission to other layers[92]. The thalamocortical afferents that supply layer IV, and also the deeper aspect of layer III, arise from parvalbumin immunoreactive (PIR) thalamic neurons, which do not arise diffusely, as with CIR neurons, but are confined to the principal sensory and motor, pulvinar, and intralaminar nuclei[103], although in the rat pulvinar is almost non-existent.

Layer V consists of large, loosely packed, pyramidal cell somata and is consequently referred to as the ganglionic or internal pyramidal layer. Within the deeper aspect of the layer is the 'inner band of Ballinger', although in the visual cortex this is referred to as the 'stria of Gennari' and, rather than consisting of thalamocortical axons, consists of corticocortical axons. The pyramidal cells of layer V, with some exceptions, particularly in deepest aspects of layer V, act as the principal source of efferents to subcortical targets and other, ipsilateral and contralateral, cortical areas. The subcortical projections from layer V are not to the principal thalamic input, but to an array of other subcortical structures; the pathways from layer V are corticospinal, corticobulbar, corticopontine, corticorubral, corticotectal, corticostriatal, and corticothalamic fibres to non-specific thalamic nuclei, although these targets are different for different cortical areas[92].

Layer VI has few large pyramidal neurons, but is relatively densely packed with small, round, spindle-like, pyramidal somata and multiform neurons, and consequently is known as the polymorphic or multiform layer, and when grouped with layer V these layers are referred to as the infragranular layers. Extending through layers VI to I is a vertical bundle of axons, known as the radial fasciculi, which consists mainly of efferent pyramidal and non-pyramidal neurons and becomes thicker with depth as more axons join the bundle. The modified pyramidal cells in layer VI send both excitatory and inhibitory efferents to the principal thalamic nucleus, which results in a reciprocal cortical and thalamic connection, and also projects to the claustrum and other, functionally similar, cortical areas[92]. In a study employing laser-scanning photostimulation in thalamocortical slices, Lam and Sherman posited that cholinergic suppression of the inhibitory output of layer VI to principal thalamic nuclei facilitated modulation of somatosensory input, which was compared to a gain control[104], which is something later studies have gone on to examine.

Olsen et al. undertook *in vivo* and *in vitro* work in the mouse visual cortex to examine the inhibitory role of layer VI. This involved selective labelling of layer VI pyramidal cells, which revealed two populations, the first projecting back to the principal thalamic nuclei, and the second having terminations in superficial cortical layers, which is similar to the connections connections of layer VI neurons in the rat sensory cortex[98]. Layer VI neurons were conditioned to express a light sensitive cation channel so that when stimulated with a light-emitting diode (LED) they would become active. In addition to this optogenetic stimulation, the mice were also presented with drifting gratings, and this was alternated with control trials, that is with visual stimulus only, and the resultant activity

was measured with a linear multichannel probe. It was found that photostimulation of layer VI resulted in rapid and reversible, monotonic suppression of MUA and single unit visually evoked activity in layers II to V, and also suppression of spontaneous activity in V1, with the suppression being irrespective of the presented orientation. Similarly, the opposite effect could also be elicited, with suppression of layer VI resulting in increased visually evoked activity in layers II to V, suggesting that, under normal conditions, layer VI maintains some level of suppression over these layers. Layer VI was also found to be able to suppress visual responses in the principal thalamic nucleus; however, as cortical suppression preceded thalamic suppression it was suggested that suppression of layers II to V was possible without thalamic input. Further study indicated that, while both intracortical and thalamocortical circuits are involved in this gain modulation, the intracortical circuit is the main pathway of layer VI mediated suppression, which is horizontally constrained, suggesting a columnar organisation to this circuit [105].

The connectivity across the neocortical layers differs within different cortical areas of the same species, for example layer IV is absent in motor cortex, but nonetheless some canonical circuitry can be described, some of which can be derived from the connectivity of different layers, and some from functional studies. Conditional cross-correlation analysis of neurons, which reveals the strength and incidence of neuronal interactions, has revealed their synchronicity and the functional connectivity of neural circuits within the neocortical laminae. This has shown, first, that stimulus-induced synchronisation occurs in all levels of the somatosensory system, including the brain stem, thalamus, and S1 and S2, but also that certain lamina are more likely to exhibit activity from thalamocortical interactions. The highest probability of detecting stimulus-induced thalamocortical interactions is found in layer IV, with neuronal discharges in these middle cortical layers following thalamic activity by 1 to 2 ms, which points to thalamocortical interactions with these middle layers being via strong, monosynaptic connections. Similarly, the probability of detecting correlated thalamocortical interactions in supragranular targets is twice that of the probability for infragranular ones. Moreover, supragranular targets have a higher proportion of time-locked thalamocortical interactions within 3 ms of a cutaneous stimulus than infragranular targets. These findings indicate that feed-forward thalamic information passes to the supragranular layers and through many synaptic connections before affecting infragranular layers [99].

With regard to input, the neurons of layer IV, and also the deepest aspect of layer III, are typically the target of all extracortical projections, especially from the thalamus, and in turn make short range connections to other layers and so are the initial disseminator of subcortical feed-forward information. Typically, projections from layers IV and III are to the supragranular layers, which in turn project to layer V, and pyramidal cells in this layer project to layer VI. Other cortical inputs include corticocortical fibres, which

terminate in layers I to IV, and non-specific terminations in layers I and VI. Neocortical output can be local, such as via the horizontal collaterals of layer III and V pyramidal cell axons, or to other cortical and subcortical areas. The pyramidal neurons have an output role, with those in layers II and III being the source of contralateral and ipsilateral corticocortical projections, and those of layer V and VI being the almost exclusive origin of extracortical projections, although layer VI has important intracolumnar projections. While extracortical projections are most prominent in the bottom of layer V, projections to the principal thalamic nuclei and functionally comparable cortical areas arise in layer VI. The feed-forward projections to higher cortical areas typically terminate in layer V, while the reciprocal feedback projections terminate in layers I and II [92;99].

In addition to the histological differences and differences in connectivity between the different laminae of the neocortex, there is a simpler difference between them, thickness. The laminae of the rat somatosensory cortex are different between each of the four cortical areas under consideration in this chapter: the forelimb, hindlimb, vibrissal and visual areas. The range of thickness for each lamina in these areas, as detailed in the literature considered in this review, and the histological studies of Zilles [106] and Krieg [107], show quite a broad range (table 1.5a). This can be attributed to a combination of intersubject variability, differences in histological preparation and shrinkage correction calculations, and different means of laminar definition; however, thorough examination of these considerations is beyond the remit of the current work presented here. To address this shortcoming, the mean of the thickness for each layer has simply been taken and this has been used to determine the depth of each lamina (table 1.5b).

1.8.4 Cortical column theory

In addition to the clear surface topological specialisation of the cortex into functional areas, such as somatosensory or visual, and the lamination of the neocortex, there is a suggested organisation of the cortex into functional columnar subunits that span layers I to VI. The concept of cortical columns as an elementary unit of functional organisation is attributed to Mountcastle: 59 recordings of neuron spiking were made in the cat cortex, and it was noted that common receptive field locations could be subdivided into vertically oriented groups of neurons related to the same submodality, such as separation of deep and cutaneous groups, and it was suggested that these were capable of significant processing independent of horizontal spreading activity [114]. These findings have been extended to the motor cortex, which shows movement vector columnar organisation, and visual cortex, with the latter being the source of substantial support for the cortical column theory.

Hubel and Wiesel investigated MUA in the cat visual cortex and revealed functional subdivisions with a seemingly columnar organisation. Whilst listening to MUA through an

	Laminar Thickness (µm)			
	Forelimb Cortex [106–108]	Hindlimb Cortex [106;107]	Vibrissal Cortex [54;106;107;109;110]	Visual Cortex [106;107;111–113]
Layer I	190 - 200	180 - 200	150 - 200	125 - 150
Layer II\III	400 - 700	350 - 400	270 - 550	300 - 500
Layer IV	200 - 260	200 - 250	150 - 250	100 - 220
Layer V	350 - 400	280 - 300	350 - 750	210 - 400
Layer VI	600 - 700	300 - 400	200 - 600	360 - 400

(a) *Thickness of laminae in each of four cortical areas.*

	Estimated Laminar Depth (µm)			
	Forelimb Cortex	Hindlimb Cortex	Vibrissal Cortex	Visual Cortex
Layer I	0 - 195	0 - 190	0 - 185	0 - 140
Layer II\III	195 - 745	175 - 550	185 - 605	140 - 555
Layer IV	745 - 975	550 - 775	605 - 810	555 - 735
Layer V	975 - 1350	775 - 1065	810 - 1360	735 - 1050
Layer VI	1350 - 2000	1065 - 1415	1360 - 1785	1050 - 1430

(b) *Depth of the top and bottom of each of the laminae, calculated from the average thickness of the laminae.*

Table 1.5: *Characteristics of the laminae of the four cortical areas under consideration in this chapter, as determined from studies detailing these laminae in the rat.*

audio system, it was found that with electrode advancement, orientation shifted in steps of 15°, and that consequently an entire rotation of 180° was covered by 12 such orientation columns, which when considered as a group were referred to as a hypercolumn [115;116]. In addition to this, normal cortical oscillations have be shown to have higher correlation along vertical lines within the cortex compared to low correlation in a tangential direction, which was suggested as evidence of columnar functional organisation [117].

As detailed above, the neocortical lamina form due to the migration of repeated waves of cells to be superficial to their predecessors. During this process, neurons migrate along a scaffold of neuroglia, which remain as neuroglial septae; these structures are referred to as ontogenetic columns, which are an order of magnitude smaller than cortical columns. In response to this, Mountcastle coined the term minicolumn and suggested that columns were themselves made of multiple subunits: horizontally connected minicolumns [118]. Subsequently, columns are sometimes referred to as macrocolumns as a means of clear delineation between them and minicolumns. The number of minicolumns constituting a column has been reported as being between 50 and 80, each with a circuit of between

80 to 100 neuronal cells, so that a column comprises approximately 4000 to 8000 cells and are 300 to 500 µm in diameter [97;119]. Although columnar functional organisation has been widely accepted, there has not been a comprehensive effort to examine the nature of such processing units [93], and some have come to question the role of the cortical column as the ubiquitous, functional subunit of cortical processing, with the key shortcomings being reviewed by Horton and Adams [120].

Horton and Adams highlighted that some uncertainty exists around how many minicolumns constitute a column, with tracer injection revealing a diffuse cloud of local connections over a diameter of approximately 500 µm, which does not match the expectation of confined short-range connections uniting minicolumns into columns. The remainder of the criticism of column theory examined the visual cortex and the vibrissal cortex, known as the barrel cortex. First, although orientation selectivity in the visual cortex has been noted in multiple species, in the rat, and many other animals, these orientation maps are absent. One suggested explanation for this has been a lower prevalence of oriented cells or coarser orientation tuning, but this cannot be the case, as, for example, more than 90 % of the rat's orientation cells have angular tuning of $\leq 30°$ and so are comparable to those found in the macaque, which does possess orientation columns. Another suggested explanation is that the absence of orientation columns reflects poor visual acuity or visual cortical representation, but this too seems incorrect, as the squirrel, which lacks orientation columns, has higher visual acuity than the shrew and mink which both have orientation columns. Another visual cortex organisational phenomenon are ocular dominance columns: axons from each eye terminate in discrete, alternating strips. However, without a clear functional reason, these are variable within a species and even individuals, and are also absent in some species, including the rat, mouse, rabbit, squirrel, sheep, goat and possum [120].

The barrel cortex is a term referring to the segregation of the vibrissal cortex, of some rodent orders, into areas representing each whisker (specific details of this in the rat are given in section 1.8.6). The barrel cortex, being modularly composed of translaminar subunits, can be viewed as an example of columnar cortical organisation. However, barrels are slightly larger and much denser than columns, and are separated by septa which have a distinct neuronal circuitry to the barrels they surround and so do not conform to the barrel-column model [97]. Consequently, rather than viewing them as versions of columns, barrels might be better described as extreme somatotopic organisation, analogous to the visual cortex's retinotopy [120]. Therefore, while there is evident value and basis for concluding that cortical columns are present and reflect some functional discretisation, they cannot be seen as the ubiquitously present, fundamental base unit of the cortex, as they do not correspond to any single structure within the cortex, nor do they have a genetic mechanism underpinning their construction, and interspecies variation undermines their

functional relevance.

1.8.5 Rat forelimb and hindlimb sensory system

In this section the anatomy and physiology of the forelimb and hindlimb are detailed, which are grouped together due to their similarity. The rat barrel cortex is covered in section 1.8.6, but as it is also part of the somatosensory cortex, some concepts that are common to both limb and vibrissal sensory processing are discussed in this section, in such cases this is highlighted.

Study of the somatosensory system in general has focused heavily on the paw or hand representation; however, in the rat this is not the case, as the representation is not as highly developed as in many other species. This shortcoming is overcome by a large whisker representation, with the representation of the forepaw in S1 being 79 % that of the vibrissal representation, and the ratio between the respective first positive-going evoked potential components (P1s) being 0.66 ± 0.27[121]. Nonetheless, the rat's paws are functionally important, which is clear in their behavioural use. For example, rats commonly stand on their hindpaws to allow free use of their forepaws to feed, perform tactile exploration, or even box during aggressive behaviour.

1.8.5.1 Receptors

Somatosensory receptors are able to detect a range of mechanical, thermal and noxious stimuli by means of the peripheral terminals of afferent neurons, which have their somata in the dorsal root ganglion, a nodule on spinal cord's dorsal root.

Cutaneous receptors include Pacinian corpuscles, Merkel, Ruffini, Golgi-Mazzoni, Lanceolate, and free nerve endings. Merkel, Ruffini, and Golgi-Mazzoni endings are all mechanoreceptors, but are found in different body regions and possess different properties. Merkel endings are touch responsive mechanoreceptors that are present in both glabrous and hirsute skin, and are associated with slowly adapting cells and have small receptive fields. Ruffini endings are also slowly adapting, but are tissue stress responsive and found in hard skin, the hard palate, periodontal ligaments, and the dura mater. Golgi-Mazzoni endings are rapidly adapting mechanoreceptors found in glabrous skin, the oral mucosa, and genitalia. Deep Lanceolate endings are also slowly adapting, while those found superficially are rapidly adapting; Lanceolate endings are coupled to hair follicles via collagen fibres. Pacinian corpuscles are sensitive to vibration, possess very large receptive fields, and are found in interosseous and mesenteric membranes. Free nerve endings are found extensively throughout the body in both glabrous and hirsute skin, in muscles, joints and viscera, and are nociceptors and thermoreceptors. In addition to these cutaneous receptors there are also deeper receptors, which include muscle spindles,

Golgi tendon organs and joint proprioceptors[122].

1.8.5.2 Ascending pathways, brainstem nuclei and thalamus

The neurons innervating the peripheral receptors collate into large nerves, such as the median and sciatic nerves in the forepaw and hindpaw respectively, which then ascend towards the cortex in ascending spinal pathways: dorsal column-medial lemniscus pathways and spinothalamic tracts.

The dorsal columns are located in the dorsum of the spinal cord and consist of the medially located gracile fasciculus and laterally located cuneate fasciculus; the topographical representation of the dorsal columns, from lateral to medial, is distributed cranial to caudal. The dorsal column pathways not only contain descending pathways, but also ascending pathways, and while they carry projections to the dorsal column nuclei, there are also termination in the grey matter of the spinal cord. Although the dorsal columns are typically viewed as carrying primary afferents, they also consist of approximately 30 to 40 % postsynaptic dorsal column neurons that are not primary afferents, but are rather activated by unmyelinated primary afferents. The spinothalamic tracts are located in the ventral aspect of the spinal cord and transmit thermal, nociceptive, and innocuous stimulus information (Figure 1.5). Approximately 50 % of the spinothalamic tracts consist of cervical fibres that respond to a wide range of stimulus thresholds, and very few are from the lumbar region, with those that are present being low threshold fibres[122].

The ascending spinal cord pathways terminate in brainstem and thalamic nuclei. The somatosensory medullary nuclei are the dorsal column nuclei, which include the gracile, cuneate and external nucleus, the nucleus Z, and the lateral cervical nucleus. The dorsal column nuclei are mostly composed of the terminations of cutaneous primary afferent fibres, which terminate topographically, with the tail being medial, in the gracile nucleus, and the upper body lateral, in cuneate nucleus, with the paws having the densest innervation and largest representation. The dorsal column nuclei also receive terminations from the trigeminal nerve, brainstem nuclei, and cerebral cortex. The lateral cervical nucleus receives information from all spinal cord levels and projects these to the thalamus[122].

The dorsal column nuclei project contralaterally in the sensory decussation and terminate in the ventral posterior thalamic complex (VP) and the posterior thalamic complex (Po), which is caudal and medial to VP. Most spinothalamic terminations are in VP, Po, and intralaminar nuclei. Some ascending fibres leave the medial lemniscus to terminate in pontine, parabrachial, dorsal reticular and mesencephalic reticular nuclei, and the inferior colliculus, inferior olive, cerebellum and spinal cord[122].

The somatosensory thalamus mainly consists of VP, which comprises the ventral posterolateral thalamic nucleus (VPL) and ventral posteromedial thalamic nucleus (VPM). The somatosensory thalamus is bounded medially by the ventrolateral nucleus, ante-

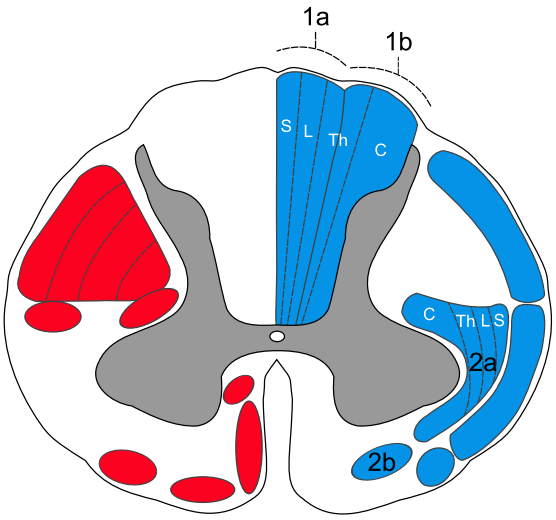

Figure 1.5: *Axial section through the archetypal mammalian spinal cord. Motor, descending tracts and pathways are indicated in red, and the sensory, ascending tracts and pathways in blue. The dorsal column medial lemniscus system is subdivided into the gracile fasciculus (1a) and cuneate fasciculus (1b), and the spinothalamic tracts as the lateral (2a) and anterior (2b). These tracts have a somatotopy, with the key regions indicated: sacral (S), lumbar (L), thoracic (Th), and cervical (C).*

riorly by the anterior nucleus and caudally by Po, and dorsally by the thin, reticular thalamic nucleus (RtN). RtN projects to VP and mediates its inhibition and consequently modulates attention. VP also receives input from the somatosensory cortex and other brainstem regions, including the raphe nuclei and locus coeruleus. VPL receives input from the trunk and limb dorsal column ascending pathways, with a larger representation for the forelimb than the hindlimb. The gracile nucleus terminations, and so the caudal representations, being in the rostral and dorsal parts of VPL, and the cuneate and more cranial representations in the caudal and ventral aspects of VPL. VPM receives input for the face and head representation via the sensory trigeminal nuclei, which carries vibrissal information. Other somatosensory thalamic groups include Po, which has a somatotopic organisation that is a mirror of that found in VP, is activated by vibrissal stimulation, and also receives terminations from the spinal cord, medullary dorsal horn, zona incerta, cortex, and dorsal column, trigeminal nuclei and RtN. Both VP and Po project to S1, with all of VPL's projections to S1, although Po projects to the dysgranular and perigranular regions of S1. Both groups also project to S2, but few of these projections are collaterals to S1 and S2[122].

Although there are strong projections from the somatosensory thalamus to S1 the amount of information that is passed onto the cortex is lower than that received by the thalamus. Conditional cross-correlation analysis has revealed that nearly 90 % of axonal discharges in afferent sensory fibres are associated with a time-locked discharge

in postsynaptic cuneate nucleus neurons, while the maximum thalamocortical efficacy is approximately 20 %, with most exhibiting efficacy rates less than 10 %[99]. First, it is noteworthy that synchronous, thalamic neuronal discharge, that is those separated by <10 ms, exhibit much higher, approximately twice as much, efficacy as asynchronously discharging thalamic neurons; synchronous thalamic discharge is a requisite of sensory feed-forward thalamocortical transmission. Secondly, those thalamocortical projections showing the highest efficiency are those with targets in layer IV and the deeper aspect of layer III, with only projections aimed at these layers achieving efficacy values greater than 10 %, with other layers rarely exceeding 5 % efficiency, which is consistent with these middle cortical layers receiving the highest density thalamocortical terminations[99]. Similar characteristics of feed-forward transmission are present in the barrel cortex and visual cortex and are discussed in the relevant sections.

1.8.5.3 Cortical organisation

The rat somatosensory cortex primarily consists of S1, which has has one body surface representation that is dominated by the face and vibrissae and receives afferents from both VP and Po, and has an overlap with primary motor cortex (M1), approximately 1 mm wide, that may respond to deep stimuli. The additional somatosensory cortical areas are S2, which is located lateral to S1 and contains another complete representation of the face and body, parietal-ventral cortical area (PV), which also contains a body representation and is anterior to S2, parietal-rostral cortical area (PR) which is ventral to PV, and parietal-medial cortical area (PM) that lies posterior to S1. In both S1 and S2 activity can be elicited with gentle stimulation of the skin and body hair, indicating they are responsive to cutaneous, rather than deep, receptors[93;122].

Within S1 the body map is inverted with the paws medial, the whiskers caudolateral, and the jaws rostrolateral, with the digits represented in an orderly pattern in the primary somatosensory forelimb region (S1FL) and primary somatosensory hindlimb region (S1HL). These representations of the digits in S1FL and S1HL is reflected in granular aggregates, resulting in the term granular zones being applied to describe them. These granular aggregates are the result of dense populations of small, densely packed, granule cells in layer IV, which are dominantly supplied by VPL. In S1 layer V is divided into two subdivisions: layer Va, which contains few somata, and layer Vb, which contains many pyramidal cells[122].

Between the granular zones of S1 are dysgranular zones, one being between S1FL and S1HL and another between S1 and S2. These dysgranular regions are activated by muscle stretch, joint manipulation, or cutaneous stimulation, but are unresponsive in the anaesthetized rat[93;122]. The dysgranular and perigranular areas of S1 receive input from Po which terminates in layers I and Va. In addition to VP and Po, S1 also receives

afferents from the raphe nuclei, which have a role in the development of somatotopy, the locus coeruleus, which modulates synaptic inputs, the basal nucleus, which modulates plasticity, and the zona incerta, which has an uncertain role[122].

S1 projects to the thalamus, striatum, other cortical regions, the spinal cord, and the dorsal column, trigeminal, red and pontine nuclei. Corticothalamic projections arise in layer V, which projects exclusively to the dorsal aspect of Po, and layer VI, which projects to VP, Po, and RtN. The corticothalamic projections to the brainstem modulate thalamic somatosensory neurons, while the projections of S1 and S2 to the thalamus allow for integration of sensorimotor and cognitive information. Corticocortical projections include reciprocal connections between S1 and M1, and callosal projections, arising from and terminating in layers III and V, which connect the midline and jaw granular representations of both S1s, and the dysgranular zones[122].

S2 has a complete, separate representation of the body surface, which is upright and rostrally oriented, immediately lateral to S1, and has larger receptive fields than S1. S2 has a large representation of the face, with an organised vibrissae representation that has vibrissae rows oriented mediolaterally[122;123], and has a role in integrating multiple sensory inputs[124]. Although the somatotopic organization of S2 is cruder than that of S1, the proportions of the areas of responsiveness for given parts of the body approximates the same proportions found in S1[93]. S2 has similar cytoarchitectural features to S1, but lacks the granular aggregates found in S1 and has a thinner layer IV. S2 receives thalamic input from VP and Po, with the latter terminating in layers I and IV, and projects to the contralateral somatosensory cortex, via callosal projections[122]. Much less is known regarding the other three association somatosensory cortical areas: PV, PM, and PR.

PV was first discovered in squirrels and has now been identified in many mammals, and in the rat is located rostral and lateral to the auditory cortex. PV, similar to S2, contains a full inverted map of the body surface that is dominated by its representation of the distal extremities and is around 20 % the size of that found in S2. Also comparable to S2, PV's layer IV is thin, in fact thinner than that found in S2[93;122;124]. PV receives some inputs from S1 and some from S2, thus having components of both parallel and serial processing, although Benison et al. recorded that activity first occurs in S1, then S2, and finally PV, although this serial activity could have readily masked other parallel connections. In this study it was also noted that stimulation of the vibrissae did not elicit activity in PV[123]. Little is known regarding the other association cortices: PM responds to stronger stimulation, and PR, which has inputs from PV, may be the highest area of processing prior to output to the limbic system and the subsequent formation of long-term memories[93;124].

1.8.5.4 Propagation of activity and functional considerations

In functional studies SEPs are often measured, and they consist of reproducible sequences of positive and negative waveforms, with the earliest component consisting of a positive-negative wave complex, the P1-N1 complex, which is followed by later slow-wave components. The measurement of SEPs offers an insight into the location, timing and duration of cortical activity subsequent to sensory stimulation. However, the majority of such information in rats relates to forepaw somatosensory evoked potentials (F-SEPs) and vibrissae somatosensory evoked potentials (V-SEPs), with a comparative paucity of information regarding hindpaw somatosensory evoked potentials (H-SEPs). In considering the cortical response to sensory stimuli it is noteworthy that repeated stimulus of an excitatory connection onto a pyramidal cell produces a larger response for the first stimulus followed by diminished peak amplitude EPSPs for subsequent stimuli. However, some populations also exhibit the opposite behaviour with the response to a rapid train of stimuli being an increase in the amplitude of EPSPs, with is known as a facilitating synapse. The nature of these short-term dynamics depend on three main factors: the rat's age, the identity of the pre- and postsynaptic cells, and the recent plasticity of the synapses [100].

Freeman and Sohmer, transcranially, recorded F-SEPs and V-SEPs in albino rats anaesthetised with pentobarbital. The onset latency for F-SEPs was 8.28 ± 0.36 ms (mean $\pm$ SD), and latencies of P1 and N1, 11.9 ± 0.7 ms and 28.8 ± 6.2 ms, respectively. The average amplitude of P1, at stimulus rates of <4 Hz, was 17.3 ± 7.8 uV. Moreover, as found in human studies, onset latency increased and response amplitude decreased as stimulus rate increased: F-SEPs had a latency increase of approximately 10 % and amplitude decrease of 40 % for a stimulus rate increase from 2 to 7 Hz [121]. Sakatani et al., epidurally, recorded F-SEPs, H-SEPs, and V-SEPs in Long-Evans rats, anaethetised with pentobarbital, with the F-SEPs wave complexes being more pronounced than those of the H-SEPs. The onset latency was reported as 7 to 8.5 ms and 11.5 to 13 ms for the F-SEPs and H-SEPs, respectively, and lateral extent of this response was $\leq$1.5 mm in diameter for the top 20 % of changes and $\leq$5 mm in diameter for the top 60 % of changes [125]. Jellema et al. measured evoked activity, with an epicortical multielectrode array, in ketamine anaethetised male, Wistar rats following median nerve stimulation, at 0.3 Hz, with a cuff electrode. The onset latency of F-SEP P1 was 3.7 ± 0.2 ms, and peak latencies of P1 and N1, 8.3 ± 0.6 ms and 12.7 ± 0.6 ms, respectively. The amplitude of F-SEPs was 1.4 ± 0.9 mV with a range of 0.45 to 2.9 mV, with the amplitude of P1 being noted to be largely constant and N1 being the cause of this variability [126]. The latencies reported by Jellema et al. are considerably earlier than those reported in other studies, there are multiple possible explanations. First, physiological variability could have contributed to some difference in latencies, as could the different choice of anaesthetic regimes between studies. In addition to this, detection of the onset of EPs is often complicated by pre-stimulus oscillations/noise. Lastly,

Jellema et al. described using 'a comb-like multi-electrode array' for surface mapping, which might refer to a 2D array with multiple rows of electrodes in a comb-like formation or alternatively a penetrative comb-like structure that was inserted into the cortex, which would explain the earlier latencies reported in this study.

In addition to surface F-SEP assessment, Jellema et al. took the site of maximal epicortical P1 as the area of thalamocortical termination and, centred on this, made intracortical recordings, perpendicular to the cortical surface at multiple sites, with a linear multi-electrode array and employed CSDA in order to examine laminar field potentials[126]. A single multi-wire array comprised 12 polymer-insulated nichrome wires with a outer and core diameter of 37 and 25 µm, respectively, and with an inter-electrode distance of 150 ± 2 µm, with the whole array being embedded in resin. These arrays were developed and manufactured by Jellema and Weijnen specifically for recordings of LFPs and CSDA in the rat cortex[127]. From the CSDA two major sink-source complexes were identified, the first located in layers I to IV and the second in layers V and VI, with these being termed the supragranular and infragranular sink-source complex, respectively. The earliest infragranular sinks, corresponding to neuronal depolarisation, were found in the border of layers IV and V, with an onset of 4.9 ± 0.4 ms, and the border of layers V and VI, with an onset of 5.0 ± 0.3 ms, both of which likely correspond to thalamocortical terminations onto these layers. The earliest supragranular sinks occur after these initial infragranular sinks, and occur in layers III and IV, with a latency of 7.4 to 7.8 ms, and after this sinks in layers II to III, with a peak latency of 9.1 ms, and then layers I to II, with a peak latency of 11.8 ms. The trend of activation was summarised as activation of specific thalamic afferents in layers III to V followed by activation of superficial pyramidal cells in layers II to III via intracortical projections, which was noted to match an expectation of upward migration of activity around layer IV into supragranular layers.

In a study primarily examining modelling, Sotero et al. considered anatomical connectivity, functional connectivity, as determined by CSDA, and compared these to modelled behaviour in the rat S1FL. The model was a neural mass model, a model which aims to examine spatio-temporal changes in neural properties, such as firing rates, in either oscillatory or evoked states. The approach is based upon mean fields, in which an approximation is made of groups of neurons and their average properties and activity. The CSDA analysis was achieved with a linear 32 contact electrode array, with a 100 µm inter-electrode spacing, that was inserted perpendicular to the cortical surface in S1FL of four rats during median nerve stimulation. The resultant CSDA was an average of repeats, to improve SNR, and over space, so that one time course for each layer was produced. Whilst the results of these recordings was not the focus of the study some conclusions were highlighted: a primary sink was identified in layer IV and the strongest connection, confirmed in the model, was an excitatory input of layer IV to layers II and III[128].

In a series of stimulation paradigms, including microiontophoretic, which is the injection of small amounts of ions, glutamate administration, corticospinal tract stimulation, and electrical stimulation of the hindpaw, Dykes and Lamour examined Sprague-Dawley rat, hindpaw cortical activity, by means of single unit recordings. Of the responsive neurons that were examined 36.4 % had cutaneous receptive fields, 9.3 % deep stimuli receptive fields, and the remaining 54.3 % being responsive to higher intensity stimuli, but neither definitively being cutaneous or deep. With all three types of stimulation the principal area of spontaneous activity was layer V, while for evoked activity it was layers IV and V[108].

Sun et al. examined the laminar spatio-temporal propagation of activity in response to both noxious, laser evoked, and innocuous, electrically and mechanically evoked, hindpaw stimuli in halothane anaesthetised rats. Intracortical LFPs were recorded with a 'Michigan' probe, a linear microelectrode array with 16 recording contacts spaced 150 µm apart, and each channel's data was averaged in order for one-dimensional CSDA to be undertaken. This analysis revealed that noxious and innocuous stimuli differed significantly: noxious, laser evoked stimuli had an early component whose amplitude correlated with stimulus intensity, while late components were not intensity-dependent, also noxious stimuli resulted in a smaller mean amplitude response and longer latencies of major sink currents. Regarding the innocuous stimuli, synaptic activation was found to arise first in layers IV and VI separately; with electrical stimulation the layer IV sink had a latency of 16.37 ± 0.38 ms (mean $\pm$ SEM) and the layer VI sink at 19.09 ± 0.90 ms, which for mechanical stimulation were 19.24 ± 0.59 ms and 23.56 ± 1.69 ms, respectively. The mid-layer IV sink was found to have a shift towards the layer IV and layer III and V borders at approximately 17.25 ms and a significant upward sweep towards layers II and III at approximately 19 ms, while the layer VI sink, initially at the layer V and layer VI border, swept deeper into layer VI at approximately 22.5 ms. In summary this hindpaw study revealed separate thalamocortical projections led to activations initially in layers IV and VI, that the layer IV activity was earlier than that in layer VI, and that both elicited sink activity in more superficial and deeper layers[129].

1.8.6 Rat vibrissal sensory system

In this section the rat's vibrissal system anatomy and physiology are examined, and, while many core aspects of the rat barrel cortex are similar to those covered in section 1.8.5, the barrel cortex stands out as an exceptionally specialised component of the rat's somatosensory system and has consequently received a large amount of study in comparison with its other sensory systems.

Functionally, vibrissae are used for gap and drop perception, and active exploration by means of whisking; during whisking vibrissae are moved back and forth, with rats doing

this at approximately 7 Hz [130;131]. The vibrissae give the rat the ability to discriminate between objects only 0.24 mm apart and texture features as shallow as 30 µm [130], while structurally the system is noteworthy for its extreme somatotopy: the barrel cortex. The discretisation of the barrel cortex into areas corresponding to a single vibrissa is a cortical topography that matches the topography of the rat's mystacial vibrissal pad and the position of the vibrissae within this [122;131]. The mystacial macrovibrissae, as opposed to other vibrissae, such as the supraorbital vibrissae, that are referred to here as vibrissae.

1.8.6.1 Receptors

Often the large mystacial vibrissae are termed macrovibrissae, in order to avoid confusion between these and smaller vibrissae present throughout the rat's facial area. These macrovibrissae are 3 to 40 mm long, with an average of 2 macrovibrissae per cm^2 (compared to the area covered by the vibrissae tips), and are organised in five rows, labelled from A to E, with rows A and B having four vibrissae and rows C to E having eight to ten vibrissae, and an additional four caudal straddler vibrissae, α to δ, and this layout is also found in the barrel cortex (figure 1.6) [130;131]. The term hyperacuity is used to refer to the fact that the average spacing of vibrissae is coarser than the resolution of features that a rat can distinguish with its vibrissae, which is achieved in a similar manner to active palpation in primates and humans, where resampling, in the form of whisking, allows for the integration of information. A similarly impressive feat of the rat's vibrissal system is that judgements are made regarding these signals, manifest in behavioural action, in <100 ms [130].

The vibrissae are held within a specialised follicle that consists of concentrically arranged membranes and a sinus. When a sinus is pressurised with blood the associated vibrissa is pressed against its receptors, therefore the vibrissa's mechanical sensitivity is increased [98;131]. Each follicle is innervated by two sensory nerves, with up to 200 axons innervating the follicle: approximately 70 % myelinated and 30 % unmyelinated. These two nerves are the superficial and deep vibrissal nerve, and in the rat around 80 % of the follicle's innervation is from the deep vibrissal nerve. Theses sensory nerves mainly lie between the sinus and on of the concentric membranes (glassy membrane), although some innervation is provided by the superficial vibrissal nerve to the top of the follicle and some Merkel mechanoreceptors in the skin at the top of the follicle [98]. Deflection of a vibrissa is believed to cause mechano-gated ion channels in the vibrissal nerves to open, leading to action potential initiation [132].

In addition to their structural and location categorisation, the primary sensory neurons have been functionally subdivided into slowly adapting and rapidly adapting fibres. Slowly adapting fibres are associated with Merkel mechanoreceptors and tonically fire

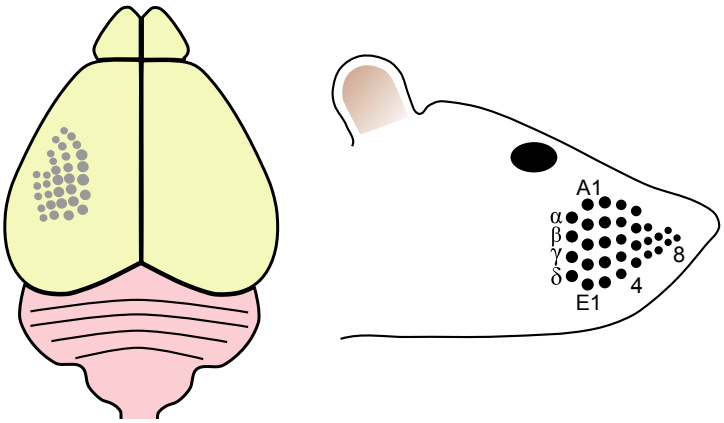

Figure 1.6: *The vibrissae topography as found in the rat's (right) mystacial vibrissal pad and on the cortex (left). The layout of the vibrissae in the mystacial vibrissal pad is indicated, with the caudal straddler vibrissae indicated from α to δ, and the first A row, (A1), and E row, (E1), are also indicated. To illustrate the caudal to cranial numbering, vibrissae columns four and eight are also indicated.*

in response to constant displacement, while rapidly adapting fibres are associated with Lanceolate endings and are only briefly active during displacement and are inactive during constant displacement. Both types of neurons have firing rates that correlate with deflection velocity, with different velocities being handled by different fibre subsets; conversely, deflection amplitude is only coded for by slowly adapting fibres [98;130].

1.8.6.2 Ascending pathways, brainstem nuclei and thalamus

The vibrissal nerves enter the infraorbital branch of the trigeminal nerve, within which it is divided into fascicles for each row of vibrissae, and this projects to the trigeminal nerve ganglion, the brainstem, and then the barrel cortex, with this route consisting of three synapses [131;133].

The neurons in the trigeminal ganglion can be defined by their direction selectivity as well as functional response, being either rapidly or slowly adapting. The activity of these neurons is both precise and reproducible with high consistency between repeated trials [134]. Directional selectivity is present in approximately 80 % of the ganglion neurons, with the majority being tuned within 135°. The slowly adapting neurons have clear angular tuning to a range or directions, while the rapidly adapting neurons are not as clearly directionally selective, but generally have greater vertical selectivity. In general more cells have an upward selectivity, with fewer having downward selectivity, or horizontal deflection sensitivity; however, the representation of directionally selectivity diminishes as information proceeds towards the cortex [97].

The sensory neurons of the trigeminal ganglion have excitatory glutamatergic pro-

jections to the brainstem, trigeminal nuclei, which form four groups: trigeminal nucleus principalis (V_p), trigeminal nucleus oralis (V_o), trigeminal nucleus interpolaris (V_i) and trigeminal nucleus caudalis (V_c). Each of theses have a vibrissal somatotopic representation similar to that found in the barrel cortex, although these are referred to as barrelettes. The main source of projections to the somatosensory thalamus are from V_p and V_i, with approximately 90 % of V_p cells projecting to VPM and 7 % to the posterior medial thalamic nucleus (POM), which is located toward the caudal end of VP, and 2 % to both thalamic nuclei. Similarly, around 75 % of V_i cells project to the ventrolateral aspect of VPM, but these do not overlap extensively with those of V_p, 17 % of V_i cells project to POM, and 7 % to both. The other projections of V_i, V_o and V_c include projections to the superior colliculus (SC) and cerebellum, and V_c also projects to the ipsilateral facial nucleus, which is involved in controlling vibrissal musculature. In addition to these projections, each of the nuclei connects with the other trigeminal nuclei, with the exception that there is no projection from V_o to V_i. The receptive fields of the brainstem nuclei are typically only of one or two vibrissae, although broader receptive fields, in cerebellar projections, and V_p projections to VPM do occur. These latter broader receptive fields range from three to sixteen vibrissae and depend on the receptive fields of V_i, with ablation of V_i causing any broad V_p receptive fields to decrease to one vibrissa.[97;134]

There are two main thalamic nuclei that supply the rat barrel cortex: VPM and POM. Both nuclei have a complete representation of the vibrissae, with receptive fields in both varying in size from one to twenty vibrissae[97]. There are structural and functional differences between the two nuclei: neuronal responses following vibrissae displacement are typically more robust in VPM, only VPM contains somatotopically arranged barreloids that are comparable to the barrelettes of the brainstem and barrels of the cortex, and the cortical and subcortical targets of the two nuclei are different[134;135].

The somatotopic barreloids of VPM are approximately 1 to 200 µm in diameter and have a corresponding principal whisker, arising from V_p projections, that evokes a stronger response than other vibrissae, although they do have a multi-vibrissae representation, with these surround responses being of smaller amplitude and longer latency than that of the principal whisker[97;132;134]. The excitatory input to VPM arises from feed-forward projections from the trigeminal nuclei and feedback projections from the cortex, while inhibitory projections arise from RtN. The inhibitory input to VPM that arises from RtN is recurrent feedback inhibition, with RtN receiving collateral input from thalamocortical feed-forward neurons and corticothalamic feedback projections, with the latter arising in layer VI and terminating in VPM[97;99]. The result of RtN's input is the sharpening of thalamic receptive fields and prevention of prolonged thalamocortical excitation[97;132]. Additionally, an oscillatory circuit exists between VPM and RtN, which results in thalamic spindle-firing at 8 to 12 Hz, with RtN being the pacemaker of this activity[97]. The V_p

projections to the barreloids results in the main feed-forward excitatory projection to layer IV in S1 and the core of the cortical barrels found there, and also weakly to the layer V and VI border, while a projection from V_i to the ventrolateral aspect of VPM results in more dispersed terminations, both in varied laminar and cortical targets[97;133]. The pathway projecting from V_p to VPM and then to layer IV is referred to as the lemniscal pathway, while the limited projections of VPM to S2 and the septae separating the barrels in S1 is referred to as the extralemniscal pathway[130;132].

Directional tuning can be identified in the barreloids of VPM, with dorsal neurons responding better to forward and upward deflection of the vibrissae[134], but, as revealed in a study by Ego-Stengel et al., the source of this complex information appears to arise from subthalamic input. Ego-Stengel et al. investigated VPM directional selectivity in 24 male Wistar rats during global, immediate surround, and paired whisker stimulus, by means of extracellularly recording neuronal activity with tungsten electrodes placed in VPM. Global stimuli involved the coordinated displacement of a principal whisker and its 23 neighbouring vibrissae, immediate surround only the eight closest vibrissae to the principal whisker, and paired only the principal whisker and one other vibrissa. This study revealed that excitatory responses in VPM were directionally selective to a global stimulus in 52 % of cases, while only 12 % of suppressive responses showed similar behaviour, and also that while excitatory responses could be either mono- or multi-vibrissae, suppressive responses were typically multi-vibrissae. The response to immediate surround stimuli was noted to be very similar to the global stimuli response, while there was a discrepancy between tuning curves for global stimuli and paired whisker stimuli, which reveals that the global motion directionality response cannot be explained by interactions between a principal whisker and the immediate neighbour preceding it in each sequence. Hence, global motion selectivity in VPM arises from nonlinear integration of the signal from the principal whisker and its immediate surround whiskers. This nonlinear processing should arise from one of the inhibitory inputs to VPM, as VPM lacks inhibitory interneurons, which Ego-Stengel et al. addressed in turn. Cortical inhibitory input was excluded as the behaviour was persistent following chemical inactivation of the cortex, RtN excluded as its inhibitory modulation is not direction selective, which implied a subthalamic source is responsible. Although V_p provides input to VPM for a principal whisker, as detailed above, the trigeminal nuclei have extensive interconnectivity, with V_i having a inhibitory role, which suggests that substantial nonlinear processing occurs at the subthalamic level, with this facilitating the processing of multi-vibrissae stimuli at subcortical levels[136].

The topographical map found in POM is rough and diffuse, and is a mirror of that found in VPM; the diffuse nature of POM's map derives from its inputs having large receptive fields: layer V cells and V_i. The main trigeminal nucleus with input to POM is V_i,

while it also receives input from the SC, zona incerta, and the cortex, which arises in layer V. An additional input is feedback projection from S1 which is then fed-forward to S2[97]. The S1 projections of POM are to the septae between the cortical barrels, terminating in the top of layer V, and in layers I and IV[97;134]. Although the projection of POM to layer IV complements the projections of VPM to the same lamina, the terminations result in a fenestrated pattern that are more laterally spread than those of VPM. As the projections of POM surround the barrels it has been suggested that they may have a role in signal integration across barrels,[97], however much less is known about the physiological role of POM, although under anaesthesia it is largely inhibited via inhibitory inputs from the zona incerta[132;134]. The projection of V_i to POM results in terminations in S1, S2 and M1, a pathway that is known as the paralemniscal pathway[130;132]. Another division of Po is the posterior caudal thalamic nucleus (POC), which can be differentiated from POM and mainly projects to S2 and posses multimodal receptive fields[97].

Other sources of projection to the cortex include those from the intralaminar thalamic nuclei which terminate in layers V and VI, these diffuse thalamocortical projections are without containment by functional area and are likely to have a role in arousal state and modulate responses in layer V. An additional source of cortical input is a sparse projection from the ventromedial nucleus of the hypothalamus that terminates in layer I and conveys nociceptive information, with a role in cortically dependent behavioural tasks[97].

1.8.6.3 Cortical organisation

The rat's posteromedial barrel subfield (PMBSF) is located medially, towards S1FL, contains the representation of the macrovibrissae, and on its own covers 4.7 to 6.4 mm^2 of the neocortex. The barrel cortex is divisible into several subfields, with the PMBSF often being the subfield referred to when the term barrel cortex is used. The rat's other subfield is the anterior lateral barrel subfield (ALBSF), which is located more laterally and cranially, contains the representation of the vibrissae of the nose, and upper and low jaw, which in combination with the PMBSF results in the barrel cortex covering an area of approximately 10 mm^2 [131].

As already detailed, the barrel cortex is so named due to the presence of a clear cortical topography of barrels for each macrovibrissa, which can be visualised in both living and stained brain preparations. This topography is fixed within a few days of birth so that while the size of the barrel cortex varies between animals and even hemispheres, even lesions within the sensory afferents leave the somatotopy largely unaffected[95;132]. The barrels are separated by septae and the cellular distribution and connectivity in these two entities is different. Each barrel and its surrounding septa in the rat PMBSF have a diameter of 450 to 500 µm, which with a cell density of 85 000 mm^{-2} possess 18 000

to 21 000 neurons[97]. Thalamocortical projections to the barrel cortex cluster to form the barrel centres where cells are sparse, while cell density is much higher in the barrel walls with the walls two to three cell layers thick, and the cells there project towards the barrel centre and spare the septae[131].

In the PMBSF the laminar connections have been extensively examined and these can be considered as consisting of the barrel and septal circuits. Layer I of the PMBSF receives input directly from POM and some input from layer II[132]. Layers II and III receive multi-vibrissae input, nonetheless the principal whisker produces the largest EPSPs and IPSPs[98]. There is some thalamic input to layers II and III, which arises in V_i and is projected from the ventrolateral aspect of VPM[97]. The intracortical connectivity of these layers is far more extensive with input to cells above the septae arising from layer Va, and further input to layers II and III arising from layer IV[132;134]. Layers II and III have substantial corticocortical connections, projecting to neurons within layers II and III, but not necessarily constrained to a barrel, with the lateral extent being potentially over several barrels[98;132;134;137]. The dendrites of layer II cells often have substantial branching within layer I, with reciprocal connections from layer I[98]. Neurons in layers II and III also project to layer V, with this pathway, which is reciprocated, being the major route of excitation to the infragranular layers. Additionally, layer II cells project to layer IV[98;134]. In summary, layers II and III have some manner of connection with all the lamina of the barrel cortex, with a horizontal distribution of several barrels.

The excitatory cells in layer IV are either spiny stellate, star pyramidal, or pyramidal[134]. Approximately 20 to 25 % of the cells in layer IV of rat barrel cortex are star pyramids with an ascending main apical dendrite that is longer than the rest of the radially arranged dendrites[100]. The pyramidal cells may have a role in within- and across-barrel connectivity as they can connect between barrels, while stellate cells are likely to have a role in within-barrel connectivity[98]. Approximately one-third of excitatory barrel neurons are synaptically coupled, however, there is limited connection between barrels, so that the barrels are somewhat independent excitatory circuits, while the septa are more widely interconnected[133]. The inhibitory cells of layer IV receive their input from VPM, are more sensitive than the excitatory neurons in layer IV, and their dendrites and axons are usually confined within their respective barrel and directed superficially, with their cell bodies located in the barrel's walls. The connectivity of the inhibitory neurons in layer IV highlights their role in limiting within-barrel excitation and the propagation of this activity to supragranular layers, consequently corticothalamic drive results in an excitatory-inhibitory sequence[98].

The subcortical input to the core of the layer IV barrels arises in V_p, which projects to the core of the VPM barreloids, with these terminations resulting in serial feed-forward terminations in layers II, III, and Va, and collaterals to the border between layer V and

VI[97]. Another input to layer IV is a projection arising in layer VI, which is then reciprocated by layer IV[98]. The excitatory barrel neurons of layer IV are axonally and dendritically confined within their own barrel, which leads to initial activity being confined here, however within this barrel there are connections with both the supra- and infragranular layers[98;132]. The layer IV neurons have substantial innervation to layers II and III above the barrel within which they are located, with more than 90 % of stellate and star pyramidal cells connections made between layer IV and layers II/III. This connection with the supragranular layers only evokes small EPSPs and so convergent input is necessary for activation of layers II and III. There is also a sparse innervation to layer Va that maintains barrel topography, and a reciprocated projection from layer IV to VI[98;131;132]. Of the outputs from IV most stay confined within the barrel system and radial connections are sparser and shorter than those of the extragranular layers, although projections to layers II and III have some diagonal axons projecting into neighbouring columns and approximately 1 to 2 % of the length of layer IV axons infiltrate neighbouring barrels[97;98;137].

The septae in layer IV have different connections to those of the barrels and are connected over a broad radius of several barrels[98]. The wide mesh formed by the septae receive their input from POM and, unlike the layer IV barrels, are the target of callosal projections from the contralateral barrel field. The differences between the inputs and outputs of layer IV results in the two being separate, parallel circuits in the barrel cortex[131].

Layer V receives input from VPM, some of these projections originate in V_p, are transmitted through VPM and terminate in layer Vb, while some separate projections originate in V_i, are transmitted through the ventrolateral aspect of VPM, and terminate in layer V[97]. Layer Va also receives input from POM, and from layers II, III, IV, and VI[98;132;137], and has projections within layer V, and to layers II, III and VI[98]. Layer V exhibits multivibrissae responses, which most likely reflect the variety of lateral connectivity in the layer. The pyramidal cells of layer V have more widespread connections than those found in layers II and III and in contrast to these layers are along arcs, rather than along the rows. Additionally horizontal spread is facilitated by collaterals of thalamic projections to the border of layers V and VI, and via layer V diagonal projections into neighbouring barrels[97]. Excitatory connections between cell clusters in layer Vb are also prominent, which have been shown to have high synaptic efficiency in response to low frequency stimulation, and these in turn project to subcortical targets, such as the pontine nuclei, tectum, thalamus, brainstem and spinal cord[137].

Layer VI receives collateral input from VPM projections that receive their input from V_p, and also input from the intralaminar thalamic nuclei and intralaminar connections[97;137]. Layer VI has substantial projections to VPM, around 50 % of layer VI

cells project to VPM, and it also has some projections to POM, and the white matter. Projections solely to VPM are more common in layer VIa, while projections to both VPM and POM arise in layer VIb. Layer VI has extensive connections to other cortical laminae, including layers III, IV and V, and horizontal connections within layers V and VI. Layer VI has a substantial number of inhibitory cells, a large proportion of these project to layer I, while other inhibitory input results from terminations on layer IV cells. Layer VI also has connections with S2 and the dysgranular cortex[98].

In addition to the interhemispheric connections detailed in section 1.8.5.3, the barrel cortex has multiple feed-forward and feedback connections, the main corticocortical connections are to contralateral S1, ipsilateral dysgranular zone, S2 and M1[132;134]. The subcortical targets are also either motor, such as the striatum, SC, and pons, or sensory, such as VPM, POM, and the trigeminal nuclei[97]. The corticocortical projections are largely glutamatergic, although there also inputs containing neuromodulatory neurotransmitters, such as acetylcholine, serotonin, or dopamine[134]. Connections to the contralateral S1 are seemingly limited to the most medial A-row whisker septae, terminating in layer V, whilst interhemispheric projections arising in S1 also terminate in the dysgranular zone[132;134]. Feed-forward corticocortical projections largely arise in the extragranular layers and terminate in layer IV, while any feedback projections from these higher areas typically terminate in the extragranular layers of PMBSF[98]. There is some direct thalamic input to S2 from VPM and also reciprocal connections between S2 and S1. The projections to S2 arises in layers III and V of S1, while the reciprocal projections terminate in layers III, V and VI of S1. The row projections to S2 are separate and so the scope for integration of information within rows is greater than that across arcs, a similar arrangement exists in the projections to M1[97;98;134]. The projections to M1 arise less uniformly than those to S2, being restricted to the regions above and below the S1 septae, there are also reciprocal connections between S2 and M1[98]. The extensive and complex connectivity between M1 and the somatosensory cortices highlights the hierarchical organisation among them, which provides information regarding the current control and location of vibrissae allowing for better interpretation of sensory information[98;134].

1.8.6.4 Functional considerations

The vibrissal system utilises both labelled-line and integrative organisation, which is reflected in the different circuits of the barrels and septae: labelled-line organisation is clear in the preservation of a single whiskers representation from the mystacial vibrissal pad to the layer IV barrels, while functional and anatomical studies have shown extensive lateral integrative connections in both cortical and subcortical areas. In order for activity to occur in the cortex significant convergence via synchronous thalamic inputs and temporal summation is required, as individual thalamocortical inputs only result in a typical

depolarisation of <1 mV. This synchronous activity is best achieved following principal vibrissa displacement, as this results in thalamic neurons activating within a 2 ms range, while their response range is 8 ms for surround vibrissae[97]. Synchronous thalamocortical activity, resulting from vibrissa displacement, causes activity in a layer IV barrel, which initially spreads to overlying layers II and III, and finally results in lateral spread across the barrel cortex[134]. In addition to studying the spatio-temporal propagation of activity in the barrel cortex, significant study has been applied to understanding stimulus parameter coding; neurons in the barrel cortex show a monotonic increases in the frequency of spiking as a result of both increasing stimulus amplitude or velocity, with the first 25 to 30 ms of a response being velocity dependent, while amplitude effects are most important in a period of 600 ms[97]. Additionally, layers II and III may have a role in sensitivity to directionality of stimulus displacement, as neurons in a given subsection of a barrel show preferential activity for a given direction of deflection[132]. Below, for simplicity, first the general principles of the spread of activity, with regard to vertical and horizontal spread, and other functional considerations are given, and subsequent to this the specifics of the spatio-temporal propagation of activity in the barrel cortex is given.

The feed-forward progression of activity is from the mystacial vibrissal pad to the trigeminal nuclei, then to VPM and POM, and finally to the barrel cortex; however, the activity in the two thalamic nuclei is not synchronous: VPM responds at 4 to 6 ms after a vibrissa is displaced, while POM has its earliest spikes between 10 to 30 ms after the stimulus[135]. The key target of the projections of the first responding thalamic nuclei, VPM, are the barrels of layer IV, with the dendritic target here mostly being from layer IV neurons, although some are the apical dendrites of layer V and VI neurons, and so consequently the first responding neurons are located in layer IV and Vb[97;132]. The layer IV neurons have excitatory connections to all layers of their respective barrel column, particularly to layers II and III. The extensive excitatory, intra-barrel connections amplify the excitation initiated by thalamocortical projections, which is prevented from becoming excessive and recursive by strong inhibitory input that is activated with a lesser degree of synchrony, and can abolishes an initial EPSP within 5 to 7 ms of a response onset[97].

Although each layer IV barrel of PMBSF has a corresponding macrovibrissa only around 30 % of the layer IV barrel neurons have a single-whisker receptive field, as determined from spike activity, which indicates the scope for integration of activity. While lateral connections are extensive and can reach over long ranges the probability of lateral connections decreases at more than the inverse square of the traversed distance[97]. The barrels that are clearly demarcated in layer IV are the site of activity only for a few milliseconds, and after this depolarisation spreads over a broader lateral extent[132]. This lateral spread was shown by Armstrong-James et al., in Wistar rats using carbon fibre electrode placed in layer IV, to be dependent on the principal barrel being intact, as

lesions of this resulted in reduced amplitude and longer latency of responses in surround barrels, and this loss of input was proportional to the volumetric loss of the principal barrel. However, the response of these surround whiskers to their respective macrovibrissae was unaffected. The conclusion was therefore that lateral spread of depolarisation in the barrel cortex depends, at least in part, on labelled-line, intracortical transmission of activity[138]. Petersen et al., using VSD imaging and whole-cell recordings, further examined the nature of horizontal spread in Wistar rats. Vibrissa stimulation was achieved with a piezoelectric wafer and the resultant VSD activity confirmed to predominantly arise in layers II and III and to be glutamatergic, as it was reduced to $3 \pm 6\,\%$ of its pretreatment level if glutamatergic activity was blocked. The lateral spread of activity was found to preferentially spread along the principal barrel's row, with a speed of $60\,\mu m\,ms^{-1}$, rather than the rows of other barrels, with arc spread being at $33\,\mu m\,ms^{-1}$. This finding was in accordance with another aspect of the study; biocytin was introduced to the cortex for histological staining and the arbors of layer II and III pyramidal neurons found to be preferential to row-wise spread. In addition to this, Petersen et al. determined that the extent of lateral spread reduced with smaller deflections[139]. The lateral spreading of sensory responses in the barrel cortex that is observed under anaesthesia, has also been noted in rats and mice during quiet wakefulness, and so, rather than being an artefact of anaesthesia, likely reflects an important aspect of cortical integrative function[132].

Inhibitory input, as in controlling intra-barrel activity, has a role in inter-barrel activation[99]. In an *in vitro* study of Wistar rat brain slices Petersen and Sakmann, with VSD imaging, examined barrel cortex responses to electrical stimulation of the layer IV barrel. Any GABA-receptor mediated activity was blocked by the administration of $10\,\mu mol\,L^{-1}$ of bicuculline, a competitive antagonist of $GABA_A$ receptors. Subsequent to this, activity recorded by VSD imaging and whole-cell recording in layers II, III, and V was of higher amplitude, and activity in layers II and III was of longer duration and over a broader area; however, this change was not found in layer IV. The effects on the lateral spread of activity following disinhibition highlight that there are significant excitatory interactions between columns through layers II and III, and that these are strongly regulated by inhibition[140].

The manner in which the horizontal, labelled-line activity, and lateral, integrative activity of the barrel cortex interact in order to provide complex and accurate information is still a topic of intense research. Key areas of interest are location, amplitude, and frequency coding, the interaction of complex combinations of this information, the interpretation of multivibrissa information and the effect on neural coding in whisking and non-whisking states. It appears as though horizontal location might be encoded by spike timing, but this immediately raised the question of what reference signal might be used for such a temporal coding mechanism, while, alternatively, radial location has been

purported to be coded by spike rate and/or count [130]. Interpretation of any such signal must integrate information from the motor system as well; however, the startling finding has been that the interplay between the two system is in contrast to the simplicity of cortical discretisation suggested by Penfield and Boldrey [91].

Intracortical microstimulation of either S1 or M1 has been found to evoke short-latency vibrissal movement; however, while selective blocking of sodium channels with tetrodotoxin in S1 results in the cessation of this response, similar inactivation of M1 does not affect vibrissal movement subsequent to S1 microstimulation. When the converse was attempted, inactivation of M1 prevents vibrissal movement subsequent to M1 microstimulation, but does not affect movement evoked by S1 stimulation; moreover, the same results have been obtained with optogenetic stimulation. These results clearly indicate that there are two motor centres, S1 and M1, responsible for whisker retraction, and that the activity mediated by S1 is, at least in part, independent of M1 [141].

Frequency coding, as a stimulation parameter that can be readily altered, has also been extensively examined, and, in addition to having an effect on response amplitude, it has been determined to affect the lateral extent of activity [132], and also spike frequency. Diamond et al. advanced a carbon-fibre electrode into POM and VPM during spiking activity evoked by piezoelectric vibrissal displacement. In response to increased stimulus frequency the firing rate of POM decreased, with peristimulus time histograms (PSTHs) being frequency dependent: at 0.2, 0.5 and 1 Hz the POM PSTHs were grouped at 10 to 30 ms post-stimulus, while at stimulus frequencies >5 Hz POM appeared to be unable to follow the stimulus and the PSTHs became more scattered. Conversely, VPM spikes were grouped at 4 to 8 ms post-stimulus in a time-locked response, and while there was some reduction in response with increased frequency, this was only marked at 10 Hz [135]. The work of Diamond et al. seems to indicate one of the possible mechanisms of the effect of frequency on the lateral extent of cortical activity. As stimulus frequency increases to 5 to 10 Hz cortical activity becomes more focused, as compared to the much broader responses that occur at lower frequencies, such as 1 Hz. Two possible mechanisms, either separately or combined, have been suggested as the mechanism for regulating this response: alterations in subcortical input and/or in the excitatory and inhibitory cortical input. Regarding altered subcortical input, work such as that by Diamond et al., indicates that VPM and POM have different frequency response characteristics, which, given that they project to the cortical barrels and septae, respectively, might functionally uncouple these two structures. With respect to changes in the excitatory and inhibitory input, there is a far greater frequency-dependent reduction in excitatory input than inhibitory input, as the respective cells have different peak firing rates, so that the lateral extent of the response will be reduced [142].

Another functional consideration is the effect of multi-vibrissae stimulation, which is

both facilitating and also suppressive. The neurons of layers II and III are most involved in multi-vibrissae facilitation; if a surround vibrissa is displaced 3 to 5 ms before a principal vibrissa then supralinear summation of the responses occurs: the facilitated response is greater than the summation of the separate individual responses. However, there is a directionality of this response with it potentially being absent if the second vibrissa displaced is caudal to the first, which is an unsurprising phenomenon given that 57 % of the layer II and III neurons showing facilitation also show directionality [97]. Multi-vibrissae simultaneous stimulation can also result in suppression, which is possible as it occurs much later than the facilitation, within a period approximately 200 ms post-stimulus. The suppression is characterised by the strongest suppression being mediated by the vibrissa with the largest excitatory component, also the amplitude of the suppression is correlated with the number of stimulated surround vibrissae. The suppression is largely mediated by intracortical projections, and the inhibitory input mediating the suppression is asymmetrical with dorsal vibrissae receiving fewer inhibitory terminations. The characteristics and effects of facilitation and suppression are most important in the functional trade-off between whisking and non-whisking states, which respectively result in increased specificity and sensitivity. During whisking more contacts are made at a higher frequency and so suppression of surround responses occurs, and, as facilitation shows directionality, the amplitude of responses is increased when deflections are concordant, which combined result in a greater contrast of the principal vibrissa versus the surround vibrissae. Alternatively, these responses are not being employed during non-whisking states, so that a relatively unbiased response can be evoked throughout the mystacial vibrissal pad [142]. This trade-off is evident from behavioural studies in which some tasks, such as width estimation or horizontal object-localisation, are better performed with multiple whiskers intact, and during non-whisking with minimal head movement, while other tasks, such as gap judgement or texture discrimination, are performed better during whisking states [130]. Ferezou et al. explored the difference between whisking and non-whisking states in awake, freely-moving mice using VSD imaging via fibre optic bundles, which based upon *in vitro* brain slice measurements recorded largely from layers I to III, and minimally from layer IV and the infragranular layers. The earliest response occurred in the principal barrel at approximately 10 ms and exhibited lateral spread throughout the cortex over the following 20 ms, with responses in awake mice having a longer response over a larger area compared to anaesthetised mice. The response evoked by single vibrissa during active whisking was reduced to 26.3 ± 16.8 % of the response during non-whisking states; however, as mice made contact with objects during whisking, large-amplitude, propagating activity resulted from object contacts [143].

1.8.6.5 Propagation of activity

The waveform of V-SEPs is comparable to that of limb SEPs, although the timing and amplitude are different, as is the areal extent of the response. In a study of limb SEPs and V-SEPs Freeman and Sohmer transcranially recorded evoked responses. The P1 response was at 11.9 ± 2.0 ms and followed by the N1 response at approximately 30 ms, with the latency of these responses increased by 6.5 %, and the amplitude decreased by 30 % subsequent to an increase in stimulus rate from 2 to 7 Hz[121]. Similarly, Sakatani et al. epidurally recorded evoked responses and noted a latency of 6.5 to 8 ms, with the area of maximal responses being $\leq$1.5 mm in diameter. Barth et al. performed epicortical mapping with a 64 contact electrode array in Sprague-Dawley rats following whisker displacement. It was noted that the V-SEP consisted of a positive-negative fast wave, followed by a similar biphasic slow wave in S1, and that a similar waveform was present in S2, but had a delay in latency of approximately 10 ms. The initial P1-N1 complex was found to be constrained to the granular and perigranular areas of S1, extending into the latter by approximately 1 mm in which there was a lower amplitude of response. The second positive-going evoked potential component (P2) component extended to cover S1 and S2, and even more medial and lateral aspects of the cortex so that it overlapped with the auditory cortex, while second negative-going evoked potential component (N2) extended further caudally, but excluded S1. Additionally, Barth et al. compared the V-SEPs resulting from stimulation of a single vibrissa and groups of vibrissae, and noted that the V-SEPs were comparable, although the latter evoked activity over the entirety of PMBSF and that P1 was followed within approximately 10 ms by a second positivity found in a region lateral to PMBSF and also medial and slightly caudal to it[144]. In a study of the effects of environment on V-SEPs, which encompassed 60 Long-Evans rats in either enriched or impoverished conditions, and 27 in standard conditions, Seo epidurally recorded V-SEPs following electrical stimulation of a single vibrissal follicle. The V-SEPs, after 100 averages, across all three condition were 9.13 ± 0.12 to 9.82 ± 0.19 ms[145]. Using carbon-fibre electrodes inserted into layer IV, Armstrong-James et al. recorded V-SEPs from 62 Wistar rats, with activity occurring at 8.4 ms in the principal cortical barrel and this response spread over a larger cortical area over a further 7 ms[138]. Di and Barth recorded the field potentials of V-SEPs in Sprague-Dawley rats using a 64 channel microelectrode array, following mechanical displacement of a single vibrissa. At the centre of the greatest response P1 had an average latency of 8 ms, N1 at 16 ms, and the following slow-wave components, P2 and N2, at 32 and 80 ms, respectively. The fast-wave responses had an areal extent of 2 mm^2, while the slow-wave components were over a broader area of 2 to 3 mm^2[146]. In a study of the effect of infraorbital nerve damage on V-SEPs Shiraki and Satoh epicranially measured evoked responses before and after nerve damage in Wistar rats. The measurements were centred at the point of the largest

response and stimulation consisted of a 5° upward deflection at 0.4 Hz of all the unilateral vibrissae. Prior to nerve damage the P1 component had an amplitude of $91 \pm 28\,\mu V$ and peak latency of 11.3 ± 1.4 ms, and the N1 component an amplitude of $164 \pm 58\,\mu V$, and following nerve crush there was prolongation of the V-SEPs' response latency[147]. The aforementioned VSD imaging study examining vibrissal sensory and motor interaction found the earliest PMBSF response was at 7.4 ± 0.5 ms and was localised in the principal cortical barrel, and after a further 6.5 ± 1.9 ms activity in occurred M1[141].

Petersen and Diamond used a 100 contact microelectrode grid-array, commonly known as the Utah array and covering $13\,mm^2$, to measure single unit activity and generate PSTHs. The array was implanted in Wistar rats using a pneumatic impulse inserter so that the tips were in layer IV and the bottom of layer III, which was found to be from 400 to 900 µm. Single vibrissae were stimulated with a piezoelectric wafer, using an up-down step function to deliver a stimulus at 1 Hz, and a subset of 50 responses selected. An initial response at 5 ms covered an area of $0.2\,mm^2$, and this principal cortical barrel response broadened over 7 to 9 ms, which soon spread so that surround vibrissae were engaged within 10 ms and the total areal extent of the response ranged from 0.5 to $2.9\,mm^2$. The early activation of surround vibrissae was suggested to be the result of multi-vibrissae receptive fields of VPM neurons, which would allow for weak, but early thalamocortical activation of surround vibrissae[148].

Following electrical stimulation of the base of a layer IV barrel in brain slices, Petersen and Sakmann measured the resultant whole-cell and VSD responses. The first response occurred 2.0 ± 0.2 ms post-stimulus in layer IV, with this signal being the narrowest response, the VSD and whole-cell recording response then propagated to layers II and III with latencies to half-maximal response of 3.4 ± 0.1 ms and 2.8 ± 0.1 ms, respectively. While the response in layers II and III was broader than the initial response in layer IV, it was maximal in a region of a similar width to the layer IV barrel. Additionally, the response in layer IV also widened, reaching its lateral limits at 12 ms and the nearest layer IV barrels at a latency of 10.6 ± 3.2 ms[140].

Armstrong-James et al. made extracellular, single-unit spike-recordings of 382 cells in the Wistar rat barrel cortex, subsequent to downward displacement of a vibrissa at 1 Hz, using carbon-fibre microelectrodes. The latency difference between laminar responses was used in the analysis in order to mitigate inter-recording absolute time variability. The first activity occurred in layers IV and Vb, and was followed by activity 2 to 3 ms later in layers II and III, and by activity in layer Va 3.2 ms after the initial response. The result was that the activity within the first 10 ms, with a mean of 8.2 ms, was confined to the principal barrel, while, subsequent to this vertical transmission, horizontal transmission occurred via the septae resulting in transmission at approximately $5\,cm\,s^{-1}$[110]. Petersen et al. made similar findings in Wistar rats; VSD signals were first confined to the principal barrel

in the first 15 ms and then, by 40 ms, spread laterally at a rate of 33 to 60 µm s^{-1}. In this study, the earliest responses in layers II and III had a full width at half maximum (FWHM) of a fitted Gaussian curve of 477 ± 27 µm along the rows and 451 ± 25 µm along the arc, which approximates the dimensions of the layer IV barrel[139].

In Sprague-Dawley rats, Di et al. made recordings of V-SEP LFPs using a 16 contact linear electrode array, from which one-dimensional CSDA, and PCA of these responses, was undertaken. PCA revealed that 98 % of the CSDA variance was in the first two components. The electrodes were advanced perpendicular to the cortical surface to a depth of 2.25 mm, stimulation consisted of a 0.5 mm dorsoventral displacement of a single vibrissa, and the LFPs and CSDA were of an average of 20 repeats. The typical pattern of fast-wave P1 and N1 components, followed by a slow wave component were noted, with the latter being determined to arise in the supragranular layers at 100 ms followed by activity in infragranular neurons at 130 ms. The CSDA identified a sink in layers III to V at approximately 8 ms, and secondary source-sink complexes between layers I and IV, and V and VI, at 12 ms[54].

Einevoll et al. examined V-SEPs in response to different 1 Hz stimulation paradigms with a 23 contact linear electrode array, which had 0.1 mm inter-electrode spacing. The array was inserted normal to the cortical surface and centred on the maximal surface response as determined from audio monitoring of evoked responses. The electrode was employed to measure MUA, LFPs and from this CSDA, iCSDA, and PCA were undertaken. The PCA of the MUA, LFPs and CSDA indicated that most of the variance was contained in the first two components, which implies the number of laminar populations accounting for these is minimal. The earliest MUA was found at a depth of 0.6 to 0.8 mm, which was attributed to layer IV, which was also the approximate site of the first CSDA sink. Typically the activity of the layer IV population preceded activity in layers II and III by 1 ms and the population in layers V and VI by 2.5 ms[53].

Roy et al. undertook CSDA, LFP, and single and MUA recordings in the cortex and VPM of Sprague-Dawley rats in order to determine what subcortical mechanisms mediate multivibrissa input to PMBSF cortical barrels. In these measurements deflection of a single whisker was characterized by a sink in layer IV which had an onset latency of 5 ms and latency to peak activity of 7.4 ms, LFP and MUA analysis also found the shortest latency responses to be in layer IV. This initial activity was followed by activity in layers II and III, while activity in the infragranular layers had an onset latency of 8.4 ms and latency to peak of 9.6 ms. In addition to these findings the amplitude of activity was determined to decrease non-linearly with distance from the principal barrel, and the onset latency of this activity increased from 5 ms at the principal barrel to approximately 10 ms at a distance of three whiskers away, with the delay in onset latency being even longer, exceeding 20 ms at the periphery of PMBSF. In addressing the key aim of the study

Roy et al. inactivated corticocortical activity with the application of the $GABA_A$ agonist muscimol to the cortex. This resulted in the loss of spontaneous cortical activity and LFPs and MUA, and, while thalamic input to layer IV was unaffected and evoked activity in this layer was unaffected, activity in layers II and III was abolished, thus confirming its corticocortical origin[149].

Kwegyir-Afful and Keller undertook extracellular unit recordings in female Sprague-Dawley rats with the aim of examining activity in S2 following vibrissa stimulation at 1 Hz. Several key properties of the activity in S2 were determined and contrasted with that found in S1. The receptive fields in S2 were found to be at least five times larger than those found in S1, with the S2 units responding equally strongly to multiple whiskers, that is they possessed multiple principal whiskers. Moreover, the amplitude of the activity in S2 was significantly smaller, by approximately 50 %, than that found in S1, and S2 neurons were found to have more selectivity for the directionality of a stimulus. Regarding the latency of S2 activity the neurons in both areas were determined to have similar onset latencies; however, unlike in S1, there was no statistically significant difference between the onset latency of the units in different layers, implying that all layers of S2 receive direct input. In addition to this, the activity in S2 layers had a not significantly different onset latency to the activity in layer IV of S1, suggesting that the neurons of S2 are receiving direct thalamic input that is in parallel to the input to S1[150]. Another means of assessing the lateral spread of activity in the cortex is the examination of propagating waves, which are spreading areas or fronts of neuronal depolarisation that have been imaged with VSD imaging. The way in which propagating waves contribute to cortical function is multifaceted: they can provide a background change in potential and thus increase firing probability, increase network sensitivity to future stimuli, and also have been found to lead to organised spatial phase distributions that are oscillatory. VSD imaging of V-SEPs shows a wave that is initiated in the corresponding cortical barrel, which rapidly spreads to cover most of S1 within 15 to 50 ms, and also spreads into more distant somatosensory association cortices and even enters V1, while subsequent to the activity in S1 another wave was found to propagate from the whisker aspect of M1. Whilst the presence of propagating waves has been found to be reproducible they have large trial-to-trial variability, which is dissimilar to the consistent visually evoked waves noted in cats, monkeys, ferrets, and rodents, and additionally whisker propagating waves are much faster than those found in the visual cortex[151].

1.8.7 Rat visual system

In contrast to the multitude of rat vibrissae studies there is a relative paucity of literature regarding the rat visual system. To understand the reason for this it is useful to consider rat, and general mammalian, vision with respect to the vision of humans. Despite mam-

malian sensory physiology showing impressive complexity in many aspects, the visual system is not one of these, with most mammals having poor colour vision in comparison to non-mammalian species, which resulted in the long held belief, posited in 1942, that the nocturnality of early mammals resulted in the loss of colour vision; however, it has since been argued that it persisted, just in a less substantial manner. There are some exceptions to these generalisations, notably primates and humans: nocturnal mammals have minimal or absent colour vision, some mammals, such as many New World primates, are dichromats, having two types of colour-receptors, while most Old World primates and humans are trichromats, having three types of colour-receptors. The hierarchical nature of colour vision was another source of forming an evolutionary basis for the differences in mammalian vision, in fact the relative novelty of trichromacy has been suggested as the cause of the frequency of colour vision polymorphism in humans that result in deviations in spectral discrimination, which is comparable to the vision of New World primates. Consequently, to better understand human vision, Old World primates, such as *Macaca*, and dichromatic mammals, such as cats, are more frequently used as laboratory models, and so work in the rodent visual system had been limited [152].

1.8.7.1 Receptors

The receptor organs of the visual system are the eyes, which in the rat are located on either side of the head with 40 to 60° of binocular vision, but it is the retina within the eye that contains the light sensitive receptors that facilitate vision. There are multiple layers within the retina, but the function related division are light detecting photoreceptors, whose signal is transmitted by bipolar cells to retinal ganglion cells, whose axons constitute the optic nerve and are the retinal output, which in turn projects toward the cortex [153]. However, the composition of retinas vary; the visual acuity of six laboratory rat strains was tested by Prusky et al. in the Visual Water Task: rats are trained to recognise a visual cue as indicative of the exit from a water tank and their correct response a measure of correct visual perception. The three hooded strains, Dark Agouti, Fisher-Norway, and Long-Evans, had a visual acuity centred at 1 cycle/degree(c/d), with the theoretical maximum for humans being 50 c/d, and for the albino strains, Fisher-344, Sprague-Dawley, and Wistar, was significantly less, being approximately 0.5 c/d [154].

There are two key types of photoreceptor, rods and cones, with the narrower cylindrical shaped rods responsible for light detection and functionality in low light levels, referred to as scotopic vision, and the cones are responsible for colour vision in well-lit conditions, known as photopic vision. While humans have three types of cones sensitive to short, medium, and long wavelengths of light, in the rat rods are predominant, with only around 0.85 % of photoreceptors being cones. In the rat retina there are two types of cones, with 93 % being sensitive to the lower green spectrum, 500 to 520 nm, and the

remaining 7% having a peak sensitivity at 370 nm, which is in the ultra-violet range[153].

The retinal ganglion cells of the rat retina have an approximately even distribution of 600 to 3000 cells per mm^{-2}, and consequently the receptive fields across the retina are not significantly different, which implies exploratory fixation is unlikely. There are approximately 100 000 and 110 000 retinal ganglion cells in the adult retina of albino and non-albino strains, respectively, which is a much lower number than the rat is born with, as many retinal ganglion cells die in the first 5 to 10 postnatal days. There are three morphologies of retinal ganglion cells, and three conduction velocities in the optic nerve and so the two properties have been suggested to be related. An additional photoreceptor has been identified, termed intrinsically photosensitive retinal ganglion cells, which respond later and more slowly than rods and cones, and signal the presence of light over longer periods. Approximately 2.3 % of the rat's retinal ganglion cells are intrinsically photosensitive, and the highest density are found in the superior and temporal quadrants of the retina[153].

1.8.7.2 Ascending pathways, brainstem nuclei and thalamus

The retinal representation of the visual field is flipped on both axes, so that the temporal visual field is represented on the nasal aspect of the retina and vice versa, and the upper temporal field is represented on the ventral aspect of the retina and vice versa. The afferents of the eye are carried in the optic nerve to the optic chiasm, which facilitates contralateral projection, and beyond this the pathway is referred to as the optic tract and this projects to subcortical targets. The optic nerve of albino strains has approximately 100 000 axons, which are mostly myelinated, while hooded strains have more axons, 114 000 to 120 000. The location from which some of the afferents of the eye arise determines their targets, as many subcortical and cortical targets also have retinotopy. Additionally afferents with ipsilateral targets, typically having high velocity, arise in the lower temporal quadrant of the retina, while those in the upper temporal quadrant of the retina project to the lateral hypothalamus and multiple other nuclei. While at its origin the optic nerve is topographical, this topography diminishes caudally in the optic tract, which includes chiasmic optic branches and connections from the contralateral brainstem, such as the parabigeminal nucleus. Binocular vision depends upon contralateral and ipsilateral projection, but in the rat ipsilateral connections only constitute approximately 3 % of the visual pathway axons, and 1.5 % in albino strains. In spite of this, there is significant activation in ipsilateral subcortical and cortical targets, which in hooded strains rats reflects connections between subcortical areas on both sides of the head. The interhemispheric connections in albino strains is largely facilitated by callosal projections from the visual cortex[153].

A key structure of the visual system is SC, which in mammals is the more common

term for the optic tectum and is a horizontally laminated structure of the midbrain. As with many of the subcortical structures of the visual system connectivity of SC is vast and complex to facilitate sensory reception, interpretation and motor responses, therefore here only some key connections and functions are given. Practically all of the rat retinal ganglion cells project to the SC. There is a retinotopic layout in SC with the upper visual field represented in the medial aspect of SC and vice versa, and the nasal aspect of the visual field represented in the anterior aspect of SC and vice versa. In SC the representation of the central visual field is not substantially magnified as compared to the peripheral field; however, the receptive fields of the superficial strata of SC are smaller than those of the deeper layers. Ipsilateral projections to SC are restricted to the rostral aspect of the structure, and here monocular and binocular receptive fields can be measured. SC also receives corticotectal projections, which arise from pyramidal neurons in the upper two-thirds of layer V and their origin define where in SC they terminate; corticotectal projections from V1 terminate in the superficial strata, lateral area of secondary visual cortex (V2L) in the intermediate strata, and medial area of secondary visual cortex (V2M) in the intermediate and deep strata. Two-thirds of the superficial strata of SC are ascending projections. One projections is to the parabigeminal nucleus, which is in the lateral aspect of the brainstem and has connections to the ipsilateral and contralateral SCs, and also to the dorsal part of lateral geniculate thalamic nucleus (dLGN). Of the descending pathways from SC there are two main pathways: one arises from the deeper strata and terminates in the ipsilateral spinal cord and also the brainstem, while the other arises from the lateral aspect of intermediate strata and terminates in the gaze centres of the brainstem. There is also a projection from the intermediate strata to the contralateral SCs and from the ventral aspect of the superficial strata to dLGNs. The cells of SC have high contrast sensitivity, a narrow dynamic range, and approximately 9 % orientation selectivity, which is typically biased upwards [153].

Another important subcortical target is the pretectum, which is a multi-part structure located on the rostral pole of the midbrain, with the nuclei of the pretectum being relatively functionally distinct. The contralateral pretectum receives approximately 13 % of retinofugal terminations, and also projections from layer V of V1 and from V2L and V2M. The anterior pretectal nucleus, which is situated at the rostral end of the pretectum, receives input from other pretectal nuclei, but has a role in nociception, rather than vision. The posterior pretectal nucleus, the function of which is unclear, receives both contralateral and ipsilateral retinal input and projections from the visual cortex, with projections from this nucleus terminating in the suprachiasmatic nucleus. The olivary pretectal nucleus, which has a role in the pupillary light reflex, receives both contralateral and ipsilateral retinal input, and projects to the Edinger-Westphal nucleus, which allows for consensual pupillary light reflex and integration of visual information occurs in both

nuclei. In albino strains the consensual pupillary light reflex is reduced as a result of the ipsilateral pathway being smaller. The nucleus of the optic tract, which is situated amongst a lateral extension of SC, known as the branchium, only receives contralateral retinal projections. This nucleus projects to the inferior olivary, pontine reticulotegmental and prepositus hypoglossal nucleus, and to the ipsilateral dLGN. The nucleus of the optic tract has large receptive fields and strong horizontal direction selectivity [153].

The primary relay of the rat visual system is dLGN, with 78 % of the neurons in dLGN being relay neurons. This nucleus is situated in the dorsolateral aspect of the thalamus, has a striated appearance due to the presence of axon bundles, and possess a retinotopic map. The retinotopy of dLGN is such that the upper temporal visual field is represented towards the anterior dorsolateral quarter of the structure, the upper nasal field toward the anterior dorsomedial quarter, the lower temporal field toward the posterior ventrolateral quarter, and the lower nasal field toward the posterior ventromedial quarter. Within dLGN the neurons can be defined, electrophysiologically, as either principal relay neurons or interneurons. Principal relay neurons, which exhibit low-frequency intrinsic activity, respond to stimulation of the optic nerve or tract with a single short latency action potential, intermittently followed by trains of 3 to 5 spikes for $\geq$1 s, and can also be activated, antidromically, from V1 and V2. Interneurons of dLGN do not exhibit post-excitatory inhibition, which is present in the principal relay neurons, have a longer time constant, oscillatory responses and their activity is marked by slow spike-frequency adaptation. Corticogeniculate input to dLGN, which arises in the ipsilateral layers V and VI, and retinogeniculate input are both found in the anterior pole of dLGN. A second group of input, transverse to the first, carries retinogeniculate, retinofugal, corticofugal, corticocollicular, and corticogeniculate projections, with the latter two arising from layers V and VI, respectively. The most numerous input to dLGN is from the upper part of layer VI of V1, while the lower aspect of this layer projects to lateral posterior thalamic nucleus (LP) and has branches to dLGN. dLGN projects to layer IV and the lower aspect of layer III, and more sparsely to layers VI and I, of the ipsilateral V1, and also to RtN. Another key thalamic target is the ventral part of lateral geniculate thalamic nucleus (vLGN), which has a role in light intensity processing, but not pattern discrimination, and the lateral division of which receives significant bilateral retinal input, input from dLGN and LP, and from V1, which arises in layer V, and V2. This division is also reciprocally connected with the zona incerta. The medial region of vLGN has no visual projections, but receives sparse input from secondary motor cortex (M2) and V2L. Between dLGN and vLGN is the intrageniculate leafle (IGL), which receives input from the contralateral IGL via the optic chiasm and posterior commissure, and has a role in integrating visual input and projecting these to the suprachiasmatic nucleus. The rodent LP is a homologue of the pulvinar nuclei and is located in the dorsolateral aspect of the thalamus, and is caudomedial to

dLGN. This nucleus is a high-order nuclei that interconnects multiple cortical areas, it receives input from the ipsilateral V1, arising in layer V, and from layer VI of V2, and projects to V1 and V1[153].

1.8.7.3 Cortical organisation

The rat V1 is part of the koniocortex, or granular cortex, and as such there is high cell density in layers IV and VI, and low cell density in layers II, III and V. However, the processing of visual stimuli goes beyond V1, as there are a total of seven subdivision of the rat visual cortex, the main area is V1 and the others are subdivisions of V2. Lateral to V1 is V2L and medial to V1 is V2M, with both of these areas, unlike V1, having relatively even cell density between layers II and VI. There are a series retinotopic maps throughout the different visual cortex areas, in V1 the upper visual field is represented caudally and vice versa, the temporal visual field is represented medially, the vertical meridian extends along the lateral border of V1 and the horizontal meridian extends diagonally from the craniolateral corner of V1 to its caudomedial corner[153;155].

The lateral aspect of V1 contains the binocular visual field and the medial aspect a monocular field from the contralateral eye only, with binocular neurons being more numerous, by approximately 19 %, in male rats than in female rats. The total cell population of rat V1 is 850 000 to 1 128 000 neurons in an area of 7.1 to 9.4 mm^2, which constitutes approximately 50 to 60 % of the visual cortex and 10 to 12 % of the entire neocortex. This, given that dLGN has 16 000 to 18 000 relay cells, gives a ratio of 50 to 60 cells in V1 for each of the dLGN relay cells, which is less than that of mammals with more developed visual systems. Other inputs to V1 include projections from locus coeruleus, with 95 % being ipsilateral and 5 % contralateral, and its projections activity being attention mediated and diminished by repeated exposure. In addition to this, there are small cholinergic basal forebrain projections to all layers of V1, with those to layers IV and VI being sparser, projections from the claustrum to V1, and small thalamic inputs from LP and intralaminar nuclei. The majority of afferents to V1 terminate in layer IV and the lower aspect of layer III, although some geniculocortical terminations are present in layers I and VI, with the latter having monosynaptic reciprocal connections to dLGN. The majority, approximately 83 %, of thalamic projections to layers IV and III synapse with the apical dendrites of pyramidal cells in layers V and VI, basal dendrites of pyramidal cells in layer III, dendrites of spiny non-pyramidal cells in adjacent layers, and other cells in layer IV, while of the remainder, 15 % terminate onto aspects of pyramidal or stellate cells in layers III and V, and 2 % onto sparsely spiny or smooth stellate cells in layers IV and III[153].

Layers I and II of the rat visual cortex exhibit a honeycombing pattern of <100 µm wide modules, with the wall of these receiving corticocortical terminations and the hollows

thalamocortical terminations, and so the two aspect of the structure contain parallel circuits comparable to the barrel-septa arrangement of the rat barrel cortex. Layers II and III are the key site of glutamatergic neurons, while aspartate, another excitatory neurotransmitter, is employed in layers II to VI. Layers II and III are also noted for having widespread intralaminar connections and strong monosynaptic projections to layer V, and projections to other areas of the visual cortex and the contralateral V1. Layer IV is the most prominent, but not exclusive site, of non-pyramidal cells in the visual cortex employing GABA, and also of spiny stellate cells that receive input from dLGN. Layer IV has strong topographical projections to the lower aspect of layer III, but weaker horizontal projections above this, and also narrow vertical projections to layers V and VI. While layer IV has sublayers in primates, which receive differing dLGN input, no such subdivisions have been identified in rats. Layer V receives input from the lower aspect of layer VI. Layer Va projects to layers II, III and VI, while Vb projects to layer I, the lower aspect of layers II and III, and the upper aspect of layers IV and V. Many of these connections are over a wide area. Layer V in V1 also projects to the ipsilateral pontine nuclei, with these projections having collaterals to SC, collaterals to the cerebellum, and to the zona incerta. Layer VI also makes wide connections, it projects to dLGN and RtN, and has clustered projections to layers I, II, the lower aspect of layer III and to layer IV, and the lower aspect of layer V. In summary, the long-ranging intracortical neurons of V1 are found in layers II, III, V and VI, while subcortical projections, not contributing to intrinsic connections, are found in layers V and VI, and layer IV makes relatively narrow, column-like, projections[153].

Comparison of the lamina of the two subdivisions of V2 reveals some differences: layers II and III are distinguishable in V2L, but not in V2M, layer V is denser in V2M than it is in V2L, and while layers V and VI occupy the bottom half of V2L, they occupy the bottom two-thirds of V2M. Additionally, V2M has a thicker layer IV and it has a higher density of granule cells. Approximately 80 % of the cells in V2L are pyramidal neurons, the non-pyramidal cells that are present are found in all layers, but are densest in layers II, III, and VI, and interneurons are most prominent in the supragranular layers. Similar to V1, V2 receives input from dLGN, LP, other thalamic nuclei, the basal forebrain, and the claustrum, and projects to dLGN, RtN, pontine nuclei, SC, and the zona incerta. In addition to this, connectivity between the visual cortical areas is extensive: V1 and V2 have reciprocal visuotopic connections, the majority in V1 are feed-forward connections arising from pyramidal cells in layers II and III, and the V2 terminations are located in layers II, III, and IV. The major route of feedback projections is from V2L, rather than V2M, with approximately 30 % of V2L feedback projection to the ipsilateral V1 having collateral projections to the contralateral visual cortex. The majority of projections to V1 arise in layers V and VI and terminate in layers II, V, and VI. All of the visuotopic areas

of V2 are reciprocally connected with the corresponding area of V1 and SC. In addition to this, each area of the visual cortex, excluding the caudal aspect of V2L, receives input from the caudal third of the eye field aspect of the motor cortex and V2[153].

There is a hierarchy in the rat visual system, with V1 receiving virtually all of the cortical projections of dLGN and sending feed-forward projections to all visuotopically organized areas of V2. However, there is some uncertainty regarding the divisions of V2 in the rat. It is most likely that the caudal aspect of V2L is the homologue of V2 in carnivores and primates, as it receives its major associational feed-forward projections from V1. The rostral area, receiving input from V1 and the caudal aspect of V2, may be more akin to a third level of the hierarchy. Lastly, V2M, which receives input from V1 and V2L and sends feedback projections to these areas, might represent a higher, fourth, level with in the visual system hierarchy. Moreover, projections from V1, the caudal aspect of V2L, the rostral aspect of V2L, and V2M, terminate in progressively deeper layers of the ipsilateral SC, which, if the proposed hierarchy were true, would represent a correlation of place within the visual hierarchy and depth of termination in SC that matches the pattern found in primates. Nonetheless, the hierarchy of the rat visual system is still contentious and uncertain[153].

The visual cortices are interconnected via the caudal part of the corpus callosum; however, most of V1 does not receive contralateral input, with most of such input being in the lateral third of V1 and terminating in all layers, but most prominently in layers I, II, III, and V. Interhemispheric projections from V1 arise in the medial two-thirds, mainly from layer V and project to the lateral aspect of the contralateral V1 and medial aspect of the contralateral V2L, with very few projections to V2M. Interhemispheric connections from V2L arise on its border with V1 and project to the contralateral V2L, while there are four areas of interhemispheric projection in V2M that terminate in the contralateral V1 and V2[153].

In discussing visual cortex functionality the work of Hubel and Wiesel is fundamental; in a cat model Hubel and Wiesel found that cells respond to different types of visual stimuli, which were termed simple and complex-cells[115], and since then a third category, end-stopped cells, also known as hyper-complex cells, have been identified. In addition to these three categories further cells with even more specific functions, such as cells that detect line and edge crossings, have been discovered. Simple cells and complex-cells show activity in response to oriented edges and gratings; however, complex-cells have some spatial invariance: complex-cells show activity in response to a certain orientation within a large receptive field, irrespective of its precise location. The activity of end-stopped cells increases as a stimulus fills more of its receptive field and then this diminishes as it exceeds its receptive field. All types of visual cortex cell have been found in the rat: simple cells, which are both pyramidal and non-pyramidal, are found in layers II, III,

and IV, while only pyramidal cells are complex or end-stopped, with complex-cells found in layers II to IV, and end-stopped cells in layers II, III, and V. Approximately half of the cells in the rat visual cortex respond to flash photic stimuli, while the remainder show little or no response to such stimulation and respond better to optimally oriented and spatial frequency moving gratings. Within the rat V1 approximately 75 to 80 % of neurons and 60 % in the entire visual cortex exhibit orientation selectivity, with around 35 % of those in V1 being selective to horizontal gratings. Layers II and III have high orientation selectivity, and respond to low velocity and high spatial frequency stimuli, while cells in layer IV have high temporal resolution and respond to high velocity stimuli, and this layer also has the lowest percentage of simple cells. Cells lacking orientation selectivity do not concentrate in any particular layer of the rat cortex. In addition to this, the orientation columns first revealed by Hubel and Wiesel, are not present in the rat; however, a study examining orientation columns with three-dimensional two-photon calcium imaging in layers II and III of the mouse visual cortex, while reiterating the absence of orientation columns, proposed the possibility of orientation mini-columns on a scale of approximately 40 µm[156]. Ablation studies have also revealed significant aspects of the function of the rat visual system: ablation of V1 causes only a relatively small reduction in spatial acuity, to approximately 0.7 to 1.0 c/d, without affecting pattern discrimination, while ablation of V2M result in the severe impairment of visuosomatic conditional responses. The conclusion of such studies is that, as in other mammals, V1 mainly processes local feature discrimination, V2L pattern recognition, and V2M other spatially oriented actions[153].

1.8.7.4 Propagation of activity and functional considerations

It has already been detailed that there are stark differences between the visual system of rats and other more popular models of visual processing, such as cats and primates. However, while studies in these models have some similarities with findings in the rat, for example epidural recordings and CSDA in awake macaque shows flash evoked activity starting, as in the rat, in layer IV[157], drawing parallels between studies in these models and rats is contentious. Nonetheless, studies have been undertaken examining the propagation of activity in the rat visual cortex. Barth et al. examined auditory, visual, and mixed auditory-visual EPs, with the auditory-somatosensory polysensory region being found to have its own thalamocortical projection, which implies that the processing of polysensory stimuli is initiated subcortically. Bilateral stroboscopic visual stimuli approximately 3 mm in diameter were presented to four Sprague-Dawley rats, and the resultant visual evoked potentials (VEPs) were recorded with a 64 contact platinum electrode array. The fast wave components, occurring at 20 to 30 ms, were subdivided into a first component, $P1_a$-$N1_a$, which was found to be centred on V1, and a second component,

$P1_b$-$N1_b$, which was shifted rostrally and laterally into V2. The slow wave components of the VEPs, P2 and N2, which respectively occurred at 43 and 105 ms, were more widely distributed and even extended to S1 and S2[158].

Kenan-Vaknin and Teyler employed CSDA to determine the spatio-temporal pattern of activity in the rat V1; in Long-Evans rats profiles were collected with an electrode advanced at 100 µm intervals and the response to 10 stroboscopic stimuli of 10 µs duration delivered at 0.2 Hz measured at each depth. The spatio-temporal pattern involved early sinks in layer IV and the lower aspect of layer III at approximately 33 ms post-stimulus, which was followed by activity in layer V at 37 to 41 ms and the supragranular layers at 40 to 55 ms. A later second group of activity was found to occur in layers II, III and VI at approximately 81 ms. In summary, flash evoked responses in the rat V1 resulted in early excitatory activity in layers IV and the lower aspect of layer III, resulting from geniculocortical thalamic input, which was followed by activity in the supragranular layers and, further delayed, activity in the infragranular layers[112].

Bode-Greuel et al. undertook one-dimensional CSDA of activity following electrical stimulation of the white matter of 350 µm thick slices of V1 from albino rats. The LFPs, that formed the basis of the CSDA, were measured normal to the pial surface at intervals of 25 to 50 µm. The earliest sink, occurring at 0.8 ms post-stimulation, was found in layer IV, another 0.9 ms later a sink at layer III was identified, and another 1.7 ms later a sink in layer II. There was also identification of a sink in layer V with an onset latency of 2.5 ms, and a sink in layer VI; however, the latter, as with the layer IV activity, was merged with a stimulation artefact[159]. In another visual cortex slice study, Aizenman et al. recorded LFPs in slices from Long-Evans rat V1 and from these undertook CSDA. Activity was evoked by bipolar electrical stimulation either at the border of layer VI and the white matter, or in the middle of the cortical depth, and the evoked activity recorded with sodium chloride (NaCl) filled glass microelectrodes inserted normal to the pial surface at depth intervals of 50 to 100 µm and approximately 50 µm lateral to the stimulation site. Stimulation at the border of layer VI and the white matter resulted in large amplitude sinks in layers II and III, and the bottom aspect of layer III, which peaked at 5.9 ± 0.3 ms post-stimulus and had diminished by approximately 15 ms post-stimulus. A smaller amplitude sink occurred in layer V, which could persist for $\geq$20 ms post-stimulus. Stimulation of the middle layers resulted in similar CSDA profiles including a prominent sink in the bottom aspect of layer III that was continuous with activity in layers II and III. One of the key differences between the two stimulation paradigms was that the activity in the bottom aspect of layer III was activated monosynaptically from both stimulation sites, while the continuous sink in layers II and III was only activated monosynaptically when stimulation was in the middle layers[160].

Osanai et al. examined mouse visual cortex slices, from which some inferences regarding the rat visual system can be made; parallel examination of the house mouse, *Mus musculus*, reveals similarities to the rat in several indices: electrophysiological, anatomical and genetic, although the mouse retina has many more ultraviolet sensitive cones than the rat[152]. The cortical slices, the layers of which were confirmed by infra-red imaging, were taken from mouse V1 and were 300 µm thick, with 310 stimulations being delivered in layer IV with a biphasic stimulator and the evoked response measured by means of CaSD imaging. Transients of calcium (Ca^{2+}) were measured within 10 ms of the stimulus administration, with the largest Ca^{2+} transient measured in layer IV at 8 ± 1 ms. The transient in layer IV spread into layers II and III at 19 ± 4 ms post-stimulus and increased in size up to 40 ms post stimulus and smaller transients in layer V were also measured. The horizontal spread of the high Ca^{2+} region was in layers II, III, and IV, and was restricted to a region 200 µm in diameter. The CaSD measured response started to diminish at approximately 60 ms so that by approximately 200 ms post-stimulus the Ca^{2+} level was comparable to baseline levels. Comparable to findings in the barrel cortex, the application of 5 µmol L^{-1} of bicuculline resulted in no horizontal restriction of the evoked response. The conclusion was made that recurrent excitatory connections are present within mouse V1 and that inhibitory signals suppresses horizontal propagation under normal conditions, particularly in layers II and III[161].

In a study examining rat cortical slices Domenici et al. investigated the spatio-temporal propagation between V1 and the caudal aspect of V2L, and vice versa. Cortical slices from Long-Evans were electrically stimulated at 0.2 Hz with bipolar electrodes either in the upper layers, layers II, III, and IV, or in the infragranular layers. This stimulation was either in V1, approximately 0.5 mm medial of its border with V2L, and the responses recorded in V2L, 0.3 to 0.5 mm medial of the border between V1 and V2L, in order to examine feed-forward transmission, or the stimulation and recording sites were reversed to examine feedback transmission. The resultant LFPs were measured perpendicular to the pial surface at intervals of 50 to 100 µm, as confirmed by histology, throughout the cortical slice, and from these CSDA was performed. Superficial stimulation of V1 resulted in a large sink in layer IV at approximately 2 ms, which peaked at 4.00 ± 0.95 ms, and this was followed by broader sinks in the bottom of layer I and in layer VI, which had an onset at approximately 4 ms and peaked at 6.00 ± 0.63 Even broader sinks occurred at approximately 5 ms in layers II and III, which then peaked at 10.00 ± 1.08 ms. Moving the stimulation site to the infragranular layers of V1 resulted in sinks in all layers of V2L, with a sink at approximately 2 ms in layer IV that peaked at 4.00 ± 0.48 ms, which was followed by sinks in layers II and III that peaked at 5.50 ± 0.91 ms, and broader sinks in layers II, III, and V at 12.0 ± 2.3 ms. Superficial stimulation of V2L, to examine feedback transmission, resulted in sinks in all layers with the earliest in layers I, V, and VI

at 4.0 ± 0.5 ms, and these were followed, at approximately 4 ms, by sinks in layers III, IV, and VI that peaked at 7.50 ± 0.58 ms, and even later sinks in layers II, III, and V at 10.0 ± 1.5 ms. Stimulation in the infragranular layers of V2L resulted in sinks in V1 in layers I, IV and VI at 4.00 ± 0.29 ms, followed by sinks in layers II, III, and VI that peaked at 7.0 ± 0.5 ms and in layers II, III, and V at 10.00 ± 1.93 ms[162].

As detailed in section 1.8.6.5, the investigation of propagating waves is an increasingly frequent means of assessing the lateral spread of neuronal activity. Xu et al. used VSD imaging to examine propagating waves in V1 and V2 in Long-Evans rats subsequent to fullscreen drifting gratings. Subsequent to the presentation of the visual stimulus a propagating wave was initiated in the monocular region of V1 which propagated towards the binocular region and also V2. This initial wave went through a compression phase and a second, reflected, wave was initiated at the border of V1/V2 and propagated back towards V1. The first evoked wave had an onset latency of approximately 100 ms (99.8 ± 18.2 ms), while the compression phase resulted in the wave being compressed to its narrowest after a further 72.7 ± 7.2 ms. A second compression was noted, more medial to the first compression, approximately at the border between V2M and the retrosplenial dysgranular region. The first wave and compression were found to be highly reproducible over trials and rats. Changes in the location of the stimulus resulted in a different primary wave initiation site, in concordance with the retinotopic map of V1, and variation in the shape of the compression wave. In contrast the second, more medial, compression was highly variable in its onset time, although its location was fixed. The variability in these phenomena and its non time-locked nature means that it may be blurred by averaging and so Xu et al. argued that it was only possible to visualise them with their technique, which employed hardware with a high dynamic range and single trial imaging. To better characterise these visual propagating waves Xu et al. applied cortical activity suppressants, lignocaine and CNQX, to the contralateral cortex and noted that the reflected wave was unaffected, which was taken to imply that contralateral contribution to the reflected wave is minimal and that contributions are more likely from higher association cortices. Similarly, Xu et al. examined some of the causes of the wave compression, which were deemed to be either a reduction in horizontal connections near the V1/V2 border, an increase in local inhibition, or a decrease in the local excitatory connections. The first was ruled out on the basis of the extensive horizontal connections between pyramidal neurons in layers II and III, the third on the fact that spontaneous waves do not exhibit compression, which left the second possibility, and this was confirmed as application of bicuculline abolished the wave compression at the V1/V2 border. Xu et al. noted an absence of the compression and reflection phase in spontaneous propagating, and that the initiation sites of the primary wave were more diffuse for spontaneous waves, and spontaneous waves were found to be quicker than evoked waves[163].

1.9 Purpose and design

The overall aim of this thesis is to advance the imaging of brain pathology and function, with particular focus on determining the feasibility of the use of EIT for neuroscientific research into the fast neural changes of brain function. Previous work, as detailed in this chapter indicates, based upon modelling, nerve and cortical measurements, that EIT imaging of fast neural activity should be technically possible, but this hypothesis needs testing in an objective fashion. However, there are multiple technical bottlenecks that must be addressed before direct cross-validation of EIT imaging of fast neural activity should be undertaken.

First, there is a question of how data should be selected for inclusion in the image reconstruction, as erroneous data, due to the ill-posed nature of EIT can be amplified into large errors in the reconstructed conductivity changes. Therefore there is a need to identify an objective method of boundary voltage rejection. In chapter 2, a comparison of reconstruction algorithms for EIT imaging in a realistic head-shaped tank was undertaken. This was accomplished for the case of MFEIT imaging which could equally be applied to the detection of acute stroke or paradigms based upon time difference imaging. Within this study there was the additional aim of assessment of boundary voltage rejection methods and quantitative analysis of image quality, with the intention of informing subsequent experimental imaging in the rat during fast neural activity. Boundary voltage rejection is essential for the application of EIT of fast neural changes, because the signals in this application are small and poor signal processing will result in the amplification of noisy data in the image reconstruction and consequent corruption of images of fast neural activity.

The next question to address is what findings have already been obtained and what technical limitations need to be overcome in order to determine the feasibility of the use of EIT for neuroscientific research. Therefore, the research already undertaken, analysis of the results it has and might yield and how this work might be improved in future studies was considered. To this end rigorous statistical analysis of the EIT dataset collected by Gilad et al. (2010) [90] was performed using the widely employed neuroimage analysis approach of SPM, which is the focus of chapters 3 and 4. Within this work, the question of the best means of image analysis, with particular focus on EIT images of fast neural activity, will be addressed. The dataset examined in these chapters had certain limitations, which included no independent validation of the imaged changes and a relatively poor temporal resolution of 8 ms, and the use of electrical stimulation, preventing somatotopic mapping. It was a key aim of this thesis to attempt to address the shortcomings of this previous study.

Finally, to examine the main hypothesis of the thesis, a novel EIT imaging study of

fast neural changes in the anaesthetised rat, with changes measured using an epicortical electrode array was undertaken. These recordings were during mechanical whisker stimulation with a time constant of 2 ms, improved imaging methods, and independent validation through the use of ISOI and LFP recording.

1.10 Statement of originality

The material in this thesis is my own work and has not been previously submitted for a degree in any University, and to the best of my knowledge contains no material previously submitted or written by another person, or group, except where due acknowledgement is made in the thesis itself. The research is a product of my own work and the intellectual content of this thesis is the product of my own work, except to the extent that assistance from others in the project's design, conception, style, presentation and linguistic expression is acknowledged within the acknowledgements of this thesis.

Within chapter 2 I used work undertaken by prior group members, including the EIT hardware and its associated code, moreover I employed an algorithm, the weighted frequency difference algorithm, previously published and this code was provided by S. Ahn of Gwangju Institute of Science and Technology, South Korea. Additionally, I used a calibration procedure provided by H. Koo of the UCL EIT group for calibrating the data in chapter 2.

The analysis in chapters 3 and 4 was performed on data acquired in the anaesthetized rat by previous researchers in the UCL EIT group. In addition to this, I received advice on the application of SPM and statistical non-parametric mapping (SnPM) from G. Barnes of the Institute of Neurology, UCL, and the meshes used for forward modelling and the code for the inverse solution were provided by other members of the UCL EIT group. However, all the analysis was undertaken by myself and the analysis in these chapters, beyond the use of SPM, was of my own conception and also undertaken by myself.

In the final experimental rat studies, detailed in chapters 5 and 6, I was assisted in engineering development by H. Koo and K. Aristovich of the UCL EIT group, but all the surgical and physiological work I undertook personally. Similar, to the work in chapters 3 and 4, the meshes used for forward modelling and the code for the inverse solution were provided by other members of the UCL EIT group, but the optimisation to the inverse solution employed in chapter 6, was developed by myself, and all data analysis and image reconstruction was undertaken by myself.

Chapter 2

Multi-Frequency Electrical Impedance Tomography of Acute Stroke in a Head-Shaped Tank

2.1 Introduction

Imaging acute stroke might be possible using EIT, as ischaemic cortical tissue, blood and normal cortical tissue have different conductivity spectra[164]. EIT could then be implemented in acute settings, such as in ambulances, to permit early utilisation of life-saving thrombolytic agents, that can substantially improve the outcome of patients[165]. However, such treatment depends upon the differentiation of the type of stroke; there are two types of stroke ischaemic and haemorrhagic. Whilst ischaemic stroke may be treated with thrombolytics, the administration of these drugs in a haemorrhagic stroke can worsen the pathology. In addition to this, such a distinction must be made rapidly, as the earlier the treatment is given the better the outcome, with little to no benefit if treatment is given later than three to six hours. Therefore there is a need for a rapid, inexpensive, safe, and effective means of differentiating the two subtypes of stroke, which might be achieved with EIT.

However, if EIT is to be implemented in the imaging of acute stroke, time difference (TD) recordings, in which a baseline data set and a perturbation data set are compared, cannot be undertaken. TD imaging is not possible in acute stroke due to the lack of a baseline data set, as patients present to medical services after the onset of symptoms. Consequently, in imaging acute stroke either absolute or frequency difference (FD) imaging must be used. However, there are specific difficulties with the use of MFEIT, and absolute imaging, such as a higher susceptibility to noise and calibration errors than in TD imaging. Additionally, EIT of the head presents challenges related to the skull, its high impedance typically limits the SNR, and the irregular geometry of the head can result in low amplitude boundary voltages and consequently low SNR data as it is difficult

to predict the location of isopotential lines between for different patients' heads. This chapter is both a comparison of the efficacy of four FD algorithms in imaging stroke-like changes in an anatomically realistic head-shaped tank and also an examination of boundary voltage rejection methods for rejecting low SNR boundary voltages.

2.1.1 Physiological and clinical background

Stroke is the most common cause of morbidity and mortality in industrialised nations [166] and in the UK leads to an estimated direct cost to the NHS of £2.8 billion annually [167]. There are two major subcategories of stroke: ischaemic stroke, typically secondary to a thromboembolic event, and haemorrhagic stroke, due to some form of vascular rupture. Although the two types of stroke have some differences in risk factors and a few differences in clinical signs and symptoms, certain differentiation is not possible without neuroimaging. The importance of making this differentiation is due to the diametrically opposed treatment regimes: ischaemic strokes can be treated with pharmacological thrombolysis and haemorrhagic stroke is treated by other means, including surgical intervention. Pharmacological thrombolysis is achieved with a tissue plasminogen activator (tPA), which encourages rapid recanalisation of the thrombus that is obstructing cerebral blood vessels and if given early enough can substantially improve the outcome of patients [165]. This benefit derives from the recovery of the penumbra, a region of tissue with reversible ischaemic tissue damage. The NINDS double-blind randomised controlled trial reported that at three months patients treated with tPA were 30% or more likely, compared to a placebo control group, to have minimal or no disability, as determined by a combination of four post-stroke performance scales [168].

However, if such thrombolytic agents are given to those suffering from a haemorrhagic stroke, they may worsen the pathology by expanding the haemorrhage, with a 5.8 to 13.3 % increased occurrence compared to placebo [169]. It is this difference in treatment that underlies the need for early and effective differentiation between the two stroke types, which can be achieved with CT or MRI. However, for tPA to be effective it should be given soon after an ischaemic event, as brain damage is generally irreversible after 3 to 6 h, and the outcome improves continuously with reduced time to treatment; the best results achieved with tPA administration are when it is given within $\leq$1 h of an ischaemic event [170]. This need for rapid treatment is the current limiting factor in acute stroke management, as the patient must be transported to a CT or MRI scanner, then imaging must be taken and reported. The latter two were found by Sattin et al., in a study of 781 patients, to typically take 60 min [170], which can result in a total time exceeding the 3 h window. Similarly, in a review of the treatment of acute stroke across 98 hospitals, including a total of 6867 admissions, Reeves et al. found that less than 25 % of patients were arriving at emergency departments in less than 3 h, with only 11 to 20 % of those

patients receiving tPA in less than 1 h [171].

2.1.2 Bioimpedance changes in acute stroke

The difference in conductivity spectra between normal cortical tissue and ischaemic cortical tissue is as a result of hypoxia caused by the ischaemic event. The effect of ischaemia on the brain has been studied in animal models, where conductivity decreases of around 10 to 20 % were recorded (see Holder and Tidswell (2006) [78] for a review). In ischaemia, neuronal cells are required to switch to anaerobic respiration; given the exceptionally high metabolic demands of neurons, they are especially sensitive to hypoxic or anoxic events and anaerobic compensation is rapidly insufficient and intracellular glucose reserves exhausted. During this anaerobic respiration, resulting from the hypoxic conditions of ischaemia, there is an accumulation of lactic acid and other metabolites that increase the intracellular osmotic pressure and the influx of water into cells. Moreover, as the availability of ATP is reduced, ATP-dependent Na^+/K^+ pumps begin to fail, worsening the transcellular ionic imbalance and causing membrane depolarisation secondary to intracellular Na^+ accumulation and reduced intracellular K^+. In response to this, there is chloride (Cl^-) and Ca^{2+} influx, with the latter leading to activation of excitatory neuronal receptors, including *N*-methyl-d-aspartic acid (NMDA) receptors, causing further Ca^{2+} influx and excitatory neurotransmitter release. The end result of this cascade of ionic influx and subsequent water influx is a concordant cell swelling. This acute cell swelling causes a reduction in the extracellular space and an impedance increase at low frequencies; current cannot pass across the capacitive cell membrane and must pass through the extracellular space. In contrast, haemorrhage produces a localised region of impedance decrease, which is approximately flat across frequencies up to 1MHz, due to the extravascular presence of conductive blood. Following a haemorrhagic stroke there is the potential, depending on the vasculature affected, for a more widespread cerebral ischaemia as a result of the interrupted blood supply. Secondary ischaemia can also be the result of the haemorrhage's mass effect, which leads to tamponade of cerebral blood flow, or the vasoconstrictive and vasospasmodic events that follow the vascular smooth muscles' exposure to haemolysed blood products.

Although there have been TD recordings made in stroke models, unfortunately, there has not been a single exhaustive study to examine the impedance changes during acute stroke, but a review of the literature, summarised by Horesh, allows for a prediction of the changes that will occur, which is in agreement with the pathophysiology described above. This review indicates that the conductivity of normal brain is about $0.1\,\mathrm{S\,m^{-1}}$ at frequencies below 100 Hz, where current passes almost entirely in the extracellular space. It increases to around $0.18\,\mathrm{S\,m^{-1}}$ at 1 MHz as current starts to pass across cell membranes into the intracellular space. In contrast, ischaemic brain is around $0.07\,\mathrm{S\,m^{-1}}$ less

conductive than normal brain at 10 Hz and this difference reduces to around $0.02\,\mathrm{S\,m^{-1}}$ by 100 Hz, with the difference remaining around $0.02\,\mathrm{S\,m^{-1}}$ up to 1 MHz. Blood has a conductivity of $0.7\,\mathrm{S\,m^{-1}}$ at frequencies up to <100 kHz and this increases to $0.82\,\mathrm{S\,m^{-1}}$ at 1 MHz (figure 2.1)[164].

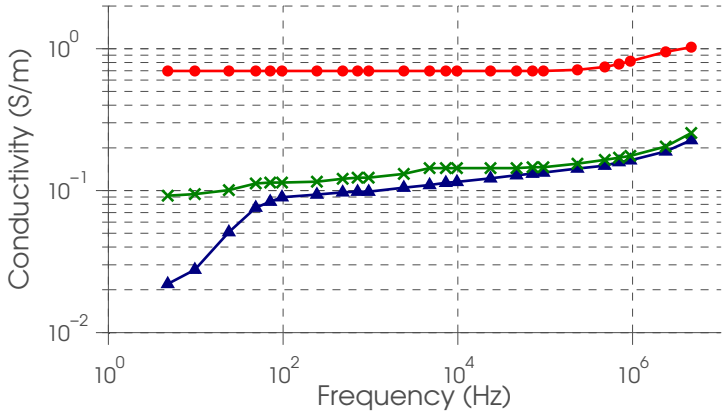

Figure 2.1: *Change in conductivity over frequency of normal cortical tissue, ischaemic cortical tissue and blood.* —×— *normal cortical tissue.* —△— *ischaemic cortical tissue.* —○— *blood. After Horesh (2006)*[164].

Romsauerova et al. undertook the one published clinical MFEIT pilot study in order to determine the sources of noise and error in such recordings and explored means of data analysis that might reveal significant changes in boundary voltages corresponding to the underlying pathology. Seven patients were considered, all of whom had pathologies, of 1.5 to 7 cm, that mimic the impedance characteristics of a haemorrhage: arteriovenous malformation, tumour and chronic stroke[172]. The spectrum range was unfortunately limited by instrumentation restrictions, so recordings were made at 16 to 64 kHz, and frequency difference reconstructions were made between these two frequencies. These reconstructions were performed using an anatomically realistic 30 000 element FEM model generated from patient MRI data and a truncated singular value decomposition (tSVD) linear algorithm. Examination of the raw data, sensitive channels and images found no reproducible changes between the three patient groups. This was attributed to be partly due to low SNR: the standard deviation of the real component being 2.5 %, while an estimate of the required accuracy was reported to be 0.1 %.

2.1.3 Acute stroke multi-frequency electrical impedance tomography instrumentation

An MFEIT system for imaging acute stroke requires high accuracy over frequency and load, as although modelled local changes are approximately 100 to 200 % in acute stroke, the corresponding boundary changes that are expected are approximately <1 to 2 %, due

to the attenuating effects of the skull[164]. Additionally, such a system should be able to record at frequencies less than 100 Hz, given that this is the point at which ischaemic brain has the largest conductivity contrast. However, this adds the problem of pain or sensation due to current injection; at frequencies below 1 kHz, skin perception is significantly increased[173]. In a study to specifically address this concern Romsauerova et al. found that with the injection of 0.28 $mA_{p\text{-}p}$, with a frequency range of 20 Hz to 1.6 MHz, to the forearm or head of four healthy volunteers, unpleasant perception occurred. This was attenuated or absent with the removal of frequencies <100 Hz[172]. Lastly, a considerable range of transfer impedances must be handled given the irregular geometry of the head: 1 to 70 Ω. Also, due to the high impedance of the skull, load impedances can be very high, and so a sufficiently high output impedance is required in order to prevent a loading effect and a non-constant current injection[174].

An example of such a system is the UCLH Mark 2.5 MFEIT device (UCLH Mk2.5), which is a serial injection and record system and can address up to 32 channels. Measurements are made using a four-electrode method, with an injected current of up to 133 $\mu A_{p\text{-}p}$ at up to 30 frequencies between 20 Hz and 1.3 MHz. It is based upon one channel of the Sheffield Mark 3.5 System[175], an eight-channel parallel system with a dedicated computer interface and full isolation to meet safety standards. The UCLH Mark 2.5 was specifically modified for imaging of acute stroke by inclusion of gain and frequency range alterations, including incorporating larger dc-blocking capacitors to allow 20 Hz measurement while still rejecting direct current[174].

Electrode placement and protocols addressing these have been designed for imaging in the adult human head. The 'spiral_s-o' protocol used in this study employs 16 electrodes and drives current between all available pairs of electrodes at 180° (five pairs), then those at 120° (12 pairs) and finally those at 60° (16 pairs). For each current injection, voltages are recorded from adjacent electrode pairs in a spiral pattern descending from the vertex[176].

2.1.4 Acute stroke multi-frequency electrical impedance tomography noise

The sources of noise in a system such as the MFEIT system implemented in this study can largely be categorised as fixed and proportional noise. Fixed noise is of a fixed amplitude, meaning that its proportional effect on a signal will depend on the signal size, hence small signals of an amplitude approaching the noise level will be most affected. In contrast to this, systematic noise or error varies in proportion to the signal size, and so as a percentage is the same for all amplitudes.

The error in MFEIT data can be best quantified in one of its three dimensions: *a*) the voltage value itself (including analysis of the different components of the complex data);

b) the voltage's variance over time (figure 2.2a); or *c*) the voltage's variance over frequency (figure 2.2b) Incorrect or inappropriate calibration applied to the data is another key source of error (figure 2.2c). It should be noted, however, that for differential MFEIT the actual voltage amplitude is not that relevant, but rather stability over time and frequency is more important [177].

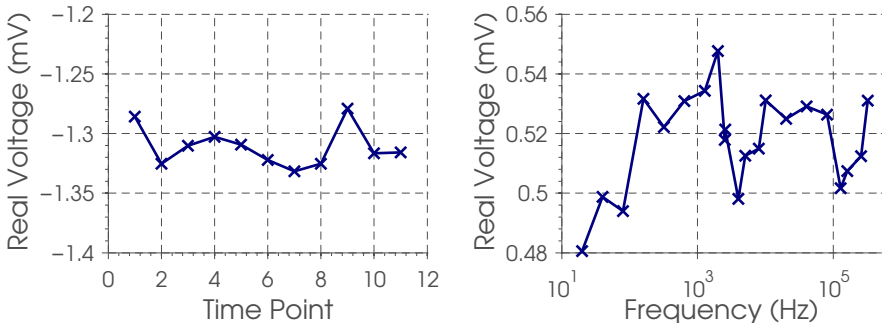

(a) *Temporal noise* (b) *Spectral noise*

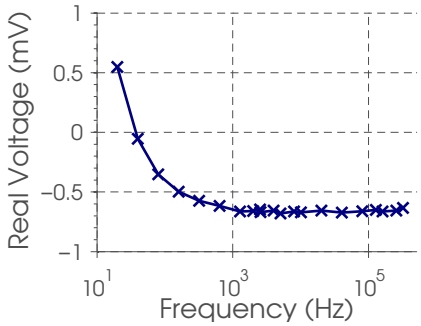

(c) *Calibration error*

Figure 2.2: *Examples of errors that occur in MFEIT data, with respect to the data's relevant dimension. All data were collected from the head-shaped tank with saline only, and so in each instance the voltage should be constant over the respective dimension.*

There are a number of ways in which noise can be suppressed, such as taking more recordings and therefore suppressing random noise through signal averaging. Another option is data removal to remove channels with noise not removed by signal averaging-either as it has too high a random noise or a systematic noise like 50 Hz mains hum. A prominent issue in MFEIT of acute stroke is that the irregular geometry of the head can result in low-amplitude boundary voltages as some voltages may by chance fall near isopotential lines. This causes a low SNR if boundary voltages are similar to the fixed noise level of the recording side.

In a modelling study Horesh suggested that the best means of producing images was

to first process the data by removing all those combinations with a signal less than the median, this is a means of removing low amplitude, low SNR data, but assumes that all noise is random[164]. Similarly, to achieve effective image reconstruction, Fabrizi et al., in a TD study, utilised boundary voltage rejection and signal processing: *a*) the removal of combinations with noise over time greater than 1 %; then removal of those channels with a larger than expected signal: *b*) changes greater than one third the expected change; and *c*) those with a signal greater than six times the standard deviation; and lastly *d*) PCA was employed[178].

2.1.5 Frequency difference reconstruction algorithms

If EIT is to be used for imaging acute stroke, then TD imaging is not possible; baseline data cannot be acquired as patients present after the event. Consequently, absolute or FD imaging must be used, and FD imaging, as a differential calculation, has the advantages of reducing instrumentation and geometric errors. In FD imaging, multi-frequency data are collected at a single time point, and the boundary voltage changes, $\Delta \boldsymbol{v}$, calculated as the difference in voltages between two frequencies.

A common approach in EIT, is to use a linear approximation to relate a map of conductivity changes, $\Delta \boldsymbol{\sigma}$, typically within a FEM mesh, to boundary voltage changes, $\Delta \boldsymbol{v}$:

$$\Delta \boldsymbol{v} = A \Delta \boldsymbol{\sigma}, \tag{2.1}$$

where A is the sensitivity matrix, a matrix defined by mesh, electrode positions, and current injection and measurement protocol. The calculation of the pseudo-inverse of this, $A^{\dagger}$, termed the inverse solution, allows for the mapping of measured $\Delta \boldsymbol{v}$ to $\Delta \boldsymbol{\sigma}$

$$\Delta \boldsymbol{\sigma} = A^{\dagger} \Delta \boldsymbol{v}, \tag{2.2}$$

with $\Delta \boldsymbol{\sigma}$ being rasterised, or otherwise displayed, as the EIT image. As A is underdetermined the solution is ill-posed, therefore the pseudo-inverse is performed with regularisation of A. The regularisation method employed in this study is tSVD, which is centred upon a decomposition of A:

$$A = U \Sigma V^{T}, \tag{2.3}$$

where the singular values are the diagonal entries of the matrix Σ and are the length of the number of measurements. The singular values are ordered from largest to smallest and each can be thought of as describing the contribution to the solution that a given measurement provides. Essentially the singular values indicate the degrees of freedom,

and inclusion of all values will result in a fuller, but noisier solution, as $\Delta\boldsymbol{\sigma}$ includes errors, while the inclusion of fewer singular values will result in a lower noise, spatially smoother solution. The need to remove smaller singular values can be understood by the fact that each singular value will be inverted so small values will become exceptionally large. Therefore those singular values/measurements determined to be below a given threshold can be suppressed in the inverse solution by replacing the entries with ≈ 0 entries, this is referred to as truncation, to result in $\widetilde{\Sigma}$. The truncation point can be chosen based upon the data noise, the decay of the singular values, or through other methods[179]. Following this $A^{\dagger}$ can be calculated as:

$$A^{\dagger} = V\widetilde{\Sigma}U^{T}. \tag{2.4}$$

For the same $A^{\dagger}$ it is possible to alter the inverse solution by calculating $\Delta\boldsymbol{v}$ in different ways: it is this alteration that is referred to in this study as different reconstruction algorithms.

The advantage of difference imaging is error suppression. The ill-posed nature of the inverse problem in EIT means that comparatively small errors in the measured data can potentially lead to arbitrarily large errors in the estimated internal conductivity. In difference imaging, time invariant noise and error, due to stray capacitance or electrode-electrolyte interaction, are better cancelled out than in absolute imaging. In TD imaging, this is achieved by calculating the voltage difference, $\Delta\boldsymbol{v}_{TD}$, as the normalized difference between the voltages at a time with the perturbation, $\boldsymbol{v}_{t_p}$, and the voltages at a time without the perturbation, $\boldsymbol{v}_{t_b}$:

$$\Delta\boldsymbol{v}_{TD} = \boldsymbol{v}_{t_p} - \boldsymbol{v}_{t_b}. \tag{2.5}$$

In FD, only voltages with the perturbation in place are used. The voltage difference, $\Delta\boldsymbol{v}_{FD_i}$, is calculated over frequency. This difference is the normalized difference between voltages at one frequency, $\boldsymbol{v}_{f_i}$ to a, typically lower, reference frequency $\boldsymbol{v}_{f_{ref}}$:

$$\Delta\boldsymbol{v}_{FD_i} = \boldsymbol{v}_{f_i} - \boldsymbol{v}_{f_{ref}}. \tag{2.6}$$

FD imaging may not benefit completely from the advantages of difference imaging as different errors are present at different frequencies. An additional consideration is that the sensitivity matrix approach assumes a linear relationship between changes in a voxel in an object and the boundary voltages, whereas this relationship is governed by Poisson's equation and is therefore non-linear. However, this approximation has been shown to be reasonable for resistance changes of less than 20 %[79]. In practice, this linear assumption produces acceptable images in EIT providing that either changes are less than about 20 %, or else that a perturbation of more than this is present against a uniform non

changing background. When the background also changes by more than 20 %, such as for FD imaging with a frequency-dependant conductivity, such as carrot cubes in saline or the human brain, then images appear as widespread dome-shaped changes against which a smaller perturbation cannot be discerned [77;172]. In order to minimize errors from this assumption of linearity, imaging may be undertaken by normalization of two frequencies spaced close together so that resistivity contrasts lie in the relatively linear range of less than 20 %, which is done when using the frequency difference adjacent (FDA) algorithm. In FDA, the voltage difference, $\Delta \boldsymbol{v}_{FDA_i}$, is the normalized difference between voltages at one frequency, $\boldsymbol{v}_{f_i}$, to the voltages at the preceding frequency, $\boldsymbol{v}_{f_{i-1}}$:

$$\Delta \boldsymbol{v}_{FDA_i} = \boldsymbol{v}_{f_i} - \boldsymbol{v}_{f_{i-1}}. \tag{2.7}$$

However, any perturbation may still be obscured against the background and the choice of closely spaced frequency pairs may also reduce the SNR, as the contrast of the perturbation will also be reduced.

Another approach is the weighted frequency difference (WFD) algorithm, in which a correction is made for the frequency-dependent variability in the conductivity of the background [180–182]. This has been shown to be successful in the presence of a background with frequency-dependent conductivity in numerical modelling, 2D cylindrical tank and hemispherical tank experiments. It may be implemented by either normalisation to a single reference frequency (WFD) or by comparing sequential frequency pairs (weighted frequency difference adjacent (WFDA)). In WFD, the voltage difference, $\Delta \boldsymbol{v}_{WFD_i}$, is calculated as the normalised difference between voltages at one frequency, $\boldsymbol{v}_{f_i}$, to a reference frequency, $\boldsymbol{v}_{f_{ref}}$, where the latter is weighted by a factor α:

$$\Delta \boldsymbol{v}_{WFD_i} = \boldsymbol{v}_{f_i} - \alpha \boldsymbol{v}_{f_{ref}}, \tag{2.8}$$

where

$$\alpha = \frac{\left\langle \boldsymbol{v}_{f_i}, \boldsymbol{v}_{f_{ref}} \right\rangle}{\left\langle \boldsymbol{v}_{f_{ref}}, \boldsymbol{v}_{f_{ref}} \right\rangle}. \tag{2.9}$$

2.1.6 Expected changes for reconstruction algorithms

For clarity, in this section, the anticipated effects on reconstructed images of the algorithms described in the preceding section are presented. The description is given for a potato test object, first in a saline background and then in a carrot-saline background, as this reflects the two conditions examined in this study. This description was achieved by applying the equations detailed in the preceding section to conductivity data for potato, saline and carrot-saline, and plotting the corresponding normalised conductivity change

(figures 2.4 and 2.5). For this illustration, smoothed data were used, by the application of a constrained cubic spline to the reference data collected as part of this study (section 2.3.1). The splines applied to the potato and carrot-saline data had a linearly increasing region imposed on the first three frequencies: the linear region was applied based upon knowledge from direct measurement.

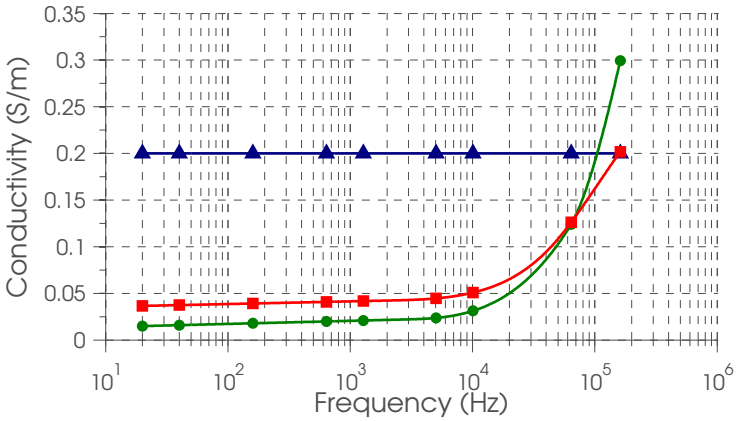

Figure 2.3: *Idealized conductivity values for 0.1 % saline, potato and a carrot-saline mixture.* —△— *0.1 % saline.* —□— *carrot-saline mixture.* —○— *potato.*

In images, the relative conductivities of the test object and background are displayed. For a saline background, the conductivity of potato is less than that of 0.1 % saline at 20 Hz, is roughly equal at 100 kHz, and then increases. For TD at different frequencies, the image contrast should reflect this. For the FD and WFD algorithms, which are normalised to the lowest frequency, the potato image contrast will gradually increase with frequency against a flat saline background. Due to the irregular spacing of frequencies for the FDA and WFDA algorithms, the potato image contrast will increase but sometimes irregularly, as the conductivity changes of subsequent frequency pairs are uneven (figures 2.4).

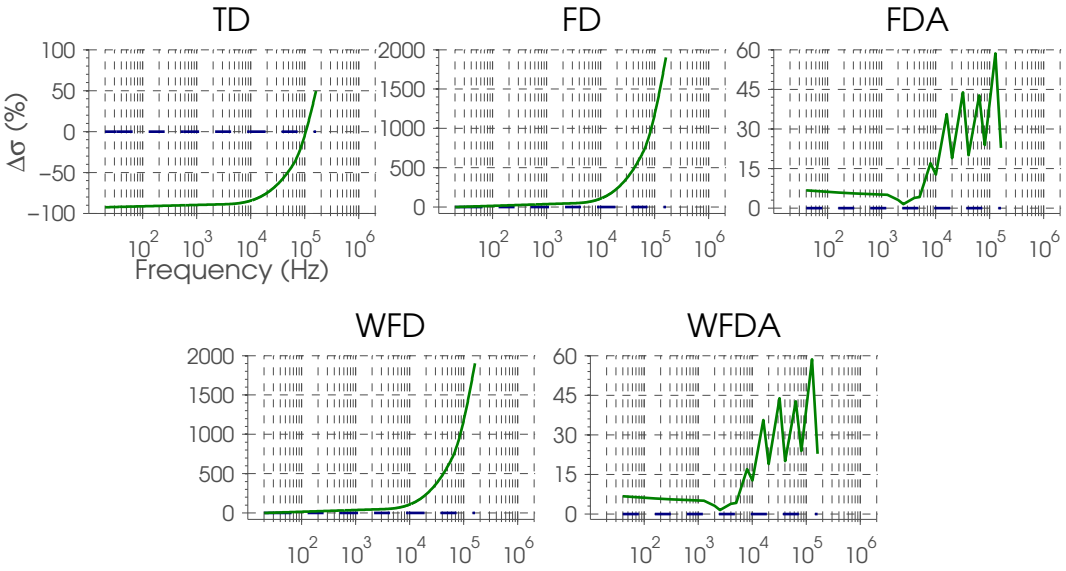

Figure 2.4: *Expected conductivity changes for potato in a 0.1 % saline background if calculated with each of the five algorithms. – – – 0.1 % saline. — potato.*

For the carrot-saline background, image appearances are similar but influenced by the change in conductivity of the background over frequency. The TD images are similar, except with equality of potato and background at 60 kHz. For FD and FDA the object change is similar, but the background conductivity increases with frequency. For WFD and WFDA, the background, by definition, does not change with frequency and, although the potato image object still increases with frequency, it is reduced because of adjustment to the corrected background. Again, the adjacent method is irregular (figures 2.5).

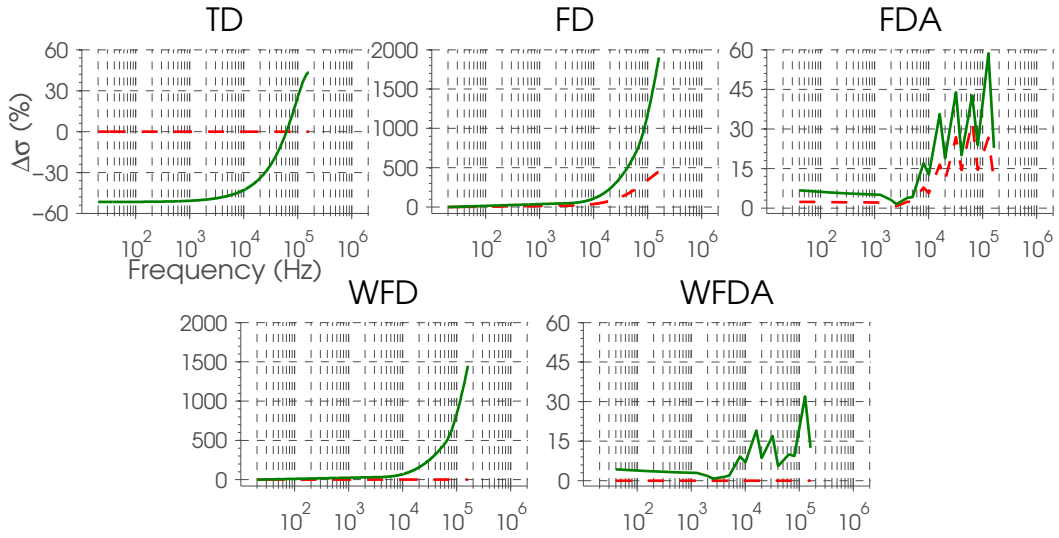

Figure 2.5: *Expected conductivity changes for potato in a carrot-saline background if calculated with each of the five algorithms.* – – – *carrot-saline.* — *potato.*

2.1.7 Purpose

The overall purpose of this study was to evaluate the performance of different FD EIT algorithms for imaging of acute stroke in the human head. As detailed above, the WFD approach has been shown to produce good images in simulation and in a hemispherical tank. In this study, imaging was undertaken in the more demanding setting of a realistic head-shaped tank, and with all the above-described algorithms, using biological materials with frequency-dependant conductivity to resemble the properties of tissues in the human head. The questions addressed were as follows:

(1) Can acceptable MFEIT images be obtained in an anatomically realistic tank with a linear FD reconstruction algorithm? If so, which FD reconstruction algorithm produces the best images?

(2) In a realistic head-shaped tank, some standing voltages by chance fall close to isopotential lines so that their SNR is low. It was necessary to remove such noisy channels. The best way to achieve this was also examined.

2.1.8 Experimental design

Imaging was undertaken with five algorithms: TD, FD, FDA, WFD, and WFDA. In order to assess the effect of geometry, tanks of increasing complexity were used: first a 2D cylindrical tank and then an anatomically realistic 3D head-shaped tank were used. In order to assess the effect of the background on the linearity assumption, imaging was

undertaken with a background of purely resistive saline, which has no significant change over frequency, and then a carrot-saline mixture, which has a conductivity that changes with frequency. The test object was a cylinder of potato, and images were collected with its placement in two and three positions for the 2D and 3D tanks, respectively. Although the spectra of the carrot-saline mixture and potato mixture are not the same as the spectra for normal brain and ischaemic brain, the real aim was to examine the imaging of a perturbation in a background media where both have a conductivity that changes over frequency.

The expectation was that the TD approach would work in all cases, but that the FD and FDA approaches would fail with the carrot-saline background due to its frequency-dependant conductivity. At the outset, it was not certain if WFD would permit the production of good images with the carrot-saline background in the head-shaped tank, and if so, whether WFD referenced to 80 Hz or WFDA would be superior.

As it has been reported that boundary voltage rejection was required for successful imaging[164;178], a portion of this study aimed at identifying the best means of performing boundary voltage rejection, by comparing the resultant image quality after rejection thresholds were applied.

2.2 Methods

2.2.1 Tanks

2D tank recordings were made in a Perspex cylindrical tank (10 cm high and 19.5 cm in diameter), with 32 stainless steel electrodes, 1 cm in diameter, evenly placed at a height of 5 cm (electrode centre to the base of the tank), with a 33rd ground electrode on the base of the tank in the centre. 3D tank recordings were made in a realistic head-shaped latex rubber tank (19.5 cm anterior-posterior and 14.6 cm side to side-interior dimensions at its widest point). Thirty-two silver electrodes, 1 cm in diameter, were positioned in a modified 10-20 EEG placement system, with a 33rd ground electrode positioned at the tip of the nose[183].

2.2.2 UCLH Mk2.5 MFEIT hardware and protocols

Data were collected with the UCLH Mk2.5, with an injected current of 133 µA at 19 frequencies between 80 Hz and 128 kHz. Measurements made in the 2D tank used all 32 channels with a polar current injection and sequential adjacent voltage record protocol, which resulted in a total of 448 measurements. In the 3D head-shaped tank, recordings were undertaken with the 'spiral_s-o protocol', which therefore only employed 16 channels[176]. In both tanks, images were produced from ten averaged complete data sets.

The temperature was monitored throughout all the measurements and did not vary from $24 \pm 1\,^{\circ}\mathrm{C}$.

2.2.3 Background materials and test objects

Background media were 0.1 % NaCl solution or approximately $2\,\mathrm{mm}^3$ cubes of carrot with 0.1 % saline added to fill the interstices to the top of the carrot cubes. Test objects were cylinders of potato 10 cm long and 4 or 2.4 cm in diameter for the 2D and 3D tanks, respectively. The test object was submerged in a 0.1 % saline solution for 45 min prior to starting any recordings to ensure ionic equilibration (appendix A). The potato perturbation was placed in two positions in the 2D tank, 2.5 and 5 cm from the first electrode (at 9 o'clock), and three positions in the 3D head-shaped tank: anterior, lateral and posterior (figure 2.6).

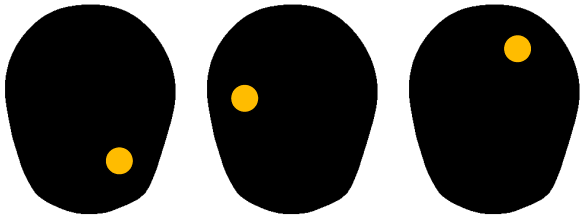

Figure 2.6: *Scale diagram of the potato locations in the 3D head-shaped tank at a rasterisation plane of 0 mm on the z-axis. The leftmost is 'anterior', middle is 'lateral' and rightmost is 'posterior'.*

The impedance of materials used was measured using a Hewlett-Packard 42847A impedance analyser (Hewlett-Packard, CA, USA) at ten frequencies from 20 Hz to 500 kHz. The saline and carrot-saline mixtures were measured using Perspex tubes, 2 cm in diameter and 5 and 10 cm long, with Ag-AgCl electrodes at each end. Cylinders of potato, 2.5 cm in diameter, and 5 and 10 cm long, were measured using Ag-AgCl electrodes. Measurements at two lengths allowed for calculation and then subtraction of the electrode impedances.

2.2.4 Boundary voltage rejection

All boundary voltages were first calibrated, as modulus and phase, and then, in order to ascertain the best method of boundary voltage rejection, the temporal noise and boundary voltage amplitude was examined in the background-only recordings. Temporal noise was defined as the standard deviation of the real component over time normalized to the mean of the real component over time.

The first stage of boundary voltage rejection was based upon visual inspection of the real component of the boundary voltages and exclusion of any data that,

a) varied over time by more than approximately 2 %; or *b*) varied over frequency by more than approximately 2 %, for saline background, or if it did not have a monotonic decrease over frequency for the carrot-saline background.

To reduce the effect of noisy data, several criteria for boundary voltage rejection were applied to the 3D head-shaped tank data, acquired with both backgrounds. The resultant images were qualitatively and quantitatively assessed, as detailed in section 2.2.6. The assessed boundary voltage rejection criteria were as follows:

(1) all boundary voltages included;

(2) removal of combinations with a boundary voltage of less than 0.1, 0.25, 0.5, 0.66, 0.75 or 1 mV in the real component;

(3) removal of combinations with a temporal noise greater than 10, 5, 3, 2, 1 or 0.5 %;

(4) a combination of methods (2) and (3).

2.2.5 Image reconstruction

Images were reconstructed with the real component of voltage differences using TD, FD, FDA, WFD and WFDA. TD data sets were reconstructed from data sets collected with the test object inserted compared to the background alone, at each of 19 frequencies. At all 18 frequencies above 80 Hz, FD and WFD images were reconstructed from data sets recorded with the test object inserted and referenced to 80 Hz. FDA and WFDA comprised 18 image sets for sequential pairs of recorded frequencies.

The voltage differences were reconstructed into conductivity difference images using a sensitivity matrix reconstruction algorithm [184], with inversion performed using 40 truncated singular values and a 60 000- or 52 000-element tetrahedral mesh of the cylindrical tank or head-shaped tank, respectively. Conductivity changes were expressed as a percentage change.

All 3D tank image reconstructions were rasterised to a plane at 0 mm on the z-axis, which was the centre of the perturbation on the z-axis (figure 2.7), and, for brevity, only three frequencies are shown for each of the five algorithms. For reconstructions of TD, FD and WFD, all images have the same colour scale across all frequencies, while for FDA and WFDA, each image is individually scaled, and so the corresponding colourbars have '+ve/-ve' as the limits. For each algorithm, a profile of the conductivity changes across the x-axis, at the centre of the perturbation on the y-axis, was extracted. This point on the y-axis was -35, 15 and 60 mm, for the anterior, lateral and posterior placements, respectively. The conductivity spectra of the perturbation and background were

also extracted. The perturbation was defined as the mean of the *reconstructed perturbation* conductivity changes, with the *reconstructed perturbation* being the largest group of connected tetrahedra with conductivity changes above half the maximum conductivity change. The background was defined as the mean of all the conductivity changes not belonging to the *reconstructed perturbation*.

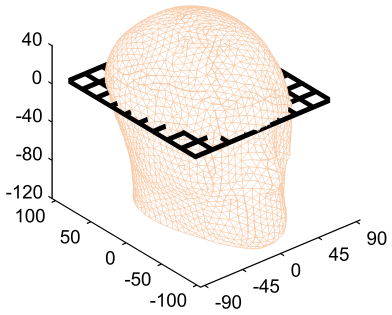

Figure 2.7: *Triangulation surface mesh of the head-shaped tank mesh with a grid at 0 mm on the z-axis where images were rasterised.*

2.2.6 Image quantification

Analysis of reconstructed images was used as the metric of the relative success of different boundary voltage rejection methods and different algorithms. Image quality was assessed quantitatively by four metrics[176]. These were defined as follows.

(1) Localization error (weight 1.5): the vector displacement of the *centre of mass* of the *reconstructed perturbation* with respect to its real position, as a percentage of the tank's diameter.

(2) Shape error (weight 0.75): the mean of the difference in each axis of the *reconstructed perturbation* to the perturbation's actual width, expressed as a percentage of the tank's diameter.

(3) Image noise (weight 0.5): the standard deviation of all conductivity changes not belonging to the *reconstructed perturbation* expressed as a percentage of the mean of the *reconstructed perturbation*'s conductivity changes.

(4) Spectral error (weight 0.25): the root-mean-square (RMS) error between the normalized spectrum of conductivity changes belonging to the *reconstructed perturbation* and a reference conductivity change calculated from the reference conductivity spectra.

Each of these was applied by first identifying the *reconstructed perturbation*, as detailed in section 2.2.5. The four metrics were combined into one value of *image error* by summing the single errors, weighted according to importance. Comparison of algorithms was done at a single frequency per algorithm, which was chosen by identifying the frequency with the least image error in these metrics. For each tank, a three-way analysis of variance (ANOVA), across background media, perturbation and algorithm, was performed. For brevity, image quantification values are shown for each algorithm and background, but averaged across perturbation locations.

2.3 Results

2.3.1 Reference data

The conductivity of the 0.1 % saline was $0.20 \pm 0.01\,\mathrm{S\,m^{-1}}$ (mean ± 1 SD) throughout the frequency range measured (20 Hz to 500 kHz), and that of the potato and carrot-saline was 0.017 ± 0.0006 and $0.0380 \pm 0.0008\,\mathrm{S\,m^{-1}}$ between 20 Hz and 1 kHz, respectively. Above 1 kHz, the conductivities of both tissues increased and diverged until at 500 kHz they were $0.65\,\mathrm{S\,m^{-1}}$ for potato and $0.29\,\mathrm{S\,m^{-1}}$ for carrot-saline (figure 2.8).

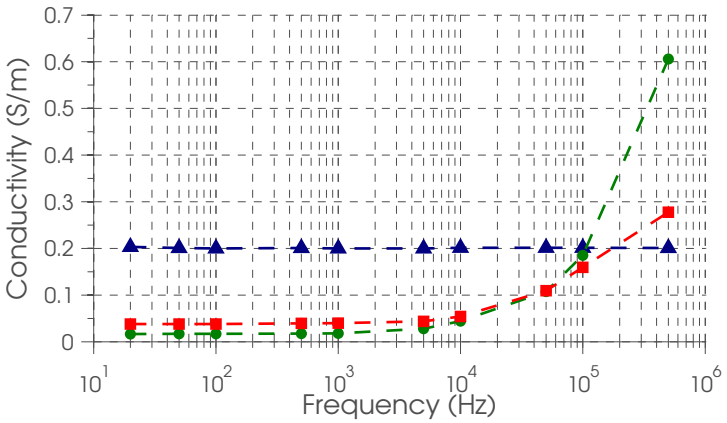

Figure 2.8: *Conductivity spectra of tank materials.* – – –△– – – *0.1 % saline.* – – –□– – – *carrot-saline.* – – –○ – – – *potato.*

2.3.2 Boundary voltage rejection

2.3.2.1 Noise characterisation

Examination of the SD over time of the boundary voltages shows that in both 2D and 3D tank recordings the amplitude of the noise was less than 15 µV. For boundary voltages between 0 and 1.25 mV the noise was dominated by fixed amplitude noise of approximately 2 µV (figure 2.9a & 2.9b). For boundary voltages above 1.25 mV the noise was

predominantly proportional, being approximately 0.1 % the amplitude of the boundary voltages, as determined by a linear fit of these data points (figure 2.9a & 2.9b). The maximum normalised noise over time for the 2D experiments in all cases was <0.6 %, but was as much as 15 % for 3D tank recordings (figure 2.9c & 2.9d). The much higher normalised temporal noise in the 3D tank recordings is reflected in the image reconstructions. Reconstructions of all the data in 2D tank experiments produces qualitatively good images in all recordings, but including all the data for the 3D tank reconstructions produces qualitatively unacceptable images in all recordings, hence boundary voltage rejection was deemed necessary.

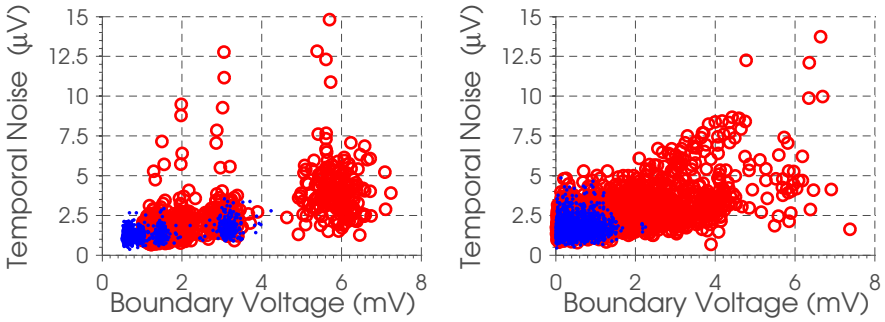

(a) *2D tank temporal noise*

(b) *3D tank temporal noise*

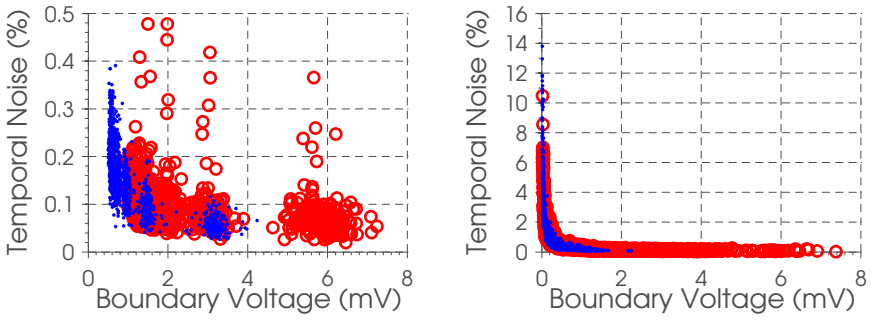

(c) *2D tank proportional temporal noise*

(d) *3D tank proportional temporal noise*

Figure 2.9: *Temporal noise for both tanks and both background media.* • *0.1 % saline.* ○ *carrot-saline.*

2.3.2.2 Manual boundary voltage rejection

Manual removal of data points led to the removal of 87 ± 2 (mean±SD), combinations for the six saline recordings, and 77 ± 1 combinations for the six carrot-saline background recordings. Images with only manual data cleaning produced images of acceptable qual-

itative quality with only the exception being the anterior placement of the perturbation in a carrot-saline background (figure 2.10).

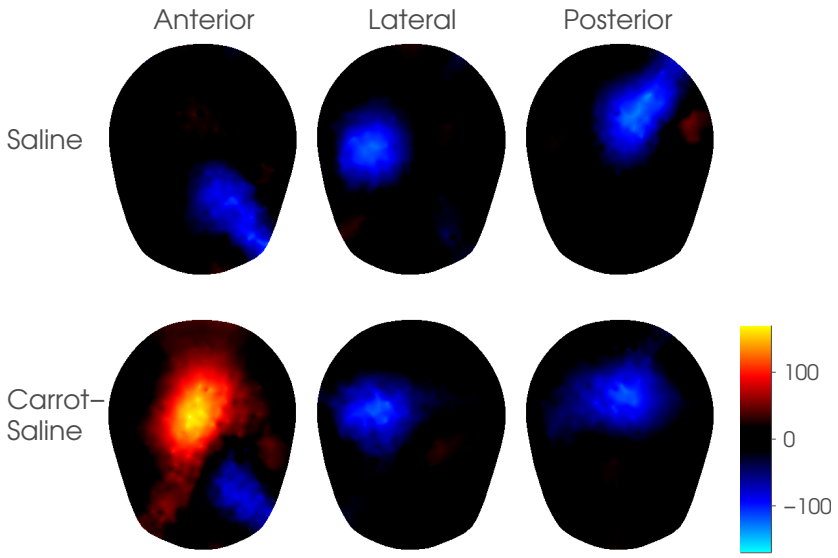

Figure 2.10: *Time difference reconstructions at 80 Hz and rasterised at 0 mm on the z-axis, after manual boundary voltage rejection only. Each column is a perturbation position, while each row is a different background media.*

2.3.2.3 Fixed threshold rejection: combinations removed

With increasingly more stringent rejection thresholds more combinations were removed: ranging from no combinations being removed for some of the least stringent thresholds and 251 combinations in the most extreme case. In addition to this, the number of combinations removed for recordings in a saline background were more than for the respective thresholds in recordings in a carrot-saline background (table 2.1).

A similar trend was present when the fixed rejection thresholds were combined: more stringent thresholds resulted in the removal of more combinations and for the same thresholds more combinations were removed in saline recordings than for carrot-saline recordings. However, for both background media applying an amplitude threshold and then temporal noise threshold of 10 % resulted in the removal of the same combinations as applying the same amplitude threshold, but a temporal noise threshold of 5 % or 3 % (table 2.2).

2.3.2.4 Fixed threshold rejection: image reconstruction

In this section, for brevity, the image quantification values are shown for all the boundary voltage rejection methods applied, but only the images resulting from rejection based

	Background Medium	
	Saline	Carrot-Saline
0.1 mV	35 ± 6	6 ± 1
0.25 mV	89 ± 3	16 ± 1
0.5 mV	161 ± 3	52 ± 2
0.66 mV	182 ± 6	70 ± 2
0.75 mV	212 ± 3	79 ± 3
1 mV	250 ± 1	113 ± 3

(a) *Amplitude threshold.*

	Background Medium	
	Saline	Carrot-Saline
10 %	3 ± 4	0 ± 1
5 %	12 ± 3	1 ± 0
3 %	20 ± 40	2 ± 1
2 %	31 ± 5	6 ± 2
1 %	83 ± 6	15 ± 4
0.5 %	148 ± 8	48 ± 4

(b) *Temporal noise threshold*

Table 2.1: *The number of combinations removed using fixed threshold rejection based upon boundary voltage amplitude and temporal noise.*

	Temporal Noise Threshold					
Amplitude Threshold	10 %	5 %	3 %	2 %	1 %	0.5 %
0.1 mV	35 ± 6	35 ± 6	35 ± 6	40 ± 5	85 ± 6	149 ± 8
0.25 mV	89 ± 3	89 ± 3	89 ± 3	89 ± 3	99 ± 4	149 ± 7
0.5 mV	161 ± 3	161 ± 3	161 ± 3	161 ± 3	162 ± 5	176 ± 4
0.66 mV	192 ± 6	192 ± 6	192 ± 6	192 ± 6	192 ± 7	201 ± 6
0.75 mV	212 ± 3	212 ± 3	212 ± 3	212 ± 3	213 ± 4	215 ± 2
1 mV	250 ± 1	250 ± 1	250 ± 1	250 ± 1	250 ± 1	250 ± 1

(a) *Saline Background Recordings*

	Temporal Noise Threshold					
Amplitude Threshold	10 %	5 %	3 %	2 %	1 %	0.5 %
0.1 mV	6 ± 1	6 ± 1	6 ± 0	8 ± 1	15 ± 2	48 ± 4
0.25 mV	16 ± 1	16 ± 1	16 ± 1	16 ± 1	21 ± 2	48 ± 4
0.5 mV	52 ± 2	52 ± 2	52 ± 2	52 ± 2	53 ± 2	61 ± 3
0.66 mV	70 ± 2	70 ± 2	70 ± 2	70 ± 2	70 ± 2	74 ± 3
0.75 mV	79 ± 3	79 ± 3	79 ± 3	79 ± 3,	79 ± 3	82 ± 4
1 mV	113 ± 3	113 ± 3	113 ± 3	113 ± 3	113 ± 3	114 ± 3

(b) *Carrot-saline background recordings*

Table 2.2: *The number of combinations removed using a combination of the fixed threshold rejection methods.*

upon boundary voltage amplitude for the posterior placement of the perturbation are shown.

Boundary voltage rejection was necessary for image reconstruction, however the

threshold had little impact on the image quality, qualitatively and quantitatively, with the exception of the most extreme thresholds: there were no images without cleaning and image quality degraded with excessive cleaning, such as removal of combinations smaller than 1 mV (figure 2.11). However, for the carrot-saline recordings quality was largely unchanged for all amplitude thresholds. The amplitude threshold producing the least *image error* across all positions, backgrounds and algorithms was 0.5 mV (figure 2.12).

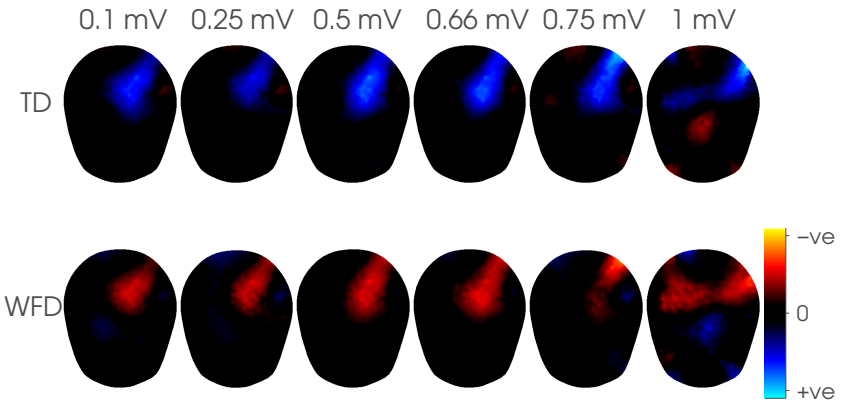

(a) *Saline background reconstructions*

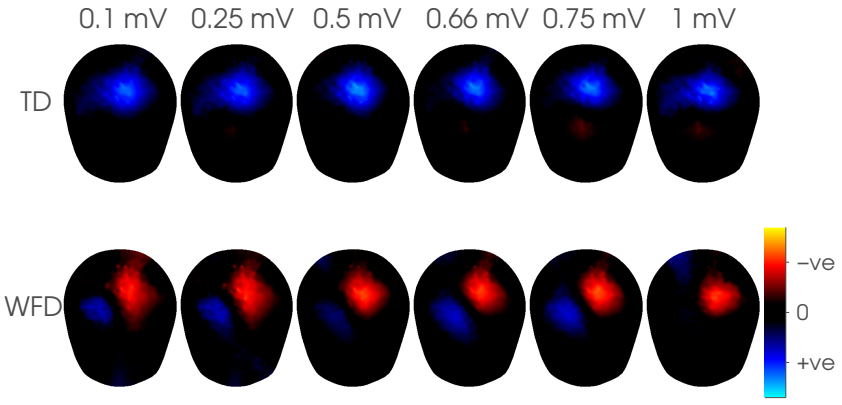

(b) *Carrot-saline background reconstructions*

Figure 2.11: *Reconstructed time difference (TD) and weighted frequency difference (WFD) images of posterior perturbation placement after removal of boundary voltages based upon the data's boundary voltage amplitude. TD images are at 80 Hz and WFD images are of 32 kHz referenced to 80 Hz. As a result of different protocol lengths after data rejection images have different amplitude changes and so images are individually scaled and the corresponding colourbars have '+ve/-ve' as the limits.*

A different trend existed for boundary voltage rejection based upon the temporal

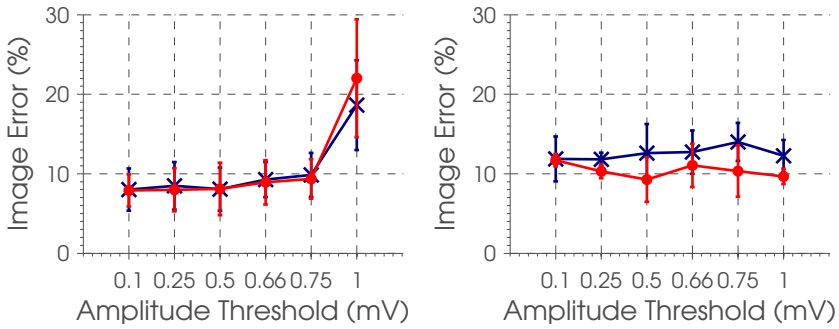

(a) *Saline background* image error (b) *Carrot-saline background* image error

Figure 2.12: Image error *resulting from different amplitude thresholds for boundary voltage rejection for each background. The marker is the mean across the three positions, for a given background, and the error bar the SD across these.* —×— *time difference.* —●— *weighted frequency difference.*

noise. Increasing the threshold slightly improved the image quality, both qualitatively and quantitatively, for the saline background images, but resulted in very little change, by either metric, for the carrot-saline background. The temporal noise that produced the least *image error* in all positions, backgrounds and algorithms was 0.5 % (figure 2.13).

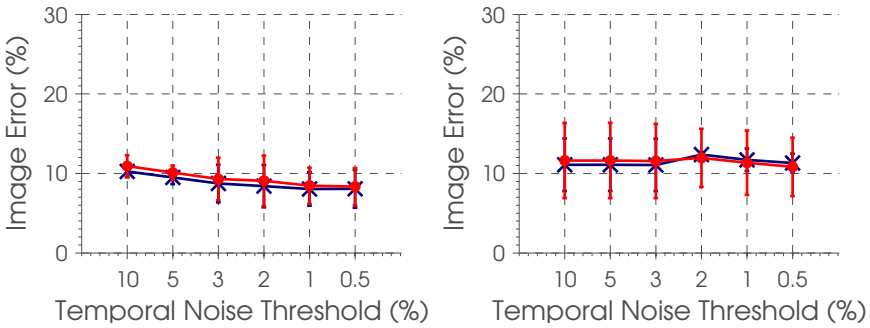

(a) *Saline background* image error (b) *Carrot-saline background* image error

Figure 2.13: Image error *resulting from different temporal noise thresholds for boundary voltage rejection for each background. The marker is the mean across the three positions, for a given background, and the error bar the SD across these.* —×— *time difference.* —●— *weighted frequency difference.*

For the combined boundary voltage rejection approach, in both the background media, the temporal noise thresholds had a comparable effect on image quality. For the saline background images, image quality was, qualitatively and quantitatively, compara-

ble throughout amplitude thresholds, but at 1 mV image quality degraded. In contrast, for the carrot-saline background image quality did not greatly change quantitatively for different amplitude thresholds, however qualitatively the images from the carrot-saline background reconstructed with WFD algorithm showed some improvement at 1 mV. The combined threshold for boundary voltage rejection that produced the least error in all positions, backgrounds and algorithms was 0.1 mV and 0.5 % (figure 2.14).

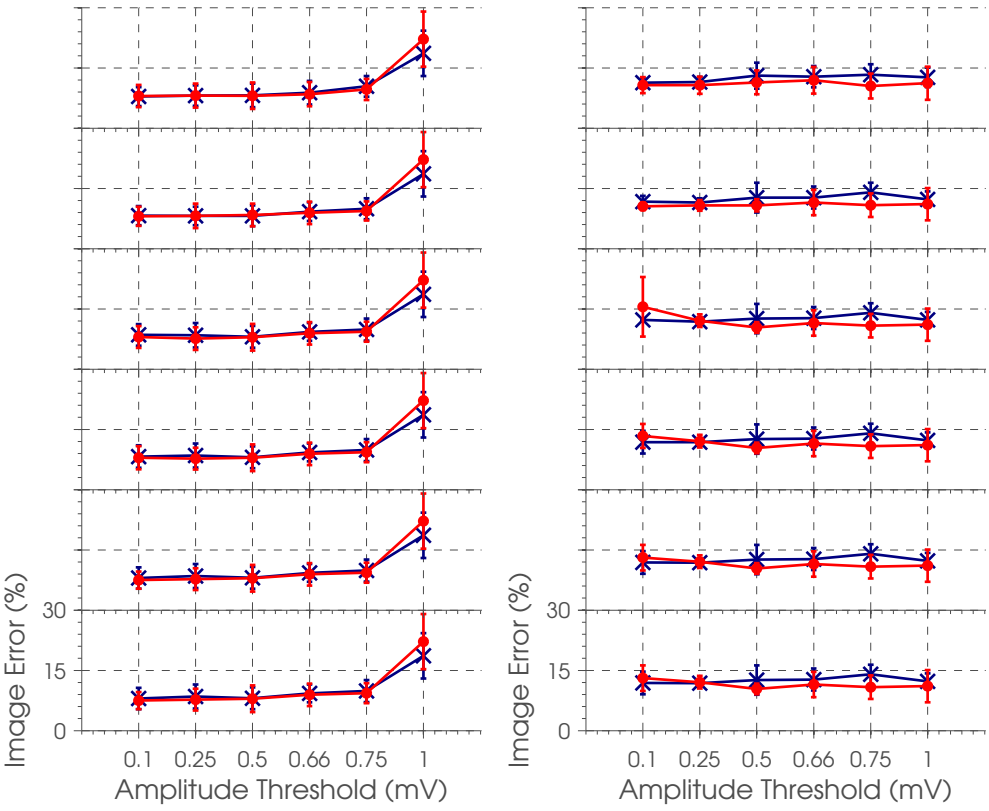

(a) *Saline background* image error

(b) *Carrot-saline background* image error

Figure 2.14: Image error *resulting from different combined thresholds for boundary voltage rejection for each background. In each subplot, each row has a plot for a different temporal noise threshold, where the lowermost subplot is for a threshold of 10 %, ascending through 5, 3, 2 and 1 %, so that the topmost subplot is for a threshold of 0.5 %. All plots are on the same scale. The marker is the mean across the three positions, for a given background, and the error bar the SD across these. —×— time difference. —●— weighted frequency difference.*

2.3.2.5 Chosen boundary voltage rejection method and threshold

The best image quality was achieved with a combination of elimination of channels according to boundary voltage amplitude and temporal noise. The combined thresholds

resulting in the lowest *image error* were the removal of combinations with a boundary voltage less than 0.1 mV and temporal noise greater than 0.5 %, which resulted in the removal of 149 ± 8 and 48 ± 4 combinations for the saline and carrot-saline background, respectively. However, these thresholds resulted in images qualitatively as good as removing a boundary voltage less than 0.1 mV and temporal noise greater than 1 %. This second threshold preserved up to 21 % and 10 % more combinations for the saline and carrot-saline recordings, respectively, and so was therefore selected as the method for further analysis, and used throughout the remainder of the study. In principle, it should have only been necessary to use one criterion, such as exclusion of data from electrode combinations with temporal noise greater than 1 %. The reason for the additional criterion of a fixed boundary voltage was empirical, but was likely to have been effective due to it excluding other sources of error, such as differences in performance over frequency.

2.3.3 Image reconstruction

2.3.3.1 2D cylindrical tank

For both saline and carrot-saline backgrounds, a change in images corresponding to the potato could be observed (*image error* 1.48 to 4.72 %), except for FD and FDA with the carrot-saline background where the perturbation was obscured by a dome-shaped conductivity increase across the entire image, of up to 216 % at 128 kHz. For brevity, only the image quantification values are shown (figure 2.15).

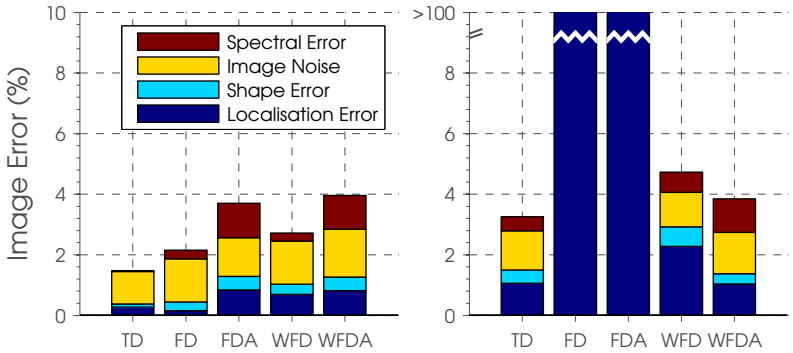

Figure 2.15: *2D tank, saline background (left) and carrot-saline background (right)* image error *values for each algorithm (mean across three positions).* Image errors *for FD and FDA in the carrot-saline background are shown as beyond the y-axis limits as images did not have an identifiable change corresponding to the perturbation. There was a significant difference between reconstruction algorithms* $p < 0.01$.

2.3.3.2 3D head-shaped tank saline background

For the saline background, a change in images corresponding to the potato could be observed for all algorithms, with an *image error* of 4.2 to 7.16 % (figure 2.16). TD images appeared subjectively superior to the next best algorithm, which was WFD (mean *image error* across positions 23 % greater).

Using the FD algorithms, images were qualitatively similar. Images using the FD algorithm had 14.1 % lower localisation error than FDA. On inspection, the images produced using FDA were better than those produced using WFDA, with respective *image errors* of 6.7 % and 7.16 %. Images using the FD and FDA algorithm had lower image noise, by 15 % and 17.4 %, than the images using the equivalent weighted algorithms (WFD and WFDA), respectively. In both weighted and simple FD algorithms the adjacent algorithm produced worse localisation error, specifically the WFD localisation error was 52.84 % less than that of for WFDA. With the saline background, the WFDA algorithm was qualitatively and quantitatively worse than all the other algorithms.

The images produced using FDA and WFDA that had the lowest *image error* across all positions was from those between the frequency pairs with the largest contrast: 81 kHz referenced to 64 kHz and 128 kHz referenced to 81 kHz. The exception being the anterior image produced using WFDA of 128 kHz referenced to 81 kHz, which had significant artefact: a lateral negative conductivity change. These images had conductivity changes, mean across positions, of 38.34 % and 10.8 % for the respective algorithms, with the contrast estimated from the reference data being 58.60 % for both algorithms at these frequencies.

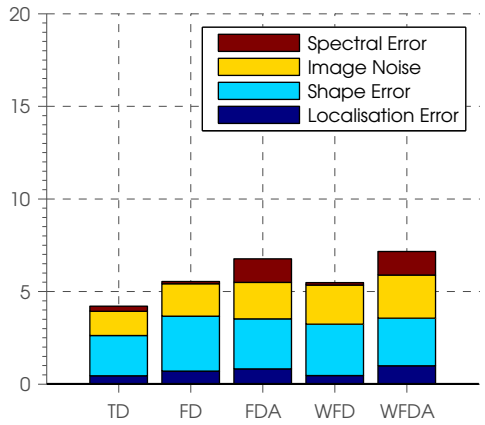

Figure 2.16: *3D tank, saline background* image error *values for each algorithm (mean across three positions). There was a significant difference between reconstruction algorithms $p < 0.01$.*

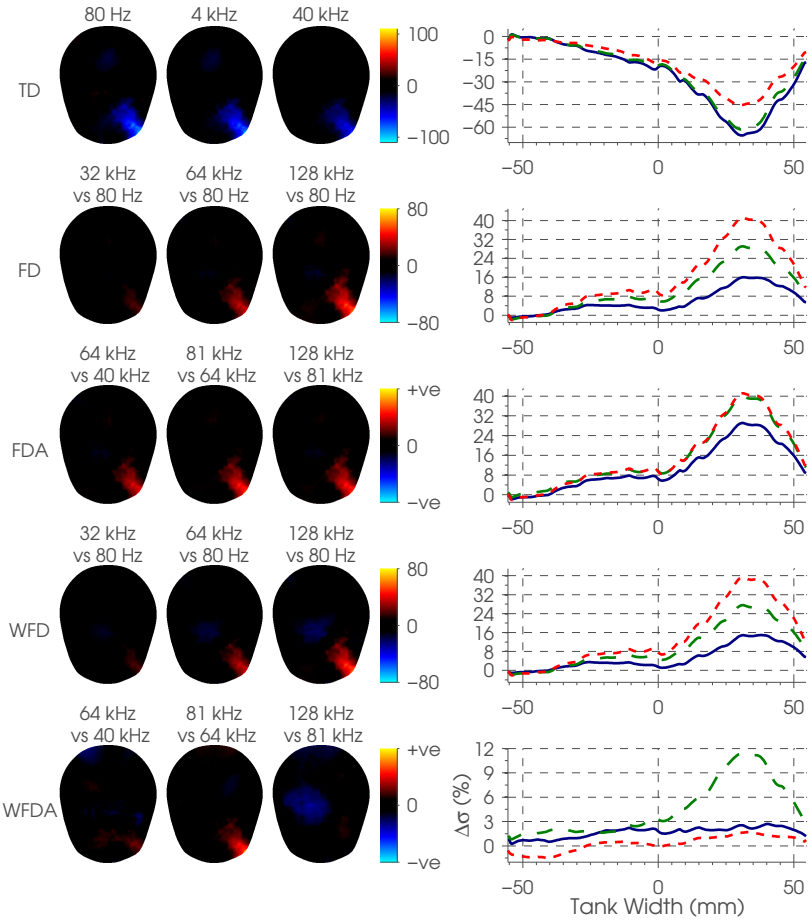

(a) *Reconstructed images and conductivity change profiles.* — *lowest frequency.* — — — *middle frequency.* - - - - *highest frequency.*

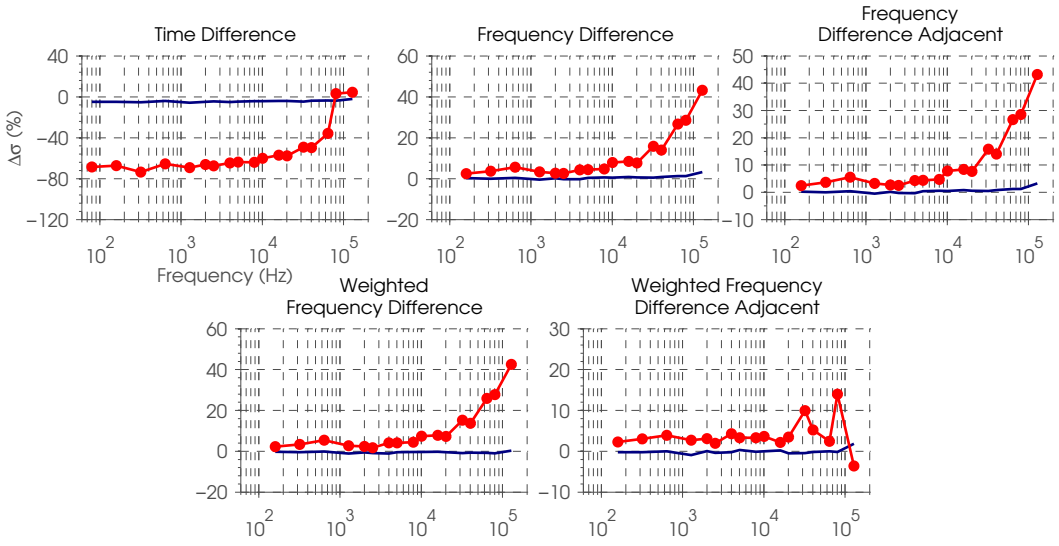

(b) *Conductivity spectra.* — *background* —●— *reconstructed perturbation.*

Figure 2.17: *Saline background, anterior perturbation placement.*

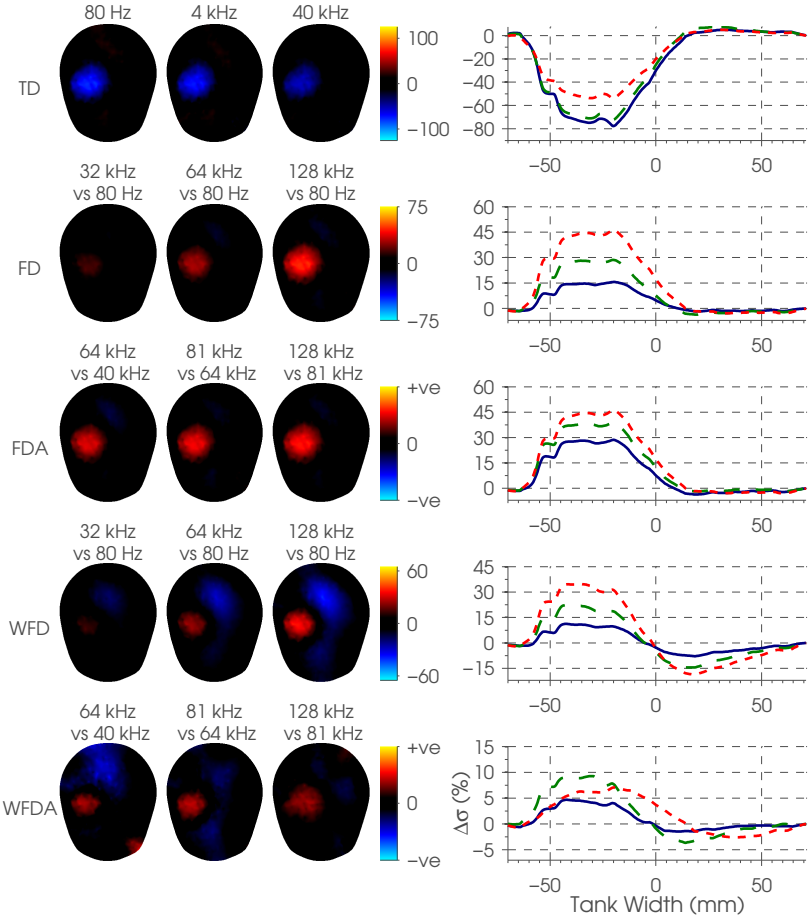

(a) *Reconstructed images and conductivity change profiles.* — *lowest frequency.* — — — *middle frequency.* - - - - *highest frequency.*

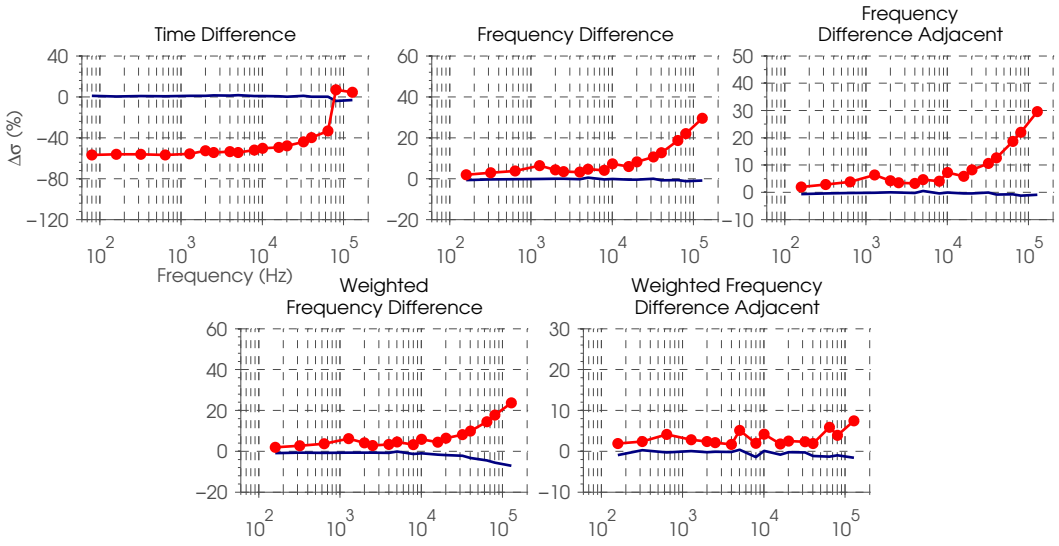

(b) *Conductivity spectra.* — *background* —●— *reconstructed perturbation.*

Figure 2.18: *Saline background, lateral perturbation placement.*

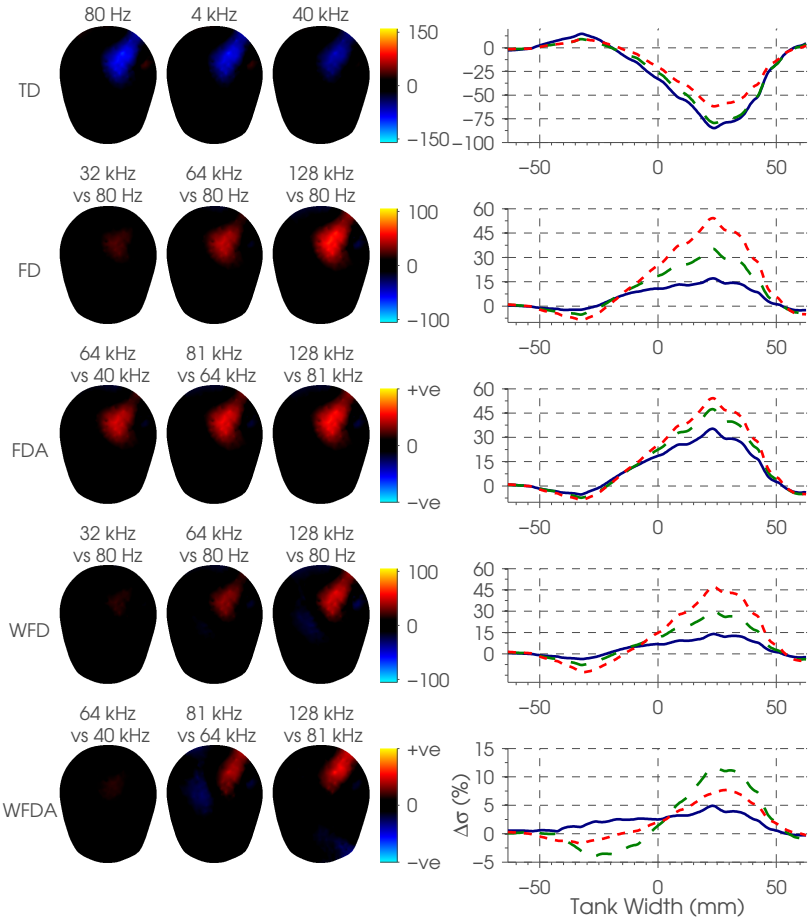

(a) *Reconstructed images and conductivity change profiles.* — *lowest frequency.* — — — *middle frequency.* - - - - *highest frequency.*

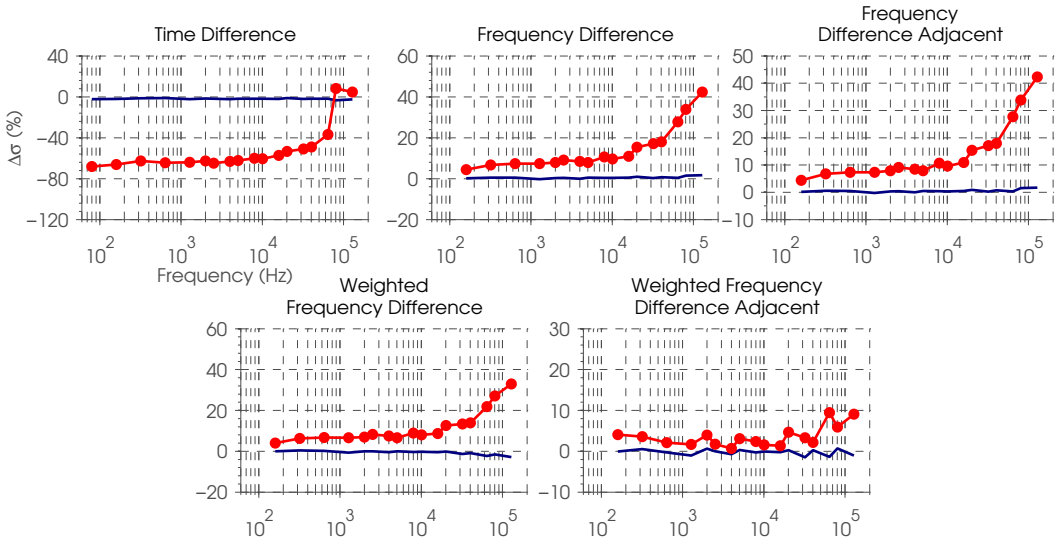

(b) *Conductivity spectra.* — *background* —●— *reconstructed perturbation.*

Figure 2.19: *Saline background, posterior perturbation placement.*

2.3.3.3 3D head-shaped tank carrot-saline background

With the carrot-saline background, images produced using the TD algorithm had a change corresponding to the potato. However, the anterior placement suffered from up to 20.9 % more noise than the other two placements. The posterior placement's reconstruction was displaced towards the centre of the tank (localization error 17.9 % higher). Images reconstructed with the TD algorithm were better than those with the FD algorithms, with 11.49 to 30.24 % less *image error* in the TD images (figure 2.20).

Images produced with either the WFD or WFDA algorithm had a change identifiable as the potato, but the best FD images were produced with the WFDA algorithm, with a mean *image error* across positions of 7.3 % as compared to an equivalent value for WFD of 9.5 %. In all three locations, the images reconstructed with the WFDA algorithm that had the lowest image error were between frequency pairs with a larger contrast. The best frequency pair was 32 kHz referenced to 20.16 kHz, which was the pair with the third highest conductivity change and had a change, mean across positions, of 12.52 % in the images, with the contrast estimated from the reference data being 5.58 % at these frequencies.

In images reconstructed with the FD and FDA algorithms, there was no identifiable change corresponding to the potato as it was obscured by a dome-shaped conductivity increase across the entire image of up to 237 % at 128 kHz.

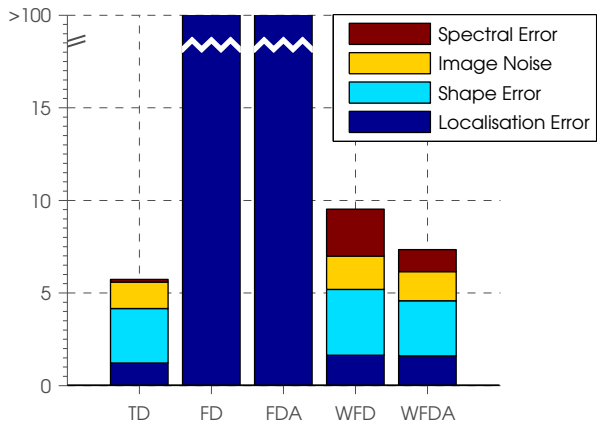

Figure 2.20: *3D tank, carrot-saline background* image error *values for each algorithm (mean across three positions). Image errors for FD and FDA in the carrot-saline background are shown as beyond the y-axis limits as images did not have an identifiable change corresponding to the perturbation. There was a significant difference between reconstruction algorithms $p < 0.01$.*

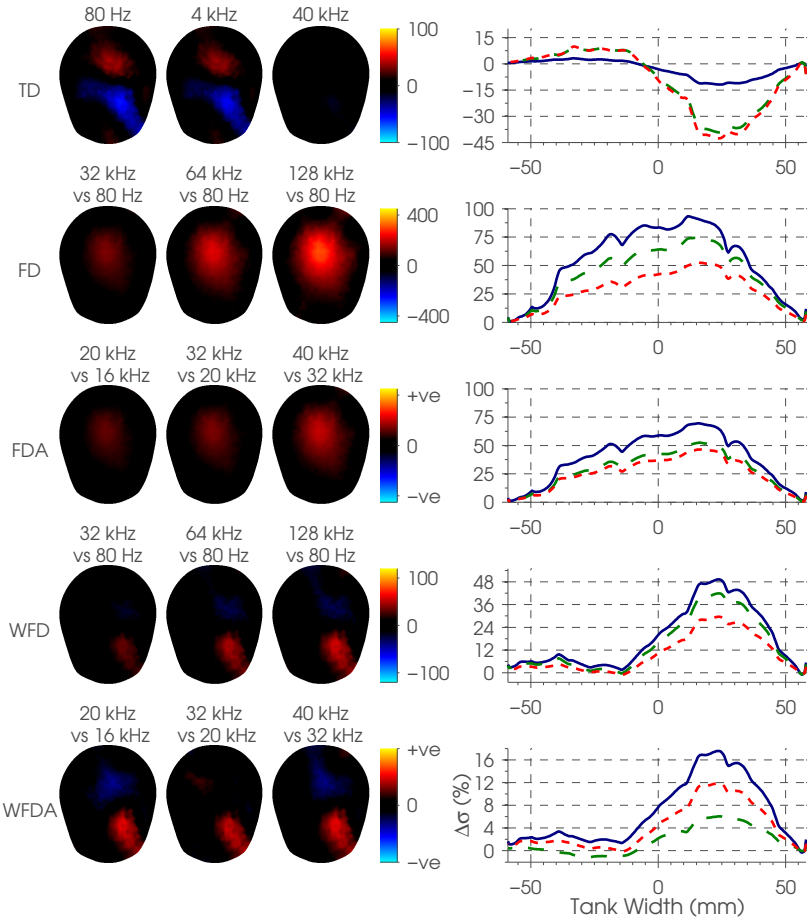

(a) *Reconstructed images and conductivity change profiles.* — *lowest frequency.* — — — *middle frequency.* - - - - *highest frequency.*

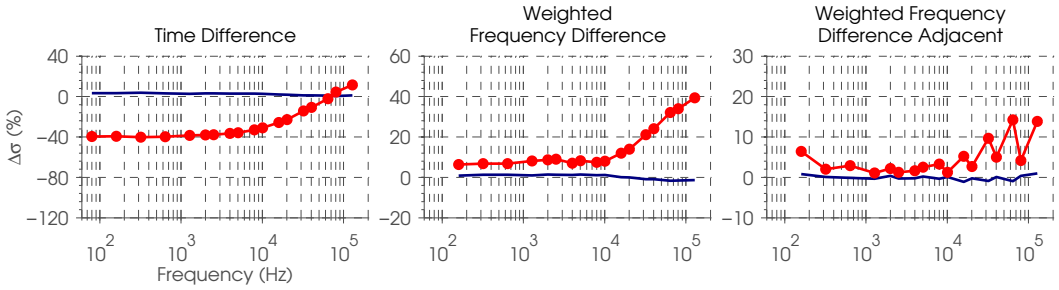

(b) *Conductivity spectra.* — *background* —●— *reconstructed perturbation.*

Figure 2.21: *Carrot-saline background, anterior perturbation placement.*

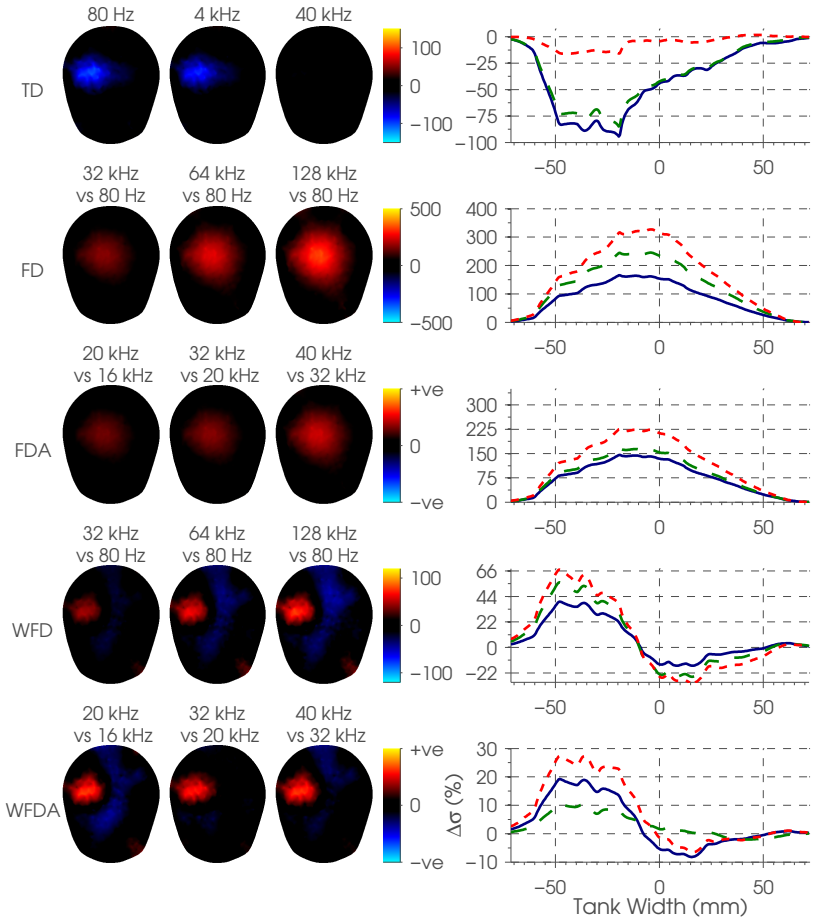

(a) *Reconstructed images and conductivity change profiles.* — *lowest frequency.* — — — *middle frequency.* - - - - *highest frequency.*

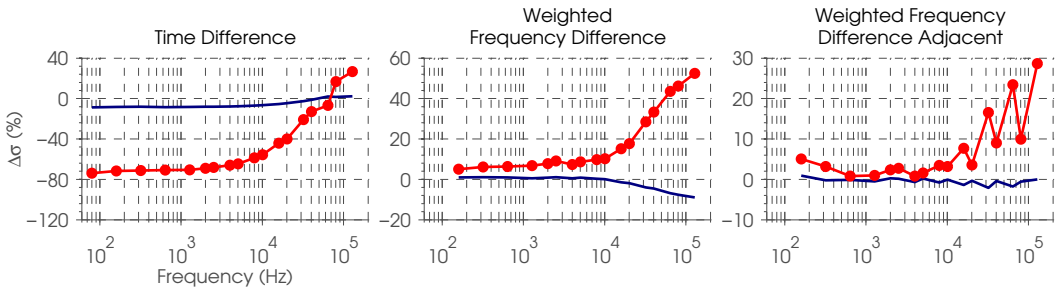

(b) *Conductivity spectra.* — *background* —●— *reconstructed perturbation.*

Figure 2.22: *Carrot-saline background, lateral perturbation placement.*

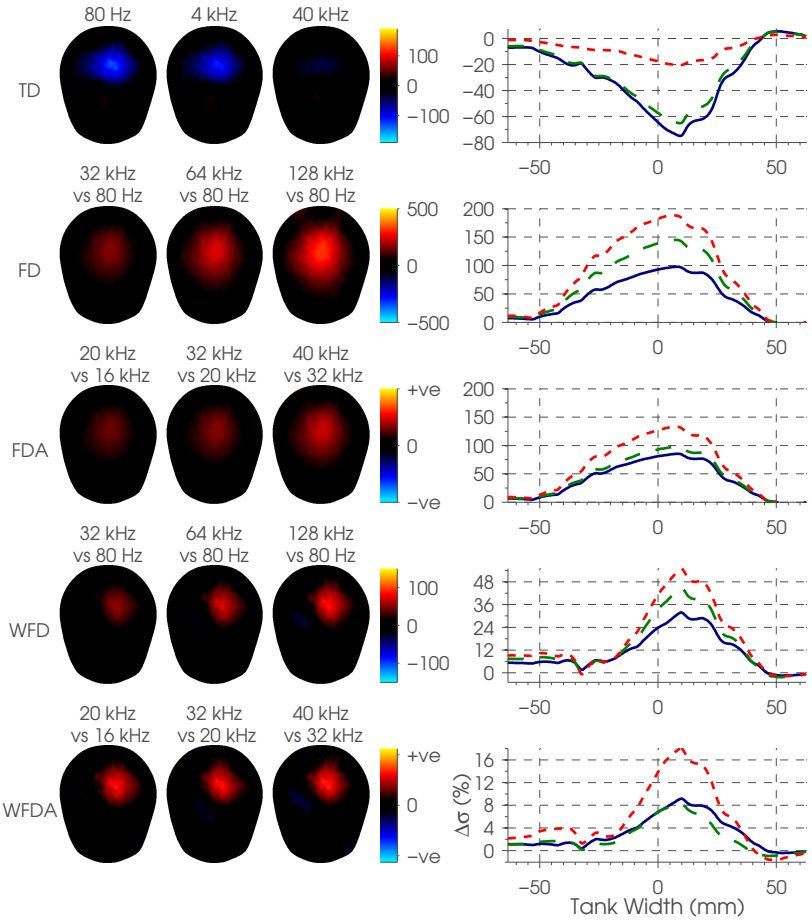

(a) *Reconstructed images and conductivity change profiles.* — *lowest frequency.* — — — *middle frequency.* - - - - *highest frequency.*

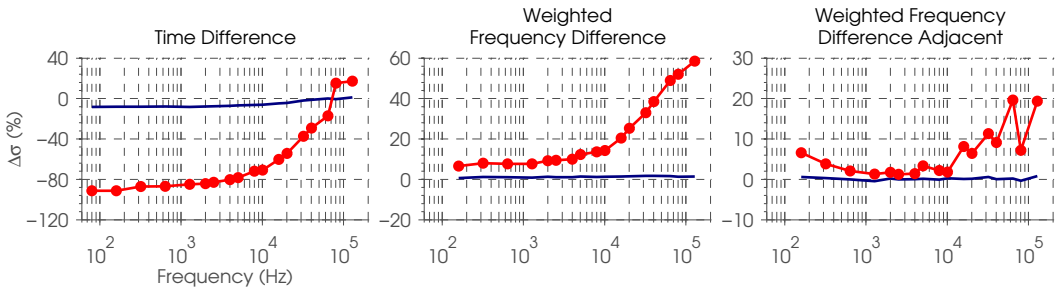

(b) *Conductivity spectra.* — *background* —●— *reconstructed perturbation.*

Figure 2.23: *Carrot-saline background, posterior perturbation placement.*

2.4 Discussion

2.4.1 Summary of results

2.4.1.1 Boundary voltage rejection

The best boundary voltage rejection method for the 3D tank recordings was the removal of all boundary voltages with a real component less than 0.1 mV or with a temporal noise of 1 % or greater. The image quality with manual boundary voltage rejection only, in contrast to reconstructions without boundary voltage rejection, gave a qualitatively identifiable reconstructed perturbation.

Analysis of the raw data revealed that a significant amount of the noise is of a fixed amplitude. This was supported by the fact that removal of data having a small boundary voltage, which were more affected by this noise, resulted in improved image quality. Moreover, the trend of a negative exponential between the normalised noise and boundary voltage amplitude (figure 2.9c and 2.9c) show that lower amplitude data were more affected by the temporal noise.

2.4.1.2 Image reconstruction

The image reconstructions revealed significant differences between the different algorithms for all the experiments.

(1) With the saline background medium, and in both the 2D and head-shaped tanks, images produced with all five algorithms had clearly identifiable reconstructed perturbations with *image error* less than 4.72 % and 7.16 % for the 2D and head-shaped tanks, respectively. Images produced using the FD and WFD algorithms, referenced to 80 Hz, had less *image error* than their adjacency counterparts. While images produced using the FD and WFD algorithms were qualitatively and quantitatively comparable, the WFD had more image noise. There was a natural negative undershoot caused by the weight, α, near the reconstructed object.

(2) In measurements with the carrot-saline background, images produced with the WFD and WFDA algorithms had clearly identifiable reconstructed perturbations, with the WFDA images having the lowest *image error*, and both compared favourably with the TD images. Images with the FD and FDA algorithms did not result in images with qualitatively identifiable reconstructed perturbations.

2.4.2 Assessment of FD algorithms

The performance of the algorithms was largely as may be expected from the first principles set out in the introduction. For the saline background with a relatively small test

object, all algorithms resulted in satisfactory images, as it appears that the violation of the assumption of linearity still results in acceptable images. However, for test object contrasts of greater than 20 %, the amplitude of the change was relatively diminished compared to its estimated value (figures 2.4 and 2.5), which was presumably, at least in part, attributable to this violation. There was therefore little qualitative or quantitative benefit gained with the use of the WFD algorithms. The pairs of frequencies which gave the best images with the FDA and WFDA algorithms were those with the largest conductivity change of up to 38.4 %. This was potentially because errors introduced by the violation of the linear assumption were smaller than the improvement in signal.

However, with the carrot-saline background recordings, the weighted frequency difference algorithms (WFD and WFDA) were clearly superior to FD and FDA for all tanks and perturbation positions. In the carrot-saline background, the comparison of sequential pairs (WFDA) produced superior images to those produced by referencing to a single frequency of 80 Hz (WFD). Nonetheless, the fact that in the carrot-saline background the best WFDA images were at 32 kHz referenced to 20.16 kHz, which gave changes of up to 16.56 %, was probably due to the limited deviation from this linear assumption using WFDA.

In summary, when selecting the best frequency pairs, if the frequency responses of the tissues are known, there are three key considerations. First, it is preferable to remain within the linear range of conductivity changes, <20 %. Second, in different parts of the frequency range, different errors dominate: when referencing changes to a low frequency, such as 80 Hz, electrode impedance errors must be considered, and if these are contrasted to higher frequencies, then stray capacitance is another error source. Lastly, at different places along the spectra, different pairs will produce a different SNR and this also depends on which frequencies an MFEIT system can address.

2.4.3 Study limitations

There were several limitations in the current study. These include shortcomings with the image quantification method, the means of determining the singular value used for tSVD and the thresholds chosen for boundary voltage rejection and uncertainties regarding the effect of this data removal. The image quantification largely agreed with the qualitative assessment of the reconstructed image quality. However, the shape error metric is not optimised. This is for two reasons, first, the localisation and shape error are currently tied together as an erroneous shape in any dimension is likely to shift the-centre-of mass even in spite of the weighting. In addition to this, the metric of shape error is one based upon comparing the reconstructed perturbations' range in each axis to the known perturbation dimensions. Therefore, in an extreme, and admittedly unlikely, situation of a cuboidal reconstructed perturbation of the right dimensions, this would have no error,

in spite of incorrect geometry, therefore a geometry based assessment of shape error may be more suitable.

The truncation level for the singular value decomposition implemented in this study was fixed so as to be the same for all of the given experimental series. This meant inclusion of singular values corresponding to 99.6 % and 99.98 % of the normalized maximum singular value for the 2D tank and 3D tank, respectively. This threshold was chosen by the empirical comparison of truncation levels and the level most consistent across all experiments was used. However, this is an unrealistic option for future non-tank and clinical studies as such a mechanism relies on the prior knowledge of the intended reconstructed change. There are several alternative methods that might be employed to objectively determine the hyperparameter (truncation level) for regularisation, among which is cross-validation of the experimental data versus simulated data.

Another point of consideration was that of highly variable spatial sensitivity, that is the expected image quality throughout the mesh. From first principles, image quality can be expected to be the same for various test object locations in a tank if three conditions are met. First, the geometry of the object is regular and symmetrical with electrodes spaced evenly around it. Secondly, the current injection and voltage measurement scheme must be symmetrical. Lastly, the test object needs to be placed at the same distance from the electrodes in all locations. Based upon this, in the 2D tank series if the perturbation had been placed at 2.5cm from a series of electrodes, and not just electrode one, then each of the resultant images would be excepted to be very similar. However, for the three different perturbation placements in the 3D tank, images of different quality were produced with a trend of the posterior being the best, lateral second to this and anterior worst. It is difficult to determine whether this is innate to the tank, protocol, data quality or some other contributing factor. The 'spiral_s-o protocol' is not geometrically symmetrical and as such the sensitivity will be different at different locations in the tank, in addition to which even if the protocol were geometrically symmetrical, the tank is not. The irregular geometry of the tank means that current injection and record across the width of the tank will be different to that across the anterior-posterior dimension of the tank, as the transfer impedance will be different and this in turn alters the sensitivity at different positions in the tank. Nonetheless, the trend in image quality would seem to grossly agree with the differences in the electrode density; the anterior region of the tank is poorly covered with electrodes, due to the eyes and supraorbital ridge, and the upper electrode ring has fewer electrodes in anterior aspect.

In principle, it should have been possible to use all the recorded data for image reconstruction, but noise within this data prevented this from being possible. The employed method of boundary voltage rejection, removal of voltages less than 0.1 mV or with a temporal noise greater than 1 %, was a balance between quantitative and qualitative as-

sessment of the images, and the preservation of as much data as possible. The need for this process could be minimised by utilising a system with a variable gain[64], increasing the applied current, or by altering the electrode addressing protocol to minimise the prevalence of small boundary voltages and therefore combinations with low SNR, possibly through implementing an adaptive protocol[185]. While these should all be effective in tank studies, in humans their application is potentially more difficult. First, current cannot be increased without limit, due to patient comfort and safety considerations. Secondly, the other proposed options, if implemented correctly, could remove the need for rejection of low-amplitude boundary voltages, but would not remove the need for rejection of other sources of data corruption present in clinical recordings, such as movement artefact, which would require signal processing schemes of artefact detection.

2.4.4 Recommendations for future work

These findings are encouraging to the view that this approach could be used to produce FD images in the adult head with scalp electrodes. The rationale for this work was to establish a lower bound of performance-had this been unsuccessful, then these approaches would clearly not be likely to work in human studies. In other words, success in this tank model, while not excluding the possibility of success with a skull or clinical success, does not ensure it either. The situation for human scalp recording is clearly more demanding: the tank used in this study lacked a simulation of the skin-electrode interface and also the skull, which may attenuate the recorded changes by up to 1000 times[186]. In addition to this the perturbations themselves are not sufficiently accurate to determine clinical usefulness, as the underlying need for a neuroimaging modality in acute stroke is to differentiate between the two main subcategories; a conductivity increase with frequency, which resembles ischaemic stroke, was simulated, but a perturbation with a flat response, as for haemorrhage, was not employed.

Future work could profit from examining these algorithms in the 3D head-shaped tank with a real human skull in place, perhaps first in simulation, as it is unclear how successful the weighted algorithms would be in the presence of heterogeneity. Furthermore, studies could profitably examine imaging with saline soaked gels to simulate blood, and with a model in which skin is simulated with the skin of a fruit or vegetable, as done previously with marrow skin[183]. Other improvements could include the identification of the existence of more robust electrode addressing protocols, with fewer low SNR boundary voltages, which should therefore minimise the necessity for boundary voltage rejection, and also improved image reconstruction methods, to eliminate the subjective selection of the regularisation hyperparameter and possibly non-linear approaches, so that no assumptions are needed to reconstruct conductivity contrasts greater than 20 %. Nonetheless, these are the expected limitations of the current study as the only means

of truly ascertaining the possible use of such a system is to apply it, preferably blinded, at least to an animal trial and ideally a clinical trial. Therefore, in spite of the detailed limitations of this study, these results at least support the prospect of imaging acute stroke with MFEIT, as the findings are that MFEIT works in a realistic 3D head-shaped tank.

Chapter 3

Statistical Analysis of Electrical Impedance Tomography Images of Fast Neural Activity

3.1 Introduction

Gilad et al., from the UCL EIT research group, produced tomographic images of fast neural activity, using EIT (as detailed in chapter 1). 57 images were generated from impedance data collected in 16 female, Sprague-Dawley rats during SEPs and VEPs. Although the method has been examined and published [64], and the individual images were in agreement with expectations, the imaging component of this work remained unfinished. The reason for this is that, although analysis of the impedance data and the individual images had been undertaken, neither grand mean statistics across stimulation groups, nor consideration of the physiological significance of any laminated changes in the images had been examined: it is these two points that are addressed in this chapter.

First, an overview of the previous study is given. Second, further analysis of the imaging cohort is detailed and the results presented.

3.1.1 Review of first electrical impedance tomography imaging study of fast neural activity

The imaging of fast neuronal activity with EIT has been reviewed in chapter 1, and the pertinent points are reiterated here. In imaging neuronal activity with EIT, the expectation is for an impedance decrease subsequent to the opening of voltage-gated ion channels in the membrane of active neurons. This is because the opening of these channels allows current to pass across neurons whose capacitive membrane otherwise blocks the passage of current, at least at low frequencies. However, if the frequency of the applied current is increased then, given the capacitive nature of the membrane, more

current passes across the neuron prior to the opening of voltage-gated ion channels, and so the impedance decrease associated with this is less. This effect has been confirmed in both modelling and experimental studies of the impedance changes associated with neuronal activity (for a review see chapter 1).

It was only in a recent, single channel study, by Oh et al., that it was first suggested that there may be advantages to applying the current at frequencies above DC. Oh et al. noted that whilst the maximum signal occurs at near DC frequencies, the maximum SNR, in cortical recordings, is at above DC frequencies. This is because the main source of noise, the ECoG signal, has most of its power $\leq$100 Hz. By using a sine wave carrier Oh et al. noted a greater attenuation of the ECoG noise than the reduction in the impedance signal. Based upon these findings, within the limitations of the employed hardware, the optimal carrier frequency was found to be 225 Hz. In this study it was also determined that 50 µA was a permissible current amplitude; no significant difference was found in the percentage, impedance change between 10, 20 and 50 µA[64]. It was based upon these findings that the multi-channel, imaging cohort, currently under consideration, were collected and reconstructed.

3.1.1.1 Imaging study: experiment methodology

Gilad et al. used a Sprague-Dawley rat model to image fast neural activity with EIT. Anaesthesia was induced in an induction chamber ventilated with 4 % halothane, and a 70:30 mix of oxygen and nitrous oxide. Subsequently, a tracheostomy was performed to introduce an endotracheal tube, the halothane reduced to 0.5 to 1.5 %, electrocardiography (ECG) leads attached to the paws, and femoral artery and vein cannulation performed. An arterial cannula was used to monitor the arterial blood pressure and measurement of arterial blood gases (ABGs). Additionally, the rat's core body temperature was maintained at 37 °C with the use of a heat mat and rectal thermometer. To minimise movement artefact related to ventilation, mechanical ventilation and bilateral pneumothoraces were performed, and so paralysis, via the administration of pancuronium bromide, was induced. Following these preparatory procedures, the rat was placed in a stereotactic frame and a craniotomy of approximately 8 mm × 8 mm performed contralateral to the side a stimulus was to be delivered and positioned in one of four locations depending on the stimulus type. Following the craniotomy, the dura mater was also resected, and a platinum-silicon electrode array with 29 electrodes, 0.6 mm in diameter and hexagonally arranged with a centre-to-centre distance of 1.2 mm, was placed on the rat cortex. The delivered stimuli were either somatosensory or visual stimuli. The somatosensory stimuli were via unilateral electrical stimulation of the median nerve, sciatic nerve or the mystacial vibrissal pad, delivered as a 10 mA pulse lasting 100 µs at a rate of 2 Hz, while the visual stimulus was a binocular photic flash stimulus delivered via LEDs, with stimulation

also at 2 Hz[90].

Once the electrodes were in place, a custom built current source was used to inject current serially, while the voltages were recorded simultaneously with a 32-channel commercial EEG system sampling at 2048 Hz (Micromed S.p.A., Treviso, Italy). The current injection electrode pair was switched via a multiplexer so that a total of 30 to 40 adjacent pairs were addressed, with the remaining 27 electrodes recording the voltage so that a total of approximately 900 four terminal traces were recorded. Each current injection was for 70 s, with the first 10 s being discarded to remove switch related settling artefacts, leaving a 60 s segment containing 120 repeats, and so the total recording lasted approximately 1 h. The injected current had an amplitude of 50 µA and was at 225 Hz, with a bandwidth of 100 to 350 Hz. The choice of a 225 Hz carrier frequency was to optimise the SNR, based upon the findings of Oh et al., but also selected to be asymmetric to the even stimulation rate and halfway between two 50 Hz harmonics. In addition to the active recordings at 50 µA and 225 Hz a number of control recordings were done: ipsilateral recordings, recordings with no stimulus, recordings in dead animals, and recordings at different current amplitudes, 10, 20 and 50 µA, and phase angles, 0, 45, 90 and 135°, for some forepaw recordings[90].

Subsequently, the final approximately 900 traces were processed offline. Each was the average of 60 1 s trials consisting of 150 ms pre-stimulus and 850 ms post-stimulus. A summation/subtraction procedure was applied to the averaged data, in order to yield the SEP/VEP and modulated impedance change, respectively. The modulated impedance change was then demodulated into change in modulus and phase. Performing this procedure over 500 ms resulted in significant artefacts at both ends of each segment. This was corrected by rejecting the first and last 100 ms of the signal, so that the final data was 300 ms long, 50 ms pre-stimulus and 250 ms post-stimulus. Some of the approximately 900 traces were rejected or not recorded on the basis of either the noise in the pre-stimulus time being greater than 0.3 µV or 0.01 % of the boundary voltages, significant 50 Hz noise being present in the data, or if an electrode could not be recorded from, such as due to damage to the electrode array. After rejection, there were, across 57 recordings, 384 ± 140 (range 137 to 691) combinations, and an average noise of 0.18 ± 0.04 µV (range 0.10 to 0.24 µV), which equated to 0.004 ± 0.001 % (range 0.001 to 0.007 %). From this process impedance change data was taken at 21 time points, 0 to 40 ms every 2 ms, for image reconstruction of SEPs, and 18 time points, 0 to 255 ms every 15 ms, for image reconstruction of VEPs[90].

3.1.1.2 Imaging study: imaging methodology

The forward model was generated for a 1 072 558 tetrahedral element FEM mesh of the rat brain, in which the dorsal third had an edge length of 0.2 mm, the lower third 0.8 mm, and

the middle third transitioned between these two values. The electrodes were then mapped on to surface triangles of this mesh, with one set of positions for each of the four stimuli (figure 3.1). The boundary voltages and sensitivity matrix were then calculated based upon a homogeneous conductivity of $0.3\,\mathrm{S\,m^{-1}}$ using the UCL SuperSolver package[164], which is based on the electrical impedance tomography and diffuse optical tomography reconstruction software (EIDORS) package[187]. Inversion of the sensitivity matrix was performed with tSVD, with row normalisation and truncation set at 25, 50, 75, 100, 125 and 150, with 50 being determined, by qualitative assessment, to be the best truncation level and therefore images with this truncation level were used for further analysis. For each recording a gain correction of the image was performed; a simulation with the given protocol for each recording was performed with a perturbation of 1 % or 0.1 %, for the SEP and VEP recordings respectively, at a depth of 1.4 mm, from which a scaling factor to make the images 1 % or 0.1 % was determined and applied to the respective image from the experimental data[90].

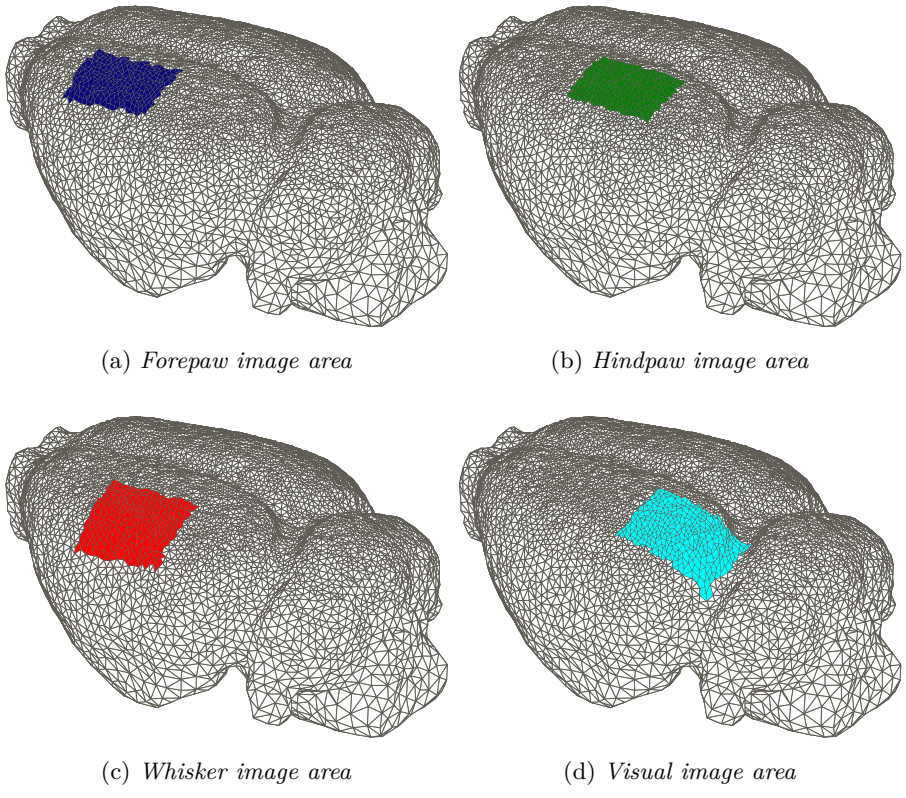

(a) *Forepaw image area* (b) *Hindpaw image area*

(c) *Whisker image area* (d) *Visual image area*

Figure 3.1: *Location of the reconstructed image volumes on FEM mesh of the rat brain.*

These scaled conductivity changes in the FEM mesh, at 21 and 18 time points for the SEPs and VEPs recordings, respectively, were then trilinearly interpolated onto a three-

dimensional Cartesian grid, with a spacing of 0.01 mm over a 6 mm × 4 mm × 3 mm, in the x-, y- and z-axes, at a region centred around the electrode array for the given stimulus. The resultant rasterised images were then boxcar filtered with a smoothing kernel of 0.5 mm × 0.5 mm [90].

3.1.1.3 Imaging study: results

In total 57 EIT recordings were deemed technically valid on the basis of stable rat condition, with an EP of >200 µA, and no serious technical fault in any of the components, such as the trigger generator. In each recording's image set the peak of the EP, the peak of the conductivity change in the images, and the depth and time of this peak conductivity change were determined. The time of the peak conductivity change was noted to be closely matched to the peak of the EPs. For the forepaw and hindpaw recordings the peak conductivity change was at a depth approximating layer III, and for the vibrissae and visual images at layer V. The validity of assessing these depths is marred by the fact that depths were calculated from the top/vertex of the mesh, rather than normal to the cortical surface. These results are summarised in table 3.1 for active recordings with a current injection of 50 µA at 225 Hz [90].

	Peak EP (µV)	Peak Conductivity Change (%)	Depth of Peak (mm)	Time of Peak (ms)	Recordings (Rats)
Forepaw	650 ± 140	−0.7 ± 0.3	0.66 ± 0.14	11 ± 2	22 (8)
Hindpaw	640 ± 190	−0.7 ± 0.3	0.4 ± 0.3	14 ± 1	5 (2)
Vibrissae	630 ± 200	−0.9 ± 0.2	1.25 ± 0.25	7 ± 1	6 (3)
Visual	390 ± 130	–0.11 ± 0.03	0.8 ± 0.3	143 ± 8	6 (3)

Table 3.1: *The maximum EP and conductivity changes in Gilad et al. (2010) imaging study for recordings with a current of 50 µA at 225 Hz.*

The conductivity changes were found, as determined by one-way ANOVA, to not be significantly different for changes in the applied current's amplitude or phase. Changes were present in recordings made from the hemisphere ipsilateral to the stimulus, but much smaller than recordings made contralateral to the stimulus. Meanwhile in recordings without a stimulus and in dead controls there were no significant EP or conductivity changes [90].

3.1.2 Expected translaminar and lateral propagation of activity

This section details a summary of the reported (as detailed in chapter 1) laminar propagation of activity for each of the stimulation modalities and a corresponding diagram

of these expected changes is given. The literature regarding the exact lateral spread of activity is less numerous than that examining translaminar propagation. Nonetheless, the areal extent of the activation, given the nature of the stimulus used by Gilad et al., would be expected to engage the entirety of appropriate primary cortical representation, and while lateral spread to association cortices should occur, these would be outside much of the respective imaging volumes.

Forepaw SEPs are noted to have an onset latency of 7 to 8.6 ms[121;125], but with P1 having an onset at around 3.7 ms and peaking at 7.7 to 12.6 ms, and N1 peaking at 12.1 to 35 ms. The lateral extent of this response is ≤1.5 mm in diameter for the top 20 % of changes and ≤5 mm in diameter for the top 60 % of changes[125]. The specific laminar activity is initiated in the bottom of layer IV at 4.9 ± 0.4 ms and 6.2 ± 0.7 ms (onset latency and peak latency), with this spreading into layers V and VI after 0.1 ± 0.3 ms and 1.2 ± 0.2 ms (difference from the respective times for the initial site of activity), then to layers III and IV after 0.7 ± 0.3 ms and 1.3 ± 0.3 ms, then to layers II and III after 1.7 ± 0.3 ms and 2.9 ± 0.5 ms, and finally to layers I and II after 3.8 ± 0.9 ms and 5.6 ± 0.5 ms[126;128].

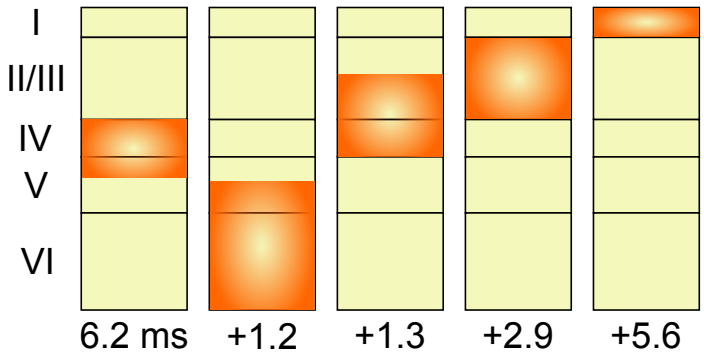

Figure 3.2: *Laminar propagation of activity following forepaw stimulation, the location of activity is indicted in orange and difference in latencies compared to the initial site detailed.*

Hindpaw SEPs are noted to have an onset latency of 11.5 to 13 ms, with the lateral extent of this response being ≤1.5 mm in diameter for the top 20 % of changes and ≤5 mm in diameter for the top 60 % of changes[125]. The specific laminar activity, for evoked activity, is initiated in the bottom of layer IV at 16.37 ± 0.38 ms. This then spreads to layers III, IV and V after 0.88 ms (difference from the time for the initial site of activity), then to layers II and III after 2.63 ms, then to layers V and VI after 2.72 ms, and finally to layer VI after 6.13 ms[108;129].

Vibrissa SEPs have an onset latency of 5 to 10.01 ms, with the typical value being approximately 7.5 ms[125;141;145;148]. The onset of P1 is around 8 ms[146], and it peaks around 9.9 to 13.9 ms[121;147], and N1 occurs at 16 to 30 ms[121;146], P2 at 32 ms[144],

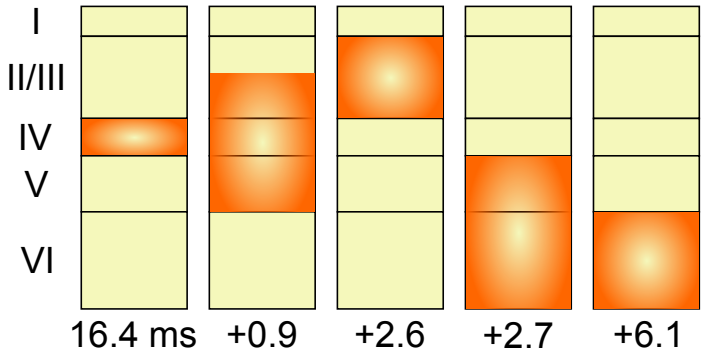

Figure 3.3: *Laminar propagation of activity following hindpaw stimulation, the location of activity is indicted in orange and difference in latencies compared to the initial site detailed.*

and N2 at 80 to 100 ms[54;144]. The fast wave P1-N1 complex is constrained to S1[144], with the initial response being confined to an area approximately 0.25 to 0.8 mm in diameter[146;148]. The activity then spreads laterally, with P2 entering S2 and N2 entering caudal areas and excluding S1[144]. This lateral spread occurs in <15 ms, the area this covers is 1 to 1.5 mm in diameter[125;146;148], while propagating waves have been found to occur over a longer time of 15 to 50 ms. This lateral spread extends to cover PMBSF, the somatosensory association cortices, M1 some 6.5 ± 1.9 ms after the S1 activity[141;151], and spreads at a rate of 5 to 6 $\mathrm{cm\,s^{-1}}$[110;139]. There are conflicting reports regarding S2 activation, with activation being noted to occur at the same time as S1[150], and also occurring approximately 10 ms after it has occurred in S1[144]. This discrepancy is likely explained by the prior reflecting direct thalamocortical input and the latter being the result of feed-forward activity from S1.

The specific laminar activity subsequent to vibrissal stimulation is initiated in layer IV and the border between layers V and VI in the cortical barrel corresponding to the principal whisker with an onset latency of approximately 5 ms and latency to peak of 7.4 to 8.4 ms[53;54;110;138;140;149]. Activity, still initially confined to the width of the cortical barrel[139], spreads into layer III, then layer II, with the difference between these being 1 to 2 ms[110;140], and so their activation is typically reported as grouped together. Activation of layers II and III has an onset occurring 1 to 3 ms and a peak within approximately 4.6 ms after the initial activity in layer IV[53;110;140;149]. Layers V to VI are active 2.5 to 3.2 ms after the first response in layer IV[53;110]. The whole column-barrel structure from layers II to Va is active within approximately 5 ms[54;110;132], while the activity in layers II to V extends beyond the lateral limits of the principal whisker's barrel after approximately 10 to 15 ms[110;140].

The P1-N1 complex of VEPs occurs at 20 to 30 ms, with the first component of this complex being confined to V1 and the later component entering V2, while P2 and N2,

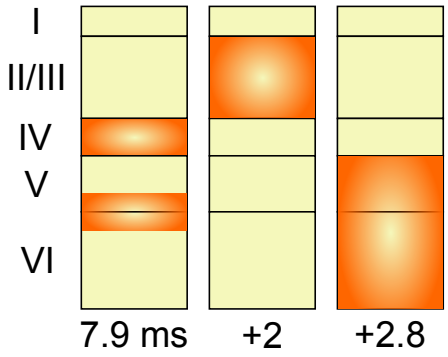

Figure 3.4: *Laminar propagation of activity following vibrissa stimulation, the location of activity is indicted in orange and difference in latencies compared to the initial site detailed.*

occurring at 42 ms and 105 ms, respectively, spread into S1 and S2[158]. The specific laminar activity is initiated in the bottom of layer III and in layer IV at 33 ms[112;159], and then a much smaller area of activity occurs in layer V 4 to 8 ms later and persists for ≤20 ms[112;160;161]. Approximately 5.6 to 17 ms after the onset of activity at the initial site, activity spreads to layers II and III[112;160], with much later, lower amplitude, activity occurring in layers II/III and VI approximately 48 ms after the initial activity[112], with the activity resulting from visual stimuli diminishing at 60 ms and having disappeared by 200 ms[161]. Feed-forward activity from V1 to V2 initiates activity first in layer IV, which in ≤5 ms has activated all the supra- and infragranular layers, while feedback activity is mainly directed towards the non-granular layers and also results in their activation in ≤5 ms. Although latencies are slightly shorter for feed-forward activity compared to feedback, the differences are not significantly different[162]. The lateral spread of activity results in a wave of post-synaptic potentials initiated in V1 at approximately 100 ms, which compresses at its lateral border at approximately 73 ms and is then reflected back[163].

3.1.3 Statistical parametric mapping

It is often complex and difficult to acquire functional neuroimaging data, but it is equally, if not more, difficult to assess the significance of the resultant images, both with respect to intra-subject scan variability and inter-subject variability. In order to address many of these issues a technique referred to as statistical parametric mapping (SPM) was developed, which as a software package now encompasses image manipulation, statistical significance testing of images, and higher model construction and testing. The SPM software package was developed at the Wellcome Trust Centre for Neuroimaging, UCL Institute of Neurology. It is written in MATLAB and is distributed under a GNU General Public

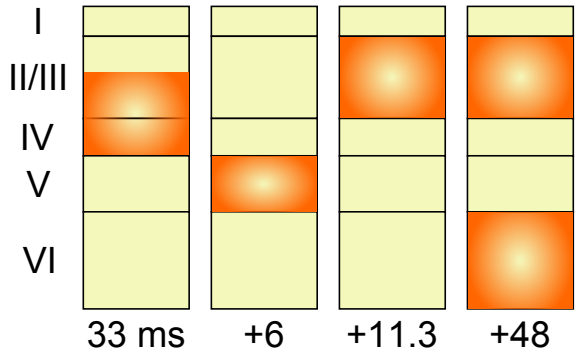

Figure 3.5: *Laminar propagation of activity following visual stimulation, the location of activity is indicted in orange and difference in latencies compared to the initial site detailed.*

License (www.fil.ion.ucl.ac.uk/spm/). The components of SPM implemented in this study are primarily focused on the construction of statistical parametric maps, which involves a mass-univariate approach: the same model is applied at each voxel. Once this model has been constructed there is an estimation of its parameters through the use of a statistical linear model known as the general linear model (GLM). Following this inferences using voxel-wise statistics are made, implementing random field theory (RFT) as a means to resolve the issues inherent to making multiple statistical comparisons, that is the false positive rate increases. The use of RFT results in adjusted p-values for the volume being tested, and is often likened to a Bonferroni correction for continuous data. These SPMs are, under the null hypothesis, distributed according to a known probability distribution, such as Student's t-distribution or an F-distribution, and the resultant maps of significance displayed as images[188–190]. Each of these areas, with particular focus upon those relevant to the current study, are briefly detailed below. Image processing procedures, such as interpolation and smoothing, are detailed at the end. While they are typically applied to images prior to employing SPM, they affect the inferences and assumptions of SPM and so better understanding of their effect requires prior knowledge of SPM.

3.1.3.1 General linear model

The basis of much of the mathematics behind SPM is the GLM, with the formulation of this model and its solution having its roots in linear regression. Under this model each data point, or the data in each voxel, y_j, where $j = 1, ..., J$, is a dependent variable that is related linearly to a l-vector of independent explanatory variables or regressors, x_{jl}, where $l = 1, ..., L$, that in some circumstances are observed, such as in data fitting, or are predetermined in the experimental design as in SPM. Typically, a constant term, the intercept, is also included in this model. In addition to these regressors there is inclusion

of a disturbance term, ϵ_i, and with this the GLM is formulated:

$$y_j = x_{j1}\beta_1 + ... + x_{jl}\beta_l + ... + x_{jL}\beta_L + \epsilon_j, \tag{3.1}$$

where β_L are unknown parameters or regressor coefficients to each of the x_{ij} regressors. There are specific assumptions placed upon the error terms, ϵ_i, which include that the errors have a constant variance in each observation with a mean around zero, and that the errors are independent, that is they are non-autocorrelative across observations [188;190].

Equation 3.1 can be expanded from a single data point so that the model is for each data point:

$$\begin{aligned}
y_1 &= x_{11}\beta_1 + ... + x_{1l}\beta_l + ... + x_{1L}\beta_L + \epsilon_1 \\
&\vdots \\
y_j &= x_{j1}\beta_1 + ... + x_{jl}\beta_l + ... + x_{jL}\beta_L + \epsilon_j \\
&\vdots \\
y_J &= x_{J1}\beta_1 + ... + x_{Jl}\beta_l + ... + x_{JL}\beta_L + \epsilon_J
\end{aligned}$$

and this can be rewritten in matrix format as:

$$\boldsymbol{y} = X\boldsymbol{\beta} + \boldsymbol{\epsilon}, \tag{3.2}$$

where $\boldsymbol{y}$ is a column vector of length J, X is a $J \times L$ matrix, commonly referred to as the design matrix, $\boldsymbol{\beta}$ is a column vector of length L, and $\boldsymbol{\epsilon}$ is a column vector of length J [190].

Typically the number or observations, or rows, of the design matrix is greater than the number of parameters, or columns, so the problem is overdetermined and there is no solution. Consequently, an estimate or approximation has to be made to solve $X\boldsymbol{\beta} \approx \boldsymbol{y}$, where $\boldsymbol{\beta}$ is the unknown. The standard approach to solving this is the use of ordinary least squares, which aims to estimate a fit of the data, $\hat{\boldsymbol{y}} = X\hat{\boldsymbol{\beta}}$, that is as close to the data as possible, with respect to the sum of squares, which can be expressed as [189;190]:

$$\hat{\boldsymbol{\beta}} = \arg\min_{\boldsymbol{\beta}} \|\boldsymbol{y} - X\boldsymbol{\beta}\|_2^2 . \tag{3.3}$$

An intuitive way of understanding the estimation of the parameters $\hat{\boldsymbol{\beta}}$ is to formulate the problem as a geometric one. The estimation $\hat{\boldsymbol{y}}$ exists in the column space of X, $\mathcal{C}(X)$, while the actual data, $\boldsymbol{y}$, does not exist in $\mathcal{C}(X)$: if $\boldsymbol{y}$ existed in $\mathcal{C}(X)$ then the solution would simply be $\boldsymbol{\beta} = \boldsymbol{X^{-1}y}$. Given this, the shortest distance, or least squares distance, between $\hat{\boldsymbol{y}}$ and $\boldsymbol{y}$ must be a vector projection of $\boldsymbol{y}$ onto $\mathcal{C}(X)$. The difference between

this projection, which is $X\hat{\boldsymbol{\beta}}$, and $\boldsymbol{y}$ will be orthogonal to $\mathcal{C}(X)$ and so belongs to the orthogonal compliment of X:

$$X\hat{\boldsymbol{\beta}} - \boldsymbol{y} \in \mathcal{C}(X)^{\perp}. \tag{3.4}$$

Given that $\mathcal{C}(X)^{\perp}$ is equal to null space of the transpose of X, $\mathcal{N}(X^{\top})$, this difference also belongs to $\mathcal{N}(X^{\top})$:

$$X\hat{\boldsymbol{\beta}} - \boldsymbol{y} \in \mathcal{N}(X^{\top}). \tag{3.5}$$

Consequently, multiplication of $X^{\top}$ by the difference between the projection and the data equals the zero vector:

$$X^{\top}(X\hat{\boldsymbol{\beta}} - \boldsymbol{y}) = \mathbf{0}, \tag{3.6}$$

with the identification of the zero vector this can be expanded and rearranged to solve for $\hat{\boldsymbol{\beta}}$:

$$\begin{aligned} X^{\top}X\hat{\boldsymbol{\beta}} - X^{\top}\boldsymbol{y} &= \mathbf{0} \\ X^{\top}X\hat{\boldsymbol{\beta}} &= X^{\top}\boldsymbol{y} \\ \hat{\boldsymbol{\beta}} &= (X^{\top}X)^{-1}X^{\top}\boldsymbol{y} \end{aligned}$$

with $(X^{\top}X)^{-1}X^{\top}$ being the Moore-Penrose pseudoinverse and denoted as $X^{\dagger}$, so that the least squares solution is:

$$\hat{\boldsymbol{\beta}} = X^{\dagger}\boldsymbol{y}. \tag{3.7}$$

As mentioned above this is the least squares solution, and is an approximation, hence the presence of an error term in equation 3.2. The minimisation of this error reflects the quality of the fit of the model in terms of the residual sum-of-squares, RSS, which is the sum of the squares of the differences between the data and model, or the square of the error terms[190]:

$$RSS = \|\boldsymbol{y} - \hat{\boldsymbol{y}}\|^2 = \boldsymbol{\epsilon}^{\top}\boldsymbol{\epsilon}. \tag{3.8}$$

The GLM and ordinary least square solution detailed above are the basis of the estimation procedure in SPM; however, multiple modifications are made to these to compensate for deviations from the assumptions underpinning this procedure. These extensions include accounting for deviations from the assumption of identically and independently distributed error terms, which is referred to as non-sphericity and, for example, can re-

sult from serial correlation in a time series of scans. One approach is the use of an additional matrix that whitens, or de-correlates, the error terms and this results in the ordinary least squares solution being solved by a restricted maximum likelihood estimation procedure [188]. An additional problem is the one of multiple comparisons; statistical inference repeated at each voxel multiplies the risk of false positives as a product of the number of voxels in the image, which for functional neuroimaging of the entire brain can be substantial. The approach employed in SPM to deal with the issue of multiple inferences is the use of RFT, which is discussed in section 3.1.3.3 [188]. However, a thorough discussion of the other extensions employed in SPM, such as those in response to non-sphericity, are beyond the scope of this chapter.

3.1.3.2 Statistical Inferences

Inferences about the parameter estimates, $\hat{\boldsymbol{\beta}}$, are made using their estimated variance, based upon RSS. This allows for testing of the null hypothesis, $\mathcal{H}_0$, with either a t-statistic or F-statistic being undertaken and presented as a map across the voxels being tested, referred to respectively as t- and F-maps [188]. The application of these inferences can be made to examine the adherence of a single subject's data to a known model, such as a single subject's haemodynamic response, as measured by fMRI during a box-car stimulation paradigm, which in SPM is referred to as first-level analysis. Alternatively, statistical inferences can be made across data collected from multiple subjects, and so a population's estimated responses tested for statistical significance, this is referred to as second-level analysis. If the results of a first-level analysis are then input into a second-level analysis, in a hierarchical fashion, then this can allow for modelling of within- and between-subject variance and formulation of formal inferences about the subjects' population, a procedure referred to as random effects analysis [191].

To date the only application of SPM to EIT images has been first-level analysis of haemodynamic responses. Zhang et al. undertook first-level analysis on simulated EIT images of haemodynamic responses, both without and with added noise. Simulations were in a sphere 200 voxels in radius and with a perturbation of 20 voxels in radius. The perturbation's impedance was altered as a function of the time frame being simulated, where a total of 36 time points were simulated. The employment of SPM allowed for the localisation of significant changes whose centre were $<8.5\,\%$ displaced from the simulated perturbation's centre. In their use of SPM Zhang et al. calculated the error terms, ϵ_i, in the EIT image sets and, by means of a χ^2-squared test, established whether the assumption in the GLM of normally distributed errors was held, which it was. Had this assumption been broken Zhang et al. intended to reconstitute the design matrix [192]. Similarly, Yerworth et al. undertook first-level analysis on simulated, tank phantom, and clinical data of VEPs. The simulation was in a four layer head FEM mesh, with a spherical perturbation

of 1 % maximal impedance change, and Gaussian noise of 0.0009 % added to the boundary voltages. The tank component of the study was in a realistic head-shaped tank which contained 0.2 % saline and a human skull, with the perturbation being a cylinder of sponge, 30 mm in diameter and 26 mm high, which gave an impedance change of 15.4 %. In both the simulation and tank experiments, averaged EIT images were compared to SPMs for the whole time series. The human clinical data were of VEPs secondary to checkerboard stimulation in 14 healthy adults. The SPM results for both the simulation and tank experiments resulted in a significant area in the occipital region of the head (p <0.001). However, the SPM results in the human data, as with the EIT images, were seemingly artefactual, with significant results also in the anterior and lateral aspects of the brain.

There are multiple means of statistical inference that can be undertaken in SPM, such as variants of Student's t-test, the F-test, ANOVA, and other options. Hence, for brevity only a description of the one-sample t-test, as one of the simplest statistical inferences and the method employed in the present study, is given here. In t-tests the results from a sample or population are compared to that of another population or value, which in the case of a one-way t-test is the comparison of values, $\hat{\boldsymbol{\beta}}_{\mathbf{1}}$, to a null hypothesis value, such as 0. In other words $\mathcal{H}_0 : \hat{\boldsymbol{\beta}}_{\mathbf{1}} = 0$, while the alternative hypothesis is $\mathcal{H} : \hat{\boldsymbol{\beta}}_{\mathbf{1}} \neq 0$, and so the t-values are a comparison of $\hat{\boldsymbol{\beta}}_{\mathbf{1}}$ to 0, which is scaled by its error, and has a probability distribution of Student's t-distribution for the relevant degrees of freedom:

$$T = \frac{\hat{\boldsymbol{\beta}}_{\mathbf{1}} - 0}{\sqrt{\hat{\boldsymbol{\sigma}}^2 / J}} \sim t_{J-1}, \tag{3.9}$$

where J is the number of scans or subjects, and $\hat{\boldsymbol{\sigma}}^2$, is the residual variance, which is estimated as RSS divided by the degrees of freedom: $\hat{\boldsymbol{\sigma}}^2 = \frac{e^\top e}{J-1}$ [190]. Once the t-statistic at each voxel has been calculated then interpretation of the values has to be made. The first step in making inferences is based upon deciding the level of significance, α, an experimenter wants to test at, which relies upon comparison to Student's t-distribution. In addition to this, correction can be made to α based upon the number of repeated tests, known as family-wise error (FWE) correction, which is achieved using RFT and is detailed in section 3.1.3.3. Alternatively, topological inferences can be made regarding peaks, clusters, or sets of clusters, with the prior reflecting the height and the latter two the extent of the t-map. In these topological inferences an alternative correction, referred to as false discovery rate, is employed, but as such inferences have not been made in the current study they are not detailed further here [194;195].

3.1.3.3 Random field theory

In rejecting the null hypothesis, $\mathcal{H}_0 : \hat{\boldsymbol{\beta}}_{\mathbf{1}} = 0$, the statistic is compared to the null distribution, which is the distribution the statistic would be expected to have under the null hypothesis. The problem with this is that a rejection of the null hypothesis is made at a significance level carrying a probability of false positives. For example, given $\alpha = 0.05$, incorrect rejection of the null hypothesis would occur for 1 in 20 rejections of the null hypothesis. Therefore in functional neuroimaging where there can be many thousands of voxels across which statistical inferences are made there can be a substantial number of voxels in which the null hypothesis is incorrectly rejected [196].

Correction for this multiple comparison issue can be made with respect to the FWE rate, which can be most simply done with the Bonferroni correction. This correction means that for each of the repeated tests, n, the significance level becomes harder to reach:

$$\alpha = p^{FWE}/n, \tag{3.10}$$

so, for example, if an image containing 100 000 voxels was tested for significance at a significance level of 0.05, then the p^{FWE} would be 0.000 000 5. The Bonferroni correction will correct for false positives voxels, but this is not what should be corrected for in functional neuroimaging, because many voxels are spatially correlated and as such the number of independent tests that need correcting for is less than the number of voxels, which is addressed in SPM with RFT [196;197].

In RFT the p^{FWE} is estimated from two parameters, the number of resels and the Euler characteristic of the domain:

$$p^{FWE} \approx \sum_{d=0}^{D} Resels_d EC_d(\alpha), \tag{3.11}$$

where resels is the number of d-dimensional resels, or resolution elements, which are spatially correlated groups of voxels, EC is the d-dimensional Euler characteristic, and D is the number of dimensions of the search region. The EC is fixed for a given statistical threshold and a domain's dimensions, while the resels are estimated from the effective FWHM for a volume V:

$$Resels = V/FWHM^D. \tag{3.12}$$

However, while the FWHM is known for a smoothing kernel, if one was employed, the effective FWHM will often be different and dependent on location, for example, in fMRI images' data is smoother in the cortex than in the white matter. Therefore the FWHM has to be estimated, and this is based upon the spatial derivative of the normalised

least-squares residuals, $\dot{\boldsymbol{u}}$, calculated in the estimation procedure:

$$\widehat{FWHM} = (4\log 2)^{1/2} \left| \dot{\boldsymbol{u}}^\top \dot{\boldsymbol{u}} \right|^{-1/2D}, \tag{3.13}$$

and so given equations 3.12 and 3.13, the resels for the number of dimensions in the search region can be estimated:

$$\widehat{Resels}_D = \sum_{volume} \widehat{FWHM}^{-D} v, \tag{3.14}$$

for which the estimation is over all voxels in the search region and v is a single voxel's volume[197]. Although RFT is often likened to a Bonferroni correction for the number of resels, this must only be considered an analogy as this is not the process that is being undertaken, and in fact an exploration of this by Nichols and Hayasaka revealed that Bonferroni correction for the number of resels, termed resel Bonferroni, failed to control FWE in simulated images[198].

The assumptions underpinning RFT are that the error fields in the data are a reasonable lattice approximation of an underlying random field with a multivariate Gaussian distribution and that the fields are continuous. These assumptions can be broken if the data is not smooth or if the GLM was incorrectly specified. The issue of isotropy in random field is overcome by estimating the FWHM at each voxel separately[188;196;197].

3.1.3.4 Image processing

There are multiple image processing steps that can or should be applied to functional neuroimages prior to their use in SPM. Some of which are related to the spatial alignment of images, such as registration, segmentation and normalisation, which is crucial in fMRI, but typically not necessary for the stationary images in EIT, which are easily segmented by tetrahedron type. Other procedures include image interpolation and smoothing, which are both commonly employed in EIT, irrespective of the use of SPM.

In fMRI interpolation is necessary for spatial transformation, which is required for the spatial alignment of images, while for EIT image interpolation is required as the calculated conductivity changes are irregularly spaced in 2-D or 3-D space, such as in a FEM mesh. For 3-D data this procedure produces two key, simultaneous results, the first of which is the rendering of 3-D data onto a 2-D domain, known as rasterisation, which can either be the rasterisation of a subset of the 3-D data onto a single 2-D image or the rasterisation of the entire 3-D data onto a series of 2-D images spanning the z-axis of the domain. The second effect of the interpolation is to produce a uniform grid of data, which can either be up- or down-sampling, and although the prior cannot generate any further data the latter will result in the loss of data. By oversampling the data during interpolation a computational cost is paid for all subsequent analyses, but the loss of data is prevented,

and by generating smaller voxels it is more likely that the data conforms to a lattice representation, which is an assumption of RFT. Moreover, all interpolation techniques are effectively spatial smoothing, as the resultant voxels are a linear combination of the pre-interpolation local voxel values, and smoothing is also required for the assumptions of RFT to be met[199].

Image smoothing is applied in fMRI to facilitate the registration and spatial alignment of images and in the analysis of group data to counter anatomic and the functional variability between individuals. EIT images are inherently smooth due to the problem being underdetermined, but in all cases smoothing can be used to improve images' SNR[200;201]. Smoothing is achieved by convolution of a filter with the image data, so that at a given voxel is replaced with the average of its neighbouring voxels. As kernels are separable they can either have the same number of dimensions as the image or be 1-D and convolved against each dimension of the image separately. The Gaussian smoothing kernel is one of the most commonly used filters, which results in a smoothed voxel being the weighted average of its neighbours, with their contribution diminishing exponentially with distance from the voxel. A Gaussian function, $g(\boldsymbol{x})$, for a zero centred function is defined as:

$$g(\boldsymbol{x}) = \frac{1}{\sqrt{2\pi\sigma}} e^{-x^2/2\sigma^2}, \tag{3.15}$$

where σ is the standard deviation of the Gaussian function, which is related to the FWHM of the function:

$$FWHM = 2\sqrt{2\ln 2}\sigma. \tag{3.16}$$

While a Gaussian function falls off to plus/minus infinity, typically $g(\boldsymbol{x})$ is examined for an $\boldsymbol{x}$ of -3σ to 3σ as this contains 99.7 % of the function's area. Another important property of Gaussian functions is that the convolution of two Gaussian functions is still a Gaussian. The convolution of an image by two separate Gaussian functions is the same as convolving the image with a single Gaussian function whose FWHM is the square root the sum of the square of the two smaller Gaussian functions' FWHM[201;202].

Smoothing is crucial to the fulfilment of the assumptions of RFT, and these assumptions are only held if the kernel's FWHM is at least twice the size of the image voxels[201]. However, there are additional effects on the statistical inferences made in SPM due to the FWHM of the applied smoothing kernel. White et al. noted in sensorimotor SPM results that from clusters of small distinct activations being present with no filtering, the activations merged first into two activations, and then into one, progressively larger and less anatomically correct activations with smoothing kernels of 3, 6 and 12 mm[200]. In addition to ensuring the lattice approximation assumption of RFT, the larger the smoothing kernel, as determined from equation 3.14, the fewer the resels, and therefore a

FWE correction will be easier to meet. In a study of single-subject, fixed-effects analysis, Hopfinger et al. convolved images with 6, 10 and 14 mm Gaussian kernels and found that after correction for multiple comparisons, smoothing with kernels >10 mm produced the most sensitive results [199].

There are multiple disadvantages of smoothing, key among which are that smoothing reduces spatial resolution with increasing filter size, and, if a kernel is too large, functionally distinct regions may be blurred together [200]. One means of addressing this was posited by Skudlarski et al., which involved multi-filtering in which the SPM results from filtered and unfiltered data were combined and the advantages of smoothing coupled with the desired higher resolution of unfiltered images [203]. Additionally, filtering introduces a phase delay, yet this is overcome by zero-phase filtering in which the same data is filtered both forwards and backwards. Another disadvantage of filtering is that to ensure the same image volume is retained the domain is normally padded, for example with zeros. However, this means that when an image's voxels are smoothed with non-image zero voxels the edge of the image possess apparent hypoactivity, for which Maisog and Chmielowska suggested a correction [204].

In conclusion, the selection of the optimal smoothing kernel is based upon a trade-off between several factors. A kernel should be sufficiently large to fulfil the assumptions of RFT, to overlap functionally homologous activations and suppress intersubject variability, and larger kernels can make a p^{FWE} less difficult to achieve. Conversely, a kernel should be small enough to ensure activity can be assigned to the correct anatomical location and to leave functionally distinct regions separate, which is best ensured by having a kernel with a FWHM that is half the expected distant between the peak of activations. Another often promoted option in fMRI is that if the shape of an activation is known then a matched filter with the same width as the true spatial extent of activity will optimise SNR and is particularly effective in first-level analysis [199–202].

3.1.4 Purpose

The rationale of this study was to extend the analysis of the dataset collected by Gilad et al. study [90]. The dataset consisted of EIT images generated from impedance data collected in Sprague-Dawley rats during SEPs and VEPs. The individual images were in agreement with expectations; however, the analysis consisted of ensuring the control recordings matched expectations, comparison of the time of the peak conductivity change in the images and peak EP and analysis of the depth of the peak conductivity change. The latter analysis was limited due to depths being calculated from the top/vertex of the mesh, rather than normal to the cortical surface.

Therefore the purpose of this study was to evaluate whether significant impedance changes occurred across each of the stimulation groups and whether such changes ex-

hibited laminar spatio-temporal propagation that was comparable to the progression of activity reported in the literature. The questions addressed were:

(1) Are statistically significant, reproducible changes identifiable in the images of conductivity changes for each of the stimulation groups?

(2) Do the reconstructed conductivity changes exhibit laminar spatio-temporal propagation that is comparable to the neurophysiological literature?

(3) With respect to the data, image reconstruction, and statistical testing of the images, what are the study's limitations and how might they be addressed?

3.1.5 Experimental design

From the dataset collected by Gilad et al. study [90], all the 'active' recordings were considered for further analysis. This encompassed recordings with a current injection of 50 µA at 225 Hz, which was, in light of the findings of Oh et al., the optimal current injection parameters [64] and included all recordings irrespective of the phase of the injected current as Gilad et al. found no significant difference due to the phase of the injected current. Some alterations were made to the image preprocessing undertaken by Gilad et al. to better meet the assumptions of SPM and to facilitate easier analysis of translaminar propagation.

Statistical testing of fast neural conductivity images was undertaken with SPM with a one-way t-test, with second level analysis of images from the same simulation group both with uncorrected and FWE corrected p-values. In both situations the temporal dependency between images was corrected for with a Bonferroni correction. First-level analysis was deemed inappropriate as such analysis requires a canonical response function and given the novelty of the dataset under consideration this could not be readily derived. FWE corrected p-values to minimise false positive results, however this resulted in no significant results for images following hindpaw, whisker and visual stimulation and so uncorrected p-values were used to facilitate the other analyses of these data. In addition to the application of SPM, the spatio-temporal propagation of activity was assessed, first, by analysing the movement of the centre-of-mass over time. This first analysis was relatively difficult to interpret and uninformative, therefore a second analysis was undertaken by comparing the relative time to maximum conductivity change in a series of regions of interest (ROIs) throughout the imaging volume. The results of this analysis were then compared to the expected pattern of activation as determined from previously published neurophysiological results.

3.2 Methods

3.2.1 Selection of data cohort

38 recordings from 15 subjects were used in the present analysis, which included $n = 22/N = 8$ (recordings/rats) with forepaw stimulation, $n = 5/N = 2$ with hindpaw stimulation, $n = 6/N = 2$ with vibrissae stimulation, and $n = 5/N = 2$ with visual stimulation.

3.2.2 Image preprocessing

The imaging undertaken by Gilad et al. was altered given the preprocessing statistical and computational requirements of SPM, and with regard to the laminar nature of the neurophysiological signals. The latter meant that the image volume should consist of planes normal to the cortical surface, while the prior meant that the number of points used to generate the interpolant and the type and size of the smoothing kernel were altered.

3.2.2.1 Mesh rotation

A region in the FEM mesh, 6 mm × 4 mm, surrounding the electrodes was selected, which was the same region used by Gilad et al. [90]. However, only the centroids, C, of the overlying surface triangulation were taken:

$$C = \frac{1}{n+1} \sum_{i=1}^{n} \boldsymbol{v}_i, \tag{3.17}$$

where $\boldsymbol{v}_1, ..., \boldsymbol{v}_n$ are the vectors defining the vertices and n is the number of dimensions. To these centroids a plane was fitted using linear regression and the ordinary least squares solution (figure 3.6a). The normal vector of this surface was calculated and this vector's angle in each axis identified. The FEM mesh's vertices were then multiplied by a rotation matrix:

$$R_{xyz} = \begin{bmatrix} \cos\theta\cos\psi & -\cos\phi\sin\psi + \sin\phi\sin\theta\cos\psi & \sin\phi\sin\psi + \cos\phi\sin\theta\cos\psi \\ \cos\theta\sin\psi & \cos\phi\cos\psi + \sin\phi\sin\theta\sin\psi & -\sin\phi\cos\psi + \cos\phi\sin\theta\sin\psi \\ -\sin\theta & \sin\phi\cos\theta & \cos\phi\cos\theta \end{bmatrix}$$

where ϕ, θ and ψ are the Euler angles for x, y and z, respectively, so that the surface's normal vector only had a z component. In other words so that it was pointed vertically (figure 3.6b). The FEM mesh's vertices were then translated so that the vertex with the largest z component was equal to zero, which was done for ease of reference. The

image volume was defined preliminarily as those tetrahedra with centroids, as defined by equation 3.16, within the original 2-D region used to fit the plane and higher than −3 mm on the z-axis. This procedure was repeated for each of the four electrode position, one for each of the four stimulation groups, so that four image volumes resulted for each time bin.

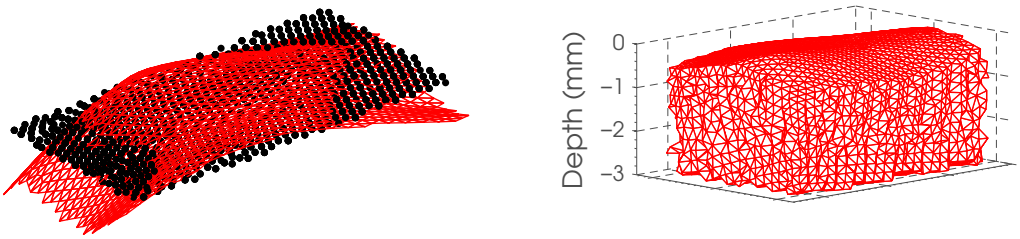

(a) *Ordinary least squares plane fitting* (●) *to triangulation mesh overlying image volume area.*

(b) *Rotated image volume.*

Figure 3.6: *Plane fitting and FEM mesh rotation, which was undertaken to allow for interpretation of translaminar activity.*

3.2.2.2 Image interpolation

The aim during the image interpolation was to interpolate the rotated image volume onto a sufficiently fine grid to prevent down-sampling and loss of data, but to do so without introducing unnecessary computational overhead for subsequent processing steps from excessive up-sampling. To achieve this, first, for each of the image volumes the shortest Euclidean distance between any pair of tetrahedral centroids was calculated (table 3.2).

Image Volume	Shortest Distance (µm)
Forepaw	51.0
Hindpaw	49.4
Whisker	49.6
Visual	48.0

Table 3.2: *Shortest Euclidean distance between tetrahedral centroids in each of the image volumes of the four cortical areas imaged.*

To ensure the data was not down-sampled during interpolation the interpolant was

calculated to result in voxels with an edge length, d, that ensured tetrahedra were at least separated by the distance between the opposing corner vertices of the voxels. Therefore d was calculated using Pythagorean theorem and the shortest distance between centroids, x:

$$\begin{aligned} d^2 &= x^2 + \sqrt{x^2 + x^2} \\ d &= \sqrt{x^2 + (\sqrt{2}x)^2} \\ d &= x/\sqrt{3}. \end{aligned}$$

So replacing x for the smallest value from table 3.2 resulted in $d = 27.7\,\mu\text{m}$, and so interpolation was calculated on a 3-D grid whose lattice points were spaced 25 µm apart in each axis.

The depth, from the FEM mesh's surface, of the resultant voxels was then defined. This was so that voxels deeper than 2.1 mm, a reasonable expected lower bound for layer VI based upon table 1.5b, could be removed before image smoothing or statistical analysis. For each voxel, $\boldsymbol{p}_i$, its depth was defined as the Euclidean distance between it and a specific surface triangulation centroid, $\hat{\boldsymbol{s}}$. The point $\hat{\boldsymbol{s}}$ was chosen by finding the surface triangulation centroid whose normal vector, $\hat{\boldsymbol{n}}_s$, had the smallest angle between it and the vector back toward it from the voxel, $\overrightarrow{\boldsymbol{p}_i\hat{\boldsymbol{s}}}$, which was achieved by minimising the l^2 norm between the cross product of these two vectors:

$$\hat{\boldsymbol{s}} = \arg\min_{\boldsymbol{s}} \left\| \hat{\boldsymbol{n}}_s \times \overrightarrow{\boldsymbol{p}_i\hat{\boldsymbol{s}}} \right\|_2 . \tag{3.18}$$

3.2.2.3 Image Smoothing

As detailed in section 3.1.3.4 the selection of the FWHM of a smoothing kernel is a complex trade-off. Given the novelty of the current work the selection of the kernel's FWHM was simply based upon the smallest expected extent of an activation, which based upon table 1.5b was chosen to be 150 µm, which also fulfils the requirement of RFT of a kernel being at least twice the voxel size. The data were filtered along each axis, both forwards and backwards, with a Gaussian function so as to be zero-phase filtering. Therefore given that the convolution of two separate Gaussian functions is the same as convolution with a single Gaussian function whose FWHM is the square root the sum of the square of the two smaller Gaussian functions' FWHM, the FWHM of the kernel was in fact:

$$
\begin{aligned}
FWHM_{large} &= \sqrt{FWHM_{small}^2 + FWHM_{small}^2} \\
FWHM_{small} &= 150\,\mu\text{m}/\sqrt{2} \\
FWHM_{small} &= 106.066\,\mu\text{m}
\end{aligned}
$$

and the Gaussian kernel extended from -3σ to 3σ. The same interpolation and smoothing were applied to each recording's respective gain correction simulation, using the same scaling procedure as undertaken by Gilad et al. [90].

The resultant smoothed image volumes were then converted to the NIfTI-1 file format that is used in the current version of the SPM software package, SPM8, and also the mean image across recordings was calculated for each of the four stimulation groups.

3.2.3 Statistical parametric mapping

Second level-analysis was performed, using SPM8, separately on each of the EIT images from the four stimulation groups. Separately at each time bin the image volumes were input into a one-sample t-test with implicit masking being selected, so that not-a-number (NaN) values were ignored in all calculations. This design resulted in a design matrix of 1s and so the estimated parameter, $\hat{\boldsymbol{\beta}}$, at each voxel was the mean of that voxel over all the recordings, and so $\mathcal{H}_0 : \hat{\boldsymbol{\beta}} = 0$.

The images were assessed for significant activations above zero with the construction of a t-map, first with p^{FWE}-values and then if this produced no significant results an uncorrected p-value was used. In both instances the p-value was set for $\alpha = 0.05$, giving a 95 % confidence interval (CI). However, this was adjusted using the Bonferroni correction for the repeated t-tests over multiple time bins. Therefore, given the effective temporal resolution of 8 ms and 21 timed bins separated by 2 ms in the SEP images, there were 5 independent tests corrected for so that the p-value was for $\alpha = 0.01$. For the VEP images, which were all separated by 15 ms and independent, correction was made for all 18 time bins so that the p-value was for $\alpha = 0.0028$. These temporally corrected p-values are hereafter denoted by the subscript $tcorr$. The connectivity of any resultant significant positive changes was then determined and those clusters whose number of voxels was less than 1 % of the total number of voxels in the image volume were assumed to be the peaks of subthreshold clusters and so were removed.

3.2.4 Further statistical analyses

After SPM had been employed to generate t-maps further analysis was done to examine the spatio-temporal propagation of activity within stimulation groups. Throughout these analyses the stimulus and time bin appropriate t-maps were used to mask the image volumes. This removed voxels whose changes were not significantly positive activations belonging to a cluster >1 % the total number of voxels in the respective image volume, which are referred to hereafter as masked images.

3.2.4.1 Whole image volume analysis

First, the mean conductivity change and centre-of-mass, $\boldsymbol{c}$, was calculated in each masked image, with the latter calculated as:

$$\boldsymbol{c} = \frac{\sum_{i=1}^{n} \sigma_i \boldsymbol{p}_i}{\sum_{i=1}^{n} \sigma_i}, \tag{3.19}$$

where $\sigma_i, ..., \sigma_n$ are masked image conductivity changes and $\boldsymbol{p}_i, ..., \boldsymbol{p}_n$ are the vectors describing the corresponding image volume Cartesian coordinates. The SEM of the mean conductivity change and centre-of-mass were also calculated. As a comparator to the mean conductivity change the time series of the maximum EP was also calculated. This was calculated by first, separately for each recording, finding the channel with the EP that had the maximum integral, then this was expressed as the mean and SEM across recordings.

In order to better examine the direction of any propagation of activity the change in each axis of the centre-of-mass was calculated. The change in the centre-of-mass was tested for significance with the non-parametric Wilcoxon signed-rank test, for a two-sided $\alpha = 0.05$. This test is preferable when a normal distribution cannot be assumed, and rather tests the null hypothesis that the median is a given value, which is typically zero. This is achieved by taking the absolute value of the sum of the signed ranks of the difference between a data series, $x_i, ..., x_n$, and the null hypothesis median:

$$w = \left| \sum_{i=1}^{n} [\mathrm{sgn}(x_i) \cdot r_i] \right| \tag{3.20}$$

where r_i is the ascending rank of the absolute difference between x_i and the null hypothesis median. The resultant w value is used to calculate a z-score and this compared to the appropriate $z_{critical}$ for the chosen α.

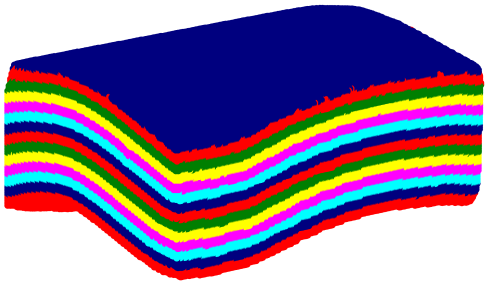

Figure 3.7: *The rotated image volume with each separate layer, as was used for* ROIs *definitions, shown in a different colour to its immediate neighbours.*

3.2.4.2 Region of interest analysis

Using the masked image conductivity changes the next analysis was to consider the data in the image volume in ROIs rather than en masse. This entailed assigning each voxel to a ROI based upon its Cartesian coordinates in the x- and y-axis, while for each voxel, $\boldsymbol{p}_i$, its z-axis location was defined as the Euclidean distance between it and a specific surface triangulation centroid, $\hat{\boldsymbol{s}}$, with this centroid chosen as already detailed in equation 3.18 (figure 3.7). Each ROI was 500 µm × 500 µm × 150 µm in the x-, y- and z-axis respectively, in order to approximate the dimensions of a cortical column and the thinnest expected neocortical lamina. This resulted in 12 divisions in the x-axis, 8 in the y-axis, and 14 in the z-axis.

The data from the ROIs were then considered with respect to the z-axis, that is each column of data from a single division in the x- and y-axis was consider as an ensemble and differences between the layers assessed. The latency to peak conductivity change in each layer within a given column was determined and normalised to the latency to peak of the bottom-most ROI with valid data, which was achieved by subtracting the bottom-most ROI's latency to peak from the latency of all the ROIs within the column of data. Some ROIs did not have significant data due to the use of the masked images.

Following this the data were assessed for significant differences between latencies to peak across layers by means of a one-way ANOVA. The $\mathcal{H}_0$ of this test was that the mean latency to peak, across recordings for a given stimulus, given its variability across recordings was not significantly different to the mean latency to peak of one of the other 13 layers, which was tested for $\alpha = 0.05$. In the ANOVA the bottom-most consecutive sequence of zeros within a column of ROIs, that is those that were the result of the normalisation, were masked with NaN values and so removed from the ANOVA.

Using the data from columns that had significantly different latency to peak values, as determined by ANOVA, multilinear regression was performed in order to determine if

a trend in the latency to peak values across the layers was present. The regression was not performed if ≥40 % of the column's data were NaN values, as would occur due to the masking of the image volume. The regression was 2$^{\text{nd}}$-order and solved using the ordinary least squares solution, and the significance probability of the regression determined using an F-test with $\alpha = 0.01$. Of those fits that were significant multiple characteristics were considered: their distribution, the sign of the parameter that was the coefficient of the squared term, as it indicates if the fit is upward or downward facing, and the value of the fit at the top-most layer, as a reflection of the difference in latencies across a column.

3.3 Results

3.3.1 Statistical parametric mapping

Visual assessment of the mean of the conductivity change images for the forepaw recordings revealed that the onset of conductivity changes was at 2 to 4 ms, appeared to peak around 10 ms and diminished over the remaining imaging time. The conductivity changes at depths less than approximately 1 mm were greater than those beneath this depth (figure 3.8). Using p^{FWE}_{tcorr}-values the forepaw recordings were found to be highly significant across the image volume. There were no significant areas in the image volume at 0 ms, which was the time of stimulation, while there was at all other time points. The image volume had the largest volume of significance at approximately 10 to 26 ms, which was trapezoidal in shape, with a larger volume at a depth of approximately 2 to 1.4 mm, above which the edges lacked significance. Prior to and following this period the volume of significance was more cylindrical in shape, however at depths less than approximately 1 mm the edges also lacked significance (figure 3.9). For the other three groups of recordings the use of p^{FWE}_{tcorr}-values did not reveal significant positive activations belonging to a cluster of sufficient volume and so p_{tcorr}-values were employed.

While in the mean of the conductivity change images for the forepaw recordings changes occurred clearly across the imaging volume in all three axes, for the hindpaw recordings the changes were confined to the anterior 30 to 50 % of the image and were of a lower amplitude. From qualitative assessment, the SNR of the changes were also poorer with negative changes visible in the more superficial images (figure 3.10). Using p_{tcorr}-values the hindpaw volume was sporadically significant at 0 to 4 ms, 18 to 22 ms, and at 30 and 48 ms, while at other time bins there were no significant activations. The volumes of significance at these times was comparatively small and variable and irregular in shape (figure 3.11).

The mean of the conductivity change images for the whisker recordings showed the onset of conductivity changes was at 2 ms and this peaked around 6 to 10 ms and diminished by approximately 16 ms to an above zero level that persisted over the remaining

imaging time. The changes were, from visual inspection, largest and comparable at depths of 0.7 to 1.4 mm (figure 3.12). Using p_{tcorr}-values the whisker imaging volume was highly significant at all time points, including at the time of stimulation at 0 ms. The volume of significance progressed through five stages during the imaging time. Initially, at 0 to 4 ms, the volume was a large trapezoidal shape located toward the anterior of the imaging volume, then, at 4 to 12 ms, reduced in volume becoming more cylindrical and located closer to the centre of the imaging volume. After this, at 12 to 20 ms, the volume of significance expanded and was again centred towards the anterior of the image volume. Subsequently, at 20 to 30 ms, the volume of significance reduced in size and centralised within the imaging volume, until at 30 to 40 ms the volume began to segment into a less smooth shape (figure 3.13).

In the mean of the conductivity change images for the visual recordings the onset of conductivity changes was at 45 to 60 ms. The activity had a gradual increase and decrease, of seemingly equally rate, around a peak conductivity change at 105 to 150 ms, with the decrease after this peak reaching its minima at 225 to 240 ms. The volume of the conductivity change were, from visual inspection, comparable at depths of 0.9 to 2 mm, with several small areas of negative change occurring at the edges of the image volume superficial to this (figure 3.14). Using p_{tcorr}-values the visual recordings' imaging volume was significant in a time window of 90 to 210 ms, either side of which there were no significant areas within the image volume. The volume of significant changes started as a volume larger at its base and centred toward the posterior of the image and then expanded at 105 ms. Subsequently, at 120 to 135 ms, the activity compressed and reoriented to be along posterolateral-anterolateral line, after which, at 165 to 190 ms the volume expanded back towards its origin in the posterior of the volume and toward the anterior of the volume, and finally, at 210 ms, began to segment into a less smooth shape (figure 3.15).

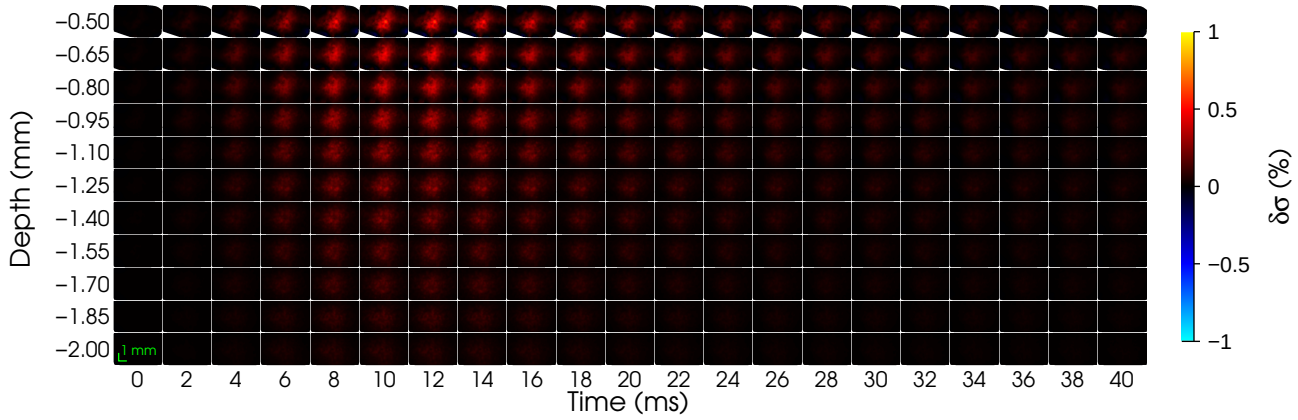

Figure 3.8: *Mean of forepaw images of percentage conductivity change: posterior-anterior and medial-lateral in the x and y axes.*

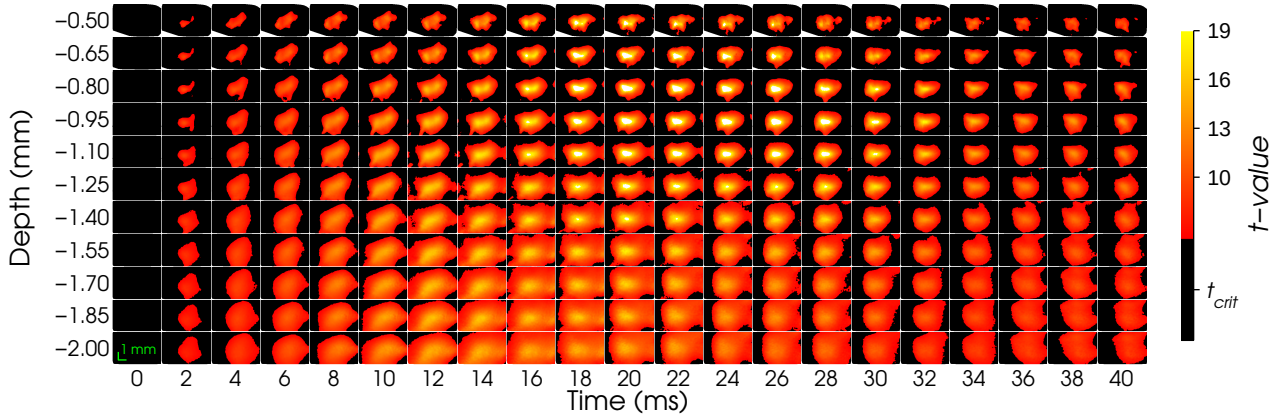

Figure 3.9: *One-sample t-test SPMs of forepaw images, $p_{tcorr}^{FWE} = 0.05$ critical value was 6.22. Non-significant changes are black.*

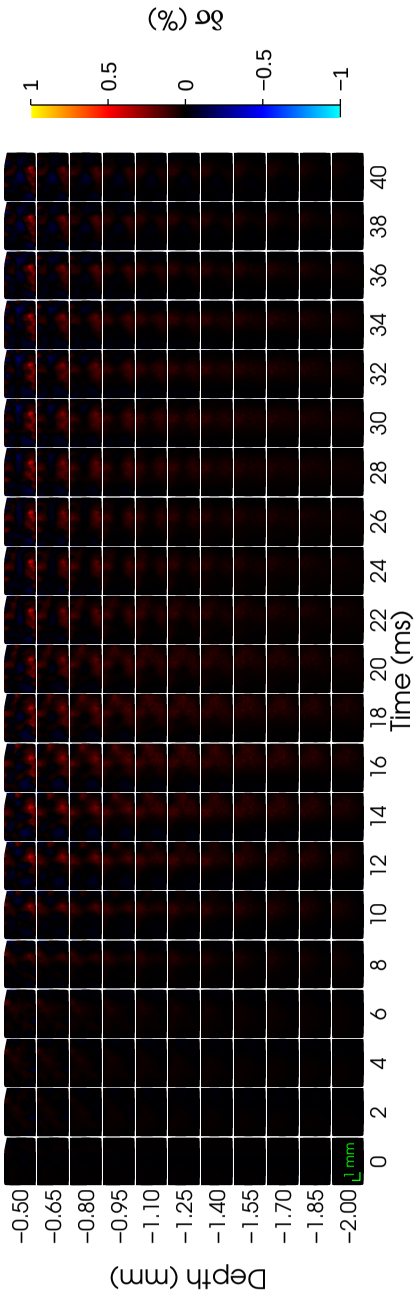

Figure 3.10: *Mean of hindpaw images of percentage conductivity change.*

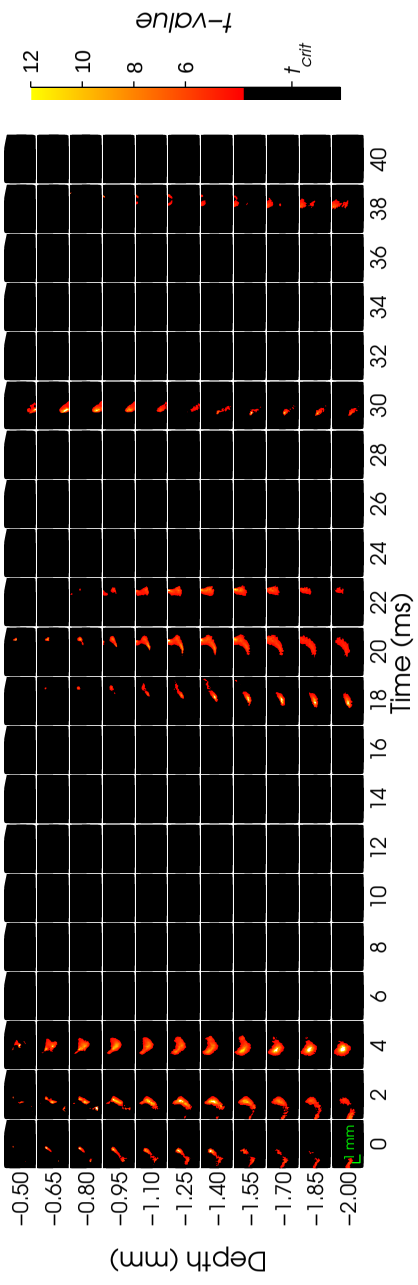

Figure 3.11: *One-sample t-test SPMs of hindpaw images, $p_{tcorr} = 0.05$ critical value was 3.75. Non-significant changes are black.*

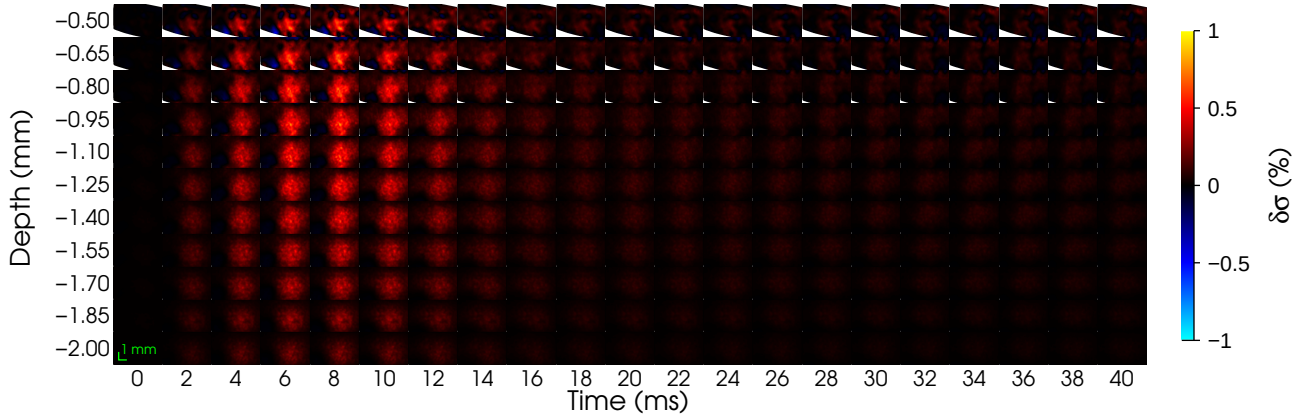

Figure 3.12: *Mean of whisker images of percentage conductivity change.*

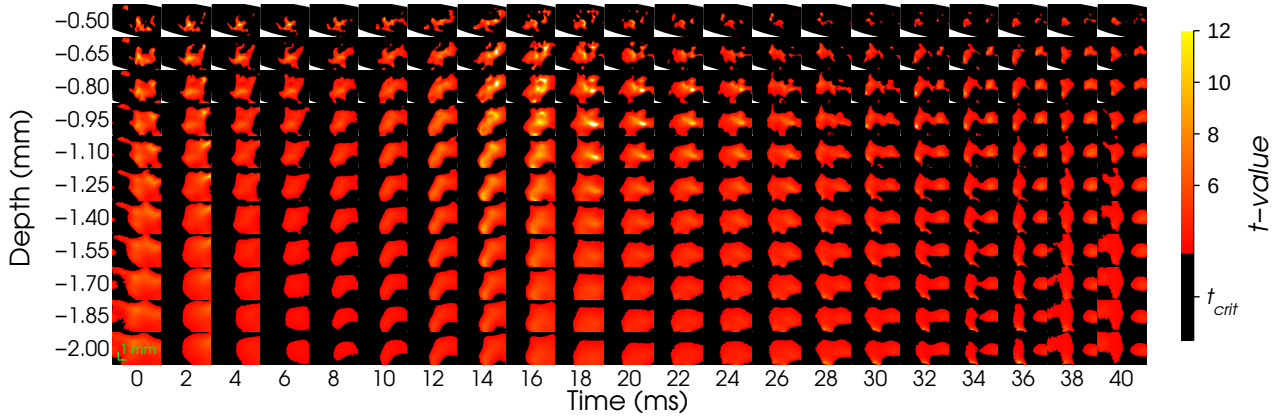

Figure 3.13: *One-sample t-test SPMs of whisker images,* $p_{tcorr} = 0.05$ *critical value was 3.35. Non-significant changes are black.*

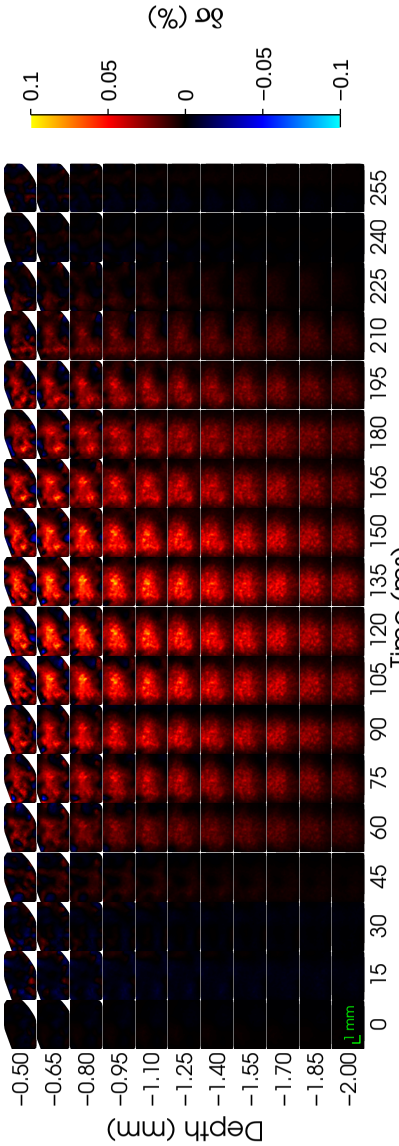

Figure 3.14: *Mean of visual images of percentage conductivity change.*

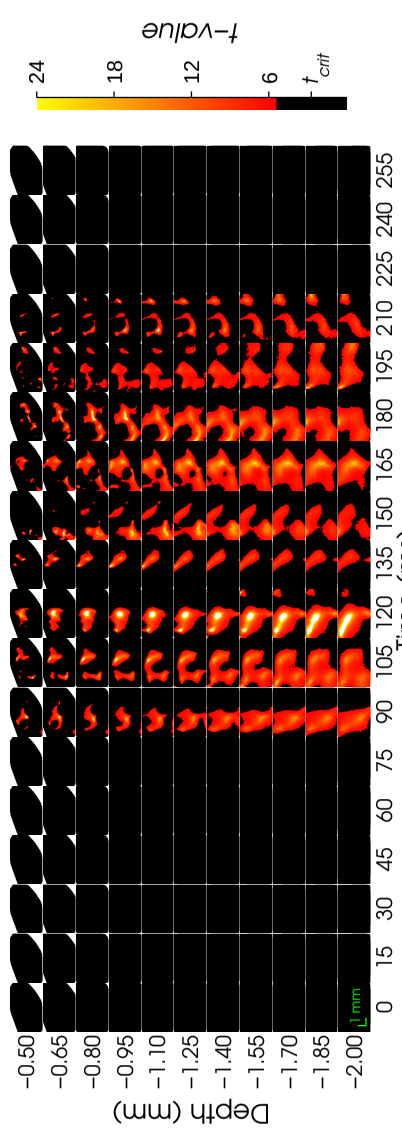

Figure 3.15: *One-sample t-test SPMs of visual images, $p_{tcorr} = 0.05$ critical value was 5.43. Non-significant changes are black.*

3.3.2 Whole image volume analysis

As a result of very little of the hindpaw image volume having significant changes the whole image volume analysis of the masked image volumes was only possible at a few time points and so was somewhat nonsensical. Similarly, only nine of the 18 time points for the visual SPMs had significant changes and this resulted in interpretation of the results being limited. As a result the decision was made to modify this part of the analysis and perform it on the non-masked image volume in addition to the masked image volume.

The masked forepaw conductivity changes were comparable in time course to those of the unmasked changes, but the amplitude of the changes were larger. The masked time series had no significant changes at 0 ms, with the first significant time bin being at 2 ms and having a mean conductivity change of 0.019 ± 0.002 % (mean±SEM). The mean conductivity increased until 10 ms when it reached 0.091 ± 0.006 %, after which it decreased rapidly to 0.042 ± 0.002 % at 20 ms and then decreased less rapidly so that by 40 ms it was 0.022 ± 0.001 %. The maximum EP was similar to the mean conductivity changes, but delayed by approximately 2 ms: the EP started to increase rapidly at 4 to 6 ms and reached its maximum of 0.600 ± 0.031 mV at 12 ms, this plateaued until 20 to 22 ms, decreased rapidly until 32 to 36 ms, at which point it plateaued again so that at 40 ms it was 0.336 ± 0.026 mV (figure 3.17a).

The mean of the unmasked hindpaw conductivity changes at 0 ms was 0.001 ± 0.001 %, and this increased so that at 16 ms it reached its maximum of 0.020 ± 0.005 %. This decreased to 0.011 ± 0.003 % at 24 ms, had an increase until 28 ms where it reached 0.013 ± 0.004 %, after which it continued to decrease so that at 40 ms the mean conductivity change was 0.004 ± 0.001 %. The maximum EP gradually increased from -0.022 ± 0.005 mV, at 0 ms, to 0.052 ± 0.007 mV, at 8 ms, after which it more rapidly increased to its maximum of 0.630 ± 0.080 mV, at 16 ms. This then plateaued until 26 ms, decreased rapidly until 36 to 38 ms, at which point it plateaued again so that at 40 ms it was 0.307 ± 0.050 mV (figure 3.17b).

The mean of the unmasked whisker conductivity changes at 0 ms was 0.013 ± 0.001 %, and this increased so that at 8 ms it reached its maximum of 0.089 ± 0.019 %. This decreased rapidly to 0.030 ± 0.006 % at 16 ms, and then decreased less rapidly so that by 40 ms it was 0.014 ± 0.003 %. The maximum EP at 0 ms was 0.058 ± 0.061 mV, had a small decrease to 0.002 ± 0.006 mV at 2 ms and then rapidly increased to 0.377 ± 0.056 mV at 6 ms. After this first peak there was a decrease to 0.262 ± 0.033 mV at 10 ms, which then, less rapidly than for the first peak, increased to 0.402 ± 0.025 mV at 18 ms, with a subsequent gradual decrease so that at 40 ms it was 0.202 ± 0.027 mV (figure 3.17c).

The mean of the unmasked visual conductivity changes at 0 ms was -0.0010 ± 0.0002 %, and, excluding a small decrease to -0.0020 ± 0.0003 % at 15 ms, gradually increased to its maximum of 0.014 ± 0.002 % at 135 ms. This then

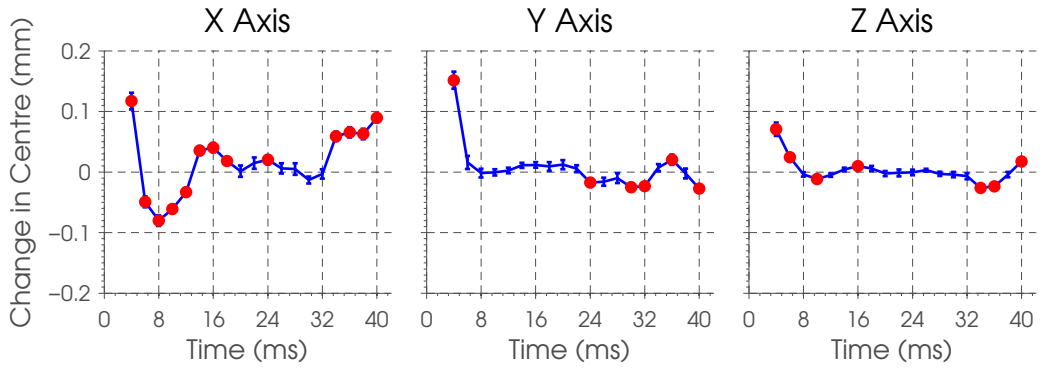

Figure 3.16: *The mean and SEM (blue line: —) of the change in the centre-of-mass for masked forepaw recordings. Significant changes are denoted with a red ○ marker*

gradually decreased to nearly zero, being $-0.0004 \pm 0.0003\,\%$ at 240 ms, and similarly small values at 255 ms. The maximum EP was similar to the mean conductivity changes: the EP at 0 ms was 0.002 ± 0.007 mV and started to increase gradually at 15 to 30 ms, reached its maximum of 0.418 ± 0.044 mV at 120 ms, then gradually decreased so that at 255 ms it was approaching zero, being 0.059 ± 0.011 mV (figure 3.17d).

For the masked forepaw image volume, in the first 4 ms the centre-of-mass significantly moved anteriorly, laterally, and superficially, by 0.117 ± 0.014, 0.152 ± 0.014 and 0.071 ± 0.011 mm. In the following 6 ms the centre-of-mass significantly moved posteriorly, but by less than in the first 4 ms. At 14, 16, 18 and 24 ms there were significant shifts of the centre-of-mass anteriorly, and larger significant anterior shifts at 34, 36, 38 and 40 ms. At 6 ms the centre-of-mass significantly moved superficially, and at 10 and 16 ms had small significant shifts deeper and superficially, respectively. At 34 and 36 ms there were small significant shifts of the centre-of-mass deeper and a small significant superficial shift at 40 ms. There were significant medial shifts of the centre-of-mass at 24, 30 and 32 ms, and small significant lateral and medial shifts of the centre-of-mass at 36 and 40 ms (figure 3.16). For the other three stimulation groups none of the shifts, in any dimension, of the centre-of-mass in the unmasked image volumes were significant.

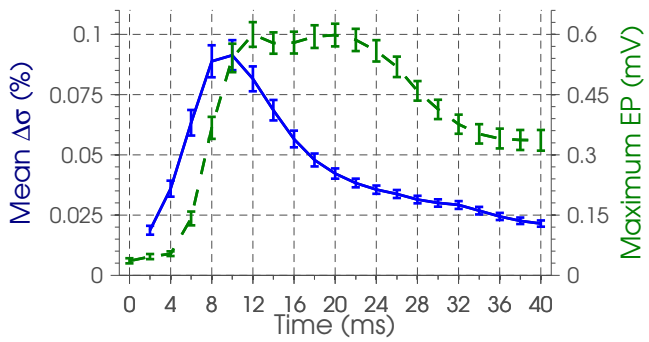

(a) *Masked mean conductivity changes and mean of maximum EPs for forepaw recordings'*

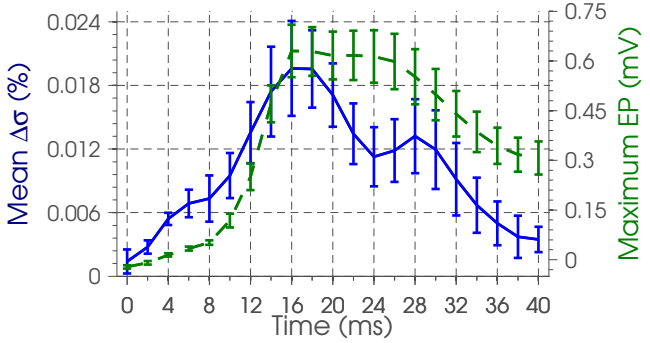

(b) *Non-masked mean conductivity changes and mean of maximum EPs for hindpaw recordings'*

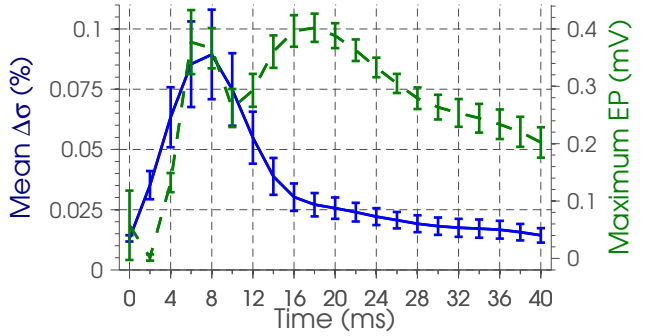

(c) *Non-masked mean conductivity changes and mean of maximum EPs for whisker recordings'*

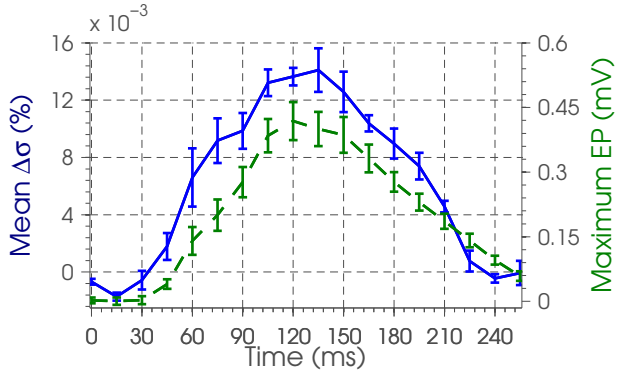

(d) *Non-masked mean conductivity changes and mean of maximum EPs for visual recordings'*

Figure 3.17: *The mean conductivity changes ($\Delta\sigma$), as mean and SEM across recordings (blue: —) on the leftmost y-axis, and the maximum EPs, as mean and SEM across recordings (green: – – –) on the rightmost y-axis.*

3.3.3 Region of interest analysis

The ROI analysis of the forepaw data resulted in 49 of 96 columns of ROIs having significantly different peak latencies across their respective layers. The columns that were significant were largely focused in a strip at the posterior of the image volume, and two regions at the anterior of the image volume in the lateral and medial corners (figure 3.18a). Of the 49 columns with significantly different peak latencies across their respective layers, five were excluded for having too many NaN values, and two for not having a significantly probable regression, which resulted in 42 columns being fitted. Of the 42 acceptable fits 5 were downward facing and were at the edge of the imaging domain, while the remainder were upward facing (figure 3.18b). In contrast the peak latency of the uppermost layer was only a negative time, -2.54 and -4.23 ms, for 2 columns at the lateral edge of the image volume, while the remainder were positive with a wide range of latencies, 1.63 to 50.60 ms. The mean of the fits had a latency of 6.97 ms (figure 3.18d), but the columns' latencies had a grouping into those with a latency of 0 to 15 ms, which totalled 12 of the columns, and those with a peak latency >15 ms, which totalled 28 of the columns, with the latter being found in the lateral aspect and anteromedial corner of the image volume (figure 3.18c).

The ROI analysis of the hindpaw, vibrissae, and visual recordings' image volume using an unmasked image volume resulted in only 4, 2 and 3 viable columns of data, respectively, while with masked image volumes the numbers were greater and so only the latter are detailed here. For the hindpaw recordings' image volume 64 of the 96 columns were excluded due to the masking, and of the remaining 32 columns, 15 were significant as determined by ANOVA. The significant results from the ANOVA were clustered in the centre of the image volume. The regression had one column excluded for having too many NaN values, while the remaining significant regressions were a spatially heterogeneous mixture of upward and downward fits, with 7 columns of both. Only one column had a peak latency in the uppermost layer that was positive, being 2.55 ms, while the remainder were negative over a large range of -1.56 to 40.40 ms, with most having a latency of -15 to -20 ms, and the mean of the fits had a latency of -21.55 ms.

For the vibrissae recordings' image volume 6 of the 96 columns were excluded due to the masking, and of the remaining 90 columns, 25 were significant as determined by ANOVA. The columns that were significant in the ANOVA were located along the lateral aspect and anteromedial corner of the image volume. The regression had one column excluded for having too many NaN values, and 4 columns for not having a significantly probable regression which resulted in 20 columns being fitted, 5 of which had upward facing fits. The latency to peak of 6 of the uppermost layers was positive with a range of 1.18 to 17.93 ms, while the remaining columns had a negative latency to peak in the uppermost layers with their range being 0.42 to 65.76 ms. The columns with a latency

greater than −23 ms were focused in the posterolateral corner of the image volume. The mean of the fits had a latency of −12.53 ms.

The ROI analysis of the visual recordings' image volume resulted in 11 of the 96 columns being excluded due to the masking, with 28 of the remaining 85 columns found to be significant with ANOVA. The significant results of the ANOVA were largely focused in a region in the posteromedial aspect of the image volume. The regression had one column excluded for having too many NaN values, and 4 columns for not having a significantly probable regression which resulted in 24 columns being fitted, 4 of which had downward facing fits. There were 4 columns that had a peak latency in the uppermost layer that was negative, which were over a range of −29.52 to −47.59 ms, while the remainder were positive, ranging over 35.61 to 237.76 ms, and were fairly heterogeneous in their spatial distribution. The mean of the fits had a latency of 67.6 ms.

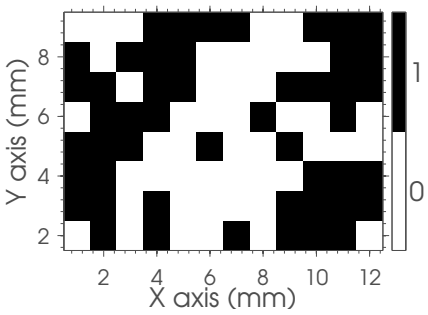

(a) *ANOVA of image volume. Black indicates a significant column and white non-significant.*

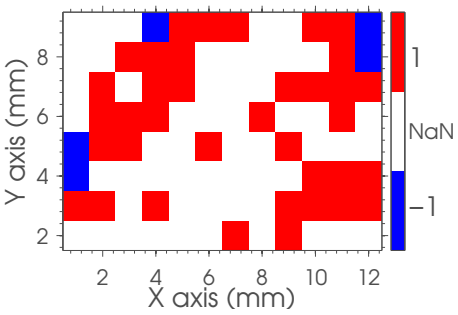

(b) *Sign of fits image volume. Red indicates upward fits, blue downward, and white excluded columns.*

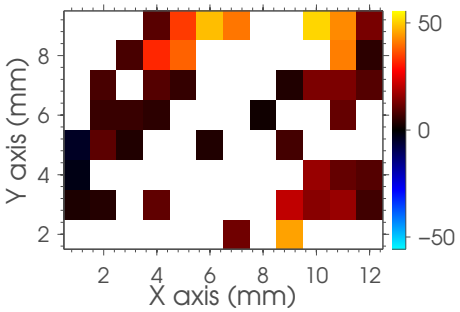

(c) *Latency to peak, in milliseconds, of top ROI of image volume.*

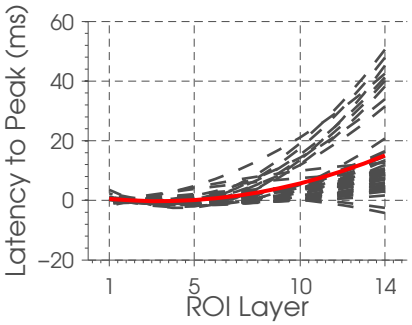

(d) *Second-order regressions (grey line: – – –) and mean regression (red line: —) of image volume. ROI layer is from deep (1) to superficial (14)*

Figure 3.18: *The ROI analysis for the forepaw recordings' image volume.*

3.4 Discussion

3.4.1 Summary of results

The mean conductivity change images showed physiologically reasonable results matching the literature for all of the stimulation groups except the hindpaw stimulus group. Using p_{tcorr}^{FWE} values only the forepaw recordings' SPMs had significant results, with p_{tcorr} values having to be used for the other 3 stimulation groups. The forepaw recordings' SPMs had a highly significant volume at all time points except 0 ms, the vibrissae recordings' SPMs at all time points, the visual at 90 to 210 ms with a compression phase between 135 to 150 ms, and the hindpaw SPMs a small volume of significance in 8 time bins.

The ROI analysis of the forepaw recordings matched the expectation of a propagation of activity from layer IV, into the infragranular layers (layers V and VI) and finally into the supragranular layers (layers II and III), but this propagation had a longer than expected latency for some columns. The ROI analysis for the vibrissae and hindpaw data sets was fairly inconclusive with few significant columns and no clear trend of laminar propagation. The ROI analysis of the visual recordings matched the expectation of activity occurring much later in layer VI than the other layers, but the analysis had few significant columns and had a longer latency than expected for several columns.

3.4.2 Assessment of results' statistical significance

That the forepaw recordings were significant following both FWE and time correction indicates a high level of reproducibility in the results. These results are unlikely to be false positives given that, first, corrections were made for the multiple comparisons, but also that no significant results occurred in the first time bin. However, the presence of significant results in the second time bin, at 2 ms, is not wholly in accordance with expectations from the physiology, as it is too early for activity to have reached the neocortex, but might be explained as a result of the temporal smoothing that is present due to the ± 125 Hz bandwidth. The depth of the significant conductivity changes also is broadly in agreement with expectations from the literature: the tapering near the surface matches the expectation of little to no activity in layer I, with the bulk of the significant conductivity change being at a depth of 1 to 2 mm matching the area approximating layers IV to VI.

While the SPMs cast doubt over the hindpaw recordings' images, visual inspection of the mean of the conductivity change images indicates that the results are questionable, and so discussion of these results here is limited. In contrast, the mean of the vibrissae recordings' images has the largest conductivity changes of the four stimulation groups, which matches the reported findings for SEPs, with vibrissae EPs being reported to have the largest amplitude of the four types of stimulation considered in this study. Despite

this, the data did not pass FWE correction. The resultant, only temporally corrected, SPMs show a large volume of significance in all time bins, with the volume at the time of stimulation perhaps being largest. It seems likely that false positives are a key contributor to these results. However, the effect of the temporal smoothing due to the bandwidth would be expected to be most pronounced in these results as the vibrissae cortical response is much more rapid in onset and spread than for the other three stimulation paradigms. As with the forepaw data it is encouraging that the volume of significance tapered towards the surface as it matches the expectation of little to no activity in layer I. It is intriguing that there is an apparent reduction-expansion-reduction sequence in the volume of significance, which might warrant consideration and comparison to propagating waves of activity. However, the reduction at 6 to 8 ms might simply reflect increased variability in the conductivity change and therefore lower significance, as this matches the peak conductivity change. Similarly, the conductivity change images do not show such a reduction in volume, the SPMs sequence is not comparable to reported propagating waves in PMBSF, and such reported waves are noted for their variability, a consequence of which means they are lost with averaging, such as was performed to collect the data currently under consideration.

The visual recordings' mean image had the smallest conductivity changes, but they were consistent across depth and clearly visible. From visual inspection of the mean images, the change is considerably later than that reported in the literature, by 15 to 30 ms. Similarly, the first time bin with significant changes was much later than expected from prior reported studies. Both of these might reflect the fact that in this study old albino rats were used in whose retina light would scatter considerably. Also that bilateral photic stimulation was used and given the abnormal decussation of fibres in albinos' the complex interaction of ipsilateral and contralateral signals is possibly responsible for this result. As with the whisker SPMs, it is intriguing to consider the presence of a reduction-expansion-reduction sequence as indicative of spreading wave-like activity. However, while this is more probable for VEPs as they are more reproducible, the orientation of the compression is incorrect by approximately 45°, and similarly the reflected wave is erroneously angled, as compared to reports of spreading waves of activity. Nonetheless, the time of the expansion of the statistical volume at approximately 90 ms matches the reported timing of 100 ms and the compression approximately 45 ms later is not too dissimilar from the reported time of compression of 72 ms[163], but any further claims beyond such comparisons seem ungrounded as these are SPMs and the sequence is not overtly evident in the conductivity images.

3.4.3 Assessment of results' spatio-temporal propagation

The time series of the forepaw recordings' masked mean conductivity changes show the volumes to have a mean conductivity increase of <0.1 %, which is in agreement with, if slightly smaller than, other cortical conductivity measurements. In addition to this the latency to peak is approximately 10 ms, which is also comparable to the reported time by which the entirety of the neocortical lamina are activated [126;128]. The conductivity change peaks somewhat earlier than the maximum F-SEP which matches the expectation from first principles, as the EP is an epiphenomenon of the underlying neuronal activity. There is a reported difference between EPs' onset and peak latency and that of the underlying neuronal activity: CSDA indicates the initiation of activity in layer IV is 2 to 3.6 ms prior to the P1-N1 latency to peak [125;126;128]. Additionally, the mean conductivity change started to return to baseline while the EP was still plateaued at its maximum. This may reflect that the bulk neuronal activity is more transient than the extracellular potentials that result in EPs. However, the morphology of the F-SEP is peculiar and dissimilar to the reported morphology, as it appears as though N1 is absent with a fusion of the two positive peaks. This is unlikely to be the result of the anaesthetic regime as comparable regimes were used in many of the studies reviewed in section 1.8. While the EPs were only meant as a comparator its abnormality does raise uncertainties about the experiment, data acquisition or data processing, as one of these is the probable source of this morphological abnormality.

The results examining the shift in the centre-of-mass over time are somewhat ambiguous and difficult to interpret, which, coupled with the fact that only for the forepaw recordings were significant shifts present, suggests that such a coarse approach is not appropriate to assess the spatio-temporal propagation of activity. This is unsurprising given that the approach attempts to simplify a vast volume of data to a single point. Hence, more consideration is given to the compartmentalised approach of the ROI analysis. The ROI analysis of the forepaw recordings has aspects implying the accurate measurement of spatio-temporal propagation, but also these are coupled with several limitations and uncertainties. The expectation was of activity ascending through the laminae and reaching the uppermost layers in approximately 5 to 6 ms [126;128]. Certainly, only a few of the regressions were downward facing and only two reached the uppermost layers in a negative time, and additionally the average time to reach the uppermost layers was 6.97 ms. However, the expectation would have been for the most central columns to be significant, but in fact the opposite was true. Additionally multiple columns had much longer latencies to peak for the uppermost layers, up to 50.60 ms, which were on the lateral aspect of the image volume. These results do not match any previously reported propagation of activity, and so the validity of these results, and consequently the results in accordance with the literature, cannot be wholly trusted.

The time series of the hindpaw recordings' unmasked mean conductivity changes show the volumes to have a mean conductivity increase of <0.02 %, which is substantially smaller than the expected changes, but understandable given the small volume of conductivity changes. Nonetheless the latency to peak is approximately 16 ms, which is comparable to the reported time by which layers II to V, the initial site of activity, are activated [129]. Comparable to the forepaw recordings' results, the conductivity change starts to diminish whilst the H-SEP is plateaued at is maximum. Also comparable to the forepaw recordings' results, the morphology of the H-SEP is similarly perturbed and lacking a N1 component. The ROI analysis of the hindpaw recordings was less encouraging than that of the forepaw results: the expectation was of activity reaching layer VI last and therefore the regression, normalised to changes in this layer, should be upward facing and reaching the uppermost layers after approximately 4 ms [129]. In contrast the hindpaw results were a mix of upward and downward facing, and the latency to reach the uppermost layers was much longer than expected. Results such as this are unsurprising given the low quality of the mean conductivity change images for the hindpaw recordings, and suggest that they should be disregarded as nonsensical.

The time series of the vibrissae recordings' unmasked mean conductivity changes show the volumes to have a mean conductivity increase of <0.1 %, which is comparable to the change measured in the forepaw recordings and as with those recordings is comparable with other reported conductivity measurements. In addition to this the latency to peak was approximately 8 ms, which is also comparable to the latency to peak of P1 and of the activity in layers IV and V [53;54;110;138;140;146;149]. Unlike for the forepaw and hindpaw recordings the vibrissae activity was well synchronised with the peak of the V-SEP. Moreover, the morphology of the V-SEP was more comparable to the reported morphology of this waveform as there is a positive-'negative'-positive sequence; however, the 'negative' section is merely a reduction and not a negative component. In addition to this, while the P1 component has a latency matching the reported P1 latency, both the N1 and P2 components are significantly earlier than expected from the literature: N1 is reported to have a latency of 16 to 30 ms and P2 a latency of 32 ms, while in the current data set they were 10 ms and 18 ms, respectively [121;144;146]. The ROI analysis of the vibrissae recordings, as with the hindpaw recordings' analysis, was underwhelming. The significant ANOVA results were not clustered and were located in the periphery of the image volume. Regarding the regression, the expectation was again of activity reaching layer VI last and therefore the regression, normalised to changes in this layer, should be upward facing and reaching the uppermost layers after approximately 0.8 ms [53;54;110;138;140;149]. In contrast the vibrissae results were largely downward facing and the latency to reach the uppermost layers was typically negative. The fact that the spatio-temporal propagation could not be discerned is unsurprising given that the entirety of the cortical columns are engaged

in <5 ms, significantly less than the 8 ms temporal smoothing from the bandwidth, and, unlike for the forepaw activity, this propagation is not a sequence up or down the laminae but a complex engagement of different non-contiguous laminae, which would be expected to further compound spatiotemporal smoothing.

The time series of the visual recordings' unmasked mean conductivity changes show the volume to have a maximum mean conductivity increase of <0.015 %, which is a tenth of that measured in the forepaw and vibrissae recordings, which can be understood from the fact that only around 50 % of V1 is flash stimulus responsive[153]. The latency to peak was approximately 120 ms, later than the reported timing of even N2[158], but as already detailed this might be explained by considering the choice of an albino strain and the bilateral nature of the stimulus. As with the other recordings the morphology of the VEPs does not match the reported morphology as it only consists of a single large positive component. The ROI analysis of the visual data, as with the forepaw and vibrissae data, had the significant ANOVA results located in the periphery of the image volume and not clustered as would be expected. Regarding the regression, the expectation was again of activity reaching layer VI last and therefore the regression being upward facing and reaching the uppermost layers after approximately 37 ms[112;160;161]. The visual results were largely upward facing and the latency to reach the uppermost layer was typically positive, but while the mean of the fits gave a the latency to reach the uppermost layers of 67.6 ms, which is reasonably comparable to expectations, again, as with the forepaw data, this is marred by some results having much longer latencies, upto 238 ms. There are complex feed-forward and feedback connections in the visual cortex, but none would support such long normalised latencies to peak.

3.4.4 Study limitations

The possible reasons for only the forepaw recordings' SPMs being significant with FWE and temporal correction are that the other three data sets did not have significant changes or that the correct statistics were not chosen. It is apparent that the former is the most probable reason the hindpaw recordings' SPMs were not significant, but the vibrissae and visual recordings appeared to have consistent conductivity changes and an explanation for their failure to have significance following FWE correction is that the number of recordings were insufficient for the probability distribution to be reasonably applied. Another limitation of the experimental paradigm is the fact that the visual stimulus was bilateral, which, although not an inherent limitation, given the lack of a cross-validation technique makes interpretation of the results unnecessarily complex.

With regard to the imaging aspect of the study the employed mesh was visibly non-anatomical, as it had a high level of asymmetry along the sagittal axis, in addition to which the mesh was not validated with a higher resolution mesh, which is the standard

means of validating FEM meshes[187]. Another limitation of the imaging aspect of the study is that the electrodes were assumed to have been in the same location for each of the four stimulation paradigms and a single mesh used for all subjects. In addition to this, the gain simulation for each recording, while compensating for the effect of boundary voltage rejection, relies upon an assumption of the volume and conductivity change that occurs, neither of which can be known for certain. Similarly, the choice of simulating a perturbation at a depth of 1.4 mm does not appear to have a physiological basis. To fulfil the requirements of SPM it would be sufficient, and have fewer assumptions, to employ proportional scaling or global normalisation.

In assessing the data several limitations are apparent: the non-objective and fixed choice of 50 singular values as the truncation level for tSVD is non-optimal. This is because this can only be made if the reconstructed change is known. The novel nature of the data considered in this study prevents this approach from being appropriate, and casts doubt over the conclusions that can be made regarding the images and the translaminar propagation of activity. The temporal smoothing effect of the 250 Hz bandwidth also makes the interpretation of the spatio-temporal propagation of activity difficult as the bandwidth has a smoothing effect over 8 ms while translaminar propagation of activity typically occurs in the time scale of 1 to 2 ms. Moreover, the lack of comparator measurements makes it difficult to ascertain the nature of some aspects of the results, such as the abnormality of the EPs morphology and the longer latency propagation of activity in the forepaw recordings' ROI analysis, which might have been found to be physiological. The spatio-temporal propagation analysis had some limitations: the analysis of the shift in the centre-of-mass was clearly not sufficient to inform conclusions regarding spatio-temporal propagation and the appropriateness of the ROI analysis could be questioned. The ROI analysis used a 2^{nd}-order model, which might not have had a sufficient number of parameters to describe the propagation; however, increasing the number of parameters would potentially over-parameterise/over-fit the data and undermine any conclusions regarding spatio-temporal propagation.

3.4.5 Recommendations for future work

This study represents the first statistical analysis of an EIT imaging set of fast neural activity, and also the first use of SPM second-level analysis on EIT imaging data, which has yielded some encouraging results, especially for the forepaw recordings' data.

Future studies could profit from investigating the effect of varying the EIT image processing steps that, for PET and fMRI, have been determined to substantially effect the results of SPM. Similarly examination of the efficacy of employing different smoothing methods, such as those employed by Skudlarski et al., and Maisog and Chmielowska might inform the future use of SPM on EIT image sets[203;204]. In addition to this, different

findings might be made if the assumption of the electrode array being in the same place for each recording within a stimulation group was examined, and, if necessary, the electrodes relocated on the mesh surface. Moreover, a different regularisation might be used for the inverse solution as a means of better imaging deeper conductivity changes.

With regard to better understanding of the spatio-temporal propagation of neuronal activity an alternative method of analysis to the ROI analysis, such as dynamic causal modelling (DCM), might be employed. Similarly, the forepaw ROI analysis was encouraging in many aspects, but there are aspects that do not match the reported translaminar propagation of activity and so are difficult to comment on. Therefore, the use of cross-validation techniques would allow for further conclusions regarding such results to be made. Hence, it would be profitable to make simultaneous or serial cross-validation measurements with an alternative method of measuring fast neuronal activity such as the use of VSD or CSDA in order to directly cross-validate any conclusions made using EIT.

Chapter 4

Statistical Analysis of Electrical Impedance Tomography images of Fast Neural Activity with Improved and Validated Methodology

4.1 Introduction

In chapter 3, a statistical analysis using SPM was applied to a cohort of tomographic images of fast neural activity, produced using EIT. The statistically significant results were then analysed in an attempt to ascertain if the conductivity change in the images had a spatio-temporal propagation matching that found in previous studies, which were reviewed in a detailed literature review in chapter 1.

While the study undertaken in chapter 3 yielded some encouraging results there were several limitations in the methodology. First among these was the use of one set of electrode positions for each recording of a certain stimulation type, that is for all 22 forepaw recordings the electrode array was assumed to be in the same location. Similarly, the mesh that was used for image reconstruction, whilst being anatomical, was non-optimal. Additionally, the inversion, which was undertaken with tSVD, was with a truncation level fixed to 50 singular values, based upon visual inspection of the images. Moreover, the resultant images were scaled based upon a gain simulation, which while compensating for the effect of boundary voltage rejection, relies upon an assumption of the volume, location and conductivity change that occurred, none of which can be known for certain. Lastly, the use of SPM second-level analysis was used without it having been validated for EIT images. Some of these limitations are reflected in the results of chapter 3; the analysis of the forepaw images, which were the most encouraging,

had significant changes at 2 ms, which is substantially earlier than expected from the neurophysiological literature, and the area with significant spatiotemporal propagation, determined using ROI analysis, was in excess of 12 mm^2 which is larger than the entirety of the head representation in the rat [131], and these changes were at the periphery of the image volume. It is the aim of this current study to address these limitations in turn and then repeat the statistical analyses undertaken in chapter 3.

4.1.1 The validity of statistical parametric mapping with electrical impedance tomography images

There are an array of neuroimaging analysis software packages available, each of which have specific roles and reasons for being preferable to other packages. Three of the most commonly used are SPM, BrainVoyager QZ (www.brainvoyager.com), and the functional magnetic resonance imaging of the brain software library (FSL) (www.fsl.fmrib.ox.ac.uk). Therefore, before even considering any mathematical basis for justifying the use of SPM with EIT images of fast neural activity it is useful to examine the key differences between these three packages. As detailed in chapter 3, SPM is a free, open-source, MATLAB-based software package developed at UCL, that accepts the 3D Analyze and 3D/4D NIfTI-1 file formats. Its implementation in MATLAB makes it accessible to all platforms, but adds an additional cost in software purchase and hardware resources as MATLAB must be running. However, it has a large, active user base that have over the years provided an array of toolboxes for SPM. BrainVoyager QZ is a commercial, semi-open software package that is optimised for C++ and runs on all platforms, with an intuitive layout, but a non-standard file format. FSL is a software package built for the UNIX platform and as such is only available on Mac OS X and Linux. It accepts the 4D NIfTI-1 file format and as an open-source package is free and easily modified by users. Differences in the statistical processes are largely limited to the sequence of events undertaken, for example when using the SPM package normalisation occurs prior to smoothing and individual statistics, while with FSL normalisation occurs after individual statistical inferences have been made. However, these differences are limited to processing steps that have not been employed in the group-level analysis of EIT images of fast neural activity undertaken in chapter 3, and so the choice of any software package is based on convenience rather than methodology.

4.1.1.1 Limitations and pitfalls of statistical parametric mapping

Assuming the SPM package is an acceptable means of making statistical inferences of EIT images of fast neuronal activity, then the next issue to consider is the validity of the mathematical procedures employed in SPM and their key pitfalls.

A common pitfall with the use of SPM is one of misinterpretation. This may be linked to the modality under consideration, for example the origin of signals in fMRI can often be complex and difficult to disentangle. Misinterpretation of the signal in SPM can occur as significance should be carefully related to the amplitude or other characteristics of the underlying signal. This was highlighted by Vul et al. in their review of the risk of drawing conclusions, specifically correlations, on areas determined to be significant, as the results may be inflated by this selection bias[205]. Regarding the work presented in chapter 3 this would perhaps only be a relevant concern to any interpretation of the amplitude of the masked mean signal (section 3.3.2).

Fundamental to the use of SPM is the multiple-comparison problem, yet it is not uncommon for inferences to be made using uncorrected p-values, as was undertaken in chapter 3 for the non-forepaw images. Despite the prevalence of this practice it is still crucial to make some manner of correction for false positives and this is often argued to have been done by using more stringent p-values or cluster-wise inferences. This practice was perhaps most famously undermined by Bennett et al.: haemodynamic response fMRI data, collected from a post-mortem salmon, were assessed using first-level analysis SPM, with an uncorrected p-value of <0.001 and an extent threshold. This cluster-level inference resulted in significant activations over an area of $81\,\mathrm{mm}^3$, however, with FWE correction or false discovery rate no significant activations were detected[206]. Despite this, and other work, illustrating the importance of correction for the multiple-comparison problem, FWE correction and other methods have their pitfalls.

The basis of FWE correction in SPM is RFT, in which the smoothness of the image noise is estimated in order to determine the number of resels that must be corrected for (this was reviewed in chapter 3). However, RFT has been found to be 'wildly conservative' for low degrees of freedom, that is when only a few images are available, as many of the assumptions have larger error, but also as it is more difficult to achieve significance with low degrees of freedom[198]. The validity and success of applying RFT rests upon a series of assumptions, for example, that the image noise smoothness is known with negligible error, which does not always hold true with some estimates indicating a $\pm 20\,\%$ in p-value if only a single image is used for smoothness estimation[207].

4.1.2 Statistical non-parametric mapping

An alternative to SPM is SnPM, which is a non-parametric alternative based upon permutation test theory, which, despite having been described in the early 20^{th} century, has only comparatively recently found popularity due to access to improved computational power[208].

The concept is perhaps easiest understood by considering a single voxel, over multiple scans, in a box-car paradigm of rest and activation. If there is no difference between the

two states, that is if the null-hypothesis is true, then it would be peculiar if observations in one state were different from those in the other state; quantifying how unexpected the result is, is what underpins SnPM. In SnPM the null hypothesis, $\mathcal{H}_0$, is that the labelling of data is arbitrary and reassigning the data to a different labelling should have no effect. By making a statistical inference, be it a t-test, F-test or other statistic, for each relabelling and comparing this to the result for the experimental labelling, unlikeliness of the experimental effect can be determined: the unlikeliness of the result is reflected by how far into the tail of the distribution of results the experimental labelling is. While the technique has few assumptions it can take an exceptionally long time to compute all possible permutations[208;209].

4.1.2.1 Randomisation testing

In the case of first-level, or intra-subject, SnPM, randomisation testing is the procedure that is undertaken. This relies upon the allocation of states being randomised prior to conducting the data collection, a $\mathcal{H}_0$ that the labelling is arbitrary, and that they are exchangeable. Under $\mathcal{H}_0$ the data might have resulted from any labelling, and the statistics for the experimental labelling should be randomly placed within a distribution of the statistical results for all possible relabellings. Therefore, the degree to which the statistical result at the experimental labelling is in the extreme, given the distribution for all other relabellings, can quantify how unlikely the result is. For example, if the experimental labelling gave the largest result within the distribution then the p-value is $1/N$, where N is the number of possible relabellings[208].

4.1.2.2 Permutation testing

Randomisation is not practicable for second-level, or inter-subject, SnPM, and so an alternative approach is taken: permutation testing. Permutation testing requires the weak assumption that the data at a single voxel is symmetrically distributed across subjects' images. With this assumption in place the data are reassigned to a new labelling, which for second-level analysis involves multiplication of data by either 1 or -1. Subsequently, as with randomisation testing, each permutation is calculated and the statistical result at the experimental labelling is compared to the distribution for all other relabellings, and inferences can be made over a population[198;208].

4.1.2.3 Sample size

Permutation testing is discrete and can only achieve a p-value of $1/N$, where N is the number of relabellings, or a multiple of this; if a permutation test allowed for 20 relabelling and the experimental labelling had the largest result then it can be determined to reject

$\mathcal{H}_0$ with $\alpha = 0.05$. Similarly, another consideration with permutation testing is one of computational cost, as the number of permutations will be 2^N, and so for relatively small data sets of ≥ 20 the number of permutations is in excess of 1 000 000. A solution in such instances is to perform a Monte Carlo test, in which a random subsample, N', of all the possible relabellings is taken. However, this will result in a less powerful test compared to calculating the full permutation distribution[208]. However, as few as 1000 permutations in the subset can be sufficient to maintain power in Monte Carlo testing[210], but it can be worse if $N' << N$. The error from using N' can be calculated as $2\sqrt{(p(1-p)/N'}$, and so a compromise can be made between computational time and error on the desired p-value[211].

4.1.2.4 Multiple testing problem

Conceptually, SnPM is easily extended to the entire image volume, and the issue of the multiple-comparison problem is dealt with by using the maximum value of the statistic image. The procedure is to determine the distribution of the maxima of the statistic images, then the omnibus hypothesis, that is all voxel hypotheses are true, is rejected if the maximal statistic of the experiment labelling is in the top 100α per cent of this distribution. The corresponding critical value is the $(c+1)$th largest member of this distribution of maxima, where $c = \lfloor \alpha N \rfloor$. For example, with 1000 permutations and $\alpha = 0.05$, $c = 1000 \times 0.05 = 50$, so the critical threshold is the 50th largest member of the permutation distribution. Therefore a corrected p-value for a voxel is calculated by determining the proportion of the distribution of maxima greater than or equal to the voxel statistic. A limitation with this correction is that areas with high variance will dominate the distribution of maximal results, which, although not invalidating the test, will result in reduced sensitivity for areas of lower variance. This effect can be assumed to be negligible if the statistic has a null permutation that is homogeneous across the volume, such as is the case with a t-test. An alternative approach, especially for low degrees of freedom (<20), is to spatially smooth the variance, giving a better estimate of the variance, with the result being termed a pseudo t-test[208].

4.1.3 Improved forward modelling

A new FEM mesh was generated from a CT scan of a rat's head with the aim of increasing the accuracy of the forward model by having a decreased tetrahedra size around the electrodes. Given the difference in electrode position between the different simulation modalities, four separate FEM meshes were generated with each being derived from the same surface, but each having refinement for the electrodes in different locations. This refinement resulted in the tetrahedra around the electrodes being ten times smaller than

those in the mesh used in chapter 3, and an up to five-fold increase in the number of tetrahedra in the FEM mesh as compared to the original FEM mesh (figure 4.1).

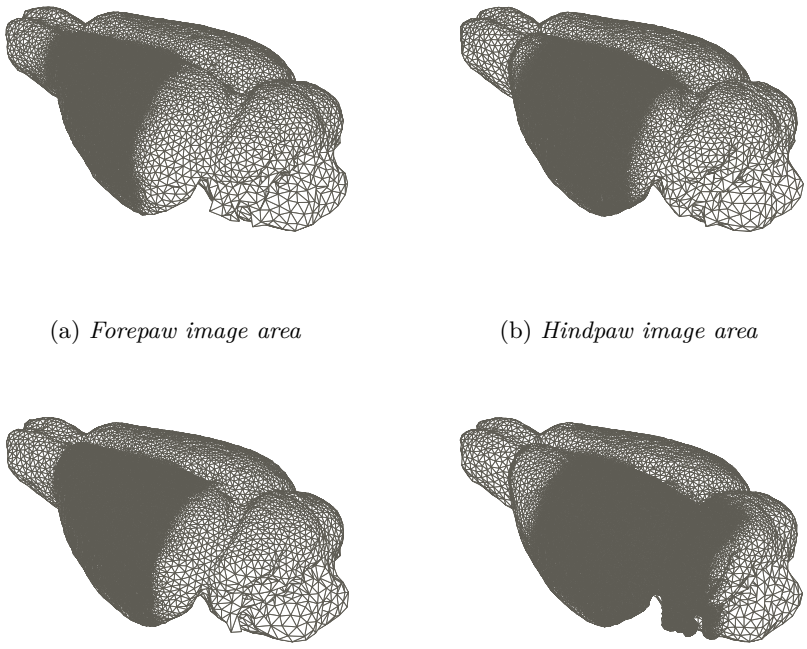

(a) *Forepaw image area*

(b) *Hindpaw image area*

(c) *Whisker image area*

(d) *Visual image area*

Figure 4.1: *Location of the reconstructed image volumes on a triangulation mesh of the surface tetrahedra of the FEM meshes of the rat brain for the four different stimulation modalities.*

The quality of the original and new FEM meshes were assessed using the Joe-Liu quality measure which considers the smallest edge ratio, volume, and angular dimensions:

$$q = 12\frac{(3V)^{\frac{2}{3}}}{\sum_{0\leq i\leq j\leq 3} l_{ij}^2}, \tag{4.1}$$

where q is quality, v is the tetrahedron volume, l is the edge length, and i and j are number of nodes. If $q = 1$ then all of the tetrahedron's edges and angles are equal, and so it is ideal, whereas if $q = 0$ the tetrahedron either has a very small volume, very short edge, or very small angle between two edges. It is often stated that if no tetrahedra have a $q \leq 0.1$ then the mesh is acceptable[212]. The lowest q for the original FEM mesh was 0.21, but was 0.223, 0.195, 0.1 and 0.05 for the new forepaw, hindpaw and visual FEM meshes, respectively. In contrast to this, the mean q for the new FEM meshes, lowest for

the visual FEM mesh ($q = 0.907$) was greater than for the original FEM mesh ($q = 0.8$) (table 4.1).

	Forepaw	Hindpaw	Vibrissae	Visual	Old
No. tetrahedra	3 000 000	4 000 000	4 000 000	5 000 000	1 000 000
Lowest q	0.223	0.195	0.1	0.05	0.21
Mean q	0.913	0.91	0.91	0.907	0.8
No. $q < 0.5$	10 000	14 000	14 000	20 000	1000
ROI tetrahedra size (mm)	0.05 to 0.3	0.05 to 0.3	0.05 to 0.3	0.05 to 0.3	0.5 to 1
Non-ROI tetrahedra size (mm)	2	2	2	2	2

Table 4.1: *Summary of mesh quality for the FEM meshes employed in chapters 3 and 4. ROI refers to the area of electrode placement*

4.1.4 Improved inverse solution

In EIT sensitivity reduces with the distance from the electrodes, therefore in the circular arrangement of electrodes around an object of interest, such as in lung or head EIT, sensitivity is minimal in the centre. A similar trend is present when a planar electrode array is used, as employed to collect the data currently under consideration, as sensitivity reduces exponentially with depth from the array. Work has been done to examine alternative inversion methods that compensate for this non-linear decrease in sensitivity in the z-axis as a perturbation moves away from the electrode array [213;214]. Work by Sato dos Santos has shown that performing the inversion of the sensitivity matrix with tSVD and a fixed level of truncation, as undertaken by Gilad et al. [90], is a highly unoptimised approach, as in noise-free simulation the movement of a simulated perturbation in the z-axis results in no change in the z-axis location of the reconstructed perturbation. Consequently, tSVD with 50 singular values is insensitive to the depth of the perturbation. An approach that has resulted in improved sensitivity to perturbation depth, in simulation and tank studies, is Tikhonov regularisation, with the hyperparameter set via cross-validation [215].

Tikhonov regularisation essentially involves adding a weighting term to the ordinary least squares approach to solving $Ax = \beta$ (for details see section 3.1.3.1). However, as this solution is ill-posed in EIT, as A is underdetermined, a least squares solution is inappropriate and the weighting term overcomes this. This weighting is via the Tikhonov matrix, λ, which trades off the solution against $\|x\|_2^2$ being too large, while if $\lambda = 0$ then the solution returns to the ordinary least square solution of $x = A^{\dagger}\beta$. Replacing the generalised terms of the ordinary least squares approach with those specific to EIT yields:

$$\widehat{\delta\sigma} = \arg\min_{\delta\sigma} \|\delta v - A\delta\sigma\|_2^2 + \lambda \|\delta\sigma\|_2^2 , \tag{4.2}$$

where $\delta\sigma$ is the conductivity matrix, δv are the changes in boundary voltage, A is the sensitivity matrix, and λ is the Tikhonov matrix.

As with tSVD there still remains the issue of determining the truncation level, or in the case of Tikhonov regularisation the value of λ. A solution is to use cross-validation to set the hyperparameter, referred to hereafter as λ_{CV}. In determining λ_{CV}, the difference between the predicated changes in boundary voltage, $\widehat{\delta v}$, and experimentally recorded changes, δv, are minimised:

$$\lambda_{CV} = \arg\min_{\lambda} \left\| \delta v - \widehat{\delta v} \right\|_2^2 . \tag{4.3}$$

Equation 4.3 is a reduced expression of the operation being undertaken, as $\widehat{\delta v}$ has to be iteratively calculated using equation 4.2, so that the minimisation can be solved. This entails taking a subsample of the experimental boundary voltage changes, δv, and using these a training set in equation 4.2 to generate $\widehat{\delta\sigma}$. With calculation of $\widehat{\delta\sigma}$, $\widehat{\delta v}$ can be calculated as $\widehat{\delta v} = A\widehat{\delta\sigma}$, and these are tested, using equation 4.3, against the boundary voltages not used as the training set in equation 4.2. With the data currently under consideration this was achieved by randomly selecting 10 % of the boundary voltages and performing the cross-validation ten times for each value of λ.

4.1.5 Purpose

The rationale of the current study was to improve upon the imaging methodology that was previously used to reconstruct the data collected by Gilad et al. [90], and then determine what effect this had on the analysis undertaken in chapter 3. The particular point of interest was whether these improvements with yield, particularly with regard to the ROI analysis, more physiological results. Specifically this regarded the lateral location of significant change for the forepaw images noted in chapter 3, the latency for some ROI being much later than previously reported in the literature and the area of significance being much larger than the expected cortical area corresponding to the forepaw representation.

Therefore, the purpose of this study was to optimise the methodology of chapter 3, with regard to the image reconstruction and validate the application of SPM to EIT images, first by consideration of controls and then by comparison to SnPM. An additional purpose of this study was to evaluate whether significant conductivity changes occurred across each of the stimulation groups and whether such changes exhibited laminar spatio-temporal propagation that were comparable to the progression of activity reported in previous literature. The questions addressed were:

(1) Are statistically significant, reproducible changes identifiable in the images of conductivity changes for each of the stimulation groups?

(2) Do the reconstructed conductivity changes exhibit laminar spatio-temporal propagation that is comparable to the neurophysiological literature?

(3) Have changes in the image reconstruction resulted in changes to the results of the analyses applied in chapter 3, and are the results more comparable to expectations from the literature?

(4) With respect to the data, image reconstruction, and statistical testing of the images, what are the study's limitations and how might they be addressed?

4.1.6 Experimental design

Improvements were made to the image reconstruction methodology through the use of new meshes, better estimation of the true electrode location and improved regularisation methods for solving the inverse problem. To determine the effect of using individual electrode positions as opposed to a single location across recordings was examined with a simulation study. To validate the use of second-level SPM of EIT images, SPM was applied to control data and the non-control images were analysed with SnPM. Subsequently, the spatio-temporal propagation of activity was assessed by comparing the relative time to maximum conductivity change in a series of ROIs throughout the imaging volume. The results of this analysis were then compared to the expected pattern of activation as determined from previously published neurophysiological results.

4.2 Methods

4.2.1 Electrode realignment

Electrode array positions were determined *post-hoc* by analysis of the distribution of the EPs' topography. Electrodes for a given rat were placed on the mesh in the forward model in such a way as to minimise the difference between its EP's topography and that of an exemplar topography collected within the same stimulation paradigm, which, to minimise assumptions, was chosen from the recorded EPs.

4.2.1.1 Defining exemplar evoked potential

The exemplar EP, for a given stimulation type, was chosen by finding the recording with an EP centre, $\boldsymbol{c}_k$, closest to that of the centre of the electrode array. For the kth EP its centre, $\boldsymbol{c}_k$, was defined as:

$$\boldsymbol{c}_k = \frac{\sum_{j=1}^{J}(\sum_{i=1}^{I} EP_{kji})\boldsymbol{p}_j}{\sum_{j=1}^{J}\sum_{i=1}^{I} EP_{kji}} \tag{4.4}$$

where $EP_{kji}, ..., EP_{KJI}$, are the EP values for the kth recording, at the jth electrode and the ith time point, and $\boldsymbol{p}_j, ..., \boldsymbol{p}_J$ are the vectors describing the jth electrode position. Having determined the $\boldsymbol{c}_k$ for each recording, the recording closest (Euclidean distance) to the centre of the electrode array was chosen as the exemplar EP for a given stimulation paradigm.

4.2.1.2 Estimating ideal electrode positions

Having identified the exemplar EP for a given stimulation paradigm, this was then interpolated over a series of translations and rotations of the electrode positions. Translation was over a distance spanning twice the area of the array (translation in each axis), in steps of 0.1 mm, while rotation was in the xy plane from $-10°$ to $10°$, in steps of $0.5°$. Then each recording's EP, EP_{kji}, from a given rat of the same stimulation type, was compared to each point, $\boldsymbol{l}$, of an interpolation of the exemplar EP for that stimulation type, $\widehat{EP}$, and the point within this that yielded the least difference was calculated:

$$\hat{\boldsymbol{l}}_k = \arg\min_{\boldsymbol{l}} \left\| EP_{kji} - \widehat{EP}_{lji} \right\|_2^2, \tag{4.5}$$

where $\widehat{EP}_{lji}, ..., \widehat{EP}_{LJI}$ are the interpolated values at the lth location, and $\hat{\boldsymbol{l}}_k$ (the *ideal placement*) is the translation and rotation yielding the smallest difference between the measured kth recording's EP and that of the exemplar EP. Having determined the *ideal placement* ($\hat{\boldsymbol{l}}_k$) for each recording within a rat, the same difference was calculated for each *ideal placement* within a given rat. The *ideal placement* yielding the smallest difference across all the recordings was chosen as the *ideal placement* for that rat. In other words, the assumption was made that the electrode array was not moved between recordings in the same rat and so one set of electrode positions could be used. Having identified the *ideal placement* for a given rat, the electrode array was placed in this location for solving the forward problem for the recordings from that rat.

4.2.1.3 Evaluating the effect of unique electrode positions

To assess the effect of using individual electrode positions for each rat, as compared to a single set of electrode positions for each stimulation group, a simulation was undertaken. Using the FEM mesh with the largest shift in electrode positions, boundary voltages were simulated for the exemplar electrode positions, V_{exemp}, and for the shifted electrode

positions, V_{shift}. The boundary voltages were a difference between baseline boundary voltages for $0.3\,\mathrm{S\,m^{-1}}$ throughout the FEM mesh and perturbation boundary voltages in which a disc-shaped area was set to have a conductivity of $0.303\,\mathrm{S\,m^{-1}}$. The diameter and thickness of the perturbation were 1.5 mm and 0.35 mm, respectively, and it was placed under the centre of the exemplar electrode coordinates at a depth of 1.72 mm from the topmost point of the FEM mesh, but normal to the electrode positions (figure 4.2).

Inversion was undertaken using Tikhonov regularisation, first with V_{exemp}, a Jacobian using the exemplar electrode positions, J_{exemp}, and $\lambda \approx 0$, then with V_{exemp} and J_{exemp}, but with a cross-validated λ, λ_{CV}, and finally with V_{exemp}, a Jacobian using the shifted electrode positions, J_{shift}, and λ_{CV}. Images were then interpolated on a 3-D Cartesian grid with a spacing of 25 µm and smoothed with a zero-phase Gaussian filter with a FWHM of 150 µm (for details see section 4.2.4.2). For each of the three images the *reconstructed perturbation* was defined (see section 2.2.5 for details), and from this the centre of mass and extent, in the x- and y-axis, of the *reconstructed perturbation* calculated and the difference in these compared to reconstruction of the perturbation, that is the centre and extent of the perturbation after interpolation and smoothing.

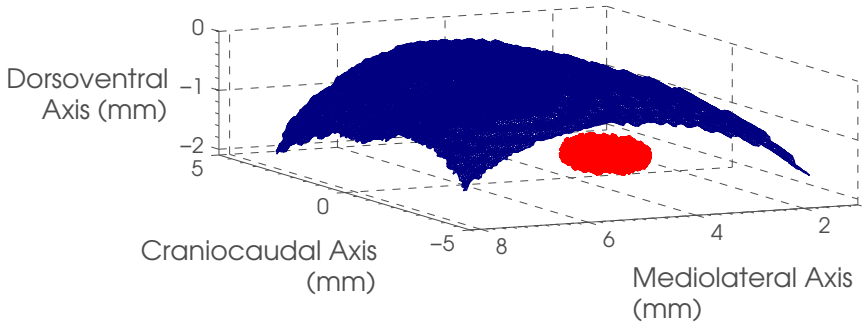

Figure 4.2: *Location of the simulated perturbation (red) relative to a triangulation mesh of the surface tetrahedra of a FEM mesh of the rat brain.*

4.2.2 Selection of data cohort

The same subjects and recordings were used in the present analysis as were used in chapter 3 (see section 3.2.1 for details). In addition to the 38 'active' recordings used in the present analysis two control recordings were also selected for use as validation of the methods employed. These controls were both from the same rat, which had been used for forepaw stimulation and EIT measurements, and after which the two controls measurements were made: first a measurement without stimulus and second a post-mortem measurement.

4.2.3 Image reconstruction

Images were reconstructed with the real component of voltage differences using a TD approach at 21 and 18 time points for the SEPs and VEPs recordings, respectively, with the signal processing as described by Oh et al. [64].

The voltage differences were reconstructed into conductivity difference images using a sensitivity matrix reconstruction algorithm [184]. Four FEM meshes based upon the same surface geometry, one for each stimulation type, were employed. Each had refinement over the region of electrode placement and had 3 000 000 to 5 000 000 tetrahedra (see section 4.1.3 for details). For solving the forward problem each rat's electrode positions were set individually using the method described in section 4.2.1. Inversion was performed using Tikhonov regularisation with the hyperparameter set using cross-validation, with λ spanning 1×10^{-20} to 1, in 2000 logarithmically spaced steps, and the cross validation being ten-fold using 10 % of the data for training (see section 4.1.4 for details).

4.2.4 Image preprocessing

4.2.4.1 Selection of area for imaging

A different area, around the electrode location, was selected for each stimulation modality, which corresponded to a region in the FEM mesh of approximately 9.25 mm × 6.725 mm (table 4.2). These areas were then rotated as described in section 3.2.2.1.

Image Volume	Imaging Area
Forepaw	9.25 x 6.4
Hindpaw	9.6 x 6.7
Whisker	8.7 x 7.25
Visual	9.55 x 6.55

Table 4.2: *Dimensions of the image area for the four new FEM meshes.*

4.2.4.2 Image interpolation and smoothing

As detailed in section 3.2.2.2, the coarsest, lossless interpolation can be determined by first ascertaining the closest distance between any two tetrahedral centroids and then dividing this by $\sqrt{3}$. This is a sound approach, but is not easily calculated for large data sets. For example, for the FEM mesh with the fewest tetrahedra used in this study (the forepaw FEM mesh) a one-step matrix approach would require >16 000 GB, or 15.74 TB, of memory. Consequently, the alternative is a brute-force iterative approach, which is the solution that was applied in chapter 3. However, such an approach is high order,

being $O(n^2)$, where n is the number points to query. An alternative approach is to employ a recursive divide-and-conquer approach, which reduces the order to $O(n \log n)$. The computation time for the brute-force approach, on the forepaw FEM mesh, would be 63.55 h, as compared to 0.13 h for the recursive divide-and-conquer algorithm*. Using this algorithm, for each of the image volumes the shortest Euclidean distance between any pair of tetrahedral centroids was calculated (table 4.3).

Image Volume	Shortest Distance (µm)
Forepaw	11.5
Hindpaw	11.9
Whisker	11.3
Visual	11.7

Table 4.3: *Shortest Euclidean distance between tetrahedral centroids in each of the image volumes of the four cortical areas imaged.*

Given this minimum distance, the interpolation grid would be calculated to have a spacing of 6.5 µm, which would result in 493 382 988 points in the 3-D Cartesian grid. This size of image was too cumbersome for the subsequent steps, with the interpolation alone taking >1 h, and, as each image required >3.6 GB, processing stages during and subsequent to SPM were made difficult. Moreover, the spatial resolution of the reconstructed EIT images is certainly worse than this, and the smallest structure of interest would be a column of approximately 300 to 500 µm in diameter [97;119]. Therefore, images were interpolated on a 3-D grid whose lattice points were spaced 25 µm apart in each axis, as in section 3.2.2.2. The depth, from the FEM mesh's surface, of the resultant voxels was then defined and voxels deeper than 2.1 mm removed before image smoothing or statistical analysis (for details see section 3.2.2.2). Image smoothing was undertaken by performing zero-phase filtering with a Gaussian kernel with a FWHM of 150 µm (for details see section 3.2.2.3).

4.2.4.3 Image scaling

Gilad et al. performed a gain correction for each image, which was achieved by using a simulation with the given protocol for each recording (for details see section 3.1.1.2) [90]. This had a two-fold purpose, first, to correct for the loss of power following truncation in tSVD, and second to ensure conductivity changes were of the same order of magnitude and therefore to facilitate statistical comparison. To move away from an approach so reliant on strong assumptions, images were proportionally scaled. The first step was to

*The calculation times were for an intel i7 2500k at 4.5 GHz

find the time point at which a recording's image set had its maximal above zero mean. The mean of above half maximum changes at this peak time point was used to determine the scaling factor by finding its ratio to one.

4.2.5 Statistical parametric mapping

Second level-analysis was performed, using SPM8, separately on each of the EIT images from the four stimulation groups. Separately at each time bin the image volumes were input into a one-sample t-test with implicit masking being selected. This design results in a design matrix of ones and so the estimated parameter, $\hat{\boldsymbol{\beta}}$, at each voxel is the mean of that voxel over all the recordings, and so $\mathcal{H}_0 : \hat{\boldsymbol{\beta}} = 0$.

The images were assessed for significant activations above zero with the construction of a t-map, first with p^{FWE}-values and then if this produced no significant results an uncorrected p-value was used. In both instances the p-value was set for $\alpha = 0.05$, giving a 95 % CI. However, this was adjusted using the Bonferroni correction for the repeated t-tests over multiple time bins. Therefore, given the effective temporal resolution of 8 ms and 21 time bins in the SEP images, there were 5 independent tests corrected so that the p-value was for $\alpha = 0.01$. For the VEP images, which were all separated by 15 ms and therefore independent, correction was made for all 18 time bins so that the p-value was for $\alpha = 0.0028$. These temporally corrected p-values are hereafter denoted by the subscript $tcorr$. The connectivity of any resultant significant positive changes was then determined and those clusters whose number of voxels was less than 1 % of the total number of voxels in the image volume were assumed to be the peaks of subthreshold clusters and so were removed.

4.2.6 Validation of statistical parametric mapping

4.2.6.1 Statistical parametric mapping of control recordings

The same SPM procedures, as detailed in section 4.2.5, were also applied to the two forepaw control image sets, and were tested for significance first with p^{FWE}_{tcorr}-values and then with p_{tcorr}, both for $\alpha = 0.05$.

4.2.6.2 Statistical non-parametric mapping

The forepaw images, as the only images in chapter 3 that had significant results when tested with a p^{FWE}_{tcorr}-value, were used for SnPM analysis. Second-level, Monte-Carlo permutation testing was undertaken, using a SnPM toolbox (www.go.warwick.ac.uk/tenichols/software/snpm) written for the SPM software package. Separately at each time bin the image volumes were input into a one-sample t-test, that is without variance smoothing, with implicit masking being selected. The t-tests were with p^{FWE}_{tcorr}-values

and so the p-value was for a corrected $\alpha = 0.05$, so that tests were made for $\alpha = 0.01$. Undertaking all permutations, which given the 22 recordings, totalled 4 194 304, would take >65 d to compute, so a subset of 1000 was taken. As detailed in section 4.1.2.3, using a subset introduces error, which in this instance is an approximately 60 % error on the p-value so that the test was for $\alpha = 0.01 \pm 0.0063$. This was deemed acceptable because to reduce the error to 10 % would require 37 500 permutations which would require 24 h of computation, per time bin[†].

4.2.7 Further statistical analyses

After SPM had been employed to generate t-maps further analysis was done to examine the spatio-temporal propagation of activity within stimulation groups. Throughout these analyses the stimulus and time bin appropriate t-maps were used to mask the image volumes. This removed voxels those changes that were not significantly positive activations belonging to a cluster >1 % the total number of voxels in the respective image volume, which are referred to hereafter as masked images.

4.2.7.1 Whole image volume analysis

The mean and SEM, over subjects, of the conductivity changes were calculated for the masked and non-masked images within each of the four stimulation groups. As a comparator to the mean conductivity change the time series of the maximum EP was also calculated. This was calculated by first, separately for each recording, finding the channel with the EP that had the maximum integral, and then by expressing these as the mean and SEM across recordings.

4.2.7.2 Region of interest analysis

Using the masked image conductivity changes the next analysis was to consider the data in the image volume in ROIs rather than en masse. The non-masked image conductivity changes were also analysed if the SPM had an insufficient number of time bins with significant activations. This entailed assigning each voxel to a ROI based upon its Cartesian coordinates, as detailed in section 4.2.7.2. The only changes applied to the previously employed methodology was that ROI analysis spanned the largest extent of the volume of significance, whilst for the non-masked analysis it included the entire imaging volume for the respective stimulation group. To simplify the procedure and make it more intuitive the use of ANOVA was no longer employed and the regression was applied to the mean, across subjects, of the latency to peak conductivity change for each stimulation group, all other procedures remained unchanged.

[†]The calculation times were for an intel i7 2500k at 4.5 GHz

4.3 Results

4.3.1 Electrode realignment

Visual inspection of the solutions offered by the electrode placement algorithm indicated that the new locations were reasonable (figure 4.3). The largest vector displacements were for the hindpaw and visual recordings (2.63 and 2.51 mm, respectively), while much smaller displacements were required for the forepaw and vibrissae recordings ($\leq$0.14 and 0.22 mm, respectively) (table 4.4).

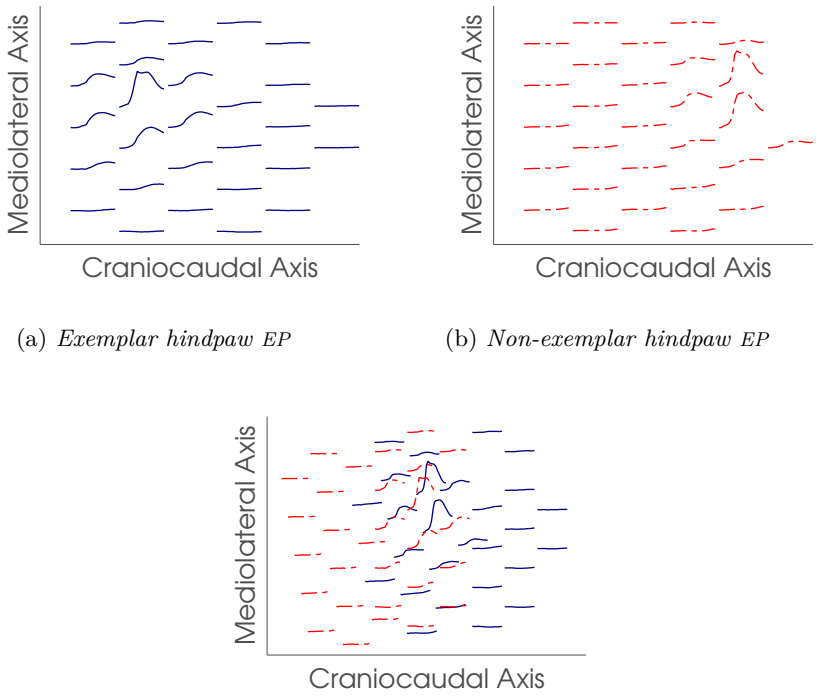

(a) *Exemplar hindpaw EP*

(b) *Non-exemplar hindpaw EP*

(c) *Realigned non-exemplar hindpaw EP and exemplar hindpaw EP*

Figure 4.3: *Visualisation of two hindpaw EP topographies, one being the exemplar rat's EP (figure 4.3a), and the other being the non-exemplar rat's EP (figure 4.3b. The solution to realign the non-exemplar rat's EP resulted in a predominantly negative shift on the mediolateral axis, that is away from the midline. Units are not given on the x and y-axis as the EPs' amplitude are normalised to have an identical peak value and because the plots are didactic. — exemplar EP. – – – non-exemplar EP.*

	Forepaw	Hindpaw	Vibrissae	Visual
Craniocaudal Axis (mm)	-0.23 ± 0.41	-2.60 ± 0	0.25 ± 0.64	-1 ± 0
Mediolateral Axis (mm)	0.3 ± 0.32	-0.4 ± 0	0.45 ± 0.78	2.3 ± 0
Rotation (°)	1.93 ± 6.52	10 ± 0	0 ± 14.14	9 ± 0

Table 4.4: *Solution to electrode realignment algorithm (mean±SD) for each of the four stimulation types. Hindpaw and visual are for a single value as there were only two rats for these recordings, hence once exemplar and one aligned EP.*

4.3.1.1 Evaluating the effect of unique electrode positions

Qualitative inspection of the reconstructed images revealed that the reconstruction of V_{exemp}, with J_{exemp}, and $\lambda \approx 0$, resulted in a readily identifiable *reconstructed perturbation*, of a comparable size and similar location to the rasterised and smoothed images of the simulated perturbation. There was a marked blurring of the reconstructed perturbation in the z-axis, with this axis having a large positive difference in *reconstructed perturbation* size, 0.43 mm, while in the other two axes the *reconstructed perturbation* was smaller than the rasterised and smoothed images of the simulated perturbation. The reconstruction of V_{exemp}, with J_{exemp}, and λ_{CV}, resulted in an image that was more blurred in the x- and y-axis than the images with $\lambda \approx 0$. Moreover, the power of the image appeared to be more shifted towards the surface of the mesh, and this was reflected in the centre of mass being 0.85 mm higher than the simulated perturbation. V_{exemp}, with J_{shift}, and λ_{CV}, resulted in a *reconstructed perturbation* of similar size to the reconstruction of V_{exemp}, with J_{exemp}, and λ_{CV}, but the *reconstructed perturbation* was shifted in an arc following the surface of the mesh towards the location of the electrode array used for J_{shift}. The result in the rasterised images was that the *reconstructed perturbation* appeared shift towards the surface. The result of this arc-shift was a centre of mass that was 2.58 mm away from the simulated perturbation's centre, as compared to the reconstruction using J_{exemp} in which the *reconstructed perturbation* centre of mass was 0.86 mm away from the simulated perturbation's centre (figure 4.4 and table 4.5).

4.3.2 Statistical parametric mapping

Visual assessment of the mean of the conductivity change images for the forepaw recordings revealed that the onset of conductivity changes was at 2 to 6 ms, appeared to peak around 10 to 14 ms and diminished over the remaining imaging time. The conductivity changes at depths less than approximately 1 mm were greater than those beneath this depth (figure 4.5). Using p^{FWE}_{tcorr}-values the forepaw recordings were found to be

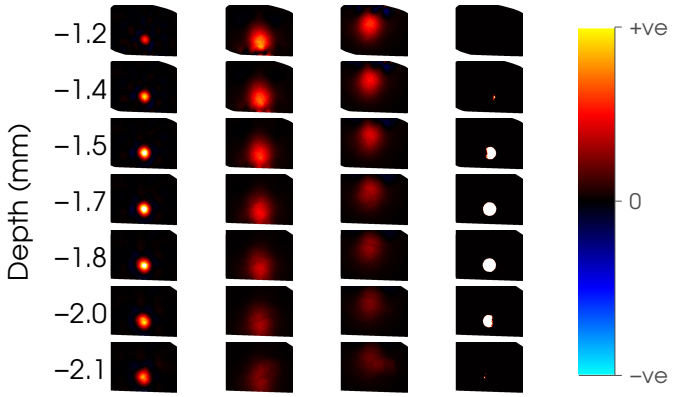

Figure 4.4: *Reconstructed images of simulation of the effect of electrode position on rat FEM mesh. From left to right, V_{exemp}, with J_{exemp}, and $\lambda \approx 0$, V_{exemp}, with J_{exemp}, and λ_{CV}, V_{exemp}, with J_{shift}, and λ_{CV}, and the rasterised and smoothed images of the simulated perturbation. The colourbar has '+ve/-ve' as the limits as the images are individually scaled.*

	Difference in Shape (mm)			Centre of Mass Shift (mm)			
	x-axis	y-axis	z-axis	x-axis	y-axis	z-axis	Distance
V_{exemp}; J_{exemp}; $\lambda \approx 0$	-0.45	-0.3	0.43	0.03	0	0.05	0.06
V_{exemp}; J_{exemp}; λ_{CV}	0.33	0.23	0.68	0.06	-0.14	0.85	0.86
V_{exemp}; J_{shift}; λ_{CV}	-0.05	-0.35	0.28	-0.83	2.18	1.10	2.58

Table 4.5: *Comparison of each* reconstructed perturbation *to the simulated perturbation.*

highly significant across the image volume. There were no significant positive activations belonging to a cluster >1 % the total number of voxels in the image volume at 0 and 2 ms, with 0 ms being the time of stimulation, and significant positive clusters were not present from 26 to 40 ms. The image volume showed the largest volume of significance, 7.53 mm^3 at 14 ms, which was trapezoidal in shape, with a larger volume at a depth of approximately 2 to 1.55 mm, above which the edges lacked significance. Prior to this, the volume consisted of two smaller cylindrical shapes, while following this period the volume of significance reduced into a smaller more cylindrical shape (figure 4.6). For the other three groups of recordings the use of p^{FWE}_{tcorr}-values did not reveal significant positive activations belonging to a cluster of sufficient volume and so p_{tcorr}-values were employed.

While in the mean of the conductivity change images for the forepaw recordings

changes occurred clearly across the imaging volume in all three axes, for the hindpaw recordings the changes were confined to the uppermost 1 mm. The conductivity changes were spatially less smooth than those in the forepaw recording mean conductivity change image, and also a greater proportion of the changes were negative, implying a worse SNR (figure 4.7). Using p_{tcorr}-values the hindpaw volume was not significant in any part of the image volume at any time point (figure 4.8).

The mean of the conductivity change images for the whisker recordings showed the onset of conductivity changes was at 2 ms and this peaked around 6 to 8 ms and diminished by approximately 16 ms to an above zero level that persisted over the remaining imaging time. The changes were, from visual inspection, the largest of all stimulation groups, both with respect to spatial extent and amplitude of change (figure 4.9). Using p_{tcorr}-values the whisker imaging volume was highly significant at all time points, including at the time of stimulation at 0 ms (figure 4.10).

In the mean of the conductivity change images for the visual recordings the onset of conductivity changes was at 45 to 60 ms. The activity had a gradual increase and decrease, which were at a comparable rate, and the peak conductivity change was at 105 to 135 ms, with the decrease after this peak reaching its minima at 225 to 240 ms. The volume of the positive conductivity change was, from visual inspection, comparable at depths of 0.9 to 1.3 mm, with several small areas of negative change occurring at the edges of the image volume at most depths (figure 4.11). Using p_{tcorr}-values the visual recordings' imaging volume was only significant at five time bins, in a time window of 90 to 165 ms, either side of which there were no significant positive activations belonging to a cluster >1 % the total number of voxels in the image volume (figure 4.12).

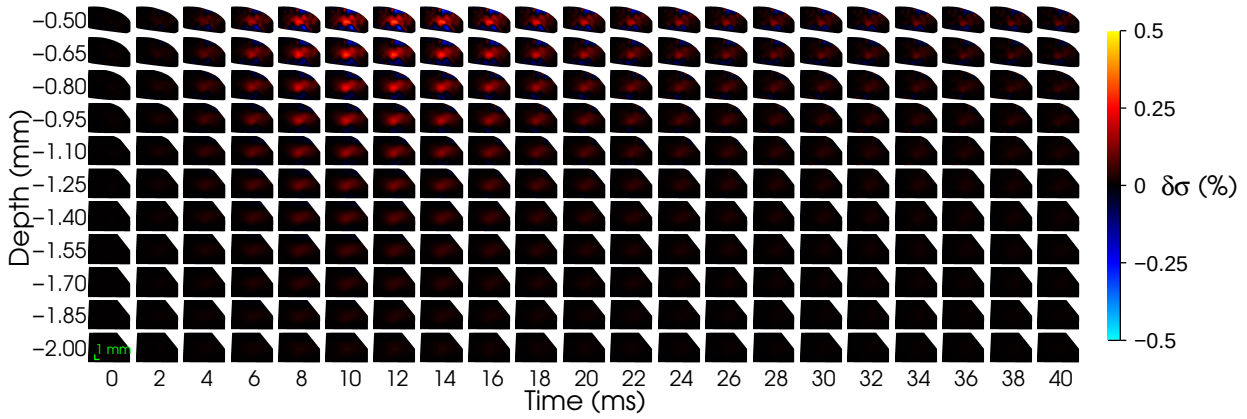

Figure 4.5: *Mean of forepaw images of percentage conductivity change: posterior-anterior and medial-lateral in the x and y axes.*

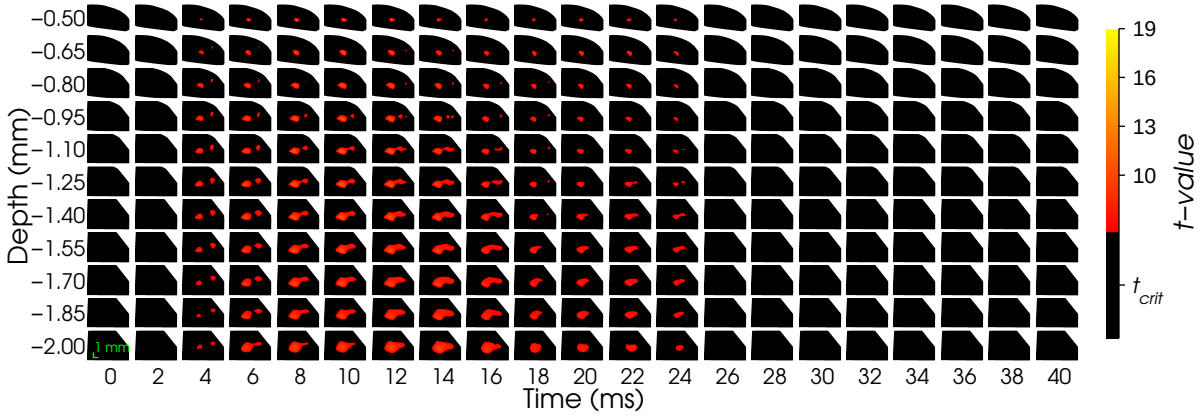

Figure 4.6: *One-sample t-test SPMs of forepaw images, $p_{tcorr}^{FWE} = 0.05$ critical value was 6.22. Non-significant changes are black.*

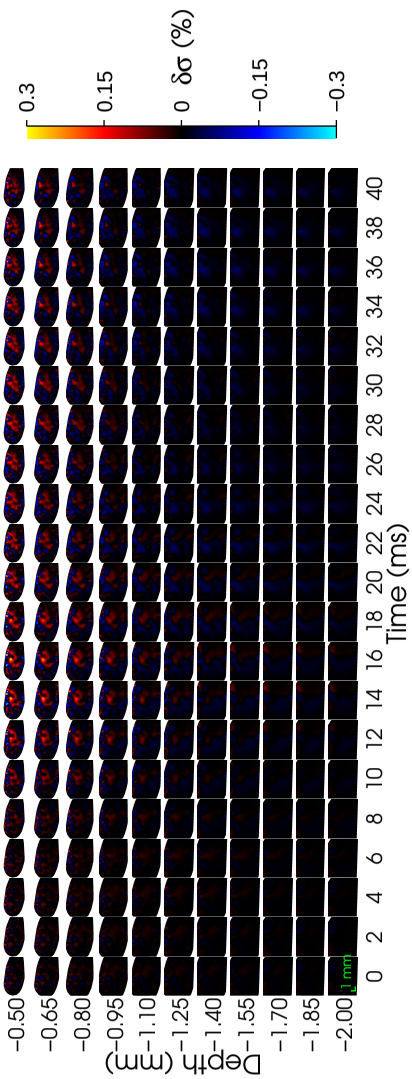

Figure 4.7: *Mean of hindpaw images of percentage conductivity change.*

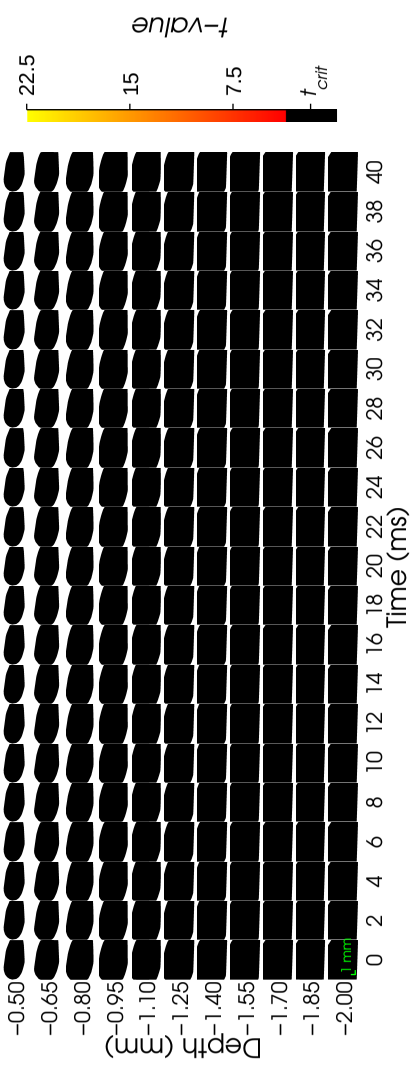

Figure 4.8: *One-sample t-test SPMs of hindpaw images, $p_{tcorr} = 0.05$ critical value was 3.75. Non-significant changes are black.*

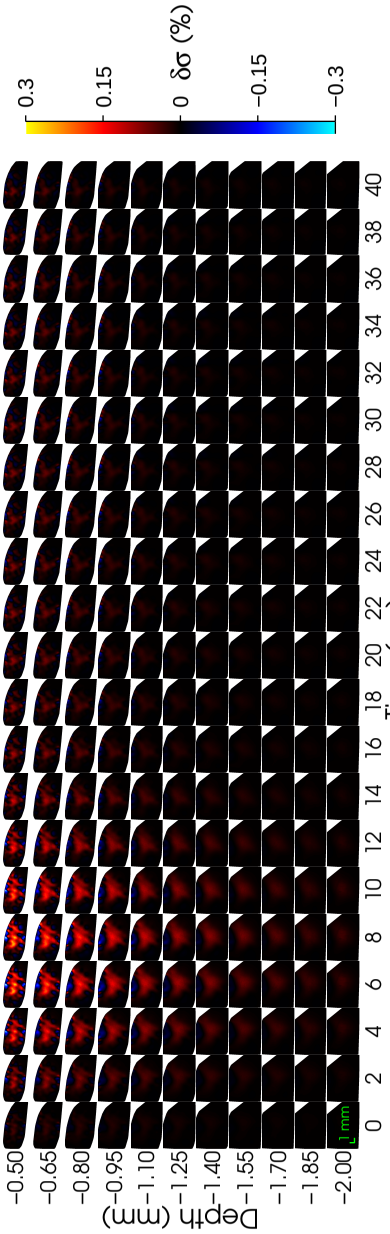

Figure 4.9: *Mean of whisker images of percentage conductivity change.*

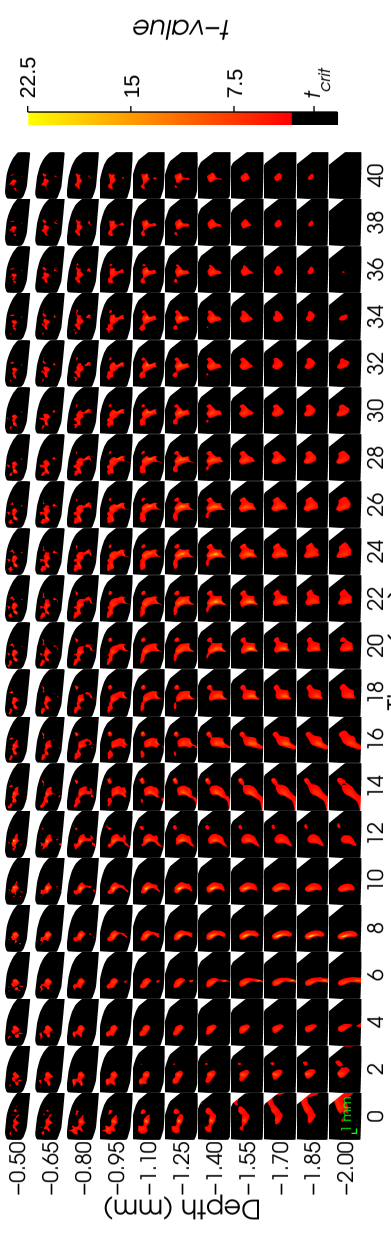

Figure 4.10: *One-sample t-test SPMs of whisker images, $p_{tcorr} = 0.05$ critical value was 3.35. Non-significant changes are black.*

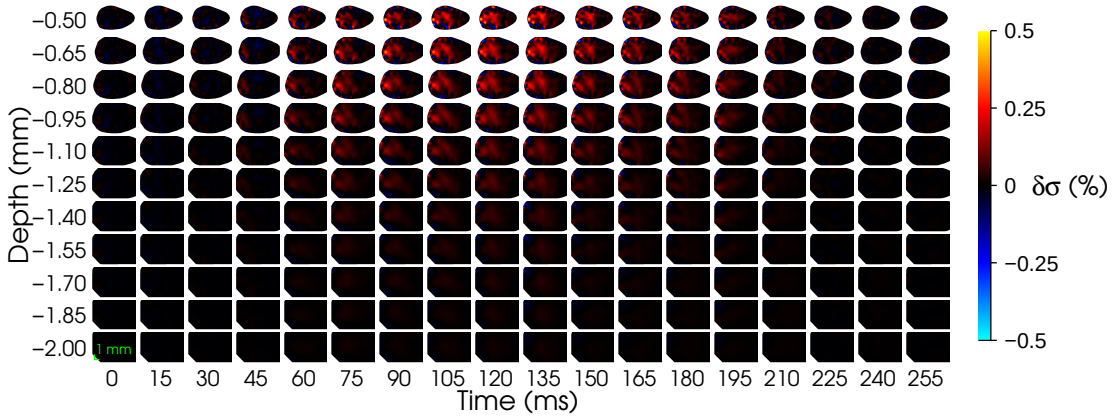

Figure 4.11: *Mean of visual images of percentage conductivity change.*

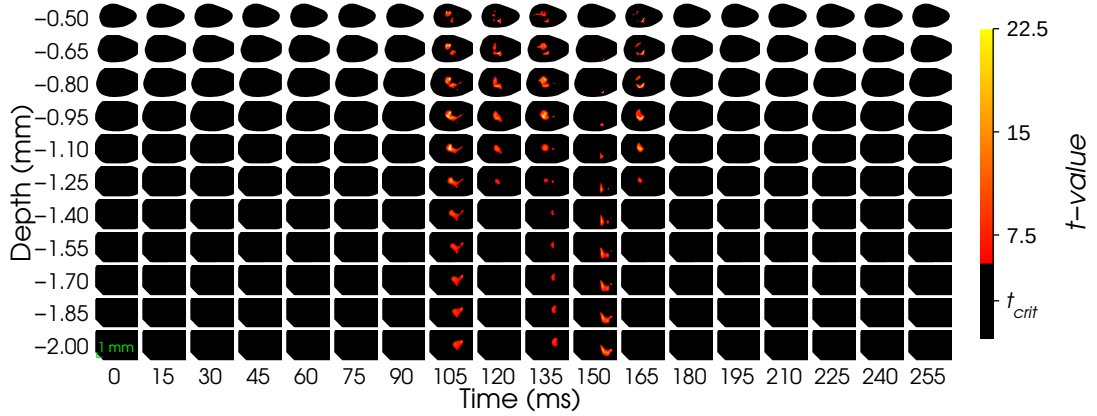

Figure 4.12: *One-sample t-test SPMs of visual images,* $p_{tcorr} = 0.05$ *critical value was 5.43. Non-significant changes are black.*

4.3.2.1 Statistical parametric mapping of control recordings

In the SPMs of the control recordings there were no significant positive changes belonging to a cluster larger than 1 % the total image volume with p^{FWE}_{tcorr}-values or with p_{tcorr}-values.

4.3.3 Statistical non-parametric mapping

The maxima permutation distribution at each time point was centred within a range of t-values between 3 to 5, with a positive skew in the distribution, an example, the distribution at 14 ms, is shown in figure 4.13. The maximum value in the 14 ms permutation distribution of t-statistic maxima was 10.23, which was the t-statistic for the correct labelling, and, since no other relabelling resulted in a higher value, the p-value was 0.01, as it is the largest value in 1000 permutations. The critical threshold, c, for $\alpha = 0.01$, is $c = 1000 \times 0.01 = 10$, therefore the tenth largest value is the critical threshold, which was $t = 5.85$.

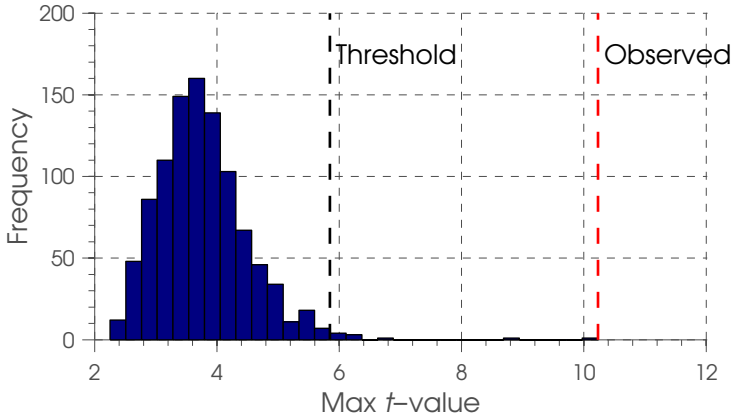

Figure 4.13: *Permutation distribution of maxima t-statistic values for the 14 ms forepaw images. The dotted lines indicate the t-threshold for significant results for* $p < 0.01$ *and the observed maximum t-value.*

The thresholds calculated with SnPM, for the images at 14 ms, were compared to those for RFT, employed in SPM and calculated from the Euler characteristic for the SPM results in section 4.3.2, at the same time bin, and for a volumetric Bonferroni correction, that is for the number of pixels: $p_{FWE} = p/6254041$. The results indicated that for a given test significance level the Bonferroni correction required a much higher t-value than that required with RFT or SnPM. In addition, while the RFT thresholds are less conservative than the Bonferroni values they are still less sensitive than the SnPM thresholds for an equivalent test level (figure 4.14).

A similar trend was present for the other time bins in which the SnPM was lowest, RFT

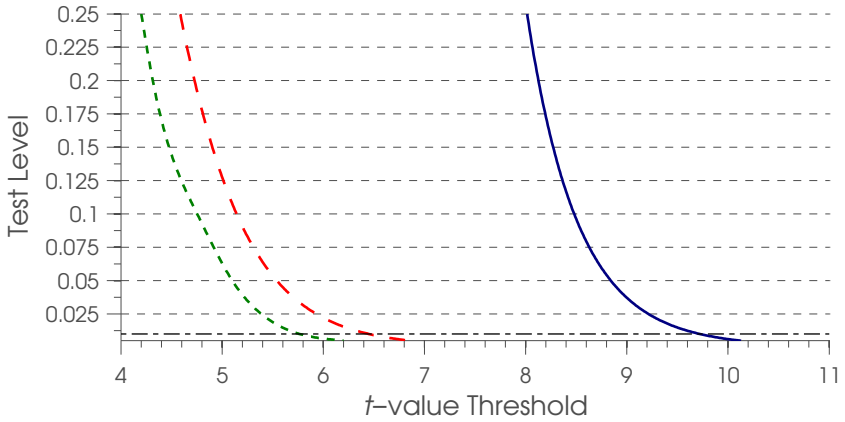

Figure 4.14: *Test level (α) versus the critical threshold for parametric and non-parametric FWE-correction methods. Horizontal — · — line indicates $\alpha = 0.01$. — Bonferroni. – – – RFT SPM. - - - - SnPM.*

was greater and the Bonferroni correction greater still (table 4.6a). The result of this was that a much larger volume of significant changes was detected with SnPM than with RFT. The Bonferroni thresholds were constant over the time bins, which is to be expected, while the thresholds for RFT and SnPM varied. There was only minimal variability over the time bins in the t-threshold with RFT SPM, with all values being within 0.08 of the mean of 6.44, suggesting the spatial smoothness of the residuals was similar in all time bins. The t-threshold with SnPM varied more than for the other FWE correction methods, 5.78 ± 0.15 (mean $\pm$ SD), but were still quite stable, suggesting a stability in intersubject variance and distribution over the time bins (table 4.6b).

Time Bin (ms)	Significant Volume (mm^3)	
	SPM RFT	SnPM
0	—	—
2	—	—
4	2.8	6.61
6	5.06	7.60
8	5.87	8.79
10	6.3	8.48
12	7.19	10.46
14	7.53	10.14
16	5.87	7.19
18	3.56	7.40
20	3.20	6.60
22	3.07	5.46
24	2.06	3.98
26	—	2.81
28	—	1.31
30	—	—
32	—	—
34	—	—
36	—	—
38	—	—
40	—	—

(a) *Volume of significance for SPM, with RFT correction of p-values, and SnPM of forepaw images.*

Time Bin (ms)	t-threshold		
	SPM Bonferroni	SPM RFT	SnPM
0	7.67	6.47	5.67
2	7.67	6.46	5.93
4	7.67	6.45	5.73
6	7.67	6.45	5.98
8	7.67	6.45	5.76
10	7.67	6.44	5.91
12	7.67	6.43	5.67
14	7.67	6.44	5.85
16	7.67	6.44	6.17
18	7.67	6.44	5.70
20	7.67	6.43	5.68
22	7.67	6.43	5.83
24	7.67	6.44	5.93
26	7.67	6.44	5.83
28	7.67	6.44	5.62
30	7.67	6.43	5.79
32	7.67	6.43	5.61
34	7.67	6.42	5.86
36	7.67	6.42	5.70
38	7.67	6.42	5.56
40	7.67	6.52	5.56

(b) *Critical t-threshold for SPM with Bonferroni volumetric correction, SPM with RFT, and SnPM, of forepaw images.*

Table 4.6: *Thresholds and volumes of significance for different correction FWE correction methods.*

As with the SPMs there were no significant positive activations belonging to a cluster >1 % the total number of voxels in the image volume at 0 and 2 ms in the SnPMs, however while for the SPMs significant positive clusters were not present from 26 to 40 ms, in the SnPMs there were significant positive clusters at 26 and 28 ms. The shape of the volume of significance in the SnPMs was similar to that found in the SPMs (figure 4.15).

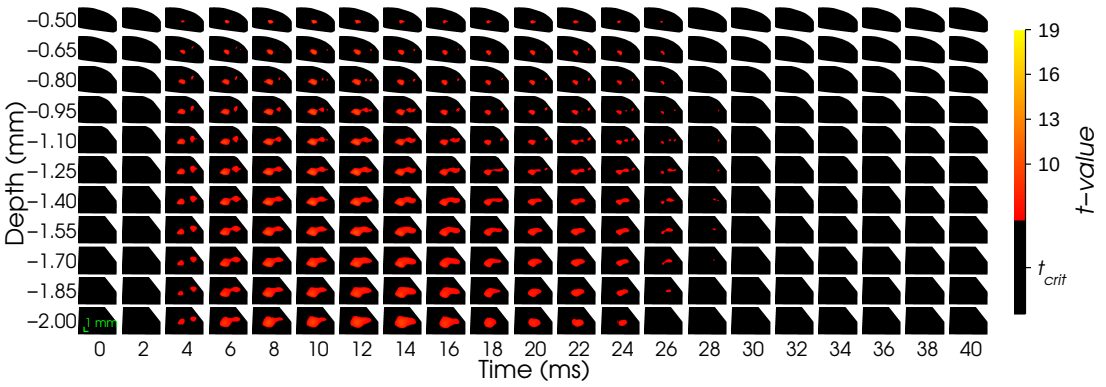

Figure 4.15: *One-sample t-test SnPMs of forepaw images. For* $p_{tcorr}^{FWE} = 0.05$ *the maximum critical value was 6.17. Non-significant changes are black.*

4.3.4 Whole image volume analysis

The hindpaw SPMs had no significant changes belonging to a cluster greater than 1 % of the image volume and so analysis of the masked image volumes was not possible. Similarly, as a result of very little of the visual image volume having significant changes the whole image volume analysis of the masked image volumes was only possible at five time points and so was somewhat nonsensical. Therefore neither are considered here.

The time series of the masked forepaw conductivity changes had no significant changes at 0 to 2 ms, with the first significant time bin being at 4 ms and having a mean conductivity change of 0.033 ± 0.003 % (mean ± SEM). The mean conductivity increased until 10 ms when it reached 0.118 ± 0.009 %, after which it decreased rapidly to 0.079 ± 0.008 % at 16 ms and then decreased less rapidly so that by 24 ms it was 0.059 ± 0.006 %. The maximum EP was similar to the mean conductivity changes, but delayed by approximately 2 ms: the EP started to increase rapidly at 4 ms and reached its maximum of 0.600 ± 0.031 mV at 12 ms, this plateaued until 20 to 22 ms, decreased rapidly until 32 to 36 ms, at which point it plateaued again so that at 40 ms it was 0.336 ± 0.026 mV (figure 4.16a). The time series for the non-masked forepaw conductivity changes showed the same three stages as that of the masked conductivity changes, but at slightly different time bins: rapid increase from 0 to 12 , rapid decrease between 12 to 24 ms, and a more gradual decrease between 24 to 40 ms. In addition to a later maxima, the non-masked

forepaw conductivity changes persisted at a comparable amplitude for a longer time: 10 to 14 ms. Additionally, the non-masked changes were of a much lower amplitude than the masked, being on average an eighth of the masked conductivity changes (figure 4.16b).

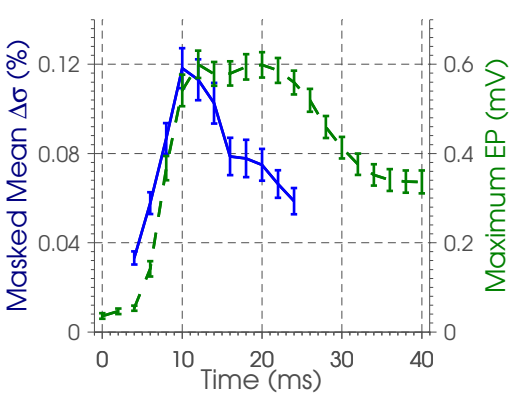

(a) *Masked mean conductivity changes and mean of maximum EPs for forepaw recordings'*

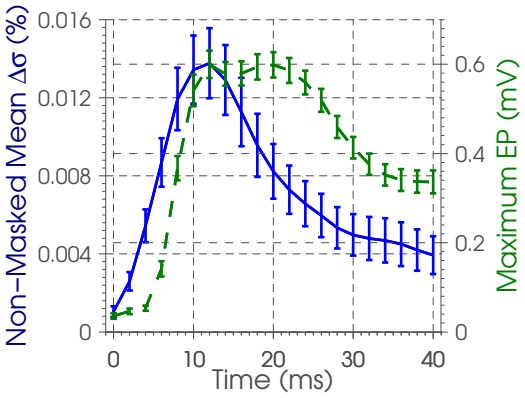

(b) *Non-masked mean conductivity changes and mean of maximum EPs for forepaw recordings'*

Figure 4.16: *The masked and non-masked mean conductivity changes ($\Delta\sigma$), as mean and SEM across recordings (blue: —) on the leftmost y-axis, and the maximum EPs, as mean and SEM across recordings (green: – – –) on the rightmost y-axis for forepaw recordings'. The same layout is used for figures 4.17, 4.18 and 4.19.*

The mean of the non-masked hindpaw conductivity changes varied from -0.0034 to $0.001\,\%$, with an SEM of up to $0.063\,\%$. There was a clear trend in the non-masked hindpaw conductivity changes over the time bins. Conversely, the maximum EP gradually increased from -0.022 ± 0.005 mV, at 0 ms, to 0.052 ± 0.007 mV, at 8 ms, after which it more rapidly increased to its maximum of 0.630 ± 0.080 mV, at 16 ms. This then plateaued until 26 ms, decreased rapidly until 36 to 38 ms, at which point it plateaued again so that at 40 ms it was 0.307 ± 0.050 mV (figure 4.17).

The mean of the masked whisker conductivity changes were significant at all time points, with the mean conductivity change being $0.0070 \pm 0.0008\,\%$ (mean±SEM). The mean conductivity increased until 8 ms when it reached $0.039 \pm 0.004\,\%$. Although there was a low gradient between 4 to 10 ms, after 10 ms the conductivity change decreased rapidly to $0.0130 \pm 0.0009\,\%$ at 16 ms and then, although varying, was plateaued over the following time bins, so that by 40 ms it was $0.013 \pm 0.002\,\%$. The maximum EP at 0 ms was 0.058 ± 0.061 mV, had a small decrease to 0.002 ± 0.006 mV at 2 ms and then rapidly increased to 0.377 ± 0.056 mV at 6 ms. After this first peak there was a decrease to 0.262 ± 0.033 mV at 10 ms, which then, less rapidly than for the first peak, increased to 0.402 ± 0.025 mV at 18 ms, with a subsequent gradual decrease so that at 40 ms it

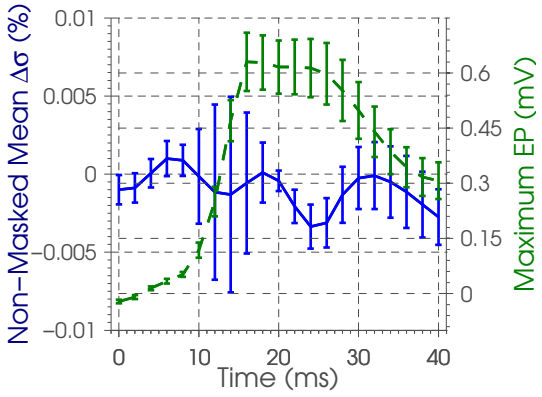

Figure 4.17: *The non-masked mean conductivity changes (blue: —) and the maximum EPs (green: – – –) for hindpaw recordings'.*

was 0.202 ± 0.027 mV (figure 4.18a). The time series for the non-masked mean whisker conductivity changes showed the same three stages as that of the masked conductivity changes, but with a sharper maxima that only plateaued over 2 time bins. Moreover, the non-masked whisker conductivity changes had a decrease between 16 to 40 ms, while this was more of a plateau for the masked changes. Additionally, the non-masked changes were of a much lower amplitude than the masked, being on average a third of the masked conductivity changes (figure 4.18b).

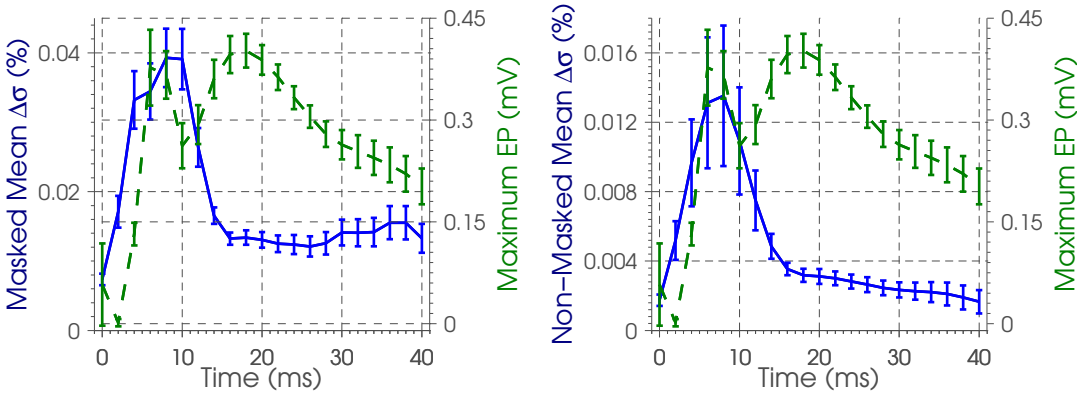

(a) *Masked mean conductivity changes and mean of maximum EPs for whisker recordings'*

(b) *Non-masked mean conductivity changes and mean of maximum EPs for whisker recordings'*

Figure 4.18: *The masked and non-masked mean conductivity changes (blue: —) and the maximum EPs (green: – – –) for hindpaw recordings'.*

The mean of the non-masked visual conductivity changes at 0 ms was -0.0020 ± 0.0004 %, and, excluding a small decrease to -0.003 ± 0.002 % at 15 ms, grad-

ually increased to its maximum of $0.016 \pm 0.004\,\%$ at 135 ms. This then gradually decreased to nearly zero, being $0.0002 \pm 0.0007\,\%$ at 255 ms. The maximum EP was similar to the mean conductivity changes: the EP at 0 ms was 0.002 ± 0.007 mV and started to increase gradually at 15 to 30 ms, reached its maximum of 0.418 ± 0.044 mV at 120 ms, then gradually decreased so that at 255 ms it was approaching zero, being 0.059 ± 0.011 mV (figure 4.19).

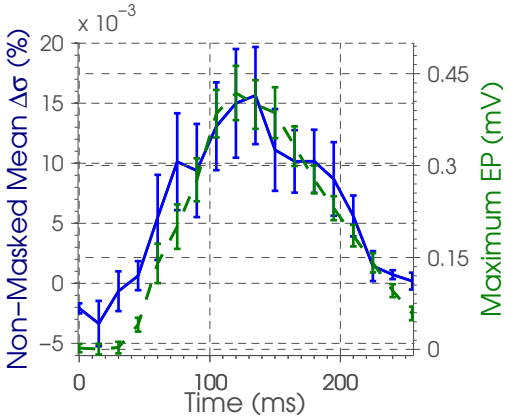

Figure 4.19: *The non-masked mean conductivity changes (blue: —) and the maximum EPs (green: – – –) for visual recordings'.*

4.3.5 Region of interest analysis

The significant (masked) area employed in the ROI analysis of the forepaw consisted of 96 columns, 60 of which were excluded for having too many NaN values, with 8 of the remaining 36 having a significant regression,. The significant regressions were located in a strip across the craniocaudal aspect of the imaging area, with one lateral significant column. All of the the 8 significantly probable fits were upward facing (figure 4.20c). The peak latencies of 3 columns were negative, -2 to -0.769 ms, but were positive for the remaining 4 columns, 0.63 to 5.364 ms. There was a group of 4 to 5 columns with a latency to the most superficial layer of 1 to 5 ms, while 3 columns on the edge of the ROI analysis area had a much slower spread from the central layers into the deepest and most superficial layers. (figure 4.20d). For all of the 7 columns the peak latency was earliest in the middle layers, that is around layer 8 (a depth of 1.2 mm), but ranged over layers 6 to 11. The mean of the fits had a latency of 1.1 ms, with the earliest peak occurring at -2.614 to -2.576 ms in layers 6 and 7, which correspond to a depth of 1.05 to 1.35 mm (figure 4.20).

For the vibrissae recordings' image volume, which, after masking, contained 330, 177 columns were excluded for having too many NaN values as a result of the masking. Of the remaining 153 columns, 57 had a significant regression, which were located throughout

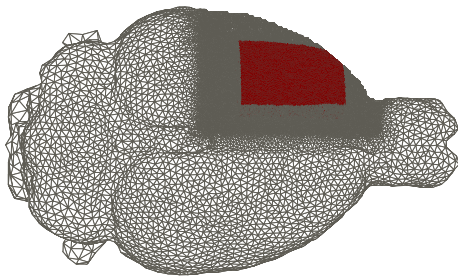

(a) *Region of forepaw FEM mesh determined to be significant using SPM and assessed using ROI analysis.*

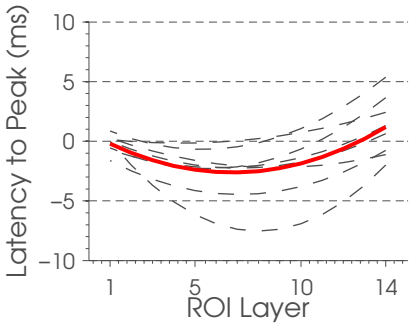

(b) *Second-order regressions (grey line: – – –) and mean regression (red line: —) of image volume. ROI layer is from deep (1) to superficial (14)*

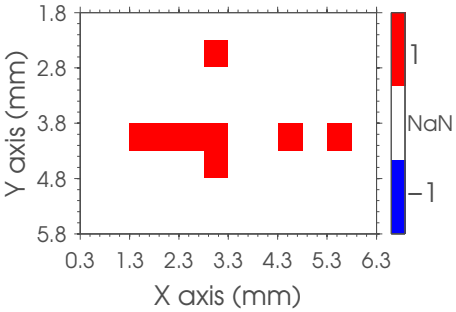

(c) *Sign of fits image volume. Red indicates upward fits, blue downward, and white excluded columns.*

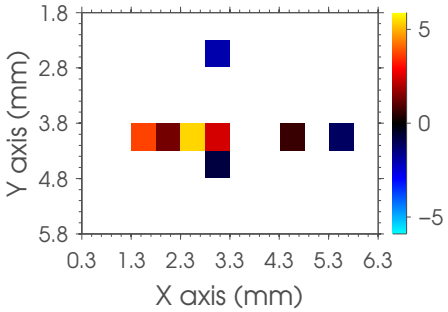

(d) *Latency to peak, in milliseconds, of top ROI of image volume.*

Figure 4.20: *The ROI analysis for the forepaw recordings' image volume.*

the image volume in a heterogeneous nonsensical fashion. Among these there were a fairly even split of 34 upward facing fits and 23 downward facing fits, each with a peak latency varying over a large range from −156 to 1000 ms. The mean of the fits had a latency of 77.38 ms, with its earliest latency at the deepest layer.

For the hindpaw and visual recordings the non-masked data was used as the SPMs revealed no significant activation and activation only in five time points, respectively. In both instances the number of columns under consideration was high as no masking had been undertaken and were 340 and 352, respectively. As with the vibrissae image volume, the significant regressions for the hindpaw and visual case were located throughout the image volume in a heterogeneous nonsensical fashion with a mixture of upward facing and downward facing regression, being 73 and 50 for the hindpaw recordings, and 47 and 58 for the visual recordings. The hindpaw peak latency varied over a large range from −32.1 to 40.4 ms, while for the visual recordings it was −169.9 to 193.2 ms. The mean

of the hindpaw fits had a latency of 4.05 ms, with its earliest latency between layers 3 and 6, which correspond to a depth of 1.2 to 1.8 mm. The mean of the visual fits had a latency of 29.12 ms, with its earliest latency at the deepest layer.

4.4 Discussion

4.4.1 Summary of results

The mean conductivity change images showed physiologically reasonable results matching the literature for all of the stimulation groups except the hindpaw stimulus group. As in chapter 3, using p_{tcorr}^{FWE} values only the forepaw recordings' SPMs had significant results, with p_{tcorr} values having to be used for the other three stimulation groups. The forepaw recordings' SPMs had a highly significant volume at all time points, except 0 and 2 ms and 26 to 40 ms; the vibrissae recordings' SPMs were significant at all time points; the visual at 105 to 165 ms, with a reduction in the significant volume at 120 and 165 ms; and the hindpaw SPMs had no volume of significance at any time bin.

The ROI analysis of the forepaw recordings matched the expectation of a propagation of activity from approximately layer IV into the infragranular and supragranular layers, with the latency of the central most columns being very comparable to the expectations based on the literature. However, propagation was somewhat slower into the deepest layers at the edge of the ROI analysis area, which resulted in the mean being somewhat brisker, with a latency of 1.1 ms, than the 5.6 ms expected from the literature. The ROI analysis for the hindpaw, vibrissae and visual data sets was fairly inconclusive with no clear trend of laminar propagation.

4.4.2 Assessment of results' statistical significance

The forepaw images, as in chapter 3, were significant with both FWE and time correction, indicating a high level of reproducibility in the results. These results are unlikely to have been false positives given that, first, corrections were made for the multiple comparisons, but also given that no significant results occurred in the earliest and latest time bins. Additionally, the results for the control recordings were not significant, and the findings using SnPM were comparable to those of SPM, which both encourage the view that the results are not false positives. Moreover, the onset of significant activity in the forepaw images was at 4 ms, which, while earlier than most reports of the onset latency of F-SEP P1, is similar to the onset latency of 3.7 ± 0.2 ms reported by Jellema et al. [126]. The depth of the significant conductivity changes was also broadly in agreement with expectations from the literature: the tapering near the surface matched the expectation of little or no activity in layer I, and the bulk of the significant conductivity change were at a depth of

1 to 2 mm matching the area approximating layers IV to VI.

The SPMs for the hindpaw recordings' images had no significant results, which is unsurprising given that the mean conductivity change images were of low amplitude with considerable noise. In contrast, the mean of the vibrissae recordings' images was large, both in amplitude and spatial extent, but, despite this, the data was not significant with FWE correction, as was the case in chapter 3. The resultant, only temporally corrected, SPMs showed a large volume of significance in all time bins, with the volume at the time of stimulation being one of the largest. Therefore, while there are encouraging features in the SPMs, such as the volume being tapered towards the surface, the issue of false positives cannot be neglected: uncorrected SPMs must be assessed with knowledge of the questionable validity of such uncorrected results.

The visual recordings' mean image had consistent and clearly visible changes. However, as was noted in chapter 3, the mean conductivity changes (figure 4.19) indicate the conductivity change was considerably later, by 15 to 30 ms, than those reported in the literature. Similarly, the first time bin with significant changes was much later than expected from the literature. These results might be explained, as detailed in chapter 3, by the use of old albino rats to whom a bilateral stimulation was presented.

4.4.3 Assessment of results' spatio-temporal propagation

The mean of the forepaw recordings' masked conductivity changes was $<0.12\,\%$ which although smaller than other cortical conductivity measurements is comparable. Similarly, the latency to peak was at 10 ms, which is comparable to the reported time by which all of the neocortical lamina are activated[126;128]. As in chapter 3, the conductivity change peaked earlier than the maximum F-SEP, and this difference is comparable to the findings noted in the literature: CSDA reveals a sink in layer IV that peaks 2 to 3.6 ms prior to the P1-N1 latency to peak[125;126;128].

The ROI analysis of the forepaw recordings appears to indicate that accurate measurement of the spatio-temporal propagation of neuronal activity was measured across the forepaw image set. The expectation was of activity starting in the bottom aspect of layer IV, spreading first deeper and then superficially, so that it ascends through the laminae and reaches the uppermost layers in approximately 5 to 6 ms[126;128]. All of the significant regressions had a pattern of propagation which was initiated at a depth of 1.05 to 1.35 mm, which corresponds to layer V, with most spreading to the deepest layers in <2 ms and then into more superficial layers in approximately 4 to 6 ms. Although, three columns' spatiotemporal propagation were somewhat different from the central columns', the difference was not due to the sign of the fit, but rather that spread downwards took a similar time to the superficial spread. It could be postulated that this difference indicates these columns are from association cortical areas, which would be further from the centre

of the area of activity. In support of this hypothesis is that association cortical areas have more numerous 'output' projections and somatosensory projections to the thalamus arise in layer VI[122]. Unfortunately, the literature review in chapter 1 did not reveal any evidence of the latency of these connections, and therefore this explanation of the origin of these latencies must remain a hypothesis.

The time series of the hindpaw recordings' unmasked mean conductivity changes showed the volumes to have no clear time course and a mean conductivity increase of $<0.0005\,\%$, which is substantially smaller than the expected changes. Consequently, and somewhat as expected from the mean images, the ROI analysis yielded heterogeneous results with no similarity to expectations from previously published results. The vibrissae and visual ROI analyses yielded similarly poor results, and therefore it seems most appropriate to disregard this aspect of the analysis for these two stimulation types as well.

The masked mean conductivity changes for the vibrissae recordings were $<0.04\,\%$, and so were around half of that of the forepaw results. However, this is likely due to the masking for the vibrissae recordings' being uncorrected, and therefore a much larger volume of the image being included, which would result in a larger variance in the results that were averaged and therefore an attenuation of the amplitude of the masked mean. This effect was apparent in comparison of the masked and non-masked means within a stimulation group. Nonetheless, the maximum conductivity changes are still comparable to those previously reported. Additionally, the latency to peak was approximately 8 ms, which is also comparable to the latency to peak of V-SEP P1 and of the activity in layers IV and V[53;54;110;138;140;146;149].

The mean of the non-masked conductivity changes for the visual recordings' was $<0.016\,\%$, which was a tenth of the masked forepaw conductivity changes and vibrissae recordings, and, as discussed in chapter 3, may be understood from the fact that only around 50 % of V1 is flash stimulus responsive[153]. The latency to peak was approximately 120 ms, later than the reported timing of even N2[158], but, as already detailed in chapter 3, this might be explained by considering the choice of an albino strain and the bilateral nature of the stimulus.

4.4.4 Assessment of effect of methodological alterations

A clear indication of the improvements yielded by the methodological alterations employed in the present study is that although in chapter 3 significant results occurred at 2 ms, they did not occur until 4 ms in the present study, which is more comparable to the reported onset latency of F-SEP P1[126].

The findings of work examining the effect of non-optimal inversion with a planar array indicate that reconstructed perturbations are expected to be mislocalised and

blurred[213–215]. Therefore, given the non-optimal inversion employed in chapter 3 it might have been expected that alterations to the inversion might have reduced the area of significance, and indeed this was the case. In addition to this, the simulations undertaken in this study indicate that the use of one electrode position for all reconstructions would result in a similar mislocalisation of the reconstructed change, and so individual electrode positions would similarly be expected to reduce the area of significance. Indeed, the area of significance, in the ROI analysis, was $1.25\,\mathrm{mm}^2$, as compared to an area of $12.25\,\mathrm{mm}^2$ in chapter 3. This is a reasonable indication of the efficacy of the methodological alterations as the significant area in chapter 3 was greater than the entirety of the rat's somatosensory representation of the face [131]. Similarly, the significant columns in chapter 3 were in the periphery of the imaged volume, whereas in the present study the area of significance was more centralised, as would be expected given that the electrode arrays were placed to be approximately centralised over the forepaw representation.

4.4.5 Study limitations

Although the electrode realignment procedure applied in this chapter is clearly preferable to the assumption of a fixed electrode location employed in chapter 3, there are still limitations in this aspect of the study. The electrode realignment, while validated in a single example and intuitively simple, was not fully validated; it is unclear how much alignment is needed, or alternatively what quantity or localisation error can be tolerated with a planar array on a curved surface. Moreover, aligning the electrode arrays based upon the EPs relies upon the cortical representations between rats being sufficiently similar and producing a sufficiently similar topography. Nonetheless, these are somewhat more reasonable assumptions than those applied in chapter 3.

The use of higher resolution and anatomically accurate FEM meshes was an improvement over the coarser asymmetrical mesh employed in chapter 3. Nonetheless, the meshes were not specific or even scaled for each rat's anatomy, and while the effect of this is presently not clear in the literature, in the absence of evidence to the contrary it would seem most appropriate to have had at least scaled the meshes to each individual rat's brain size, perhaps based on bony landmarks. On a similar note, whilst improvements in the inversion were employed there are still uncertainties regarding the optimal approach in imaging fast neural changes with EIT using a planar array. The choice of Tikhonov regularisation was one based upon published work, simulation studies and tank studies, but in all instances the perturbation is a continuous spheroidal or ellipsoidal object, which is unlikely to be representative of the nature of the conductivity changes, which might be expected to consist of more internally diffuse changes existing in multiple spatially separate groups.

The image scaling employed in this current study was an attempt to compensate

for the effect of different hyperparameter values introducing an artificial inter-recording variance, and so was done for a similar reason to the scaling employed by Gilad et al., but with fewer assumptions[90]. Nonetheless, this approach of proportional scaling was not rigorously validated: proportional scaling did not result in the control recordings reaching significance, but it did limit the ability to analyse the amplitude of the conductivity changes.

Many of the uncertainties regarding the validity of employing second-level SPM for EIT images of fast neural activity that were detailed in section 3.4.4, were addressed by employing SPM on control images and by using SnPM. However, this in turn raises new questions, as it will not always be possible to undertake the same SnPM for all EIT images of fast neural activity. Therefore further examination the appropriateness of variance smoothing in EIT images of fast neural activity, or suprathreshold cluster analysis may be required. These approaches may be essential for the technique to be applied to data with lower degrees of freedom than the forepaw cohort.

There are also limitations that are inherent to the paradigm employed by Gilad et al., which were discussed in chapter 3 and so are only briefly revisited here. The temporal smoothing effect of the ±125 Hz bandwidth makes interpretation of the spatio-temporal propagation of activity difficult as the bandwidth has a smoothing effect over 8 ms, whereas translaminar spread of activity typically occurs in the time scale of 1 to 2 ms. Similarly, much of the neurophysiological literature is derived from somatotopic stimulation as opposed to the coarser stimulation employed by Gilad et al.[90], which, without comparator measurements, makes it difficult to ascertain the nature of some aspects of the results.

Of particular note is the amplitude of the electrical stimulation employed by Gilad et al., which is approximately two orders of magnitude greater than the threshold at which the stimulation would be insensible[172], and is certainly therefore resulting in an additional nociceptive component to the stimulation. The consequence of the stimulation having such a component is that nociceptive stimuli are transmitted by different neurons along different pathways compared to those of mechanoreception and other sensory inputs. Consequently, the spatio-temporal propagation of neural activity resulting from such stimuli is different to that which does not contain a nociceptive component[129], which therefore makes comparison to the literature reviewed in chapter 1 difficult.

In addition to the limitations of the data set, the spatio-temporal propagation analysis itself had some limitations: the ROI analysis used a 2^{nd}-order model, which might not have a sufficient number of parameters to describe the propagation; however, increasing the number of parameters would potentially over-parametrise/over-fit the data and undermine any conclusions regarding spatio-temporal propagation.

4.4.6 Recommendations for future work

This study was a more rigorous and refined application of the first statistical analysis of an EIT imaging set of fast neural activity that was undertaken in chapter 3, and has yielded even more encouraging results for the forepaw recordings' data.

As detailed in chapter 3 future studies could profit from investigating the effect of varying the EIT image processing steps and their effect on the results of SPM. In addition to this, the application of SnPM might be further explored, particularly its use with smaller data sets and the use of pseudo-t-tests.

Future work should be aimed at undertaking EIT imaging of fast neural changes in the presence of cross-validation measurements, such as the use of VSD, LFP or CSDA in order to directly cross-validate any conclusions made using EIT, and then not only could population statistics and conclusion be made, but analysis of individual images be confidently undertaken. Moreover, the use of cross-validation techniques would offer the unique opportunity to determine the most appropriate FEM mesh approaches, such as the validity of generic against generic scaled or unique, specific meshes, and to determine the optimal inversion technique to yield results that best reflect the underlying neurophysiological changes.

Chapter 5

Electrical Impedance Tomography of Fast Neural Activity Following Physiological Vibrissae Stimulation: a Feasibility Study

5.1 Introduction

The work undertaken by Oh et al. and Gilad et al. [64;90], coupled with the analyses performed in chapters 3 and 4, yielded encouraging results suggesting that EIT of fast neural activity is possible in an anaesthetised rat model. However, there were several aspects of these studies that would need to be refined before EIT of fast neural activity might be employed in neuroscientific research applications. The previous work employed a non-physiological stimulus: electrical stimulation to the entirety of the forepaw, hindpaw or vibrissal pad, or bilateral stroboscopic visual stimulation. In addition to this, the results suffered from a poor temporal resolution of 8 ms, and the results could only be compared to the neurophysiological literature. Therefore it would be beneficial for a study to employ a higher carrier frequency, facilitating an improved temporal resolution, a physiological somatotopic stimulation and undertake such recordings in parallel with other neurophysiological measurements. However, this would require alteration of many aspects of the established fast neural EIT paradigm. Moreover, the use of a somatotopic physiological stimulus, and a higher carrier frequency would be expected to reduce the amplitude of the impedance changes. Within this chapter the feasibility of making such alterations is explored.

5.1.1 Rat vibrissal sensory system as a physiological model

The requisite first step in assessing the feasibility of a new paradigm is to establish what aspect of cortical processing is to be investigated: the chosen system was the rat vibrissal sensory system. This decision was made on multiple grounds: prior experience within the UCL EIT group, the existence of a substantial body of literature regarding the rat vibrissal sensory system, and because of several unique characteristics of the rat vibrissal sensory system. As detailed in chapter 1, the vibrissal cortex has a clear cortical topography of modular translaminar subunits, known as barrels, which are visible in unstained slices with light microscope, with each barrel having a one-to-one mapping with each of the mystascial macrovibrissae[97], which, coupled with the ease of stimulation, by whisker vibration, allows for comparatively simple somatotopic mapping. In addition to this, variation of whisker stimulation parameters is comparatively simple and such variation is known to yield different results. Therefore it is ideal to explore these in a cross-validation study. Lastly, of the four previously employed stimulation paradigms, the rat vibrissal sensory system has the largest cortical representations, with macrovibrissae's cortical representation being 4.7 to 6.4 mm^2, and vibrissal stimulation produces the largest amplitude EPs[131], therefore making the difficult task of EIT following physiological stimulation easier.

5.1.2 Rat vibrissal stimulation

5.1.2.1 Processing of different stimulation parameters

The functional processing of the rat vibrissal sensory system was covered in section 1.8.6.4 of chapter 1, although some aspects of the processing of different stimulation parameters were not explored. Therefore, further detail is given here regarding the processing of the direction of whisker displacement, the frequency of stimulation, and the processing of stimulus amplitude and velocity.

It has been known for some time that the rat vibrissal sensory system has direction selectivity when responding to whisker deflection, as is apparent from single unit recordings, in which different single units have been shown to have different direction selectivity[109]. This selectivity is present in the primary afferents, trigeminal ganglion and in the thalamic structures[216], with RtN having a modulatory role in direction selectivity[217]. This direction selectivity reduces with each step towards S1: the trigeminal ganglion has marked selectivity, VPM has somewhat less selectivity and this is reduced further in the cortex[216]. Furthermore, direction selectivity is greater with lower velocity displacements, although unaffected by the amplitude of whisker displacement[218]. Wilent and Contreras explored the intracoritcal mechanism of this direction selectivity by making intracellular measurements in layers III and IV, whilst randomly displacing

a single whisker in one of eight directions, each spaced 45° apart. It was determined that direction selectivity results from a temporal shift of excitation relative to inhibition, with excitation preceding inhibition in the preferred direction of displacement, which in their work was the forward/rostral displacement. This separation between excitation and inhibition progressively decreases as the deflection direction moves further from the preferred direction [219].

The effect of stimulation frequency has also been explored. Until recently, the most common understanding of the effect of stimulation frequency was that, with increased stimulation frequency, there is a decrease in the probability of spiking [109], and with frequencies of 5 to 10 Hz there is adaptation in the cortical response and spatial tuning as compared to stimulation at 1 Hz [142;220]. Further exploration has revealed that for stimulation frequencies of 2, 5 and 8 Hz, the spike activity in the brainstem, thalamus, and cortex is at first the same for all frequencies. However, once a steady state is reached, after 3 s of stimulation, higher frequency stimulation results in a lower response. In addition to this, once this steady-state has been reached, the onset latency for the higher frequencies is delayed compared to the immediate post-stimulus onset latency and the 2 Hz stimulation onset latency, while the offset latencies are unchanged [221;222].

However, there have been additional studies indicating that coding of much higher frequencies also occurs. While there is significant VPM and S1 spiking adaptation for stimulation at 2 to 5 Hz, the highest firing rate after 5 s post-stimulus is in the 5 to 12 Hz range, implying a high pass effect of increased total spike rate over a longer time window. Moreover, the fundamental resonance frequencies of the whiskers range from 100 to 700 Hz and sensitivity to deflection amplitude is greater at 8 Hz than at 1 Hz [220]. Ewert et al. suggested that the lack of previous high stimulation frequency data was due to the choice and depth of anaesthesia and so examined high frequency stimulation in lightly isoflurane anaesthetised rats. MUA recording for stimulation from 15 to 700 Hz revealed phase-locked responses up to 700 Hz which did not suffer from adaptation [223].

The effect of stimulus deflection velocity and amplitude has also been examined. Whisker deflection velocity is coded in layer Vb and linear increases in spiking activity occur with increases in velocity. The same trend, although the trend maybe offset, is observed over the different macrovibrissae [109;224]. Similarly, increases in whisker deflection amplitude result in linear increases in spiking, with deflection amplitude resulting in changes in the layer IV responses [109;224].

5.1.2.2 Choice of stimulators

While undertaking a study centred upon whisker stimulation there are certain key requirements of the stimulator. The key considerations are an ability to stimulate any single whisker, and ideally subsets of whiskers, in any direction of displacement, and

to be able to adjust the parameters of the whisker stimulation. Stimulation frequency should be adjustable up to around 10 Hz, as the natural whisking frequency is approximately 8 Hz[225], and adjustment to the displacement amplitude and velocity up to several millimetres and hundreds of millimetres per second, respectively, is also desirable. In stimulating the whisker it is important that the stimulator does not produce audible artefacts that may result in auditory EPs nor any electromagnetic noise that might affect experimental apparatus.

There are multiple choices of stimulation method, each with their own advantages and disadvantages. The simplest option is manual stimulation[135], with either a brush or one's fingers. However, while this is an ideal option for preliminary testing, such as ensuring correct electrode localisation, the approach suffers from inherent non-reproducibility, an inability to accurately vary stimulation parameters, and difficulties with synchronisation preventing reliable averaging of trials. Another option is electrical stimulation, which can be achieved with the insertion of a pair of stimulating electrodes in the vibrissal pad[54;121;145]. While electrical stimulation is technically simple and allows for repeated trials to be averaged, the resultant signals can be obscured by stimulus artefact[121], the stimulation can cause unnecessary pain for the animal, and the stimulus cannot be easily confined to a single whisker. An alternative class of stimulators are mechanical stimulators, which offer reproducibility, varying ability to alter stimulation parameters and an ability to confine the stimulus to a subset of whiskers or a single whisker. However, mechanical stimulators are not without drawbacks and are also more technically complex to implement.

Air-puff simulators allow for relatively simple mechanical stimulation[221], with easy adjustment of stimulus frequency, although the maximum achievable displacement velocity is limited as is control of the displacement amplitude. Also exact quantification of stimulation with air-puff based stimulators can prove difficult, as can stimulating a subset of whiskers. Solenoid based stimulators have also been used for whisker stimulation[123], and while these offer better control of the stimulus, they also generate loud auditory signals that may result in unwanted EPs and also produce electromagnetic interference. Magnetic whisker stimulation has also been undertaken[124;141], which involves the attachment of wires or small magnetic clips to whiskers, or the application of magnetic paint to the whiskers. Magnetic stimulation allows for all the desirable features of whisker stimulation, such as variance of stimulation parameters. However, the use of electromagnetic equipment may disrupt other experimental apparatus.

Servo-controlled stimulators provide precisely controlled displacement and velocity[226], moreover, servo-controlled displacement is widely implemented commercially, therefore they are easy to obtain and simple to implement. However, the inertia inherent to the operation of a servo-controlled stimulator limits the maximal velocity, additionally

they produce substantial electromagnetic noise. Piezoelectric actuators offer an alternative approach for precise displacement, and allow for high velocity displacement without electromagnetic noise and have proved so popular for whisker stimulation that a 24 bender system allowing individual displacement of 24 macrovibrissae was developed by Jacob et al. [227]. However, piezoelectric actuators are expensive, are complex to control, and the maximum possible displacement is much smaller than for other stimulation techniques.

Given the above considerations, certain stimulation techniques are not appropriate for an EIT study of fast neural activity following whisker stimulation. Manual stimulation cannot be used as averaging is required in EIT, electrical and air-puff based stimulators are not appropriate for future somatotopic stimulation, and solenoid, magnetic and servo-controlled stimulators carry a risk of electromagnetic noise which given the low SNR of EIT recordings may prevent accurate data collection. The remaining most appropriate option would be a piezoelectric stimulator, which given the stereotactic frame required for the animal preparation has the additional benefit of occupying very little space. Moreover it allows for accurate variation of stimulation parameters, and with the addition of an armature to a piezoelectric wafer the maximum possible displacement amplitude can be increased.

5.1.3 Purpose

The overall purpose of this study was to determine the feasibility of using EIT to image fast neural activity following physiological vibrissae stimulation. This was to be examined using a higher carrier frequency to allow for improved temporal resolution. To validate the ability to record impedance changes following physiological vibrissae stimulation the stimulation parameters were varied during single channel measurements to determine answers to the following questions:

(1) Are the impedance changes significantly different for different stimulation parameters and are these trends in agreement with previously published results?

(2) Which stimulation parameters would be optimal for EIT imaging of fast neural activity following physiological vibrissae stimulation?

(3) If a future cross-validation study were to incorporate imaging the effect of varying a stimulation parameter which parameter should this be?

In addition to this, the use of a higher carrier frequency needed to be validated through the use of control recordings. The final aim was to determine how few whiskers need to be stimulated to allow for EIT imaging to be undertaken.

5.1.4 Experimental design

At the outset of this study it was unclear whether impedance changes could be measured following physiological vibrissae stimulation and so this was examined with a series of single channel impedance measurements. Therefore, initially stimulation of a group of 16 whiskers was undertaken and variation of stimulation parameters explored. In addition to this, while the literature suggested that a maximal response was expected for low frequency stimulation, all previous EIT recordings of fast neural activity in the UCL EIT group had been undertaken with 2 Hz stimulation. Thus, whilst examining the effect of varying stimulus deflection amplitude and velocity, with stimulation of 16 whiskers, recordings were made for 1 and 2 Hz stimulation.

The results collected with stimulation of 16 whiskers indicated that reproducible changes were measurable and that the impedance changes were largest for a 1 Hz stimulation. Therefore the effect of altering stimulation parameters was examined when only a single whisker was stimulated, and, whilst examining the effect of varying stimulus deflection amplitude and velocity, recordings were only made for 1 Hz stimulation. To ensure that the recorded changes were not artefactual or affected by the injected current, current-only/no stimulus, post-mortem and variable current amplitude control recordings were made.

The single channel measurements indicated that impedance changes could be measured following physiological vibrissae stimulation and that they were not due to artefactual changes. Therefore, using a maximal amplitude and velocity displacement, with stimulation at 1 Hz, EIT imaging of these changes was undertaken for stimulation of 1, 4, 8 and 16 whiskers and the impedance changes and reconstructed images compared.

5.2 Methods

5.2.1 Animal preparation

Female Sprague-Dawley adult rats were used for recordings. Anaesthesia was induced in a perspex box into which a mixture of $4\,\mathrm{l\,min^{-1}}$ O_2 and isoflurane at 4 % was introduced. Once anaesthesia had been induced, the rat was placed on a nose cone and the isoflurane reduced to <3.5 %, ensuring an areflexic state and respiratory effort were maintained. Areflexia was determined by assessment of withdraw response to painful stimuli (toe pinch) and corneal reflexes; minimal corneal reflexes were tolerated during EP and EIT recordings, but not during the surgical procedures. First, 1.5 ml of carprofen was administered subcutaneously for pain relief, then an endotracheal tube (Vet Tech Solutions Ltd., UK) was introduced following a tracheostomy and mechanical ventilation, using a Harvard Apparatus Inspira Ventilator (Harvard Apparatus, Ltd, UK), was

commenced. The isoflurane concentration was reduced to $\leq 2\,\%$, with the dose adjusted to ensure maintenance of an areflexic state. The respiratory rate and tidal volume were calculated automatically by the ventilator based upon the weight of the rat. The rat was initially ventilated in assisted volume mode and switched to a constant-volume mode once the ventilator detected reduced respiratory effort. With mechanical ventilation, a 50/50 gas mixture of O_2 and air, at $0.3\,\mathrm{l\,min^{-1}}$ was used, and the exhaled gases (O_2, CO_2 and isoflurane) were monitored (Cardiocap 5, Datex Ohmeda).

Arterial and venous access was established through cannulation, using 24 G cannulae (BD Insyte/Vialon, Becton, Dickinson U.K. Ltd.), of the right femoral vessels. The arterial blood pressure was monitored using an anaesthetic monitor (Cardiocap 5, Datex Ohmeda) and the mean arterial pressure (MAP) was kept between 90 and 110 mmHg using labetolol and adrenaline as necessary. Increased MAP following a painful stimuli was taken as a sign of inadequate anaesthesia and the anaesthesia was adjusted accordingly. Once intravenous access had been established a constant infusion of propofol (4 to $6.5\,\mathrm{ml\,kg^{-1}}$) was initiated, and the isoflurane reduced to 0 % with adjustment of the propofol to ensure an areflexic state. After 3 to 5 h the required dose of propofol reduced sharply, and became approximately half of the required initial dose.

The rat was then fixed in a stereotactic frame (Narishige International Ltd., UK) in the prone position using earbars. The rat's head was then shaved and the skin incised using a scalpel. The bone was then freed from the periosteum and the suture lines identified. The insertion of the temporal muscle on the left side was cauterized using a bipolar cauterization system (Malis CMC 2, Codman, USA). The insertion line was then incised with a scalpel and the muscle bluntly dissected and reflected off the bone until the zygomatic arch came into view. A craniotomy was performed with the paramedial edge extending 2 to 3 mm rostral to bregma and just rostral of lambda, and the lateral aspect was at the junction of the zygoma to temporal bone, so that the resulting craniotomy was trapezoidal in shape. The craniotomy was performed using a veterinary bone drill (Ideal Micro-Drill$^{\mathrm{TM}}$) with frequent irrigation using 0.9 % saline to prevent heating of the bone. The bone flap was then lifted and the dura incised with micro scissors in a crescent shape and reflected over the midline to avoid damage to the superior sagittal sinus. The electrode array was then placed over the PMBSF using a micromanipulator (SM-15 Micromanipulator, Narishige International Ltd., UK). The brain was frequently irrigated with warm (38 °C) 0.9 % saline solution; to aid this process a piece of cotton wool was placed over the array and this keep moist. A $2.25\,\mathrm{cm^2}$ silver-silver chloride ground electrode was placed under the skin of the right side of the head, opposing the electrode grid. Throughout experiments the core body temperature of the rat was controlled with a homeothermic heating unit comprising a heating blanket in which the rat was wrapped and a rectal probe used to provide temperature feedback to

the system (Harvard Apparatus, Kent, UK). All animal works undertaken in this study were approved by the UK Home Office and in accordance with its regulations (Project number: PPL 70/7450).

5.2.2 Piezoelectric whisker stimulation

A stimulator based on a piezoelectric actuator (PL140.10, PI ceramic, Germany) was used throughout this study. The chosen piezoelectric actuator had a 2 mm maximal displacement, although an extended armature, consisting of a glass capillary tube, was added to the actuator which facilitated easier manipulation of whiskers and increased the maximal possible displacement. The maximal possible displacement, measured using a laser displacement sensor (optoNCDT 1607, micro-epsilon, UK) was found to be 4 mm ($\pm$2 mm) and the minimal rise time was 5 ms[177;228].

The stimulator was held in a 3D printed armature, and the small headstage to hold a glass capillary tube was also 3D printed, which allowed for any of the macrovibrissae to be stimulated. The driving electronics consisted of a driving power unit and a smart self-calibrating control unit, with strain-gauged sensor feedback and proportional-integral-derivative control employed to ensure the desired displacement waveform was achieved[228]. The stimulator was used to displace a whisker or whiskers in the cranio-caudal axis.

5.2.3 Hardware and protocols

Electronic instrumentation comprised a PC controlled, serial-injection, constant current source, which could produce a sinusoidal waveform from 1 Hz to 2 kHz with an amplitude of 0.1 to 100 µA. The system is known as the 'UCL-CS2'[64]. Voltages were recorded with a BioSemi EEG system, which is a parallel record, dc-coupled, battery-powered system, and therefore is fully isolated from the mains power supply, and it communicates with a PC via an optical fibre (ActiveTwo, BioSemi, Netherlands). The system was configured to use 32 channels, although it can measure up to 128 channels, resulting in a sampling rate of 16 kHz per channel and a signal bandwidth from DC to 3.2 kHz.

The employed electrode array was a stainless steel in silicone, 30 channel variant of the platinum in silicone array used previously by Oh et al.. The electrodes were laser cut to provide 30 circular electrodes, 0.6 mm in diameter, hexagonally arranged with a centre-to-centre distance of 1.2 mm. The electrodes were platinised to reduce contact impedance and noise from the electrode-electrolyte interface[64;229].

During single channel measurements, single injection pairs were used for current injection. The pair giving the largest impedance change, based upon a short semi-adjacent protocol centred upon the centre of the EP's activity, was chosen and used throughout

all single channel recordings in a given rat. For EIT data acquisition a protocol referred to as 'combined-protocol' was employed. The 'combined-protocol' was centred upon the area of maximal EP activity with injection pairs made with adjacent, semi-adjacent and injections spanning the entirety of the array[228]. For all impedance recordings, single and multi-channel, the injected current was 50 µA in amplitude at a frequency of 1725 Hz, with the impedance changes demodulated as the changes in a ±300 Hz bandwidth around this carrier frequency.

5.2.4 Single channel impedance data

During single channel measurements, current was applied to a single pair of electrodes for 60 s and voltages were recorded through the remaining 28 electrodes, and averaging was undertaken over repeated trials of one second. In these recordings the boundary voltages were processed to reject noisy channels, defined as channels with, *a*) a boundary voltage less than 100 µV, or; *b*) an interstimulus standard deviation, after averaging, of more than 0.5 µV. 10 % of the remaining channels with the largest impedance changes, typically 3 channels, were then used for analysis. In these channels the peak changes for both the forward and backward whisker deflection were identified and the results assessed by N-way ANOVA. For ANOVA the data were grouped with respect to the parameter being varied, the direction of the whisker deflection, and the rats across which repeats were drawn. Using ANOVA significance was tested for $\alpha = 0.05$. The results of the ANOVA were then examined with multiple comparison tests, using critical values from the t-distribution, after a Bonferroni adjustment to compensate for multiple comparisons significance was tested for $\alpha = 0.05$. All example values are given as the mean±1CI of the FWE corrected 95 % confidence interval for the respective grouping. In one instance, for the effect of stimulus deflection amplitude and velocity with a group of whiskers, this procedure was repeated for the forward and backward deflections separately.

The no stimulus and post-mortem controls were not analysed in this manner. For both of these controls significant impedance changes were defined as changes, after averaging over trials, that were significantly different from the SEM for the corresponding channels over trials by means of a two-sided t-test.

5.2.5 Single channel measurements: whisker group stimulation

While assessing the effect of altering the simulation parameters on impedance measurements while stimulating a group of whiskers, 16 whiskers (α, β, γ, δ and whiskers 1 to 3 for rows C to E) were tied together and attached to the piezoelectric stimulator. Within a given paradigm, for example variation of stimulation frequency, the order of delivering different simulation parameters was randomly permuted using a Mersenne Twister

pseudo-random number generator, that was reseeded based on the current time.

Data were collected to assess the effect of stimulation frequency ($n = 32/N = 2$), with 3-way ANOVA performed on this data, and for effect of the stimulus deflection amplitude and velocity ($n = 80/N = 1$), with 4-way ANOVA performed on this data.

5.2.5.1 Effect of stimulation frequency

To assess the effect of stimulation frequency on a group of whiskers, four stimulation frequencies were employed: 1, 2, 4 and 8 Hz. For all recordings the deflection amplitude was 4 mm with a rise time of 5 ms, giving a velocity of $800\,\mathrm{mm\,s^{-1}}$. Eight repeats at each stimulation frequency were collected in two rats: two repeats in the first rat and six repeats in the second rat.

5.2.5.2 Effect of stimulus deflection amplitude and velocity

To assess the effect of stimulation amplitude and velocity on a group of whiskers, four stimulus deflection amplitudes (1, 2, 3 and 4 mm) and four stimulus deflection velocities (200, 400, 600 and $800\,\mathrm{mm\,s^{-1}}$) were employed. As the velocity for a given amplitude is inversely proportional to the rise time, to alter the velocities this equated to alteration of the rise times. As the shortest achievable rise time of the piezoelectric stimulator was 5 ms this meant that all four velocities were not possible for all four stimulus deflection amplitudes. For all deflection amplitudes and velocities data were collected with a 1 Hz and 2 Hz stimulation frequency. Four repeats at both stimulation frequencies were collected in one rat.

5.2.6 Single channel measurements: single whisker stimulation

While assessing the effect of altering the simulation parameters on impedance measurements while stimulating a single whisker, E2, the whisker was held in a glass capillary tube that was attached to the piezoelectric stimulator. Within a given paradigm, for example variation of stimulation frequency, the order of delivering different simulation parameters was randomly permuted using a Mersenne Twister pseudo-random number generator, that was reseeded based on the current time.

Data were collected to assess the effect of stimulation frequency ($n = 32/N = 2$), stimulus deflection amplitude ($n = 40/N = 2$) and stimulus deflection velocity ($n = 40/N = 2$), with 3-way ANOVA performed on each dataset.

5.2.6.1 Effect of stimulation frequency

To assess the effect of stimulation frequency on a single whisker, four stimulation frequencies were employed: 1, 2, 4 and 8 Hz. For all recordings the deflection amplitude

was 4 mm with a rise time of 5 ms, giving a velocity of 800 mm s^{-1}. Eight repeats at each stimulation frequency were collected in two rats, with four repeats in each rat.

5.2.6.2 Effect of stimulus deflection amplitude

To assess the effect of stimulation amplitude on a single whisker, five stimulus deflection amplitudes were employed: (2, 2.5, 3, 3.5 and 4 mm). For all recordings the stimulation frequency was 1 Hz with a deflection velocity of 400 mm s^{-1}, therefore the rise time was varied depending on the deflection amplitude to maintain the same velocity: (5, 6, 7.5, 8.75 and 10 mm s^{-1}). Eight repeats for each stimulus deflection amplitude were collected in two rats, with four repeats in each rat.

5.2.6.3 Effect of stimulus deflection velocity

To assess the effect of stimulation velocity on a single whisker, five stimulus deflection velocities were employed: (150, 320, 480, 640 and 800 mm s^{-1}). For all recordings the stimulation frequency was 1 Hz with a deflection amplitude of 4 mm, therefore the respective rise times were (25, 12.5, 8.3, 6.25 and 5 ms). Eight repeats for each stimulus deflection velocity were collected in two rats, with four repeats in each rat.

5.2.7 Controls

5.2.7.1 Effect of current controls

To ensure that the injected current was not affecting the neuronal activity, effect of current control recordings were made. Single pair current injection was undertaken at 10 current amplitudes: 5 to 50 µA in 5 µA increments, with the impedance changes analysed as a percentage normalised to the pre-stimulus period. Four repeats for each current amplitude were collected in two rats, with two repeats in each rat ($n = 40/N = 2$).

5.2.7.2 No stimulus controls and dead controls

To ensure that the electronics driving the piezoelectric actuator were not introducing artefactual changes and that any sound produced by the stimulator was not eliciting an auditory EP, control measurements with the stimulator detached were undertaken. This entailed single current pair injections with the piezoelectric actuator in the same positions as used for non-control recordings, but with the headstage and glass capillary tube removed. This control recording was undertaken twice, once in two different rats ($n = 2/N = 2$). Two post-mortem control measurements were also collected, once in two different rats ($n = 2/N = 2$), this entailed making recordings with all components of the experimental set-up in place, but with data collected after the rat had been culled.

5.2.8 Multichannel EIT imaging data

5.2.8.1 Boundary voltage rejection

Multichannel EIT imaging data were collected with stimulation of 1, 4, 8 and 16 whiskers, with stimulation at 1 Hz, and a deflection amplitude and velocity of 4 mm and 800 mm s^{-1}, respectively. These recording were repeated twice in two different rats ($n = 16/N = 2$).

In the multichannel EIT imaging data sets consisted of multiple injection pairs, through which current was injected for 30 s, voltages were recorded through the remaining 28 electrodes. The boundary voltages were processed to reject, by trial, noisy channels, which were defined as channels with, *a*) a boundary voltage less than 100 µV, or; *b*) an interstimulus standard deviation, after averaging, of more than 0.75 µV. The noise rejection based upon the interstimulus standard deviation, was increased as the number of averages was decreased compared to the single channel measurements. The resultant boundary voltages were then averaged over each one second trial for a given injection pair. Of the number of channels remaining after these boundary voltage rejection steps, those that had an impedance change greater than the interstimulus impedance change, that is the noise, were compared for each stimulation type and fit with first-order linear regression.

5.2.8.2 Image reconstruction

Images were reconstructed with the real component of voltage differences using a TD approach at 6 time points centred upon the maximal impedance change, which coincided with the forward deflection. The total time span was 0, 5, 5.65, 5.8, 5.9, 6, 6.1, 6.2, 6.35 and 11 ms, where 0 ms was the time of the forward deflection. The voltage differences were reconstructed into conductivity difference images using a sensitivity matrix reconstruction algorithm[184]. An FEM mesh with refinement over the approximate region of electrode placement and 4 084 974 tetrahedra was used (see section 4.1.3 for details). The position of the electrode array was recorded using a Microscribe 3D digitizer (3DLX, Immersion, USA), although the error in measurement was ±1 electrode diameter and so manual correction had to be performed to ensure electrodes were placed with the correct inter-electrode spacing for the forward modelling. Inversion was performed using Tikhonov regularisation with the hyperparameter set using cross-validation, with λ spanning 1×10^{-20} to 1, in 2000 logarithmically spaced steps, and the cross validation being ten-fold using 10 % of the data for training (see section 4.1.4 for details).

5.2.8.3 Image analysis

To allow for qualitative assessment of the reconstructed images, images of a region around the electrodes, 9.4 mm × 6.5 mm, in the x and y-axis, respectively, were rasterised at

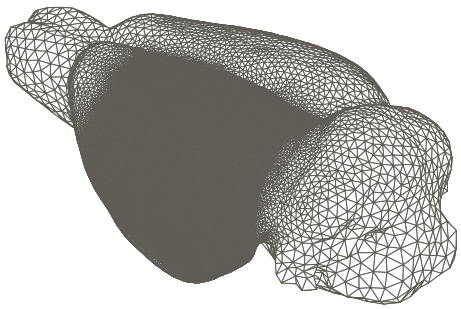

Figure 5.1: *Triangulation mesh of the surface tetrahedra of the FEM mesh of the rat brain used for image reconstruction.*

700 µm on the z-axis, as the approximate depth of layer IV (see table 1.5b). Rasterisation was performed using linear interpolation on a 2-D Cartesian grid whose lattice points were spaced 25 µm apart in each axis. Images were determined, qualitatively, to have a readily identifiable perturbation if there was a single contiguous conductivity increase in the image, that was absent at 0 ms, and that this was clearly separable from any high spatial frequency noise. In addition to this, the tetrahedral solution was partitioned into 100 µm layers normal to the surface (see section 3.2.2.2 for details), and the resultant images were rasterised over a 3-D Cartesian grid whose lattice points were spaced 25 µm apart in each axis. Within these 3-D images the *reconstructed perturbation* was defined as the largest connected group of pixels with conductivity changes greater than 25 % of the maximal conductivity change. The mean of the conductivity changes and volume of the *reconstructed perturbation* were calculated, and the images' SNR was calculated as the ratio between the mean of the *reconstructed perturbation* and the standard deviation of the changes not belonging to the *reconstructed perturbation* (see section 2.2.5 of chapter 2 for details of this procedure).

5.3 Results

5.3.1 Single channel measurements: whisker group stimulation

5.3.1.1 Effect of stimulation frequency

There was a trend of lower amplitude impedance changes with increasing stimulation frequency, with 1 Hz stimulation resulting in a change of -2.866 ± 0.168 µV and 8 Hz

stimulation a change of $-2.018 \pm 0.168\,\mu V$ (figure 5.2). However, a significant difference only existed for the 1 Hz stimulation as compared to the other three stimulation rates ($p < 0.05$), which were not significantly different from one another. In addition to this there was a significant difference between the two rats' data ($p < 0.001$) and the direction of deflection ($p < 0.001$), with the forward deflection having larger changes.

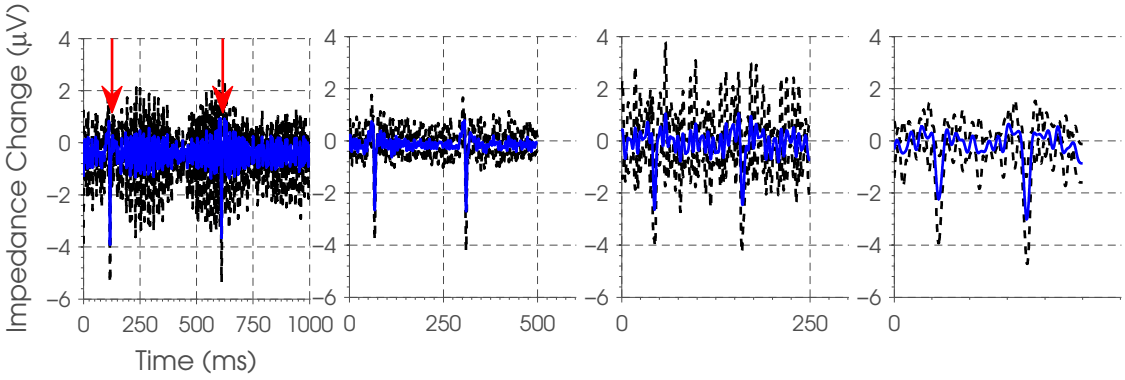

(a) *Average impedance changes for first rat*

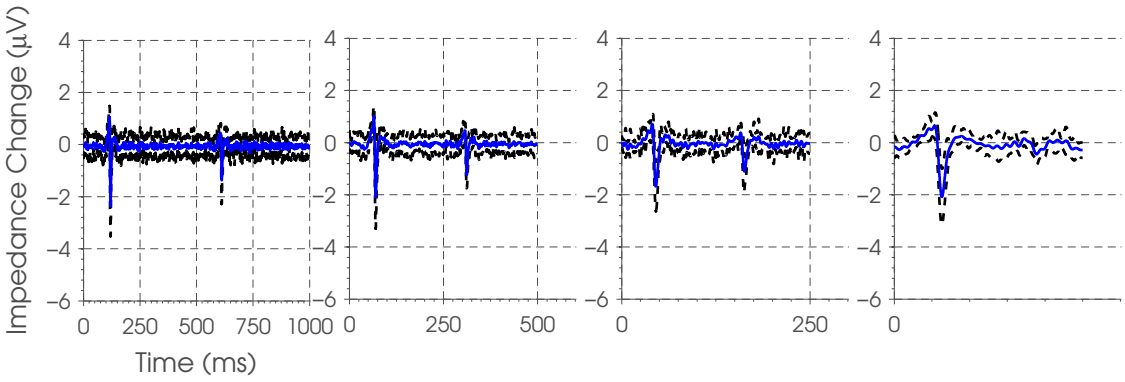

(b) *Average impedance changes for second rat*

Figure 5.2: *Effect of stimulation frequency on a group of whiskers. Each row of subplots show the average (±2SD), over repeats and the top 10 % of channels, for (from left to right) 1, 2, 4 and 8 Hz stimulation frequencies in a single rat. The first peak is the forwards deflection and the second the backward deflection. In the top left subplot the two red arrows are the time of the forward and backward deflection, respectively*

5.3.1.2 Effect of stimulation amplitude and velocity

As for the effect of stimulation frequency, there was a significant difference between the direction of deflection ($p < 0.001$), with the forward deflection having larger changes, and also between the two stimulation frequencies ($p < 0.001$) with the recordings at 1 Hz having larger amplitude impedance changes than those at 2 Hz. Increasing displacement amplitudes resulted in larger amplitude impedance changes. This was most visible in the

first deflection peak. There was a significant difference due to displacement amplitude at both stimulation frequencies ($p < 0.001$): the 4 mm displacement was significantly different from all other displacement amplitudes, and the 3 and 1 mm displacements were significantly different from one another. Despite an observable trend of larger amplitude impedance changes with increasing displacement velocities in the impedance changes associated with the backward deflection, this was not a significant trend ($p > 0.05$). Separate analysis of the two peaks still did not yield significant results ($p > 0.05$) for the effect of displacement velocity, although it did reveal that the effect of displacement amplitude is only significant for the forward going displacement (figure 5.3 & figure 5.4).

Figure 5.3: *Effect of stimulus amplitude and velocity on a group of whiskers stimulated at 1 Hz. Each subplot shows the average (±2SD), over repeats and the top 10 % of channels, for a given amplitude and velocity of displacement. From the bottom row to top row the amplitude of displacement is increased, while from the left column to right column the velocity of displacement is increased. The first peak is the forwards deflection and the second the backward deflection.*

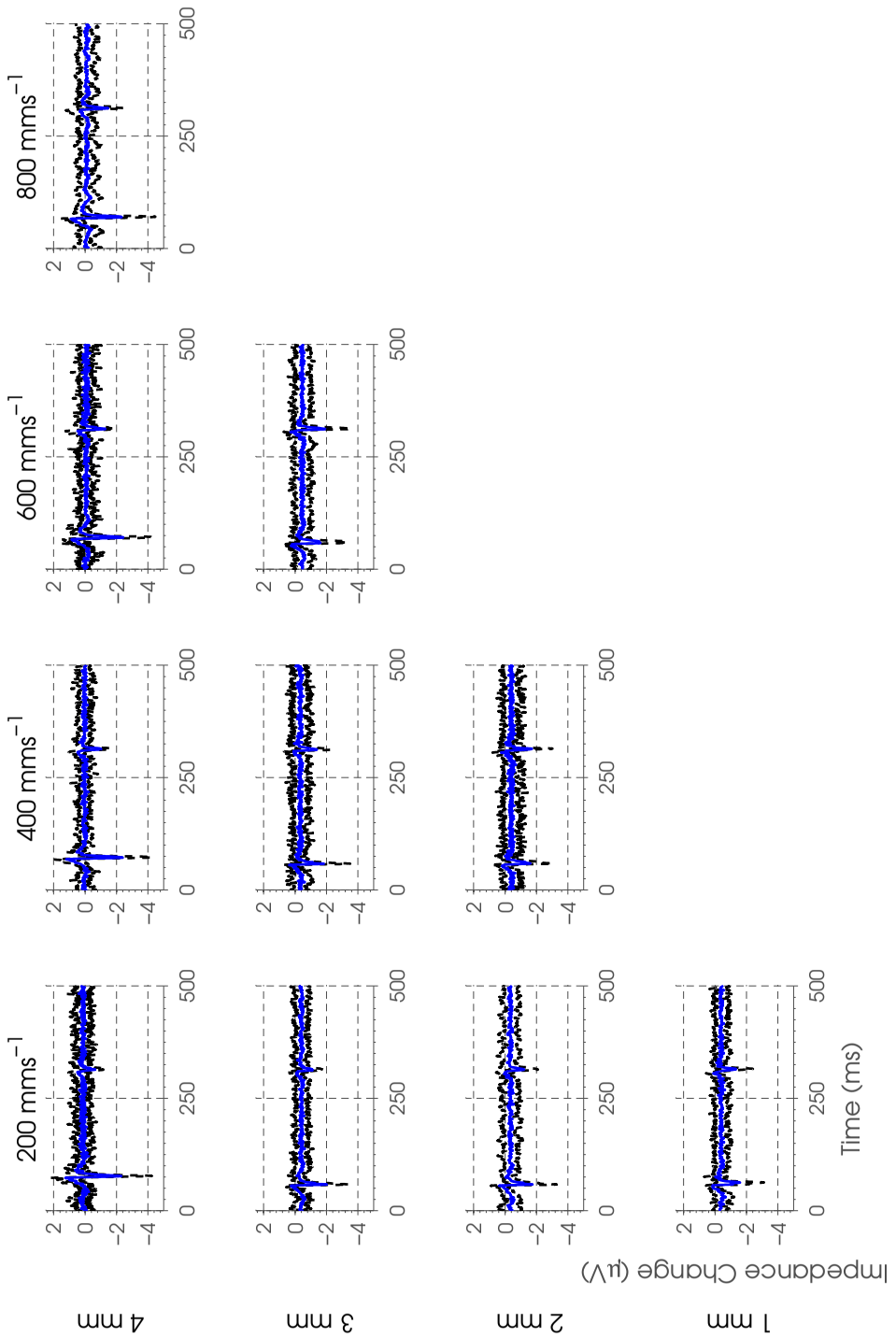

Figure 5.4: *Effect of stimulus amplitude and velocity on a group of whiskers stimulated at 2 Hz. Each subplot shows the average (±2SD), over repeats and the top 10 % of channels, for a given amplitude and velocity of displacement. From the bottom row to top row the amplitude of displacement is increased, while from the left column to right column the velocity of displacement is increased. The first peak is the forwards deflection and the second the backward deflection.*

5.3.2 Single channel measurements: single whisker stimulation

The amplitude of the impedance changes was substantially different between the recordings from the two rats used for the single channel impedance measurements of single whisker stimulation; the same discrepancy between rats was also present in the EPs. A result of this was that fewer channels were above noise (0.5 µV) for the rat with lower amplitude changes, therefore the top 10 % of channels above noise only constituted two channels.

5.3.2.1 Effect of stimulation frequency

As with stimulation of a group of whiskers, there was a trend of lower amplitude impedance changes with increasing stimulation frequency, with 1 Hz stimulation resulting in a change of -3.952 ± 0.328 µV and 8 Hz stimulation producing a change of -0.506 ± 0.328 µV (figure 5.5). The 1 and 2 Hz stimulation frequencies were significantly different from all other stimulation frequencies ($p < 0.05$), while 1 and 2 Hz stimulation were not significantly different from one another ($p > 0.05$). In addition to this there was a significant difference between the two rats' data and the direction of deflection, with the forward deflection having larger changes.

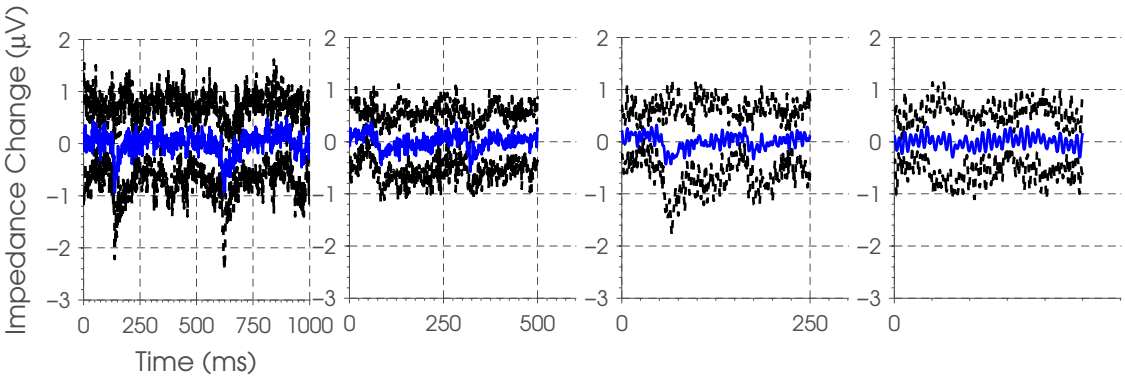

(a) *Average impedance changes for first rat*

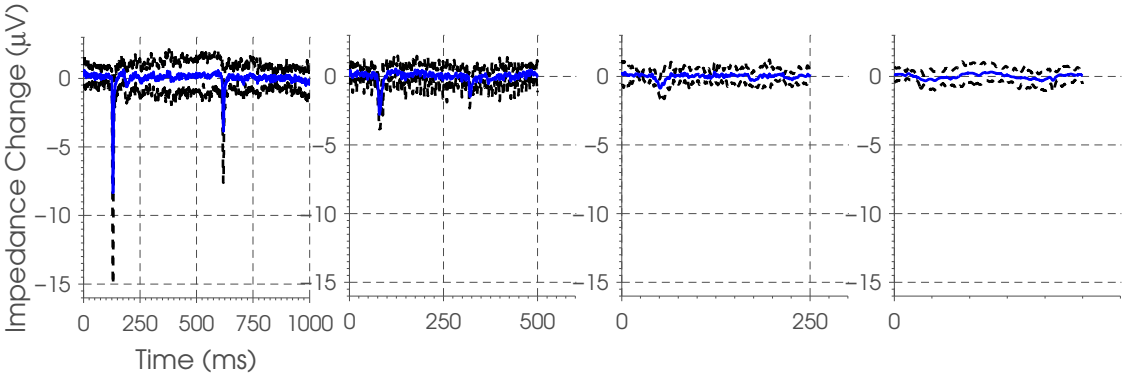

(b) *Average impedance changes for second rat*

Figure 5.5: *Effect of stimulation frequency on a single whisker. Each row of subplots show the average (±2SD), over repeats and the top 10 % of channels, for (from left to right) 1, 2, 4 and 8 Hz stimulation frequencies in a single rat. The first peak is the forwards deflection and the second the backward deflection.*

5.3.2.2 Effect of stimulation amplitude

There was no clearly observable trend with altered stimulus displacement amplitude (figure 5.6); the only displacement amplitude results that were significantly different from any other displacement amplitude were those for a displacement of 3 mm ($p < 0.05$). In addition to this, unlike for all the other data, there was no significant difference between the impedance changes for the two deflection directions ($p > 0.05$). There was, however, a significant difference between the two rats' data ($p < 0.001$).

5.3.2.3 Effect of stimulation velocity

There was no clearly observable trend with altered stimulus displacement velocity (figure 5.7); the only displacement velocity results that were significantly different from any other displacement velocity were those for a velocity of 480 mm s^{-1} which were signif-

icantly larger than those for a velocity of $800\,\mathrm{mm\,s^{-1}}$ ($p < 0.05$). There was a significant difference between the two rats' data ($p < 0.001$) and the direction of deflection ($p < 0.01$), with the forward deflection having larger changes.

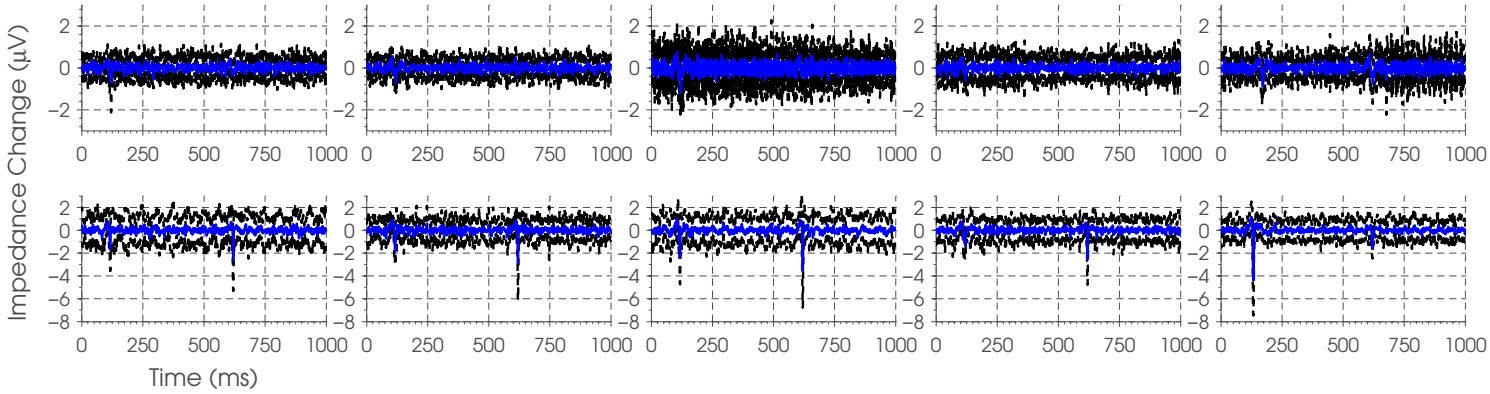

Figure 5.6: *Effect of stimulus amplitude on a single whisker, average (±2SD) over repeats and top 10 % of channels, for amplitudes of (from left to right) 2, 2.5, 3, 3.5 and 4 mm. The first peak is the forward deflection and the second the backward.*

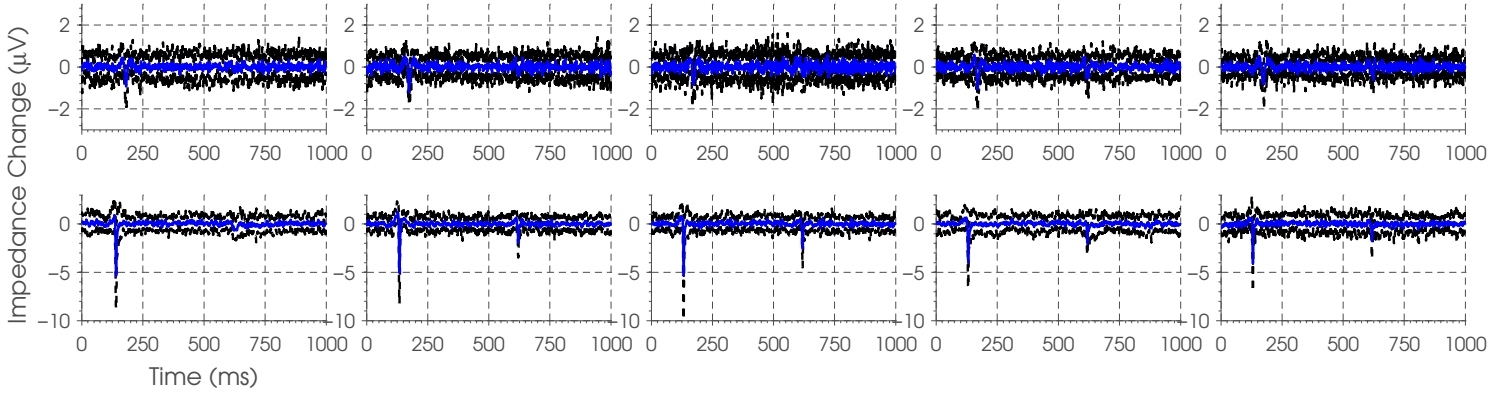

Figure 5.7: *Effect of stimulus velocity on a single whisker, average (±2SD) over repeats and top 10 % of channels, for velocities of (from left to right) 150, 320, 480, 640 and 800 mm s^{-1}. The first peak is the forward deflection and the second the backward.*

5.3.3 Controls

5.3.3.1 Effect of current controls

ANOVA revealed a significant difference with different applied current amplitudes ($p < 0.001$). However, there was no significant difference between the percentage impedance change with a current of 10 to 50 µA ($p < 0.001$). The significant difference in the ANOVA was because there was a significant difference between the data collected with an injected current amplitude of 5 µA and current amplitudes up to 35 µA ($p < 0.001$) (figure 5.8).

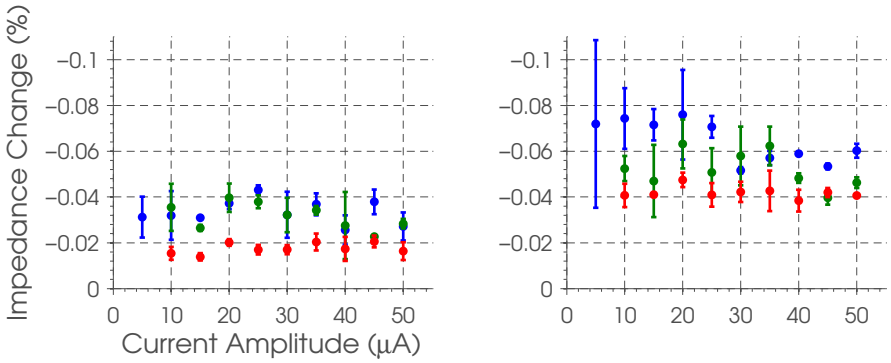

(a) *Impedance changes for first rat and first deflection*

(b) *Impedance changes for first rat and second deflection*

(c) *Impedance changes for second rat and first deflection*

(d) *Impedance changes for second rat and second deflection*

Figure 5.8: *Variable current amplitude control. Each subplot shows the average (±1SD), over repeats and the top 10 % of channels, for different injected current amplitudes. Each subplot is for a given rat and deflection, with the first deflection being the forwards deflection and the second the backward deflection. Within each subplot the differently coloured markers are for different channels.*

5.3.3.2 No stimulus controls and dead controls

There were no significant impedance changes in any of the no stimulus controls or dead control recordings ($p > 0.05$).

5.3.4 EIT with stimulation of variable numbers of whiskers

5.3.4.1 Change in boundary voltages

Visual inspection reveals that as the number of whiskers being stimulated was increased the impedance change was larger and the number of channels with an impedance change increased. In addition to this, the synchronicity of the peaks reduced as more whiskers were stimulated. This most likely occurred because, with stimulation of more whiskers, a larger number were attached to the stimulator at a non-resting angle. As the number of whiskers being stimulated increased, the difference between the impedance changes for the two peaks, due to forward and backwards deflection, reduced (figure 5.9).

The area of central activity was shifted within the electrode array between the two rats' recordings, which reflected a difference in electrode placement, and as a result the number of channels in the protocols was different: 840 channels for the first rat and 1064 for the second rat. The number of boundary voltages rejected in the boundary voltage rejection was similar across number of whiskers being stimulated, except for the the single whisker recordings in the second rat. The number of channels with changes above the interstimulus change in boundary voltages, which was approximately 2 µV, was greater for 4 whiskers as compared to single whisker stimulation for both rats. There was less difference between 4 and 8 whisker stimulation, and there were more channels above noise for stimulation of 16 whiskers (table 5.1).

The mean, over channels, of the changes above the interstimulus change in boundary voltages for the recordings showed a significant linear trend ($p < 0.0001$) of larger amplitude impedance changes with increasing numbers of whiskers, with the coefficient of x for the linear regression being $\beta = -0.056$; the coefficient is negative as larger changes are more negative (figure 5.10).

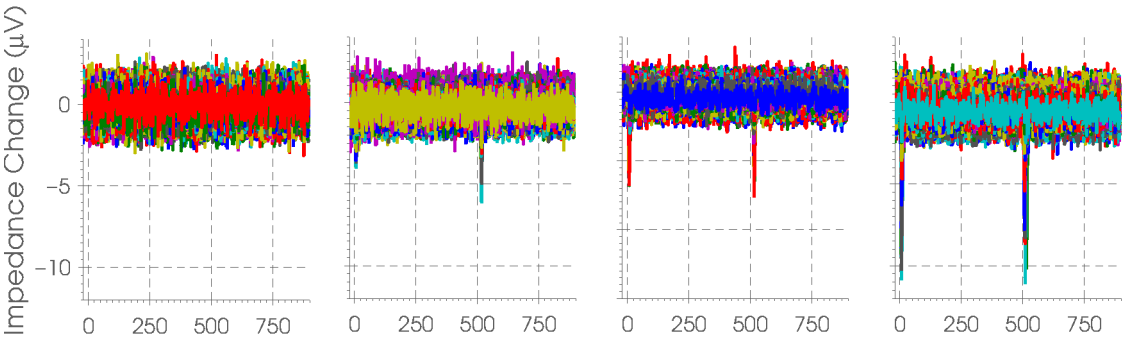

(a) *Example of impedance changes when different numbers of whiskers are stimulated*

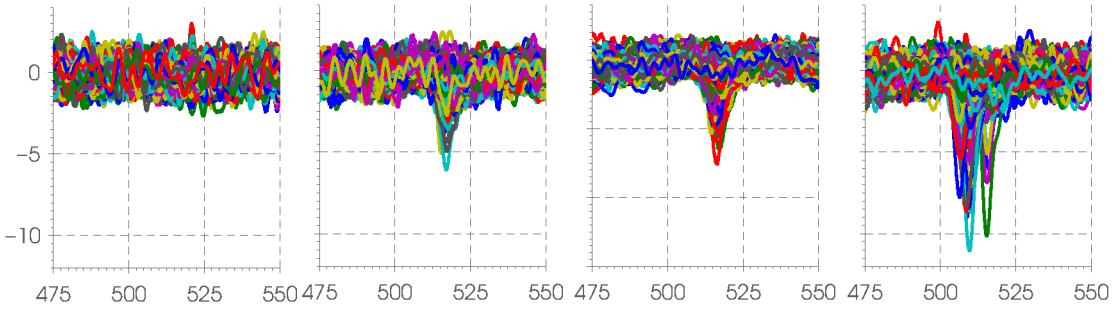

(b) *Magnification of the impedance changes around the second/forward deflection when different numbers of whiskers are stimulated*

Figure 5.9: *Each subplot shows the impedance changes, above the noise threshold, for stimulation of (from left to right) 1, 4, 8 and 16 whisker(s). The first peak is the backwards deflection and the second the forward deflection. Different coloured lines are different recording combinations from the respective imaging dataset*

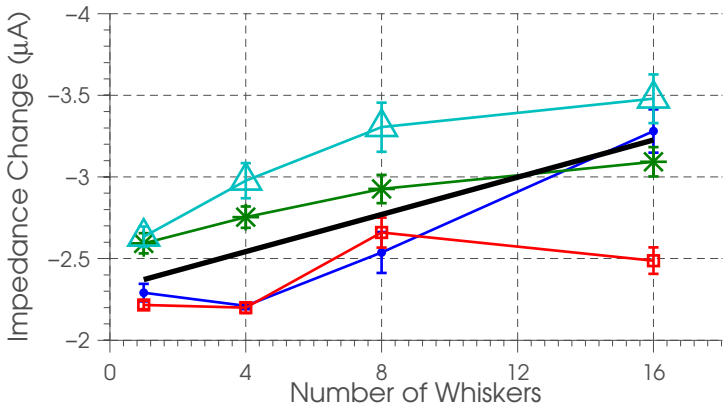

Figure 5.10: *The mean (±SEM) of the impedance changes for stimulation of different numbers of whiskers and the linear regression of these points.* —●— *rat 1 repeat 1.* —×— *rat 1 repeat 2.* —■— *rat 2 repeat 1.* —▲— *rat 2 repeat 2.* — *linear regression.*

No. Channels	1 whisker	4 whiskers	8 whiskers	16 whiskers
Total		840		
Post-rejection	801/783	795/795	806/810	813/812
Above noise	14/34	39/95	63/104	106/153

(a) *Boundary voltages for rat 1*

No. Channels	1 whisker	4 whiskers	8 whiskers	16 whiskers
Total		1064		
Post-rejection	899/871	978/986	985/981	984/988
Above noise	24/37	51/59	86/69	107/105

(b) *Boundary voltages for rat 2*

Table 5.1: *Summary of the number of channels after boundary voltage rejection and the number of channels with an impedance change greater than 2 μV. The above noise values are of the second/forward deflection. In the second two rows the forward slash delimiter separates values from the repeat recordings within a rat.*

5.3.4.2 Image reconstruction: qualitative assessment

In none of the four images of single whisker stimulation was there a readily identifiable reconstructed perturbation, while in only one of the two repeats for each rat was there a readily identifiable reconstructed perturbation of four whisker stimulation. In all of the images of eight and 16 whisker stimulation there was a readily identifiable reconstructed perturbation (figure 5.11). In all images there was high spatial frequency noise in the first 350 µm from the surface.

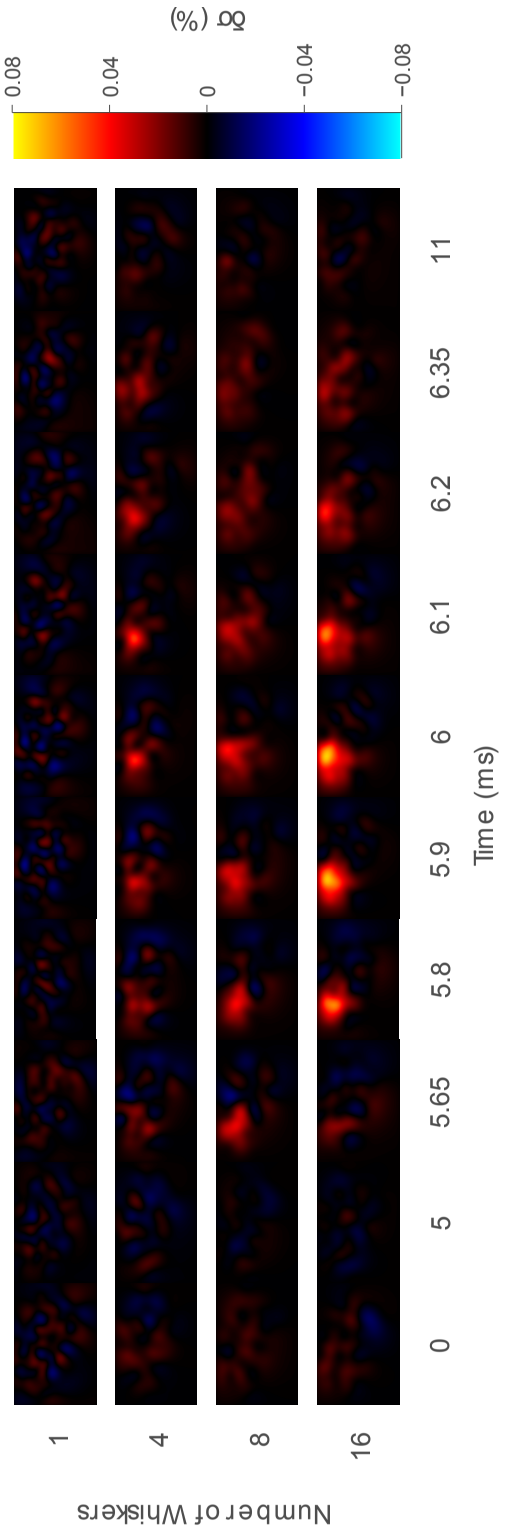

Figure 5.11: *Images of the percentage conductivity change for the first recordings in the first rat: posterior-anterior and medial-lateral in the x and y axes. Each row is for stimulation of a different number of whiskers, while each row shows the conductivity change for a different time point, where 0 ms is the time of stimulation. Images were rasterised at 700 µm on the z-axis.*

5.3.4.3 Image reconstruction: quantitative assessment

As the number of stimulated whiskers increased, the volume constituting the *reconstructed perturbation* increased (figure 5.12a). In addition to this, the activity had a sharper spatial peak, which was most marked for stimulation of 4 four whiskers in the first rat, which resulted in the mean of the conductivity change of the *reconstructed perturbation* for this image being substantially larger than for the other images (figure 5.12b). The noise in all the images was fairly comparable, with the average SNR across recordings being 5, ranging from 4.8 to 6.4 over all the images, and there was no clear trend in SNR across the images for stimulation of different numbers of whiskers (figure 5.12c).

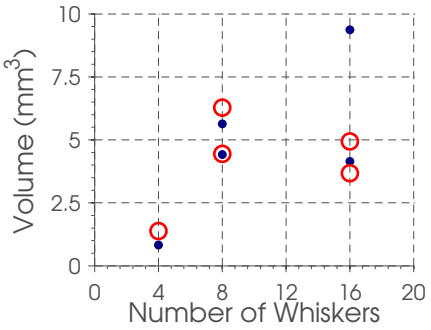

(a) *Volume of the* reconstructed perturbation

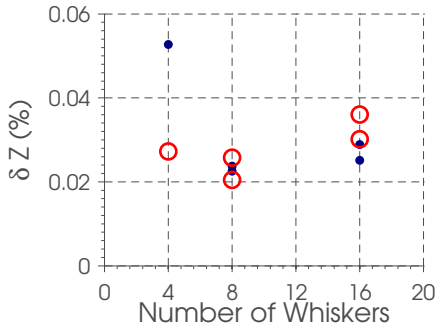

(b) *Mean conductivity change of the* reconstructed perturbation

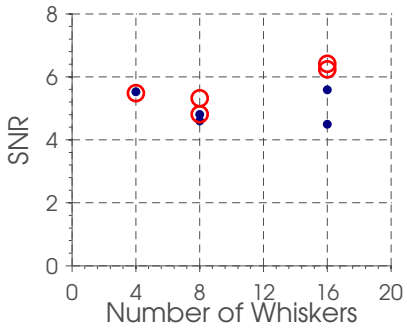

(c) *Image SNR*

Figure 5.12: *Quantitative analysis of the images for stimulation of different numbers of whiskers.* ● *values for the images from rat 1.* ○ *values for the images from rat 2.*

5.4 Discussion

5.4.1 Summary of results

With stimulation of a group of whiskers, increasing stimulation frequency resulted in a significant decrease in the amplitude of impedance changes. In addition, impedance changes increased significantly with increasing stimulus deflection amplitude. Although such a correlation appeared to exist for increasing stimulus deflection velocity this was not statistically significant. With stimulation of a single whisker, there was no clear trend related to increasing stimulus deflection amplitude or velocity, but there was a significant decrease in the amplitude of impedance changes with increasing stimulation frequency. In both sets of recordings there was substantial intra- and inter-subject variability, with impedance changes following single whisker stimulation being up to an order of magnitude different from one another.

All control recordings confirmed that the recorded impedance changes were not artefactual and that the percentage impedance change is independent of the injected current amplitude.

The images for stimulation of a single whisker did not yield a readily identifiable perturbation, while only one of the two repeats in each rat for stimulation of four whiskers had a readily identifiable perturbation. However, all imaging of stimulation of eight and 16 whiskers resulted in reconstruction of a readily identifiable perturbation.

5.4.2 Effect of varying stimulation parameters

The encouraging result from this component of the study is that all the significant trends were comparable to those reported in the literature (sections 1.8.6.4 and 5.1.2.1). However, the trends with stimulation of a group of whiskers for variation of stimulus deflection amplitude and velocity were somewhat less clear than expected. The effect of variation of the amplitude was only significant for the first peak, and while a trend for the effect of stimulus deflection velocity seemed apparent in the second peak of the impedance change it was not significant. This could have been for a number of reasons. First, the grouping of multiple whiskers might have led to complex lateral inhibition, due to slightly offset stimulation times. Alternatively, the small impedance changes of the second peak may have been too close to the noise floor to facilitate any trend becoming apparent. In addition, for stimulation of a single whisker, while for variation of the stimulation frequency a clear trend existed there was no trend apparent for variation of the stimulus deflection amplitude or velocity. This may have been for one of three reasons. First, the ability of the stimulator to deliver the desired displacement might be called into question. Second, it might be argued that impedance changes may have the same correlations with altered stimulation parameters as other techniques, and so might not

correlate with expectations from the literature. Third, physiological variation may have meant that with so few repeats trends could not be uncovered. The first point seems unlikely, given the thorough calibration and testing of the stimulator that has previously been undertaken [177;228]. In addition to this, there was a clear trend for increasing stimulus deflection amplitude for stimulation of a group of whiskers, which also addresses the question of whether impedance changes should have the same correlations with altered stimulation parameters as those reported in other studies. Therefore, it seems most probable that physiological variability prevented any trend being apparent. Indeed for single whisker stimulation, changes were barely apparent for one of the two rats, and when single whisker recordings were repeated for the imaging component of this study no changes were apparent for any of the four single whisker stimulation imaging data sets.

5.4.3 Recommendations for a cross-validation study

Expectations from the literature were that the largest response should be achieved with a low frequency stimulation, which was confirmed in this present study, and that with higher stimulus deflection amplitude and velocity impedance changes would be largest, both of which have been, to some extent, confirmed in this present study. Therefore, it would seem that any future study intending to employ EIT for imaging fast neural activity following physiological vibrissae stimulation, should stimulate at 1 Hz, with the maximal possible stimulus deflection amplitude and velocity, which with the stimulator employed in this study, would be 4 mm and 800 $\mathrm{mm\,s^{-1}}$. In addition, if a future study were to incorporate imaging the effect of varying a stimulation parameter, it would seem that variation of stimulation frequency would be best, as it was the only parameter to have a significant effect for both group and single whisker stimulation.

5.4.4 Feasibility of using a higher carrier frequency

It would be expected that the use of a wider bandwidth for demodulation would increase the signal amplitude, as more information is retained, but also increase the noise in the impedance changes. Certainly, the SNR of the images reconstructed in the current study (SNR$\leq$6.4) was substantially smaller than that reported by Gilad et al. (SNR$\leq$50) when using a bandwidth of $\pm$125 Hz. However, the reconstructed changes in the current study were also much smaller (0.02 to 0.06 %) than those reported by Gilad et al. (0.90 ± 0.06 % for vibrissae stimulation) [90]. Therefore, it is clear that the use of a physiological stimulus, and stimulation of only a part of the vibrissal pad has substantially reduced the amplitude of impedance changes, by around 1.5 times, while the use of a broader bandwidth has also increased the noise as the SNR was reduced by a greater amount, although the

amount of averaging in the present study was only half that employed by Gilad et al. [90]. Nonetheless, the use of a higher carrier frequency, with a temporal resolution of 3.3 ms, as compared to the previously employed 8 ms resolution (see chapters 3 and 4 for details), did not prevent measurement of impedance changes and resulted in a SNR of >4:1, which was sufficient for image reconstruction in which there was a readily identifiable reconstructed perturbation. In addition to this, all the control measurements indicted that, for the sources of error considered, the results were not artefactual.

5.4.5 Number of whiskers to be stimulated in future studies

Given the electrode array, current amplitude and frequency, and all other parameters used in this study, future work with the same set-up should stimulate at least four whiskers to ensure sufficient SNR for imaging. Although in two of the four rats in which single whisker stimulation was undertaken impedance changes could be identified, only one of these rats had impedance changes with an SNR greater than 2:1. In fact this rat appears to have been somewhat of an outlier as the impedance changes recorded during single whisker stimulation were comparable to the largest impedance changes recorded in other rats during stimulation of 16 whiskers. In addition, none of the images with single whisker stimulation had a readily identifiable reconstructed perturbation. Therefore, impedance changes during single whisker stimulation cannot be consistently and reliably recorded with the employed experimental set-up. In contrast to this, half of the imaging recordings with stimulation of four whiskers resulted in an image with a readily identifiable reconstructed perturbation, and whilst the area of conductivity changes was smaller than for eight or 16 whisker stimulation, the SNR for four whisker stimulation was comparable to that for stimulation of more whiskers.

5.4.6 Study limitations

Although 268 single channel measurements were made over 5 rats, these recordings were used to test a plethora of different hypotheses and as such in some instances more repeats might have elucidated trends related to stimulation parameter variation, as, particularly for the single whisker measurements, the physiological variability was substantial. Nonetheless, this study was intended as a feasibility study and the questions posed in the purpose of this study have all been sufficiently addressed.

It was apparent from examination of the literature that imaging a single whisker was going to be difficult. The approximate size of a single barrel is 450 to 500 µm at its widest point [97], and the diameter of a single electrode in the array employed is 600 µm, with each electrode spaced 600 µm apart. Therefore small differences in placement of the electrode array could result in highly variable sensitivity to the changes in a single barrel.

Furthermore, the early spatially constrained responses expected following single whisker stimulation would be difficult to image, because even if one electrode were centred on the appropriate barrel, only a few electrodes would be sensitive to this barrel's activity. Therefore, while the question of how many whiskers need to be stimulated for EIT imaging of fast neural activity following physiological vibrissae stimulation with the current available set-up has been addressed, this study could not address whether, in principle, EIT of the neural activity following single whisker stimulation would be possible. This is important if EIT is to be used for neuroscientific research into the rat vibrissal sensory system.

The effect of stimulus deflection direction was not formally addressed in this study. Nonetheless, the results matched expectations from the literature: for two diametrically opposed deflections the response in one direction should be significantly greater than the response for the opposed deflection. However, it might have been desirable to randomise the deflection direction between trials, so as to prevent any attenuating effects of repeated predictable stimuli.

Although a higher carrier frequency was used, and an improved temporal resolution achieved, it would have been interesting to explore the effect of altering the bandwidth for demodulation to examine whether a further improvement in temporal resolution could be achieved. As this was a feasibility study, this was not explored as increasing the bandwidth would have increased the noise, making the challenging aims of this study even more difficult. Nonetheless, while a temporal resolution of 3.3 ms is not ideal for future work that might examine translaminar propagation, it is a substantial improvement on the 8 ms employed in previous work (see chapters 3 and 4 for details).

5.4.7 Recommendations for future work

Future work might look to address improvements in the experimental set-up that might facilitate imaging the impedance changes that occur during single whisker stimulation. The first step would be to undertake a simulation study to determine what electrode density would be necessary to achieve this. However, this would be constrained by the limitations of electrode manufacturing techniques and the requirements of EIT on electrode diameter. With regard to the injecting electrodes, if they are too small then the current density will rise to intolerable levels, and any alteration in current injection electrodes would require more current control studies, to ensure the increased current density is not affecting cortical function. In addition, decreased electrode diameter will require improved output impedance in the current source to ensure a constant current is delivered. Therefore it would seem logical that an array of variable electrode diameters is employed, with large injecting electrodes, among which are small recording electrodes. However, small recording electrodes have high contact impedance, which might result

in voltage division and signal loss if the input impedance of the recording amplifiers is insufficient. The raised contact impedance would also increase noise susceptibility, although this might be addressed with a preamplification stage, as used in LFP recordings. Another possible improvement for imaging the effects of stimulating a single or even four whiskers would be examination of the current injection protocol. The 'combined-protocol' employed in this study is designed to offer sensitivity throughout the array, but is not ideal for imaging the spatially constrained responses found in the reconstruction of stimulation of four whiskers. It might be beneficial when attempting to image a single or four whisker response to have a protocol in which the injections are in a spiral or rosette shape around the centre of activity, to ensure maximal sensitivity in this small area. However, simulation would be required to determine the efficacy of such a protocol as compared to that of the 'combined-protocol'. For the image reconstruction, the use of the 3D digitiser was insufficient for accurate electrode position measurement and placement in the forward modelling. This was not a key concern in the present study, as the exact localisation of changes was not required, nor was comparison between recordings and rats. However, for future work that might examine somatotopy with EIT, the use of the 3D digitiser is non-optimal and alternative techniques should be explored, such as the use of photogrammetry.

Future work might examine whether a broader bandwidth for demodulation can be used, which would facilitate improved temporal resolution. A study would need to explore the effect this broadening has on the SNR and the ability to image the small (in amplitude and spatial extent) changes associated with physiological stimulation of vibrissae. The ideal bandwidth would be at least $\pm 500\,\mathrm{Hz}$, yielding a temporal resolution of 2 ms, but it may be, for reasons related to SNR, that a compromise between 300 to 500 Hz is required.

The study presented here suggests that future work could explore EIT imaging of fast neural changes in the presence of cross-validation measurements, such as the use of LFP and CSDA, using a physiological, somatotopic stimulus. If using the rat barrel cortex as the physiological model, and the experimental set-up employed in this study, such a study should use a 1 Hz stimulation with a stimulus deflection amplitude and velocity of 4 mm and $800\,\mathrm{mm\,s^{-1}}$, respectively. Moreover, simultaneously stimulation of 4 whiskers should be employed to ensure consistent results with changes that can be reconstructed. In addition, if such a study were to incorporate imaging the effect of varying a stimulation parameter, this parameter should be variation of stimulation frequency.

Chapter 6

Cross-validation of electrical impedance tomography of rat primary barrel cortex somatotopy and translaminar propagation

6.1 Introduction

Previous work to attempt imaging of fast neural activity with EIT has yielded some success[64;90], and the analyses performed in chapters 3 and 4, built upon this body of work suggesting EIT of fast neural activity may be a useful neuroscientific technique. Nonetheless, as detailed in the preceding chapters, many aspects of the use of EIT require further examination before it might be employed for neuroscientific research. These foci of improvement and investigation include the imaging of changes following a physiological stimulus, improvements beyond the previously employed temporal resolution of 8 ms, and direct cross-validation of the findings of EIT against other neurophysiological recording techniques. In chapter 5 it was concluded that the fast neural changes associated with physiological vibrissae stimulation could be imaged with EIT and that these changes could be imaged with a temporal resolution of 3.3 ms through the use of a higher carrier frequency and broader demodulation bandwidth. Moreover, it was noted that, with the experimental set-up used in chapter 5, simultaneous stimulation of four whiskers could be imaged in 50 % of recordings and the suggested best parameters for stimulation were also identified. Therefore, there is a possibility for directly cross-validating EIT imaging of fast neural activity of vibrissae stimulation. The first aspect of EIT imaging of fast neural activity that needs further examination is the somatotopic mapping ability of EIT, as although previous work has employed different sensory stimulation paradigms (forepaw, hindpaw, vibrissae and visual stimulation) the electrode arrays were moved between recordings[90]. The second focus of investigation should be to address the ability

of EIT to image translaminar propagation. A variety of techniques might be employed to examine these two questions; however, there was a requirement for robust and readily implemented techniques: the chosen techniques were therefore ISOI and LFP/CSDA.

6.1.1 Intrinsic signal optical imaging

ISOI was briefly described in chapter 1, and so a more detailed consideration of the technique is given here. ISOI is a technique that allows for the imaging of BOLD-like responses, which can in turn facilitate functional mapping of the cortex [230]. ISOI is referred to as intrinsic as it does not require the application of extrinsic materials, such as dyes. ISOI allows for imaging of the haemodynamic changes that are coupled to neuronal activity. The signal source in ISOI is related to the imaging of total haemoglobin, oxyhaemoglobin and deoxyhaemoglobin, with the relative contribution of each dependent on the wavelength used for illuminating the cortex. The signal is affected by changes in blood volume, blood flow, and scattering gated to physiological changes, such as the heart rate, and other neurophysiological changes, such as swelling and ionic movement. ISOI can be used for functional mapping, examination of global effects, and exploration of functional preference. The key focus of this introduction to ISOI is centred upon the use of ISOI for functional mapping as within this study ISOI was employed for this purpose.

In ISOI a camera is positioned over the cortical area of interest and the brain is imaged, either directly or through thinned bone. The data are collected representing the cumulative activity integrated over the cortical area orthogonal to the surface. Typically for functional mapping a single wavelength of illumination is employed, with the choice being between green or red/orange light. Green light is sensitive to changes in blood volume as an isosbestic point of oxyhaemoglobin and deoxyhaemoglobin (the point at which they have the same molar absorptivity) exists within the green component of the visible light spectrum. Conversely, red/orange light allows for imaging of the difference between oxyhaemoglobin and deoxyhaemoglobin. In addition to this, green light illumination results in a larger signal, but poorer depth penetration into the cortex than red/orange light illumination. In a functional mapping study, in which one is interested in the cortical point-spread for a given stimulus, and not interested in applying modelling of spatiotemporal dynamics, imaging with green-light illumination is common [231].

Recent work has revealed further insights into the signals recorded with ISOI. A larger area than the area of suprathreshold activity show a haemodynamic response, and while this was originally thought to be haemodynamic overspill, more recent work has shown this area to match the area of subthreshold activity [232], which often extends beyond the that of suprathreshold activity. Similarly, work with red light illumination has revealed that the ISOI signal, originally found to be biphasic, is actually triphasic in a manner comparable to the BOLD signal of fMRI, although further work is required to

determine how this is dependent on the illumination wavelength and employed stimulus. In a functional mapping study the signal component of interest is the initial dip that occurs after approximately 0.5 s, peaks at 1 to 1.5 s, has a fractional amplitude of 0.0001 to 0.001, and diminishes by 2 to 3 s[231]. In summary, there is still much work to be undertaken to understand the complexity of the signals recorded with ISOI, although these do not all pertain to functional mapping of cortical point-spread.

Much work has been undertaken using ISOI in the rat. The rat's heart rate is fast enough to not cause artefacts, unlike when recordings are made in cats or monkeys. Similarly, breathing artefacts are limited in the rat due to reduced breathing-gated brain motion, and because it can be prevented by imaging through a thinned, intact skull. However, there are global spontaneous and vessel related artefacts that are significantly larger than the initial dip signal imaged for functional mapping. Averaging is employed to remove the global spontaneous artefacts, but as vessel artefacts are gated to the stimulus this does not help to remove these. There are options to minimise this effect, moreover vessel artefacts are slower than the initial dip signal and so consideration of the first 2 s post-stimulus can aid in minimising their effect[231].

As detailed above, the collected data in a ISOI mapping study are averaged over trials, each of which consists of a pre- and post-stimulus time. The data are then expressed as a fractional change in reflectance compared to the pre-stimulus baseline. The resultant images are then typically smoothed with a Gaussian filter and the images thresholded, typically at 50 %, to isolate the areal extent of the area of activation. The choice of a 50 % threshold is not ideal if the second phase of the ISOI signal is considered, as it is much larger than the initial dip. Therefore if considering the multiphasic nature of the data then different thresholds might be employed, although the choice of thresholds is often arbitrary and not validated[231].

6.1.2 Local field potentials and current source-sink density analysis

The measurement of LFPs and CSDA were discussed in some detail in chapter 1 as results collected/analysed with these techniques were discussed. Within this chapter a more detailed discussion of the assumptions, limitations and interpretation of LFPs and CSDA is given.

6.1.2.1 Principles of local field potentials

The LFP is the component of extracellular potentials in a band less than 500 Hz and originates from summated dendritic synaptic currents arising from pyramidal neurons, possibly through the formation of dipoles[233], with action potentials having limited participation in the production of LFPs[49]. LFP recordings sample slow events that originate

from a large volume, which has the advantage that their measurement is stable to small changes in electrode placement. These features underpin some of the characteristics, limitations and assumptions of recording LFPs, which include a filtering effect on LFPs and a large poorly defined sampling volume.

LFPs have a frequency scaling/attenuation of $1/f$, which means that they suffer from a low-pass filtering effect due to the dendritic distribution of transmembrane return currents and dampening from interactions with the extracellular medium. These interactions are from several mechanisms, such as capacitive effects, polarisation, or ionic diffusion[234]. This manifests in the FWHM of the latency being narrower closer to the synapses than the soma, as extracellular potentials near synaptic current generators have higher frequencies included. In other words, extracellular potentials close to soma are low pass filtered, and this effect is stronger for potentials than for currents. In addition to considering these effects in assessing LFP measurements, it is important to note that LFPs are not point measurements, but rather sample a larger volume. Consequently, the LFP amplitude does not decay monotonously with distance from synaptic inputs and large extracellular responses are measured almost a millimeter away. Experimentally, it has been shown that while MUA is reduced by a factor of 30 when measurements are moved by 0.5 mm, LFPs are only reduced by a factor of 5[235]. Similarly, Kajikawa and Schroeder noted that the LFP signal extends laterally beyond 200 to 400 µm and spreads beyond the boundaries of activated neuronal tissue, as might be expected from the larger extent of subthreshold activity as compared to the area of tissue with action potentials[236].

LFP measurement depends upon multiple assumptions, which once defined allow for simple formalisation of the measurement. The key assumptions in the measurement of LFPs are:

(1) A quasistatic approximation of Maxwell's equations is used, so that the electric and magnetic components of these equations decouple (see equation 1.3), which is comparable to the assumptions in EIT. This is a reasonable assumption for neural activity less than 1 kHz, which includes the frequency-band considered in LFP measurement.

(2) The extracellular medium is assumed to be purely ohmic (resistive), so that the imaginary part of the conductivity is ignored/assumed to be zero, and the extracellular conductivity is assumed to be frequency-independent.

(3) The extracellular medium is assumed to possess linearity, so that the current density is linearly related to the tissue conductivity and electric field (see equation 1.4).

(4) The extracellular conductivity is assumed to be isotropic and therefore representable as a scalar. This assumption that the conductivity is the same in all

directions has been shown not to be true in frog and toad cerebella[52], nor in the rat barrel cortex, which has significant radial and translaminar conductivity aniostropy[237].

(5) The extracellular conductivity is homogeneous, which is broadly fulfilled in grey matter, but not if considering other neurological tissue types.

Under these assumptions the LFP can be formalised for a punctual current source as:

$$V(r) = \frac{1}{4\pi\sigma}\frac{I_0}{|r - r_0|}, \tag{6.1}$$

where $V(r)$ is the extracellular potential measured at point r, I_0 is the current source, and $|r - r_0|$ is the absolute distance between point r and the location of the current source, r_0. This can be extended, by linear superposition, to a series of current sources as:

$$V(r) = \frac{1}{4\pi\sigma}\sum_j \frac{I_j}{|r - r_j|}, \tag{6.2}$$

with this formulation being referred to as the 'standard model'[238].

With this model the expectation for the LFPs produced from a single pyramidal neuron can be predicted. Near the apical synaptic input the extracellular signal is negative, while close to the soma the potentials derive from positive-return currents.

6.1.2.2 Current source-sink density analysis

Due to the inherent assumptions and limitations of LFP its analysis is largely restricted to the estimation of the CSDA, which is the volume density of net transmembrane currents through the neuronal membranes[52] (see section 1.2.3 for details of the formalisation of CSDA), and the application of laminar population analysis (LPA). LPA allows for separation of active populations, through the use of LFP and MUA recordings. The LFP and MUA are modelled jointly to interpret stimulus-evoked laminar-electrode data, by assuming that MUA reflects the firing rates of the laminar populations while the LFP is assumed to be due to postsynaptic activation following the observed population firing, and modelling includes spatial, temporal and firing rate terms, and a time delay for the LFP[53].

CSDA is more easily related to neuronal activity than extracellular potentials and so is the standard approach to analysis of LFP with linear, translaminar, multi-electrode arrays[52;55], and while it is an inverse-problem, which requires priors, the forward problem (CSDA to LFP) is well-posed[52]. CSDA offers better spatial resolution and allows for better definition of the proximity of activity than LFP as it is calculated from the second spatial

derivative. In a simple three contact model a far source will contribute to the measured field in each electrode, and the difference between the middle and further electrodes will be small, so that the second spatial derivative of this will be small indicating a distant source. By contrast, for a close source the field will be different in each electrode and so the second spatial derivative will be large, which indicates that the source of the current is local[239].

Despite the advantages CSDA has over LFP it is still a mesoscopic metric, with changes averaged over the volume between electrodes which limits the spatial resolution, in other words the inverse is underdetermined. Therefore, CSDA cannot separate contributions from different spatially intermingled neuronal populations, and, with a single linear electrode array, geometrical assumptions must be made in addition to the assumptions of LFP. As changes are larger along the vertical axis than in the lateral plane, it has been common to assume infinite activity diameter in the lateral plane, and variation in extracellular potentials in x and y are neglected (this assumption yields equation 1.6, which is simplified to equation 1.7). Effectively, the CSDA within each electrode's domain is assumed to be located in an infinitely thin and wide sheet at the height of the electrode. This assumption introduces errors[52], with 3D CSDA, which minimises these assumptions, being preferable, but technically demanding[240;241]. An additional analysis can be performed on 3D CSDA referred to as iCSDA, which can overcome some of the limitations of CSDA (see section 1.2.3 for further details).

6.1.2.3 Local field potential and current source-sink density analysis of rat barrel cortex

The LFP within the barrel cortex should result in the upper layers having a small positive deflection, followed by a main negative deflection and then positive and finally slow negative deflection that reaches the pre-stimulus baseline. In the middle layer (layers III to IV) there should be a main negative deflection followed by a slow positive and slow negative component. Within the bottom layers there is typically a main negative deflection followed by slow positive and negative deflections[242;243]. The depth polarity variance and polarity inversions help reveal locally generated activity, that result in CSDA sinks[53].

The sink-source distribution for the rat barrel cortex is relatively well described: sinks are negative current-density (current leaving the extracellular medium/inward transmembrane current) due to post-synaptic potential activity, and sources are positive current-density (current entering the extracellular medium/outward transmembrane current) with each coupled to its opposite effect. The initial activity is identified as a sink centred upon layer IV, with an onset of 5 ms and a peak at 7.4 to 8 ms. Approximately 1 ms after this, activity occurs in layers II and III, which appears as a secondary source-sink

complex between layers I and IV. Finally activity occurs in layers V and VI, which has an onset latency of 3 ms after the initial sink in layer IV, with the activity peaking at approximately 4 ms[53;54;149]. The layer activation order in CSDA can be calculated as time of the first sink, or the peak of the first sink[54], or a combination of both[126], although oscillations can occur due to calculation of CSDA and so onset can be hard to detect accurately, therefore the peak is often employed.

6.1.3 Optimisation of electrical impedance tomography image reconstruction

Within this study two main alterations to the image reconstruction methodology were employed. First, dual scheme image reconstruction, was used to reduce computational time, and second, noise-based data scaling was performed to improve the localisation of impedance changes in the z-axis.

6.1.3.1 Dual scheme image reconstruction

Fine FEM meshes are required for accurate forward modelling, by ensuring that electrode positions and surface geometry are correctly modelled, and that the electric potential can be calculated accurately. However, the resultant sensitivity matrix, A^f, can be of the order of several million tetrahedra. This presents three key issues, (1) the resolution of the mesh is greater than the actual spatial resolution, therefore; (2) the problem is more ill-posed than is necessary, and; (3) the inversion of such matrices can require in excess of 100 GB of memory. Therefore it is desirable to use a dual scheme so that a coarser sensitivity matrix, A^c, is used for the inverse computation. The choice of the coarseness of A^c should be made based upon the available measurements and spatial resolution of the imaging technique[244].

The procedure to move from A^f to A^c requires determining which columns of A^f belong to a column of A^c, and summation of these values. This is achieved by the formation of a projection matrix, P, that identifies which columns of A^f are summated to generate A^c: '1' entries in the rows of P identify which columns form A^c. Therefore the calculation of A^c is:

$$A^c = A^f P. \tag{6.3}$$

6.1.3.2 Improvement of depth localisation

It is well established that in EIT sensitivity reduces exponentially with distance from the surface electrodes. This is particularly exacerbated for planar arrays, with simulation and tank studies indicating that perturbations are reconstructed displaced towards the

surface upon which the electrodes are placed[214]. The regularisation method can aid in compensating for this, although the choice of regularisation method is largely based upon the priors that can be employed. For example if the amplitude or the sparsity of gradients of the reconstructed perturbation is known then this will inform the choice of regularisation technique. However, due to the novel nature of imaging fast neural activity with EIT the priors that can be used are limited, as are the tank studies that can be undertaken, as the expected changes are not yet known. Therefore more novel approaches to compensating for this error in depth localisation are required. An alternative assumption, not based upon the nature of the expected change, is that, for a given location in the reconstructed image, the noise normal to the electrodes' location (the noise over depth) will be correlated, but scaled by the decay in sensitivity over depth. Therefore, it may be possible to normalise the reconstructed conductivity changes by considering the ratio of the noise over the depths in this axis. This hypothesis is examined within this study.

6.1.4 Purpose

The overall purpose of this study was to determine if EIT is a reliable means of imaging the conductivity changes associated with fast neural activity. This was examined by comparing the findings of EIT with other established techniques, to determine:

(1) Do EIT reconstructed images exhibit somatotopy comparable to the findings of ISOI and the known anatomy?

(2) Are there translaminar changes in the EIT images that match simultaneous LFP recordings, CSDA, and the neurophysiological literature?

The ability to improve depth localisation through the use of noise-based data scaling was also examined.

6.1.5 Experimental design

ISOI of single whisker stimulation for two whiskers was employed, first, to localise the area of the PMBSF containing the whiskers to be studied, second, to undertake cortical functional mapping for validation of the ability of EIT to be used for somatotopic mapping, and lastly to aid EIT and LFP electrode placement. The second aim of the current study was to obtain reliable independent information on the translaminar propagation of activity. LFP and CSDA were chosen as the independent measure as it is a comparatively easy technique to employ and has a large body of literature to which findings can be compared. Furthermore, LFP measurement was desirable as the lower band used for analysis of LFP ensures that the injected current would not affect the LFP. Simultaneous

measurements were made possible by modifying the electrode array used in chapter 5 to have a series of holes through the silicone between the electrodes. MUA recordings were not possible as the sampling volume of the technique from a single shank would be insufficient for the intended comparison study. Similarly, 3D/multishank LFP recordings were discounted because of their greater complexity and also because linear arrays had to be inserted through the holes in the planar EIT electrode array which were approximately 2 mm apart, and irregularly spaced at 23 locations throughout the array. The EIT and LFP electrode were centred upon the area corresponding to the δ whisker, as determined by the ISOI, and recordings were made with stimulation of groups of four whiskers to ensure sufficient SNR for EIT imaging. To facilitate reliable comparison between the EIT images and the LFP and CSDA it was important to optimise the depth localisation of the reconstructed changes. Therefore a simulation was undertaken to examine the effectiveness of noise-based data scaling. The results of this simulation indicated that this is an effective method of depth correction and so was applied to the reconstructed images.

6.2 Methods

6.2.1 Animal preparation

Four female Sprague-Dawley adult rats were used for recordings. The surgical and anaesthetic procedure were identical to those described in chapter 5, although all procedures were performed on a vibration isolated table (Thorlabs Inc., USA). Following reflection of the dura mater the electrode array was not placed upon the cortex as in previous studies, but instead ISOI was performed. Following collection of ISOI data, the planar electrode array for EIT recordings was placed over the PMBSF using a micromanipulator (SM-15 Micromanipulator, Narishige International Ltd., UK), so that the central hole in the EIT electrode array was centred over the area corresponding to the δ whisker as determined by ISOI (see section 6.2.2 for details). Subsequent to this a linear, multi-contact electrode was inserted into the cortex for LFP measurement (see section 6.2.3 for details). The brain was frequently irrigated with warm (38 °C) 0.9 % saline solution between recordings and to aid this process a piece of cotton wool was placed over the array and kept moist. A 2.25 cm^2 silver-silver chloride ground electrode was placed under the skin of the right side of the head, opposite the electrode grid. All animal works undertaken in this study were approved by the UK Home Office and in accordance with its regulations (Project number: PPL 70/7450).

6.2.2 Intrinsic signal optical imaging

6.2.2.1 Hardware

Following the animal preparation a 1.3 megapixel monochrome charge-coupled device camera (STC-MB133USB, Sentec, Sensor Technologies America, Inc., USA) with a macroscopic zoom lens (MLM3X-MP, Computar, CBC Corp., USA) was positioned orthogonal to the exposed cortical surface using the micromanipulator and a 3D printed adaptor. The brain was illuminated with a high brightness, ripple-free LED light source (Schott KL 1500 LED, Schott North America, Inc., USA) with a green insert filter (peak 520 nm, FWHM ±30 nm). The camera was connected to a PC via a USB cable, which triggered the image acquisition and stimulator, and 12 bit images were collected at 11 frames per second.

6.2.2.2 Stimulation Paradigm

Each ISOI trial consisted of 30 s of imaging and a 2 s 'rest' period. Trials consisted of 8 s of pre-stimulus data acquisition, then 2 s of 5 Hz whisker stimulation, during which data were still acquired, and finally 20 s of post-stimulus data acquisition. These trials were repeated 30 times for each recording. For each rat two recordings of single whisker stimulation were made: stimulation of the δ whisker and stimulation of the D2 whisker. During recordings all illuminated experimental equipment, such as PC monitors, were switched off or covered with blackout material (Thorlabs Inc., USA). Whisker stimulation was undertaken using a piezoelectric actuator (PL140.10, PI ceramic, Germany) (see section 5.2.2 for details) with a deflection amplitude and velocity of 4 mm and 800 mm s^{-1}, respectively. The stimulator was used to displace a whisker or whiskers in the cranio-caudal axis.

6.2.2.3 Data processing

Data were processed using custom written software in MATLAB (The MathWorks, Inc., Natick, Massachusetts, USA). All frames were written to disk with a time-stamp, which was used for processing. Each trial was identified by the jump in timing between trials, due to the 2 s 'rest' period. The timing of frames within each trial were normalised to the first trial and then frames within the same 0.5 s bin were averaged together to give a total of 60 images per trial. Within each trial, the images were subtracted and expressed as a fraction of the average of the 8 s of pre-stimulus images (16 images). This was done within trials to eliminate any potential slow drift in the baseline image over trials. The fractional differences were then averaged across trials to yield a total of 60 images.

6.2.2.4 Image processing and analysis

First, images were filtered with a Gaussian filter with a FWHM of 5 pixels. Then image segmentation was undertaken to identify the change at 2 s. This was required because a simple thresholding, such as 50 % of the maximum, was not effective on its own due to speckle artefacts and large changes at the edge of vessels and at the edge of the craniotomy. Both of these were most likely due to respiratory artefact, which was exacerbated in the animal preparation due to a full craniotomy being performed.

The first step of segmenting the ISOI change was to identify the edges of changes. This was undertaken on the assumption that the gradient of the change would be different from the background and performed using the Sobel approximation to the derivative. The resultant binary mask was dilated to fill holes in the binary mask. Then to remove outlier areas of change and leave one contiguous area of change the binary mask was eroded, and of the resultant mask the largest connected group of pixels selected. All procedures were undertaken using the image processing toolbox in MATLAB (The MathWorks, Inc., Natick, Massachusetts, USA). Finally, the centre-of-mass of the segmented area of change was calculated, and the distance between the centres for stimulation of the δ whisker and stimulation of the D2 whisker was calculated for each rat.

6.2.3 Local field potentials and current source-sink density analysis

6.2.3.1 Hardware

LFP recordings were made with a single shank, linear, 16 contact, iridium in silicone probe (A16, NeuroNexus Technologies, Ann Arbor, MI, USA). Each electrode contact was 30 µm in diameter with a centre-to-centre spacing of 100 µm, with all contacts having an impedance $<1\,\mathrm{M\Omega}$ at 1 kHz. The probe was positioned orthogonal to the exposed cortical surface using a micromanipulator and advanced until, under microscopic assessment, the uppermost electrode entered the pial tissue. Confirmatory recordings were then made to ensure correct electrode placement. LFP data were passed through a headstage amplifier (E2a, Plexon, TX, USA), with unity gain, and recorded with a BioSemi EEG system (ActiveTwo, BioSemi, Netherlands) (see section 5.2.3 for details) with a sampling rate of 8 kHz. LFPs and EIT data were collected simultaneously.

6.2.3.2 Stimulation Paradigm

Whisker stimulation was undertaken using a piezoelectric actuator (PL140.10, PI ceramic, Germany) (see section 5.2.2 for details), and at 1 Hz with a deflection amplitude and velocity of 4 mm and $800\,\mathrm{mm\,s^{-1}}$, respectively. Groups of four whiskers were tied together and attached to the piezoelectric stimulator, with the first group being γ, δ, E1

and D1, and the second group being D2, C2, D3 and C3. The stimulator was used to displace a whiskers in the cranio-caudal axis.

6.2.3.3 Data processing

LFP signals were low pass filtered at 500 Hz, and then within each 1 s trial (see section 6.2.4.1 for details) the 50 Hz component of the signal was determined using fast Fourier transform. If this was greater than 25 % the amplitude of the remainder of the spectrum the trial was rejected. The remaining trials were then notch filtered (50 ± 2 Hz) and averaged. For a given rat and stimulation of a given whisker group a grand average of the recordings was calculated, resulting in two grand average LFP results for each rat, with these being used for didactic plots within this study. However, due to physiological jitter in the responses, for accurate comparison to the reconstructed EIT images, the simultaneous LFP recording, only averaged over trials, was used. The exception to this was if EIT recordings had an insufficient number of channels with a 'significant impedance change' (see section 6.2.4.3 for details) and were averaged then the corresponding LFP recordings were also averaged.

LFPs were used to undertake CSDA with the assumption made that the conductivity was a stationary scalar, and calculated as the discrete derivative (see equation 1.7) [52]. To remove oscillation in the resultant CSDA and prevent incorrect analysis, only significant sources and sinks were considered. These were defined as those sources and sinks with an amplitude greater than three times the SD of the first 75 ms pre-stimulus. For each depth of the CSDA, and at each whisker deflection direction, the peak response was detected and the onset of the sources and sinks was defined as the first time point before the peak at which the changes became significant.

6.2.4 Electrical impedance tomography

6.2.4.1 Hardware and protocols

The EIT instrumentation was the same as that employed in chapter 5 (see section 5.2.3 for details). Electronic instrumentation comprised the 'UCL-CS2' current source [64], and voltages were recorded with a BioSemi EEG system (ActiveTwo, BioSemi, Netherlands) with a sampling rate of 8 kHz. The employed electrode array was a 30 contact stainless steel in silicone array with 23 holes through the silicone in the spaces between the electrode contacts to facilitate the insertion of a depth electrode for LFP measurement. The electrodes were platinised to reduce contact impedance and noise from the electrode-electrolyte interface [64;229].

For EIT data acquisition a protocol referred to as 'spiral-protocol' was employed. The 'spiral-protocol' is centred upon the area of maximal EP activity with injection pairs

made in a spiral/rosette pattern around the centre of activity, which yields maximal sensitivity for the small (relative to the electrode diameter) area activated by stimulation of four whiskers*. For all EIT recordings the injected current was 50 µA in amplitude at a frequency of 1725 Hz, with the impedance changes demodulated as the changes in a ±500 Hz bandwidth around this carrier frequency.

6.2.4.2 Stimulation Paradigm

Whisker stimulation was undertaken using a piezoelectric actuator (PL140.10, PI ceramic, Germany) (see section 5.2.2 for details), and at 1 Hz with a deflection amplitude and velocity of 4 mm and 800 mm s^{-1}, respectively. Groups of four whiskers were tied together and attached to the piezoelectric stimulator, with the first group being γ, δ, E1 and D1, and the second group being D2, C2, D3 and C3. The stimulator was used to displace a whisker or whiskers in the cranio-caudal axis.

6.2.4.3 Boundary voltage rejection

The multichannel EIT imaging data sets consisted of multiple injection pairs, with each pair consisting of 30 s of current injection, during which the remaining 28 electrodes were used for voltage recording. The resultant boundary voltages were then averaged over each one second trial for a given injection pair. The boundary voltages were processed to reject noisy channels. This was first done, by trial, by removing channels with a boundary voltage less than 100 µV. The second step was to remove channels, after averaging, based upon their interstimulus SD. The standard deviation threshold of each recording was the harshest threshold that preserved 90 % of the channels with a 'significant impedance change'. Channels with a 'significant impedance change' were defined as those with an impedance change three times greater than the average interstimulus SD. If this threshold resulted in less than 30 channels with a 'significant impedance change' then the trial was averaged with another recording from the same rat with stimulation of the same whisker group and the SD threshold procedure repeated.

6.2.4.4 Image reconstruction

Images were reconstructed with the real component of voltage differences using a TD approach at all 8192 time points of the, post-averaging, 1000 ms image length, with whisker deflection occurring at 105 and 605 ms. The voltage differences were used to reconstruct conductivity difference images using a sensitivity matrix reconstruction algorithm [184]. A FEM mesh with refinement over a region covering the electrode placement for all rats and 7 930 313 tetrahedra was used. The quality of the mesh, using the Joe-Liu quality

*As determined by simulation studies undertaken within the UCL EIT group [245]

measure, had a mean of $q = 0.9147$, a minimum of $q = 0.2074$, and 20 tetrahedra had $q < 0.3$ (see section 4.1.3 for details of this quality metric). The position of the electrode array was measured at the end of each experiment by means of photogrammetry, which entails deriving the electrode positions in a 3D coordinate system using a collection of photographs taken at known angles from one another and the identification of fiducial markers[246]. Three photographs were taken using the ISOI camera, at 0, 20 and 40°, and the fiducial markers were the bregma and lambda points on the skull. Additionally, the FEM mesh was scaled for each rat according to the distance between the bregma and lambda points on the skull.

The fine sensitivity matrix resulting from the forward computation was then projected onto a coarse sensitivity matrix, so the summated volume was over cubic volumes with an edge length of 100 µm. This was because simulation studies undertaken within the UCL EIT group revealed that the spatial resolution is at best 100 µm for the impedance changes recorded with stimulation of 4 whiskers[245]. The resultant sensitivity matrix was the equivalent of a hexahedral mesh of approximately 140 000 hexahedra, which was readily invertible with less than 20 GB of memory while preserving the maximal spatial resolution. Inversion was performed on this coarse sensitivity matrix using Tikhonov regularisation with the hyperparameter set using cross-validation, with λ spanning 1×10^{-20} to 1, in 2000 logarithmically spaced steps, and the cross validation being ten-fold using 10 % of the data for training (see section 4.1.4 for details).

6.2.4.5 Noise-based data scaling simulations

Simulations were performed using the mesh, sensitivity matrix and inverted sensitivity matrix from one of the recordings used for the experimental data. Simulations were performed for 20 perturbation locations, with centres at a depth of 0.5 mm to 2.4 mm, in steps of 0.1 mm. For each simulation boundary voltages were simulated for a 1 % conductivity change. This was by multiplication of an area of 300 µm × 300 µm × 300 µm in the coarse sensitivity matrix against a vector of $\delta\sigma$. These boundary voltages were than multiplied by the inverted sensitivity matrix to recover a reconstructed $\delta\sigma$. Simulations were first noise free and then with Gaussian noise with a SD of 0.5 µV, which was the mean interstimulus noise in the present study and the study undertaken in chapter 5. In addition to these simulations, the ratio of SD by depth was calculated and this used for noise-based data scaling, so that for each of the perturbation locations, four simulations were undertaken: noise free uncorrected simulations; uncorrected simulations with Gaussian noise; noise free noise-based data scaled simulations; and noise-based data scaled simulations with Gaussian noise. The centre-of-mass (see equation 3.19) of the changes greater than 50 % of the maximal change was calculated for each simulation. Due to the findings of these simulations the experimental reconstructed images were expressed as

noise-based scaled data.

6.2.4.6 Image analysis: somatotopy

To determine the somatotopy of the reconstructed EIT images, the images at the time of the maximal impedance change were considered. This was the time point at which either whisker deflection resulted in the largest impedance change, averaged across channels. The area of significant conductivity changes was determined by identifying columns of hexahedra with four or more layers (z segments) with a conductivity change greater than 3SD of the conductivity changes in the interstimulus interval. The conductivity changes at this time point within the two most superficial layers were not considered to prevent electrode artefacts dominating the analysis.

Having defined the area of significant conductivity changes, the largest group of connected hexahedra within this area with a conductivity change greater than 50 % of the maximum conductivity change was identified. The centre-of-mass (see equation 3.19) of this group of connected hexahedra was calculated and the distance between the centres for stimulation of the two whisker groups calculated for each rat.

6.2.4.7 Image analysis: translaminar propagation

To examine the translaminar propagation of the reconstructed EIT images the conductivity changes over time and depth for two ROIs were considered. The hexahedra (100 µm edge length ROI) closest to the location of insertion of the electrode used for LFP recording was plotted first, and then the hexahedra closest to the centre-of-mass (see section 6.2.4.6 for details) was plotted. Within these ROIs the onset and the peak of the conductivity change per layer were determined. For this analysis only significant conductivity changes were considered. These were defined as conductivity changes with an amplitude greater than three times the interstimulus SD. For each depth, and at each whisker deflection direction, the peak response was detected and the onset of the conductivity change was defined as the first time point before this peak at which the changes became significant.

6.3 Results

6.3.1 Noise-based data scaling simulations

The centres-of-mass of the uncorrected noise free reconstructions is comparable to the actual perturbation centre for depths up to 1 mm, with the largest error being 0.4 mm. However at depths greater than this the error increases supralinearly, as the reconstructed centre-of-mass becomes deeper with progressively smaller increments, with the error at 2.4 mm being 1.2 mm (figures 6.1a and 6.2a). The noise-based scaled reconstructions

are also comparable to the actual perturbation centre for depths up to 1 mm. However, while the uncorrected reconstructions' centre-of-mass are incorrectly superficial, the noise-based scaled reconstructions are deeper than the simulated perturbation, with the largest error for depths up to 1 mm being 0.2 mm. Over greater depths the noise-based scaled reconstructions show two responses; at depths from 1.1 to 1.9 mm the centres-of-mass are deeper than the simulated centres with the maximal error being 0.4 mm. At depths from 2.0 to 2.4 mm the centres-of-mass are erroneously superficial with the maximal error being 0.4 mm (figures 6.1b and 6.2a).

The centres-of-mass for the uncorrected reconstructions with Gaussian noise are comparable to the actual perturbation centre for depths up to 0.9 mm, with the largest error being 0.3 mm. However, at depths greater than this, centres-of-mass are almost unchanging with increasing simulated perturbation depth, with the maximal error being 1.8 mm (figures 6.1c and 6.2b). The noise-based scaled reconstructions with Gaussian noise show a three stage trend comparable to that for the noise free simulations. The best match between simulated perturbation and centres-of-mass is for depths up to 0.9 mm, with the largest error being 0.2 mm. At depths from 1.0 to 1.5 mm the centres-of-mass are deeper than the simulated centres with the maximal error being 0.6 mm. At depths from 1.6 to 2.4 mm the centres-of-mass are mostly erroneously superficial with the maximal error being 0.9 mm (figures 6.1d and 6.2b).

(a) *Uncorrected noise free simulations*

(b) *Noise free noise-based scaled simulations*

(c) *Uncorrected simulations with Gaussian noise*

(d) *Noise-based scaled simulations with Gaussian noise*

Figure 6.1: *Simulations of noise-based data scaling. Red boxes indicate the simulated perturbations' limits and the bullet marker the centre-of-mass. Each simulation is scaled separately.*

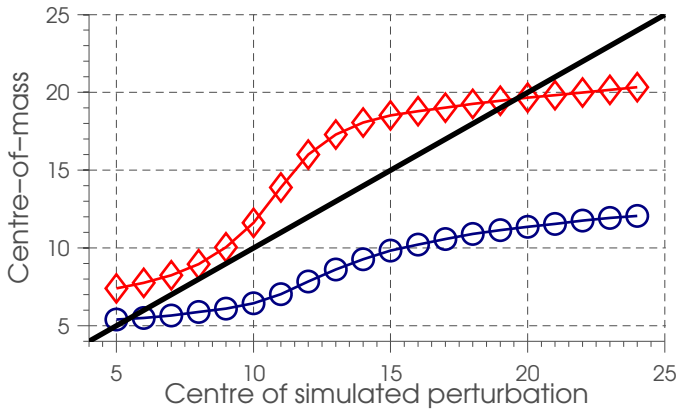

(a) *Noise free simulations*

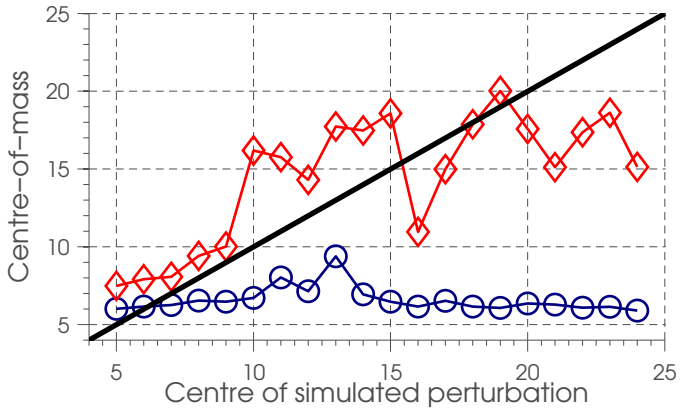

(b) *Simulations with Gaussian noise*

Figure 6.2: *Centre-of-mass comparison for uncorrected and noise-based data simulations.* —○— *uncorrected simulations.* —◇— *noise-based scaled simulations.*

6.3.2 Data Cohort

Data were collected from four rats. For each rat a set of ISOI images was collected for stimulation of the δ and D2 whiskers separately. A total of 73 EIT and LFP recordings were made ($n = 9$, $n = 21$, $n = 23$, $n = 20$) (table 6.1). From these recordings, as a result of averaging some recordings together and others having an insufficient number of channels with a 'significant impedance change' (see section 6.2.4.3 for details), a total of 27 images were reconstructed ($n = 8$, $n = 8$, $n = 8$, $n = 3$) (table 6.2).

	Rat 1	Rat 2	Rat 3	Rat 4
δ group stimulation	5	11	12	10
D2 group stimulation	4	10	11	10

Table 6.1: *Summary of collected data*

	Rat 1	Rat 2	Rat 3	Rat 4
δ group stimulation	4	6	5	1
D2 group stimulation	4	2	3	2

Table 6.2: *Summary of reconstructed images*

6.3.3 Imaging of somatotopy

The ISOI images display considerable variability in areal extent and location for stimulation of the two whiskers. Nonetheless, the direction of displacement between the two areas of activity was comparable. The separation of the two whisker barrels ranged from 0.91 mm to 1.6 mm, which is comparable to the expected distance of approximately 1 mm[247](figure 6.3 and table 6.3).

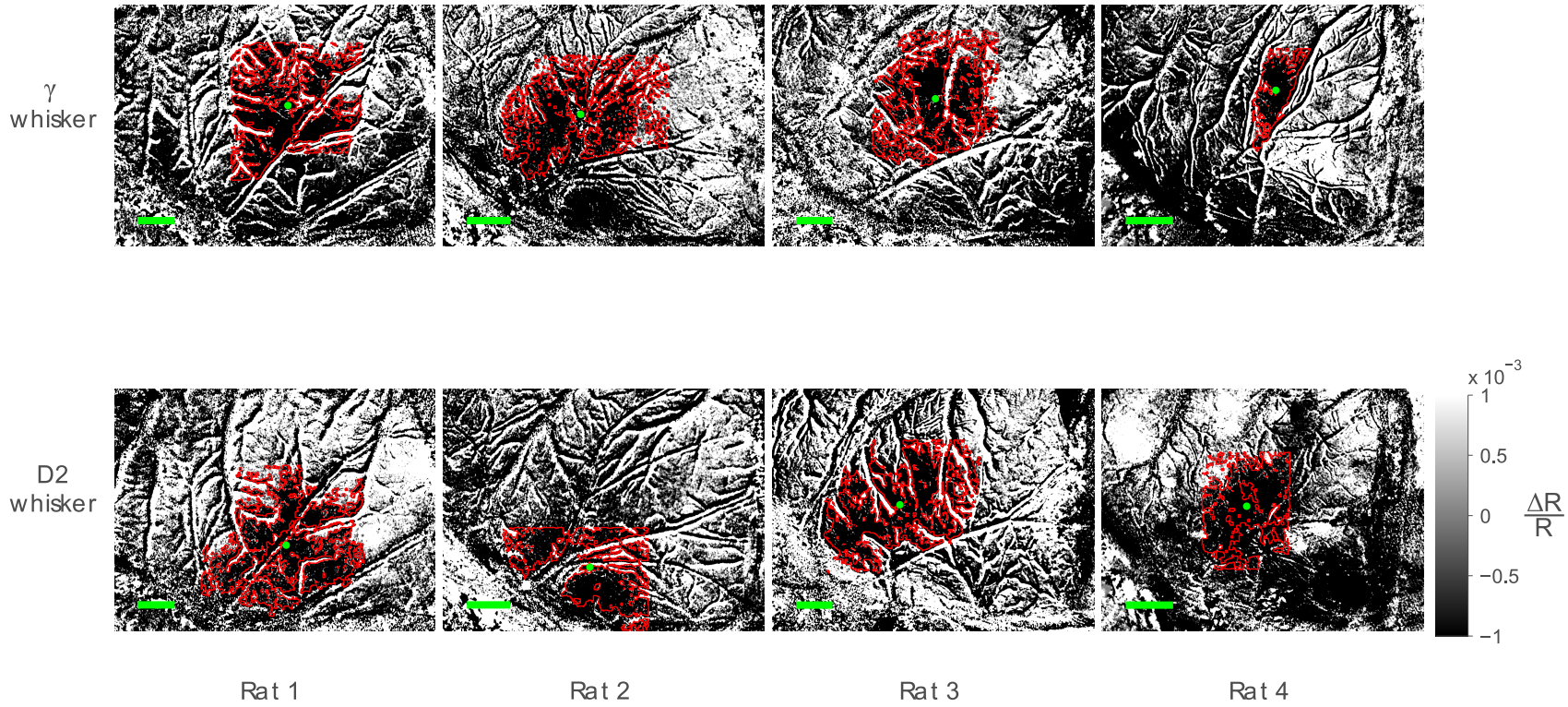

Figure 6.3: *ISOI images. Each column show the ISOI image for a given rat, while each row is for stimulation of one of the two whiskers. The red outline show the area of segmentation and the bullet marker the centre-of-mass. The scale bar in the bottom left of each figure is 1 mm*

All of the EIT images had centres-of-mass closer together than their ISOI counterpart. For three of the rats the spacing was approximately 0.6 mm, while for the remaining rat the spacing was 1.32±0.12 mm. Nonetheless, the directions of displacement between the two areas of activity were comparable to one another and to the ISOI images. Furthermore, the areal extent of the above half maximal changes of the same condition (same whisker group within the same rat) had overlapping areas (figure 6.4 and table 6.3).

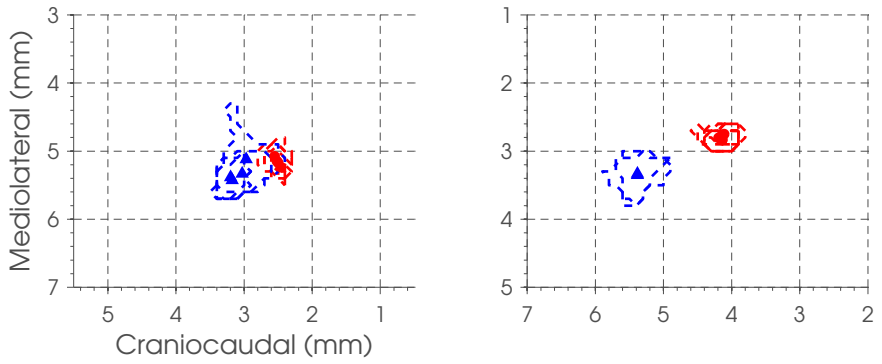

(a) *Rat 1*

(b) *Rat 2*

(c) *Rat 3*

(d) *Rat 4*

Figure 6.4: *Centre-of-mass for EIT images of different whisker groups.* ▲ *D2 group stimulation centre-of-mass.* ● *δ group stimulation centre-of-mass. Dashed outline show the outline of the conductivity changes above 50 % the maximal conductivity change.*

	Rat 1	Rat 2	Rat 3	Rat 4
ISOI Barrel Separation (mm)	1.49	1.60	1.15	0.91
EIT Barrel Separation (mean±SD (mm))	0.62±0.12	1.35±0.03	0.56±0.98	0.62±0.02
Difference in Barrel Separation (mean±SD (mm))	0.87±0.12	0.25±0.03	0.59±0.1	0.29±0.02

Table 6.3: *Separation of barrels from ISOI EIT.*

6.3.4 Local field potentials

The maximal amplitudes of the LFP were quite variable for the difference rats, but fairly consistent for stimulation of the different whisker groups and throughout experiments. The LFP measured from rat 1 was up to 2 mV in amplitude, with the bottommost 11 electrodes having predominantly negative components, while in the superficial electrodes there was a second positive peak that was largest at the pial surface. The LFP measured from rat 2 was up to 700 µV in amplitude, with most of the power of the LFP being in the upper third of the electrodes. A negative-positive waveform was evident in all electrodes, with the uppermost electrode having a positive-negative-positive waveform. Unlike for the other three rats there is a clear difference between the LFP for the two peaks, with the second peak (the forwards deflection) being larger than the first. The LFP measured from rat 3 had the smallest amplitude of 500 µV, but nonetheless there was a polarity inversion between electrodes five and six, with positive changes predominating in the upper electrodes and negative changes in the lower electrodes. The LFP measured from rat 4 was of a similar amplitude to that recorded from rat 2. As for rat 3, there was a polarity inversion between electrodes five and six, with positive changes predominating in the upper electrodes and negative changes in the lower electrodes (figure 6.5).

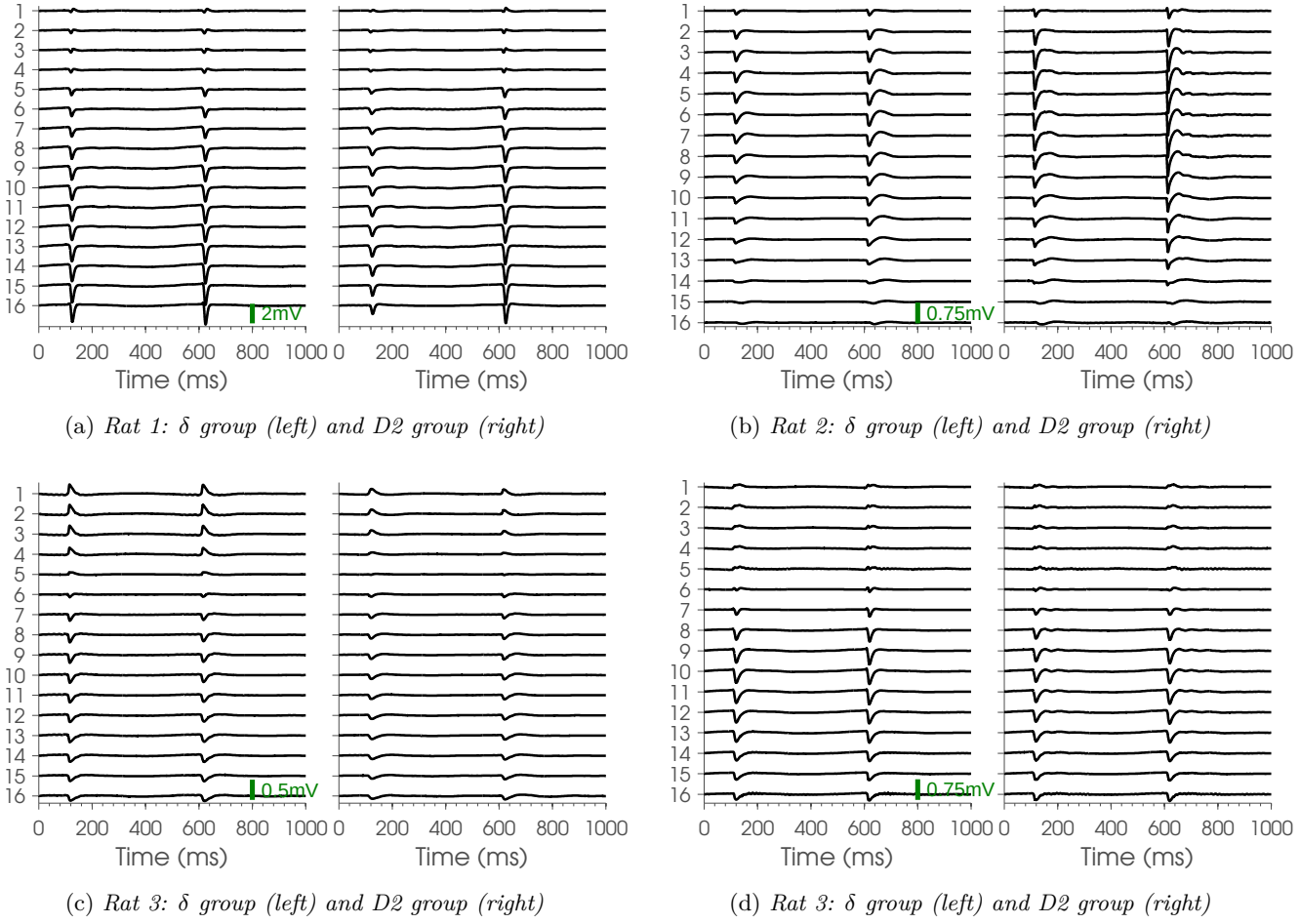

(a) *Rat 1: δ group (left) and D2 group (right)*

(b) *Rat 2: δ group (left) and D2 group (right)*

(c) *Rat 3: δ group (left) and D2 group (right)*

(d) *Rat 3: δ group (left) and D2 group (right)*

Figure 6.5: *Grand average LFP measurements. In each subplot the LFP for stimulation of each whisker group in a given rat is shown. The y-axes are numbered for the electrode numbers, with 1 being the uppermost, and each being 100 μm apart.*

6.3.5 Current source-sink density analysis

The CSDA for rat 1 had its earliest sink, which is assumed to be layer IV, at electrodes 11 to 13, which was followed by infra- and supragranular source-sink complexes. This pattern was apparent for stimulation of both whisker groups and for both deflection directions, although the response was somewhat reduced for the first/backward deflection of the D2 group. The earliest sink in the CSDA for rat 2 was at electrodes 11 to 13, which was followed by an infragranular source-sink complex, and a supragranular sink, which can be seen to be coupled to a supragranular source for stimulation of the D2 group of whiskers. There were far fewer significant changes in the CSDA of rat 3 and 4. The distribution of sources and sinks was much more limited in the CSDA for rat 3: the earliest sink was at electrodes 6 to 8. This sink was almost absent during stimulation of the D2 group of whiskers, and this sink was coupled to a supragranular source. There was a late infragranular source for all of the CSDA of rat 3, excluding the second deflection of the D2 group of whiskers. In the CSDA of rat 4 the earliest sink was at electrodes 8 to 9, and was coupled to a supragranular source. In the second deflection, for both whisker groups, there was an infragranular source-sink complex.

(a) *δ group first deflection*

(b) *δ group second deflection*

(c) *D2 group first deflection*

(d) *D2 group second deflection*

Figure 6.6: *CSDA for Rat 1*

(a) *δ group first deflection*

(b) *δ group second deflection*

(c) *D2 group first deflection*

(d) *D2 group second deflection*

Figure 6.7: *CSDA for Rat 2*

(a) *δ group first deflection*

(b) *δ group second deflection*

(c) *D2 group first deflection*

(d) *D2 group second deflection*

Figure 6.8: *CSDA for Rat 3*

(a) *δ group first deflection*

(b) *δ group second deflection*

(c) *D2 group first deflection*

(d) *D2 group second deflection*

Figure 6.9: *CSDA for Rat 4*

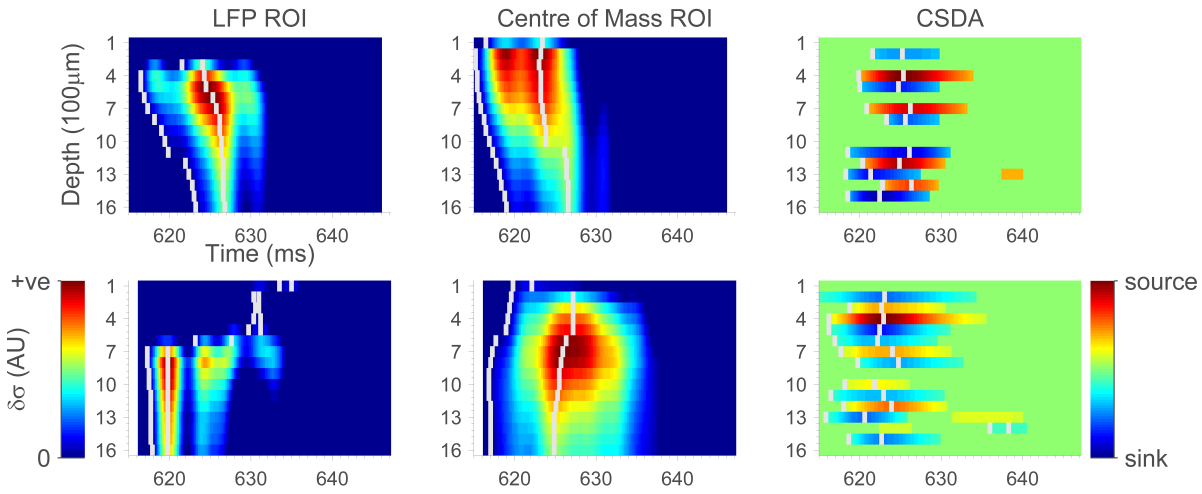

Figure 6.10: *Translaminar activity: Rat 1. The four left most subplots are depth-time series plots for ROI and the rightmost column of plots are the corresponding CSDA. The top row is for stimulation of the δ whisker group and the bottom row for stimulation of the D2 whisker group. In each subplot the leftmost vertical white lines indicate the onset time and the rightmost vertical white lines indicate the peak time for a given depth. The conductivity changes are expressed in arbitrary units as the noise-scaling results in the conductivity changes no longer being in percentage. Figures 6.11, 6.12 and 6.13 have the same layout.*

6.3.6 Imaging of translaminar propagation

The time of onset for the earliest sink and the onset of the EIT were well synchronised with less than 1 ms difference between them. Similarly the peak of the impedance change was also well synchronised to the peak of the CSDA (figure 6.10). In addition, in multiple instances in different rats it could be observed that when the duration of the CSDA was increased the changes reconstructed by EIT also persisted for longer (figure 6.10 and 6.13). It is also of note that, when the CSDA jittered, most probably due to physiological or stimulation variability, the conductivity changes also jittered in the same manner (figure 6.11). In some reconstructions the timing profile of the LFP ROI in the EIT image was well matched to the corresponding profile for the CSDA: in the second rat the CSDA showed engagement of the supragranular layers at a slower rate than that of the spread from layer IV to the infragranular layers. A similar physiological point of note is that the reconstructed EIT showed greatly reduced or non-significant conductivity changes when the CSDA showed minimal significant source/sinks (figure 6.12 and 6.13).

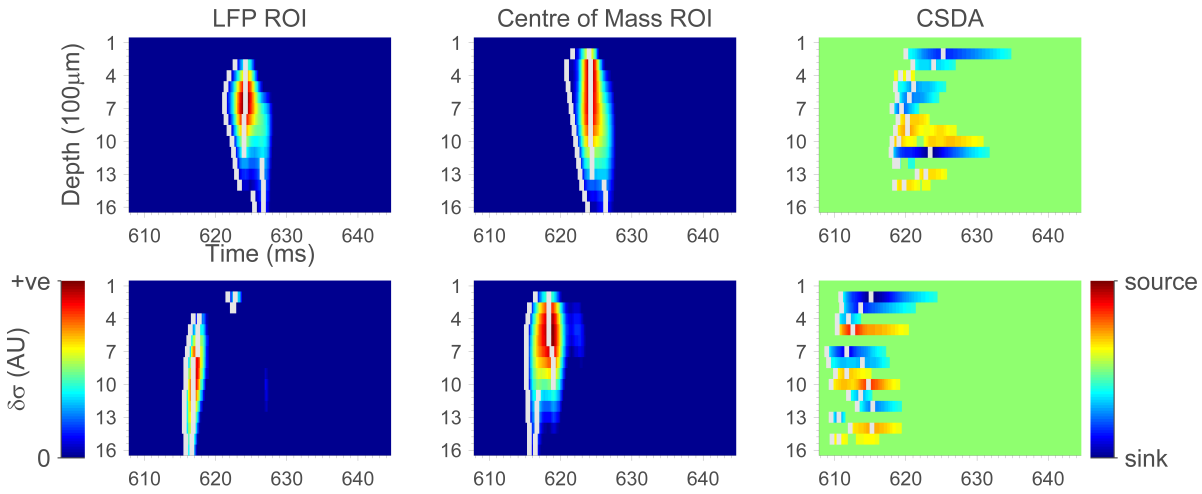

Figure 6.11: *Translaminar activity in Rat 2.*

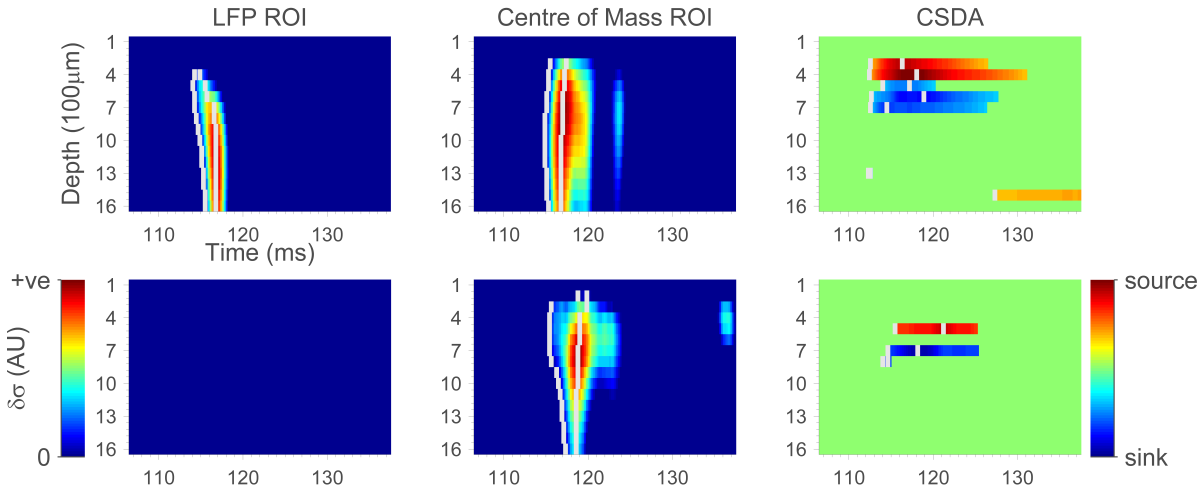

Figure 6.12: *Translaminar activity in Rat 3.*

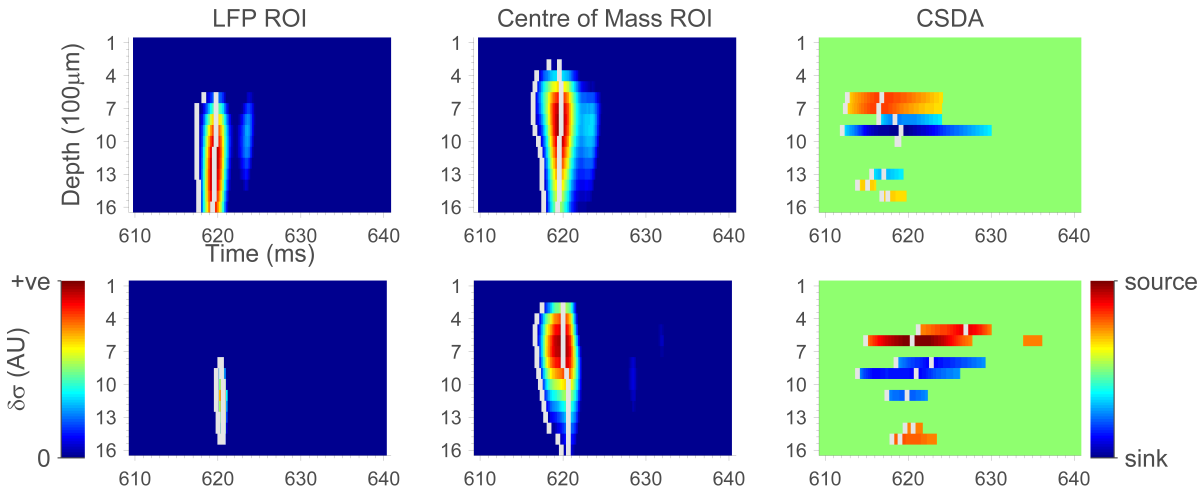

Figure 6.13: *Translaminar activity in Rat 4.*

6.3.7 Imaging of lateral spread of activity

By plotting multiple depth-time series for multiple contiguous hexahedra, as opposed to a single ROI, and detecting the time of onset, it is possible to examine the lateral spread in the x-y-plane. By doing so the areas of the earliest activity can be identified, and with increasing distance from these areas the time to onset of activity increased by 1 ms over a distance of approximately 4 mm (figure 6.14). If a larger area is explored then the time to onset increased by 4 ms over a distance of approximately 4 to 5 mm in the mediolateral axis, while over similar distances in the craniocaudal axis time to onset increased by approximately 2 ms (figure 6.15). The interpretation of these plots is complex as there are multiple sites of earliest activity and timings are increased moving away from one, but as the distance to another source reduces the timings of onset start to reduce, as might be expected from four whisker stimulation, which will activate four areas simultaneously. In fact in such plots three or four separate areas of earliest activity can be identified (figure 6.15). For the areas of earliest activation the depth of the earliest significant conductivity change was at 500 to 800 µm, which approximates the depth of layer IV, which is from 600 to 800 µm.

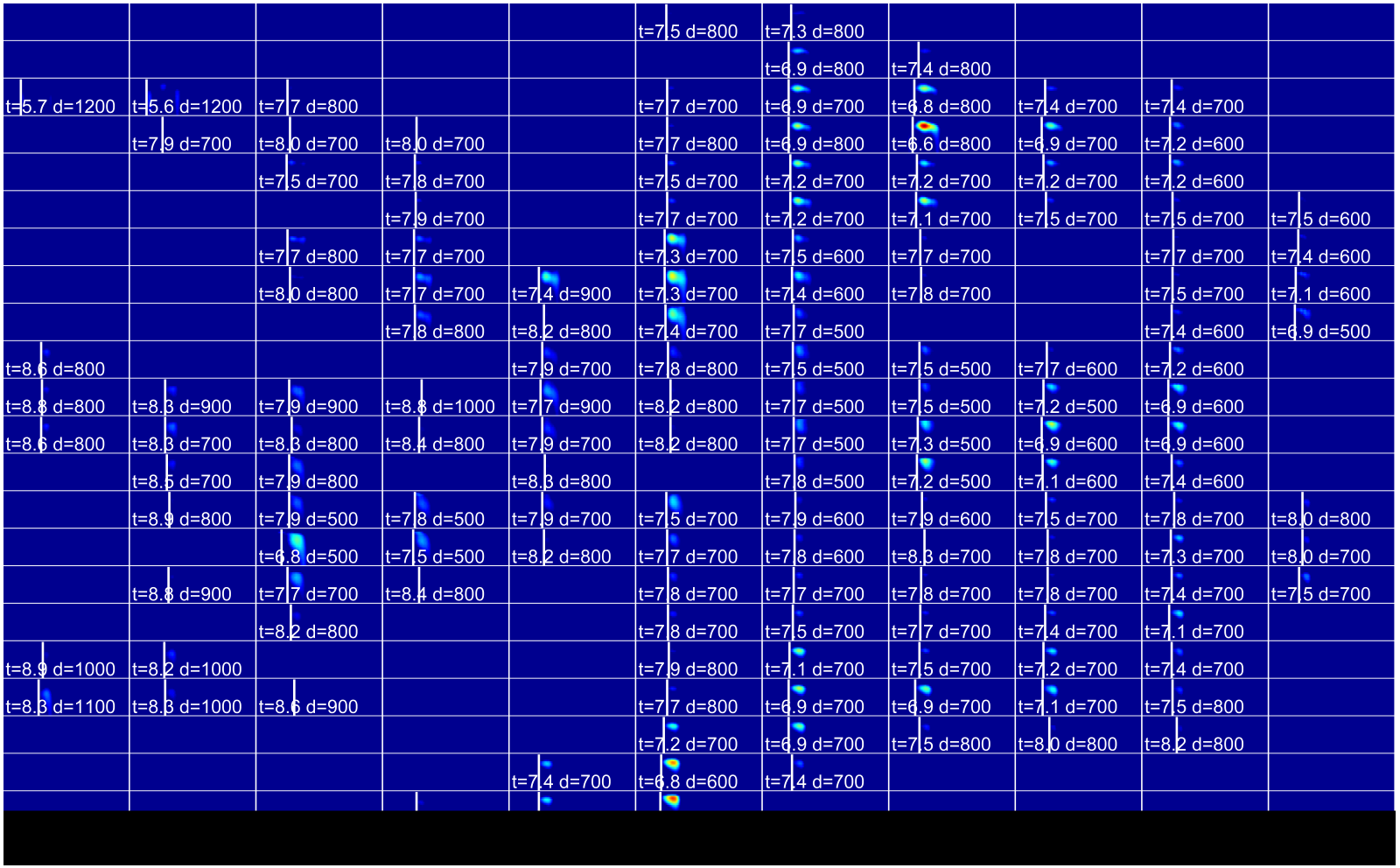

Figure 6.14: *Multiple depth-time series for rat 2, following δ whisker group stimulation. Each subplot is a contiguous 100 μm × 100 μm hexahedral area, with the y-axis being depth from deep to superficial, and the y-axis being time. The central plot is at the location of the centre-of-mass for the respective recording and form right to left subplots span the mediolateral axis and from bottom to top they span the craniocaudal axis. The vertical white lines indicate the onset time for a given cell and this is labelled with 'd=' for the depth of the earliest onset and 't=' for the post-stimulus time of the earliest onset. The conductivity changes are expressed in arbitrary units as the noise-scaling results in the conductivity changes no longer being in percentage. Figure 6.15 has the same layout.*

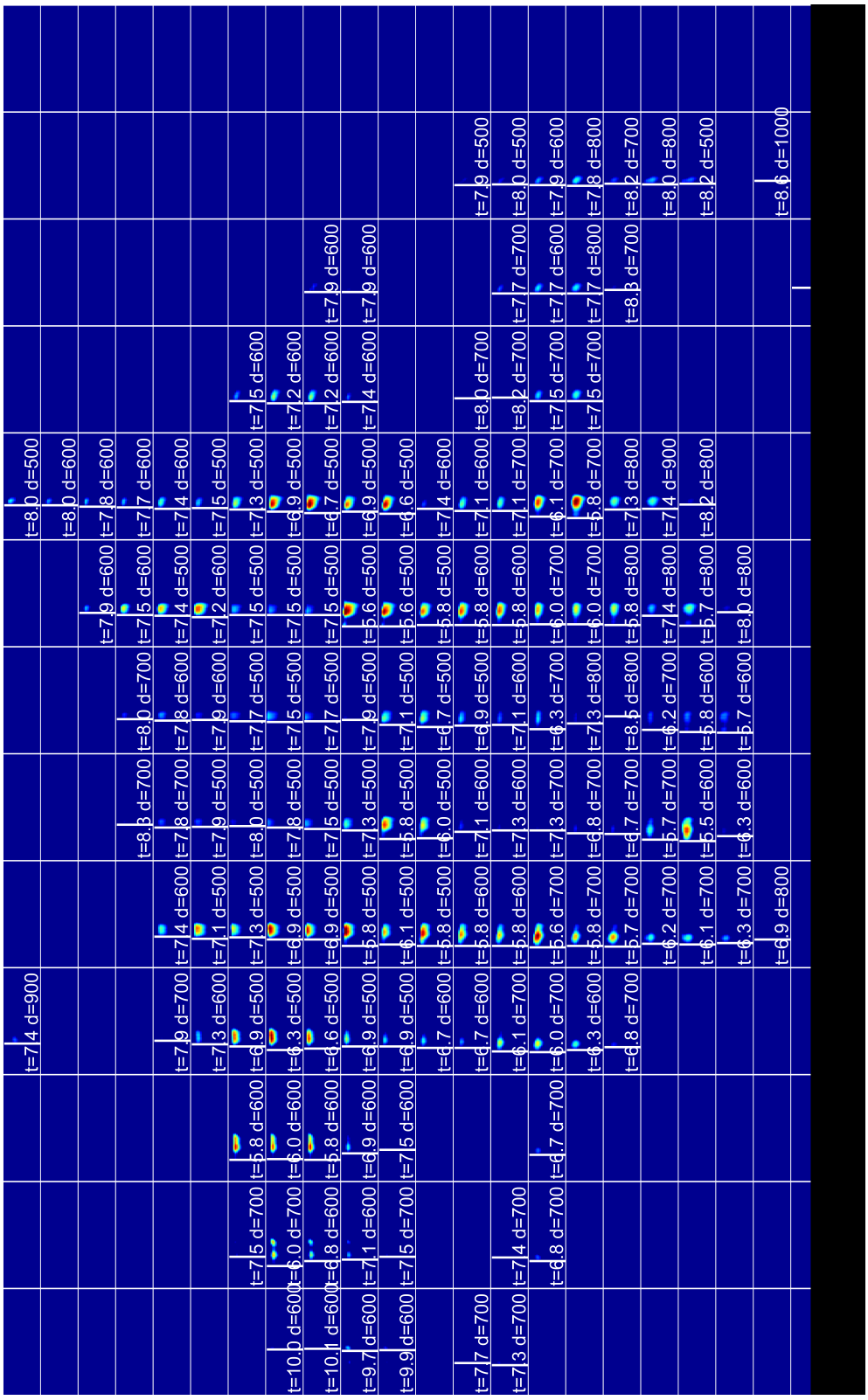

Figure 6.15: *Multiple depth-time series for rat 3, following δ whisker group stimulation.*

6.4 Discussion

6.4.1 Summary of results

As noted in chapter 5, imaging the fast neural response following stimulation of four whiskers yields a signal at the edge of detectability with the current experimental set-up and paradigm, and this was reflected in the high loss rate of data, with multiple datasets having to be averaged together. Nonetheless, various improvements were identified from previous studies and these were successfully implemented in the present work: projection was used to have a coarse sensitivity matrix for the inverse solution; depth localisation was improved with the use of noise-scaled data; the temporal resolution of images was improved to 2 ms, which is a four times improvement over the previously employed temporal resolution of 8 ms[90]. These incremental, but crucial, improvements enabled the first cross-validation of EIT of fast neural activity.

Somatotopic mapping was undertaken with ISOI and EIT, with both techniques yielding separation of whiskers/whisker groups along a comparable vector, with the EIT separation between centres of activity being somewhat smaller than that detected by ISOI, but still comparable. Qualitative analysis of multiple depth-time series indicated that the translaminar activity recorded EIT share many commonalities with LFP/CSDA: (1) the time of onset for the earliest sink and the onset of the EIT are well synchronised; (2) increases in the duration of the CSDA are matched by an increased duration in the EIT conductivity changes; (3) jittering in the CSDA was coupled to jittering in the conductivity changes; (4) the onset profile of the conductivity changes is broadly similar to that of the CSDA. In addition, by examining a wider area with depth-time series plots lateral spread was identified and found to be non-uniform: spread in the mediolateral and craniocaudal axis were at different rates.

6.4.2 Somatopy of EIT for different whisker groups

The barrel/whisker group separation for EIT and ISOI were comparable, but not perfectly matched, which could be attributed to several causes. ISOI is commonly employed for mapping the PMBSF, with a good correlation between the ISOI and histological location of the barrels being noted[247]. However, the difference in separation distance was up to 0.87 mm, which is approximately equivalent to the diameter of two barrels. Given that the vector of separation between the two areas was comparable with the two techniques it seems unlikely that this error reflects an inability of EIT to detect a shift in the location of activity. Rather, it would seem most likely that multiple factors have contributed to this difference. First, only single whiskers were stimulated for ISOI, as it was apparent from the literature that ISOI of multiwhisker stimulation is poorly understood[248], while during EIT recordings, to ensure sufficient SNR for imaging, four whiskers were stimulated.

In addition, the spatial correlation between the signals recorded with EIT and other neurophysiological recording techniques has not been established and the signals being detected by the respective techniques might not be expected to spatially align. Lastly, one of the fundamental flaws of EIT is that the technique suffers from poor spatial resolution and a broad point-spread-function, which could potentially result in artificially reduced separation of the centres of activity.

6.4.3 Translaminar and lateral propagation in EIT images

Within the scope of the qualitative analysis undertaken within this study, the evidence thus far is that the translaminar propagation of activity is comparable to that measured with LFP/CSDA based upon numerous observations of similarity in multiple aspects of the signals. In several instances the depth of the first response in the EIT does not precisely match the depth of the first response of the CSDA, although, there are two key confounding factors. First, there is the issue of poor depth localisation and poor spatial resolution in EIT. Second, there is potential error in LFP electrode depth location, as the scales under consideration are of the order of 100 µm. Experimental error, even with microscopy and a micromanipulator would be expected to be at least 100 µm, so that the uppermost contact of the electrode might in fact not be just below the pial surface, but rather could be most of the way through layer I, which would offset all data by 100 µm. Nonetheless, the similarity of many of the temporal aspects of the two techniques implies a commonality between them. In addition, examination over a volume of the EIT image implied lateral spread could be identified. The velocity in the approximate axis of the whisker rows (the craniocaudal axis) was 200 µm ms^{-1}, while in the orthogonal axis, in the approximate axis of the whisker arcs (mediolateral), the velocity was 100 µm ms^{-1}. Previously reported values for lateral velocity across whisker rows are about 50 to 60 µm ms^{-1}, and so a quarter of the values noted here, with the velocity along arcs being 30 µm ms^{-1} [110;139]. Thus, there is a clear discrepancy in the amplitude of the velocities noted here and those previously reported, although the same spatial trend/scaling of the velocities is present: a greater velocity across rows than arcs. There are multiple factors that might explain the discrepancies between these values, but the key among them is that the literature on this matter is almost wholly related to single whisker stimulation and the stimulation of multiple whiskers would certainly have affected the lateral integration and spread of activity and result in a far more complex pattern of activity that would require a more detailed analysis to fully elucidate the underlying causality.

6.4.4 Study limitations

Although substantial improvements in the experimental methodology have been made over the previously implemented set-up, it would still be preferable to achieve a temporal resolution of 1 ms. However, this would require the impedance changes to be demodulated with a bandwidth of ±1 kHz, which would introduce more noise, which in turn would most likely result in fewer channels having a sufficient SNR for imaging. This trade off would require further examination before a ±1 kHz might be employed. Furthermore, there are other aspects of the current experimental set-up that might yield improvements in SNR, such as higher density electrode arrays, which would allow for a broadening of the bandwidth, and perhaps it would be wisest to address these first.

Many of the uncertainties in the present study, such as the barrel separation and the depth at which the LFP was being measured, might be addressed through histological preparations from the culled animals' brains, but unfortunately resources were not available to undertake this component of the study.

It is also necessary to undertake further analyses, beyond the largely qualitative analyses employed here, before any bold conclusions can be made. This was not undertaken at present as such analysis requires a substantial body of work that needs to encompass a furthering of the current understanding of the origins of the fast neural EIT signals. Although the effect of ion channel opening is undoubtedly a component of the fast neural EIT signal, it would seem logical to incorporate the effect of the currents that are being generated in the brain. One of the prior assumptions in EIT is that there are no current generators inside the object being imaged, which clearly is not true in the brain. It has been assumed that the current generated in neural tissue is a negligible component compared to the conductivity change. However, as imaging of fast neural activity has only become possible in the last 5 years or so, it may be pertinent to revisit some of these assumptions. Another reason for not undertaking broader analysis is that the dataset to be analysed is very large and its analysis is not trivial; many years of neuroscientific research have been dedicated to the analysis of large datasets and to assume the tasked would be easier with EIT data would be naive. It seems sensible to first examine these techniques and determine which, if any, are most appropriate for analysis of the present dataset. Simple grand average statistics, or even SPM, are not possible with the dataset in its present state as there is considerable physiological temporal jitter. Consequently, a temporal correction would need to be first applied to the dataset, but again given the relatively novel nature of the data the best means for applying this temporal correction would need careful examination.

6.4.5 Recommendations for future work

Future work should be focused on two tasks. The first is to address the technical limitations that persist with the experimental paradigm, and the second is to perform thorough quantitative analysis of the dataset acquired in the present study. As discussed in chapter 5 there is a need for higher density electrode arrays to facilitate improved SNR and the imaging of the small changes that occur with single or four whisker stimulation. Additionally, further examination of the optimal electrode addressing protocols is required and ideally a fully parallel system could be implemented to allow for more rapid data acquisition, and therefore greater averaging and reductions in random noise.

Analysis of the present data set might include further exploration of the underlying signals of fast neural EIT, which could include modelling of the effects of internal current generators and solving the EIT problem with consideration of the conductivity change alone and with the inclusion of these current sources. There are a plethora of neuroscientific analysis techniques, and a thorough literature review on the matter would be required before the most appropriate analyses could be determined. Nonetheless, a reasonable starting point might be the exploration of the spatiotemporal causality of the data with a technique such as Granger causality. Within Granger causality statistical testing is performed on time-lagged data to determine if they provide statistically significant information about other future values.

Chapter 7

Discussion and future work

7.1 Summary of studies

The main objective of this thesis was to advance the imaging of brain pathology and function, with particular focus on determining the feasibility of the use of EIT for neuroscientific research into the fast neural changes of brain function. Within chapter 2 reconstruction algorithms for EIT imaging in a head shaped tank were compared, with an additional aim of assessing boundary voltage rejection methods and quantitative analysis of image quality. The work undertaken in chapters 3 and 4 examined an EIT dataset of fast neural activity that had been previously collected in the anaesthetised rat model. The analysis included parametric and non-parametric mapping, simulations to elucidate the importance of correct electrode positions, and analysis of the spatiotemporal propagation of fast neural activity. In the final two chapters an attempt was made to try and address the shortcomings of the dataset analysed in chapters 3 and 4. To this end EIT imaging of fast neural changes following physiological vibrissae stimulation was undertaken. This was a difficult task as even stimulation of four whiskers resulted in a comparatively low SNR. Nonetheless, images were produced and so a dataset was collected with ISOI and LFP/CSDA measurements made within the same model to validate the findings of EIT.

7.2 Boundary voltage rejection

From the work undertaken in chapter 2 it was concluded that EIT image reconstruction is sensitive to the method and thresholds used for boundary voltage rejection. Insufficient rejection can result in images without a readily identifiable reconstructed perturbation. Equally, excessive boundary voltage rejection results in insufficient data to correctly solve the inverse problem so that images again lack a readily identifiable reconstructed perturbation. In the tank study described in chapter 2, multiple thresholds could be employed,

and the threshold and method yielding the 'best' images could be identified and employed for subsequent studies. However, such an approach is not feasible in the long term as only tank studies allow thresholds to be set based upon improvement in the reconstructed image. Similarly, a chosen threshold will only be appropriate to a given system, as the choice to reject small boundary voltages will be inherently tied to the random noise of the system, the degree of oversampling that occurs in the ADC, and the gain setting of the system. Therefore it is clear that more robust and universal approaches are required to ensure that unacceptably noisy data is not used in the image reconstruction. The approach adopted in chapter 5 was to employ a fixed threshold based upon the temporal noise, which resulted in the number of rejected boundary voltages being fairly consistent across the two rats from which data had been collected. However, initial preprocessing of the dataset used in chapter 6 indicated that during such long recordings over multiple rats a fixed threshold was insufficient for some data and resulted in an excessive number of boundary voltages being rejected in other cases. Therefore the chosen approach was to consider the threshold that preserved the majority of channels with a significant impedance change (greater than three SDs) whilst rejecting noisy channels. Further work is required to develop a robust and objective means of managing noisy data, and certainly the ideal scheme for a given application of EIT, such as MFEIT, will be different to the ideal scheme for other applications.

7.3 Analysis of electrical impedance tomography images

Image analysis, or some aspect of image analysis such as statistical testing, was employed in all the studies that were undertaken. In chapter 2, modification was made to an image quantification scheme previously employed[176], with these chosen modifications based upon the particular foci of MFEIT studies. Although there are other EIT image quantification schemes[249] the differences are largely superficial, with the key difference being the means of detecting the reconstructed perturbation. Different thresholds of detection are employed by different research groups with the choice seemingly being arbitrary. The selection of the reconstructed perturbation as a fraction of the maximal conductivity change is the most common procedure, but different thresholds yield considerably different results. This is less of a concern for tank studies with a spatiotemporally stationary perturbation of uniform conductivity contrast. However, neither condition is expected to be true in the application of imaging fast neural activity with EIT, and so thresholding images with respect to their significance, rather than based upon the amplitude of changes is a more sound methodology. This has the added advantage of avoiding a threshold based upon a fraction of the maximum amplitude conductivity change from being dominated by artefacts, such as the electrode artefacts prevalent in the imaging

of fast neural activity with a planar array. With a large sample size techniques such as second-level SPM can be employed as was undertaken in chapter 3, and validated, through the use of SnPM, in chapter 4. However, with a smaller sample size it is more appropriate to analyse images individually, rather than with population statistics. This approach was examined in chapter 6, by considering the noise in the images in the interstimulus interval. Not only did this approach allow for the masking of non-significant changes, but also through normalisation to this correlated noise the exponential decay in sensitivity over depth was partially countered. This approach certainly needs more rigorous validation and mathematical formalisation.

7.4 Validity and future of electrical impedance tomography of fast neural activity

The key limitations identified in the previous studies, particularly the novel work by Gilad et al. were: non-somatotopic/non-physiological stimulation, an absence of cross-validation and poor temporal resolution. The first two limitations were both addressed by determining the feasibility of mechanical vibrissae stimulation, which was determined to be feasible for simultaneous stimulation of four whiskers. The issue of temporal resolution was addressed by using a higher carrier frequency and broader bandwidth for demodulation, yielding a temporal resolution of 2 ms. With these improvements EIT imaging of fast neural activity was directly cross-validated against ISOI and LFP/CSDA. In all aspects there was broad agreement between the results obtained with the validation techniques and with EIT. Most notably the conductivity changes over depth were well aligned, temporally, and in depth, to the results obtained using LFP/CSDA.

Further analysis of this dataset could be undertaken with neurophysiological data analysis techniques. However, assuming that the current conclusion that the results of EIT have similarity with the findings of the validation techniques, then the question arises as to whether EIT could be used for neuroscientific research into the fast neural changes of brain function. The natural evolution of new techniques is that the limitations should be explored, formalisation of procedures should be undertaken, and the nature of the underlying signal should be explored. The latter two points must be addressed for EIT to be truly feasible for use in neuroscientific research into the fast neural changes of brain function. In addition to this, it is commonplace for multi-modalities to be employed in single studies as they are often complimentary, and the differing signal origins of the respective techniques can be combined. An ideal technique to combine with EIT of fast neural activity is LFP measurement, not only because it offers direct intracortical information, but also because it can be used for EIT. The small contact surface area, and resultant high contact impedance, of electrodes used for LFP measurement prevents cur-

rent injection through these electrodes. However with an amplifier with sufficient input impedance these electrodes can be used for recording impedance changes. Data could be collected with minimal invasiveness, as compared to multishank electrode approaches, over a large volume, and with depth information improved by the presence of the depth electrode.

It is arguable that EIT in its current state is ready for neuroscientific research, as, although there are questions regarding the technique that need addressing, these can be approached by acquiring empirical data. This rests upon some incremental improvement to the experimental set-up, such as the development of new epicortical electrode arrays and electrode addressing protocols, but with such improvements EIT could have a clear role in neuroscientific research. For the technique to have a broader series of applications there are three key hurdles that must be addressed in future studies. First, it would be desirable to be able to image subcortical structures, such as thalamic nuclei. A natural extension of the study undertaken in chapter 6 would be to attempt cross-validated measurement, with depth electrodes, of activity from the thalamic nuclei associated with sensory stimulation of the barrel cortex. Second, there is a question of the feasibility of using EIT in an awake animal model, as much work has shown anaesthesia results in abnormal neurological responses. This can be addressed by determining the robustness of EIT imaging of fast neural changes in the presence of increased ECoG noise, and additional physiological artefacts, such as movement artefact, and the effect of the long term tissue response on the ability to undertake EIT imaging of fast neural changes. Finally, the greatest hurdle to overcome, but the one that would allow for the broadest variety of questions to be examined, is the ability to image fast neural changes from scalp measurements. However, the findings presented in this thesis would suggest that at present this seems unlikely. Large displacement of multiple whiskers resulted in impedance changes with an SNR of approximately 4, given that the skull would only reduce this, it seems unlikely that imaging from scalp electrodes would be feasible at present. Nonetheless, the findings of this thesis indicate that EIT can be used to image fast neural activity with a temporal resolution of 2 ms and spatial resolution of approximately 100 µm and that these findings are in accordance with other measurement techniques, but unlike these techniques data can be acquired over the thickness of the neocortex and over a large sampling volume.

Appendix A

Monitoring Temporal Variability of Biological Tissues

A.1 Purpose

Given the requirement in the tank study in chapter 2 to undertake a wide range of measurement iterations there was a need to be certain that the perturbation and carrot background would not vary over time as they equilibrated with the saline solution. It is expected from simple biological principles that by osmosis the concentration of solutes in a potato perturbation will alter if it is soaked in a solution with a different osmotic pressure to its own. The purpose of this pilot study was to ascertain the rate at which a potato cylinder and carrot cubes would equilibrate with a background saline solution of 0.1 %.

A.2 Methods

The resistance of the saline and biological tissues used were measured using a Hewlett-Packard 42847A impedance analyser (Hewlett-Packard, California, USA) which has an accuracy of ±1 %, which also has shielded wires to minimise the effect of stray capacitance. The temporal stability of biological tissues was determined by measuring the resistance of a known volume of the tissue. Potato, which was used as the perturbation in the tank studies in chapter 2, was cut, using a cork bore, to a size of 2 cm in diameter and 10 cm in length. Carrot, which was used for the studies with a complex background, was cut into 2 mm^3 cubes. These cubes were then placed in a Perspex tube 2 cm in diameter and 10 cm long, with a minimal amount, <5 ml, of 0.1 % saline added to ensure conduction between two Ag-AgCl electrodes on each end of the tube. The resistance was measured when the tissues were freshly cut and then were submerged in a 0.1 % saline solution and measured at 45, 100 and 400 min. The temperature was monitored

throughout all the measurements and was not found to vary from 25 °°C.

A.3 Results

The results revealed that the resistivity of both the potato and carrot are stable between 20 to 100 Hz and there is a small, given the ±1 % error margin, decrease between 100 Hz and 1 kHz, after which both tissuesŠ resistivity decreases until at 1 MHz it is less than a tenth of that at 20 Hz. In addition to this, the resistivity of the potato increased, by around 50 %, after being soaked in the 0.1 % saline solution for 45 min and remains at a similar value for a further 315 min. Moreover, this difference is mostly prominent at frequencies below 5 kHz, implying this change is due to a change in the extracellular space and would imply some osmotic movement of solutes from the extracellular spaces of the tissue into the background solution. In contrast to this, the carrot does not show this trend, implying that if any osmotic equilibration is occurring then it is more rapid, unsurprising given the higher surface area to volume ratio of the tissue after cutting it into cubes. Also any change that occurs over time is effecting both the extracellular and intracellular space, which would seem most likely to be due apoptosis, which also might be a consequence of cutting the carrot into cubes.

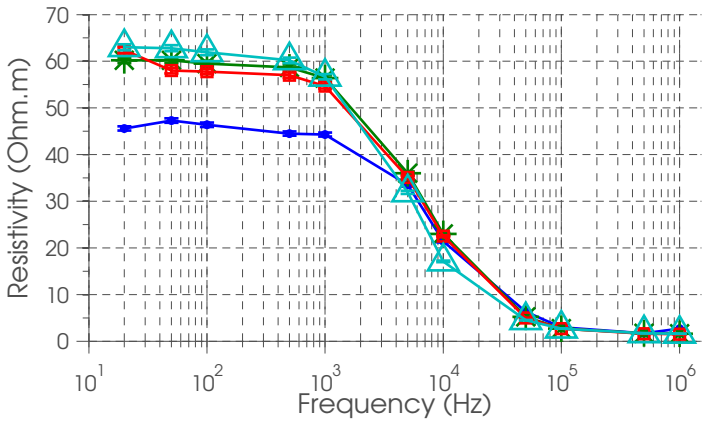

(a) *Temporal variability of potato's resistivity*

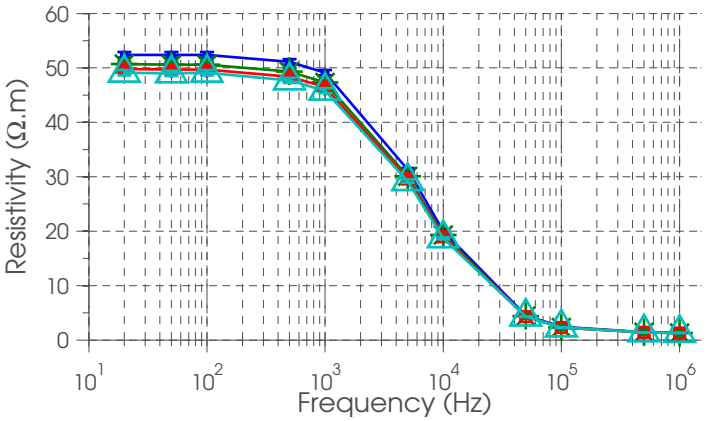

(b) *Temporal variability of carrot cubes' resistivity*

Figure A.1: *Temporal variability of potato and carrot cubes' resistivity.* —○— *0 min resistivity.* —★— *45 min resistivity.* —□— *100 min resistivity.* —△— *400 min resistivity.*

A.4 Conclusion

The conclusion of this preliminary study was that the potato perturbations should be pre-soaked in the 0.1 % saline background solution for at least 45 min prior to formal recordings being made and that recordings of this would be reliable for up to 315 min after this. In addition to this, it was concluded that the carrot background need not be pre-soaked in the background solution prior to any recordings and that it would be reliable for up to 400 min after its preparation.

References

[1] F. López-Muñoz, J. Boya, and C. Alamo. Neuron theory, the cornerstone of neuroscience, on the centenary of the nobel prize award to santiago ramón y cajal. *Brain Research Bulletin*, 70(4-6):391–405, 2006.

[2] T. Araki and C. Terzuolo. Membrane currents in spinal motoneurons associated with the action potential and synaptic activity. *Journal of Neurophysiology*, 25(6): 772, 1962.

[3] A. Hodgkin and A. Huxley. Action potentials recorded from inside a nerve fibre. *Nature*, 144(3651):710–711, 1939.

[4] H. Bowditch. On the peculiarities of excitability which the fibres of cardiac muscle show. *Mathematisch-Physische Klasse*, 24:653–689, 1871.

[5] H. B. Steinbach and S. Spiegelman. The sodium and potassium balance in squid nerve axoplasm. *Journal of Cellular and Comparative Physiology*, 22(2):187–196, October 1943.

[6] A. Hodgkin and B. Katz. The effect of sodium ions on the electrical activity of the giant axon of the squid. *The Journal of Physiology*, 108(1):37–77, 1949.

[7] E. Neher and B. Sakmann. Single-channel currents recorded from membrane of denervated frog muscle fibres. *Nature*, 260:799–802, 1976.

[8] A. Hodgkin and R. Keynes. Active transport of cations in giant axons from sepia and loligo. *The Journal of Physiology*, 128(1):28, 1955.

[9] P. Caldwell, A. Hodgkin, R. Keynes, and T. Shaw. The effects of injecting 'energy-rich' phosphate compounds on the active transport of ions in the giant axons of loligo. *The Journal of Physiology*, 152(3):561, 1960.

[10] R. S. Lillie. Factors affecting transmission and recovery in the passive iron nerve model. *The Journal of general physiology*, 7(4):473–507, March 1925.

[11] I. Tasaki. The electro-saltatory transmission of the nerve impulse and the effect of narcosis upon the nerve fiber. *American Journal of Physiology*, 127(2):211–227, 1939.

[12] L. Axel. Cerebral blood flow determination by rapid-sequence computed tomography: theoretical analysis. *Radiology*, 137(3):679, 1980.

[13] K. A. Miles. Perfusion ct: a worthwhile enhancement? *British Journal of Radiology*, 76(904):220–231, April 2003.

[14] M. König. Brain perfusion ct in acute stroke: current status. *European Journal of Radiology*, 45:S11–S22, March 2003.

[15] S. Ogawa, T. M. Lee, a. S. Nayak, and P. Glynn. Oxygenation-sensitive contrast in magnetic resonance image of rodent brain at high magnetic fields. *Magnetic Resonance in Medicine*, 14(1):68–78, April 1990.

[16] L. Pauling and C. D. Coryell. The magnetic properties and structure of hemoglobin, oxyhemoglobin and carbonooxyhemoglobin. *Proceedings of the National Academy of Sciences of the United States of America*, 22(4):210, 1936.

[17] A. P. Koretsky. New developments in magnetic resonance imaging of the brain. *NeuroRx : The Journal of the American Society for Experimental NeuroTherapeutics*, 1(1):155–64, January 2004.

[18] M. M. Ter-Pogossian, M. E. Phelps, E. J. Hoffman, and N. A. Mullani. A positron-emission transaxial tomograph for nuclear imaging (pett). *Radiology*, 114(1):89–98, 1975.

[19] R. O. Robinson, C. D. Ferrie, M. Capra, and M. N. Maisey. Positron emission tomography and the central nervous system. *Archives of disease in childhood*, 81 (3):263–70, September 1999.

[20] C. Ludwig, C. Chicherio, L. Terraneo, P. Magistretti, A. de Ribaupierre, and D. Slosman. Functional imaging studies of cognition using 99mtc-hmpao spect: empirical validation using the n-back working memory paradigm. *European Journal of Nuclear Medicine and Molecular Imaging*, 35(4):695–703, April 2008.

[21] A. P. Gibson, J. C. Hebden, and S. R. Arridge. Recent advances in diffuse optical imaging. *Physics in Medicine and Biology*, 50(4):R1–R43, February 2005.

[22] M. A. Franceschini, S. Fantini, J. H. Thompson, J. P. Culver, and D. a. Boas. Hemodynamic evoked response of the sensorimotor cortex measured noninvasively with near-infrared optical imaging. *Psychophysiology*, 40(4):548–60, July 2003.

[23] Y. Chen, A. D. Aguirre, L. Ruvinskaya, A. Devor, D. a. Boas, and J. G. Fujimoto. Optical coherence tomography (oct) reveals depth-resolved dynamics during functional brain activation. *Journal of Neuroscience Methods*, 178(1):162–73, March 2009.

[24] E. M. C. Hillman. Optical brain imaging in vivo: techniques and applications from animal to man. *Journal of Biomedical Optics*, 12(5):051402, 2007.

[25] D. Holder, A. Rao, and Y. Hanquan. Imaging of physiologically evoked responses by electrical impedance tomography with cortical electrodes in the anaesthetized rabbit. *Physiological Measurement*, 17:A179–A186, 1996.

[26] T. Tidswell, a. Gibson, R. H. Bayford, and D. S. Holder. Three-dimensional electrical impedance tomography of human brain activity. *NeuroImage*, 13(2):283–94, February 2001.

[27] P. Bandettini. What's new in neuroimaging methods? *Annals of the New York Academy of Sciences*, 1156:260–93, March 2009.

[28] J. Hursh. Conduction velocity and diameter of nerve fibers. *American Journal of Physiology*, 127(1):131–139, 1939.

[29] P. L. Nunez and R. B. Silberstein. On the relationship of synaptic activity to macroscopic measurements: does co-registration of eeg with fmri make sense? *Brain Topography*, 13(2):79–96, January 2000.

[30] S. Baillet, J. C. Mosher, and R. M. Leahy. Electromagnetic brain mapping. *Signal Processing Magazine, IEEE*, 181(6):14–30, 2001.

[31] S. Baillet, J. J. Riera, G. Marin, J. F. Mangin, J. Aubert, and L. Garnero. Evaluation of inverse methods and head models for eeg source localization using a human skull phantom. *Physics in medicine and biology*, 46(1):77–96, January 2001.

[32] S. Rose and J. Ebersole. Advances in spike localization with eeg dipole modeling. *Clinical EEG Neuroscience*, 40(4):281–287, 2009.

[33] D. Cohen. Magnetoencephalography : Evidence of magnetic fields produced by alpha-rhythm currents. *Science*, 161(3843):784–786, 2011.

[34] J. Bodurka and P. a. Bandettini. Toward direct mapping of neuronal activity: Mri detection of ultraweak, transient magnetic field changes. *Magnetic Resonance in Medicine*, 47(6):1052–8, June 2002.

[35] A. D. Liston, A. Salek-Haddadi, S. J. Kiebel, K. Hamandi, R. Turner, and L. Lemieux. The mr detection of neuronal depolarization during 3-hz spike-and-wave complexes in generalized epilepsy. *Magnetic Resonance Imaging*, 22(10):1441–4, December 2004.

[36] G. E. Hagberg, M. Bianciardi, and B. Maraviglia. Challenges for detection of neuronal currents by mri. *Magnetic Resonance Imaging*, 24(4):483–93, May 2006.

[37] J. Xiong, P. T. Fox, and J.-H. Gao. Directly mapping magnetic field effects of neuronal activity by magnetic resonance imaging. *Human Brain Mapping*, 20(1): 41–9, September 2003.

[38] R. Chu, J. a. de Zwart, P. van Gelderen, M. Fukunaga, P. Kellman, T. Holroyd, and J. H. Duyn. Hunting for neuronal currents: absence of rapid mri signal changes during visual-evoked response. *NeuroImage*, 23(3):1059–67, November 2004.

[39] L. M. Parkes, F. P. de Lange, P. Fries, I. Toni, and D. G. Norris. Inability to directly detect magnetic field changes associated with neuronal activity. *Magnetic Resonance in Medicine*, 57(2):411–6, February 2007.

[40] G. Gratton, C. R. Brumback, B. a. Gordon, M. a. Pearson, K. a. Low, and M. Fabiani. Effects of measurement method, wavelength, and source-detector distance on the fast optical signal. *NeuroImage*, 32(4):1576–90, October 2006.

[41] M. A. Franceschini and D. a. Boas. Noninvasive measurement of neuronal activity with near-infrared optical imaging. *NeuroImage*, 21(1):372–386, January 2004.

[42] F. Syre, H. Obrig, J. Steinbrink, M. Kohl, R. Wenzel, and A. Villringer. Are vep correlated fast optical signals detectable in the human adult by non-invasive nearinfrared spectroscopy (nirs)? *Advances in experimental medicine and biology*, 430:421–431, 2003.

[43] J. Steinbrink, F. C. D. Kempf, A. Villringer, and H. Obrig. The fast optical signal–robust or elusive when non-invasively measured in the human adult? *NeuroImage*, 26(4):996–1008, July 2005.

[44] S. Chemla and F. Chavane. Voltage-sensitive dye imaging: Technique review and models. *Journal of Physiology - Paris*, 104(1-2):40–50, 2009.

[45] D. C. Barber and B. H. Brown. Applied potential tomography. *Journal of Physics E: Scientific Instruments*, 17(9):723–733, September 1984.

[46] M. S. Hamalainen. Basic principles of magnetoencephalography. *Acta radiologica. Supplementum*, 1(377):58–62, 1991.

[47] D. Ogden and P. Stanfield. Patch clamp techniques for single channel and whole-cell recording. In D. C. Ogden, editor, *Microelectrode techniques, The Plymouth workshop handbook.*, chapter 4, pages 53–78. Company of Biologists, Cambridge, 2nd edition, 1994.

[48] D. R. Humphrey and E. M. Schmidt. Extracellular single-unit recording methods. In A. A. Boulton, G. B. Baker, and C. H. Vanderwolf, editors, *Neurophysiological Techniques: Applications to neural systems*, chapter 1, pages 1–64. Humana Press, 1 edition, 1990.

[49] U. Mitzdorf. Current source-density method and application in cat cerebral cortex : Investigation of evoked potentials and eeg phenomena. *Physiological Reviews*, 65 (1):37–100, January 1985.

[50] Y. Chen, M. Dhamala, A. Bollimunta, C. E. Schroeder, and M. Ding. Current source density analysis of ongoing neural activity: Theory and application. In R. P. Vertes and R. W. Stackman, editors, *Electrophysiological Recording Techniques*, volume 54 of *Neuromethods*, chapter 2, pages 27–41. Humana Press, Totowa, NJ, 1st edition, 2011.

[51] Y. Kajikawa and C. E. Schroeder. How local is the local field potential? *Neuron*, 72(5):847–58, December 2011.

[52] C. Nicholson and J. A. Freeman. Theory of current source-density analysis and determination of conductivity tensor for anuran cerebellum. *Journal of Neurophysiology*, 38(2):356–368, 1975.

[53] G. T. Einevoll, K. H. Pettersen, A. Devor, I. Ulbert, E. Halgren, and A. M. Dale. Laminar population analysis: estimating firing rates and evoked synaptic activity from multielectrode recordings in rat barrel cortex. *Journal of Neurophysiology*, 97 (3):2174–2190, March 2007.

[54] S. Di, C. Baumgartner, and D. S. Barth. Laminar analysis of extracellular in rat vibrissa/barrel cortex field potentials. *Journal of Neurophysiology*, 63(4):832–840, 1990.

[55] K. H. Pettersen, A. Devor, I. Ulbert, A. M. Dale, and G. T. Einevoll. Current-source density estimation based on inversion of electrostatic forward solution: effects of finite extent of neuronal activity and conductivity discontinuities. *Journal of neuroscience methods*, 154(1-2):116–33, June 2006.

[56] S. Leski, D. K. Wojcik, J. Tereszcuk, D. A. Swiejkowski, E. Kublik, and A. Wrobel. Inverse current-source density method in 3d: Reconstruction fidelity, boundary effects, and influence of distant sources. *Neuroinformatics*, 5(4):207–22, January 2007.

[57] D. S. Holder. Brief introduction to bioimpedance. In *Electrical Impedance Tomography: Methods, History and Applications*, pages 411–422. 2004.

[58] T. Stieglitz. Electrodes. In R. Brette and A. Destexhe, editors, *Handbook of Neural Activity Measurement*, chapter 2, pages 8–43. Cambridge University Press, Cambridge, 1st edition, 2012.

[59] R. H. Bayford. Bioimpedance tomography (electrical impedance tomography). *Annual Review of Biomedical Engineering*, 8:63–91, January 2006.

[60] H. Curtis and K. Cole. Transverse electric impedance of the squid giant axon. *The Journal of General Physiology*, 21(6):757, 1938.

[61] K. S. Cole and H. J. Curtis. Electric impedance of the squid giant axon during activity. *The Journal of General Physiology*, 22(5):649–70, May 1939.

[62] K. Boone. *The possible use of applied potential tomography for imaging action potentials.* Ph.d. thesis, University of London, 1995.

[63] O. Gilad, A. Ghosh, D. Oh, and D. S. Holder. A method for recording resistance changes non-invasively during neuronal depolarization with a view to imaging brain activity with electrical impedance tomography. *Journal of Neuroscience Methods*, 180(1):87–96, May 2009.

[64] T. Oh, O. Gilad, A. Ghosh, M. Schuettler, and D. S. Holder. A novel method for recording neuronal depolarization with recording at 125-825 hz: implications for imaging fast neural activity in the brain with electrical impedance tomography. *Medical & Biological Engineering & Computing*, 49(5):593–604, May 2011.

[65] W. H. Freygang and W. M. Landau. Some relations between resistivity and electrical activity in the cerebral cortex of the cat. *Journal of Cellular and Comparative Physiology*, 45(3):377–392, June 1955.

[66] A. Van Harreveld and J. Schade. Changes in the electrical conductivity of cerebral cortex during seizure activity. *Experimental Neurology*, 5(5):383–400, 1962.

[67] W. Adey, R. Kado, and J. Didio. Impedance measurements in brain tissue of animals using microvolt signals. *Experimental Neurology*, 5(1):47–66, 1962.

[68] N. A. Aladjolova. Slow electrical processes in the brain. *Progress in Brain Research*, 7:155–237, 1964.

[69] K. Klivington and R. Galambos. Rapid resistance shifts in cat cortex during click-evoked responses. *Journal of neurophysiology*, 31(4):565–573, 1968.

[70] R. Henderson and J. Webster. An impedance camera for spatially specific measurements of the thorax. *Biomedical Engineering, IEEE Transactions on*, c(3):250–254, 1978.

[71] A. L. Benabid, L. Balme, J. C. Persat, M. Belleville, J. Chirossel, M. Bulve-Bodin, J. de Rougemont, and C. Poupot. Electrical impedance brain scanner: principles and preliminary results of simulation. *T.-I.-T. journal of life sciences*, 81(1-2): 59–68, 1978.

[72] B. Brown and A. Seagar. The sheffield data collection system. *Clinical Physics and Physiological Measurement*, 8:91–97, 1987.

[73] R. D. Cook, G. J. Saulnier, D. G. Gisser, J. C. Goble, J. C. Newell, and D. Isaacson. Act3: a high-speed, high-precision electrical impedance tomograph. *IEEE Transactions on Bio-Medical Engineering*, 41(8):713–22, August 1994.

[74] Q. Zhu, W. R. Lionheart, F. J. Lidgey, C. N. McLeod, K. S. Paulson, and M. K. Pidcock. An adaptive current tomography using voltage sources. *IEEE Transactions on Bio-Medical Engineering*, 40(2):163–8, February 1993.

[75] R. Halter, A. Hartov, and K. D. Paulsen. Design and implementation of a high frequency electrical impedance tomography system. *Physiological Measurement*, 25 (1):379–390, February 2004.

[76] Q. S. Zhu, C. N. McLeod, C. W. Denyer, F. J. Lidgey, and W. R. Lionheart. Development of a real-time adaptive current tomograph. *Physiological Measurement*, 15 Suppl 2:A37–43, May 1994.

[77] R. J. Yerworth, R. H. Bayford, B. Brown, P. Milnes, M. Conway, and D. S. Holder. Electrical impedance tomography spectroscopy (eits) for human head imaging. *Physiological Measurement*, 24(2):477–89, May 2003.

[78] D. S. Holder and T. Tidswell. Electrical impedance tomography of brain function. In D. S. Holder, editor, *Electrical Impedance Tomography: Methods, History and Applications*, pages 127–161. Institute of Physics Publishing, 2006.

[79] D. S. Holder and A. Khan. Use of polyacrylamide gels in a saline-filled tank to determine the linearity of the sheffield mark 1 electrical impedance tomography (eit) system in measuring impedance disturbances. *Physiological Measurement*, 15 Suppl 2:A45–50, May 1994.

[80] M. Molinari, S. Cox, B. Blott, and G. Daniell. Comparison of algorithms for non-linear inverse 3d electrical tomography reconstruction. *Physiological Measurement*, 23(1):95–104, 2002.

[81] R. Bayford and A. Tizzard. Bioimpedance imaging: an overview of potential clinical applications. *The Analyst*, 137(20):4635–43, October 2012.

[82] A. Liston, R. Bayford, and D. Holder. A cable theory based biophysical model of resistance change in crab peripheral nerve and human cerebral cortex during neuronal depolarisation: implications for electrical impedance tomography of fast neural activity in the brain. *Medical & biological engineering & computing*, 50(5): 425–37, May 2012.

[83] I. Segev and W. Rall. Excitable dendrites and spines: earlier theoretical insights elucidate recent direct observations. *Trends in Neurosciences*, 21(11):453–60, November 1998.

[84] W. Rall, G. Stuart, N. Spurston, and M. Hausser. An historical perspective on modelling dendrites. In *Dendrites*, pages 193–204. Oxford Univ Press, Oxford, 1999.

[85] O. Gilad, L. Horesh, and D. S. Holder. Design of electrodes and current limits for low frequency electrical impedance tomography of the brain. *Medical & Biological Engineering & Computing*, 45(7):621–33, July 2007.

[86] O. Gilad, L. Horesh, and D. S. Holder. A modelling study to inform specification and optimal electrode placement for imaging of neuronal depolarization during visual evoked responses by electrical and magnetic detection impedance tomography. *Physiological Measurement*, 30(6):S201–24, June 2009.

[87] A. T. Tidswell, A. P. Bagshaw, D. S. Holder, R. J. Yerworth, L. Eadie, S. Murray, L. Morgan, and R. H. Bayford. A comparison of headnet electrode arrays for electrical impedance tomography of the human head. *Physiological Measurement*, 24(2):527–44, May 2003.

[88] D. Holder. Impedance changes during evoked nervous activity in human subjects: implications for the application of applied potential tomography (apt) to imaging neuronal discharge. *Clinical Physics and Physiological Measurement*, 10(3):267–274, 1989.

[89] O. Gilad and D. S. Holder. Impedance changes recorded with scalp electrodes during visual evoked responses: implications for electrical impedance tomography of fast neural activity. *NeuroImage*, 47(2):514–22, August 2009.

[90] O. Gilad, A. Ghosh, T. I. Oh, and D. Holder. Imaging fast neural activity in the brain with electrical impedance tomography using a low frequency sinusoidal applied current during somatosensory and visual evoked potentials with epicortical electrodes in the brain of the anaesthetised rat. *International Conference on Electrical Bioimpedance (Florida, USA)*, 2010.

[91] W. Penfield and E. Boldrey. Somatic motor and sensory representation in the cerebral cortex of man as studied by electrical stimulation. *Brain*, 60(4):389–443, 1937.

[92] E. G. Jones. Cerebral cortex. In L. Squire, editor, *Encyclopedia of Neuroscience*, pages 769–773. Elsevier, Amsterdam, 1st edition, 2009.

[93] J. H. Kaas. Somatosensory cortex. In L. Squire, editor, *Encyclopedia of Neuroscience*, pages 73–77. Elsevier, Amsterdam, 1st edition, 2009.

[94] J. O. Coq and C. Xerri. Environmental enrichment alters organizational features of the forepaw representation in the primary somatosensory cortex of adult rats. *Experimental Brain Research*, 121(2):191–204, July 1998.

[95] D. R. Riddle and D. Purves. Individual variation and lateral asymmetry somatosensory cortex of the rat primary somatosensory cortex. *The Journal of Neuroscience*, 15(6):4184–4195, 1995.

[96] A. T. Kulics, C. G. Lineberry, and J. R. Roppolo. Neurophysiological correlates of sensory discrimination performance to electrical cutaneous stimuli in rhesus monkey. *Brain Research*, 136(2):360–365, November 1977.

[97] K. Fox. Sensory physiology. In *Barrel Cortex*, chapter 5, pages 111–149. Cambridge University Press, Cambridge, 1st edition, 2008.

[98] K. Fox. Anatomical pathways. In *Barrel Cortex*, chapter 2, pages 14–48. Cambridge University Press, Cambridge, 1st edition, 2008.

[99] K. D. Alloway. Neural circuitry in the somatosensory system. In L. Squire, editor, *Encyclopedia of Neuroscience*, pages 97–103. Elsevier, Amsterdam, 1st edition, 2009.

[100] K. Fox. Cellular and synaptic organization of the barrel cortex. In *Barrel Cortex*, chapter 3, pages 49–78. Cambridge University Press, Cambridge, 1st edition, 2008.

[101] L. Cauller. Layer i of primary sensory neocortex: where top-down converges upon bottom-up. *Behavioural Brain Research*, 71(1-2):163–70, November 1995.

[102] P. Rubio-Garrido, F. Pérez-de Manzo, C. Porrero, M. J. Galazo, and F. Clascá. Thalamic input to distal apical dendrites in neocortical layer 1 is massive and highly convergent. *Cerebral Cortex*, 19(10):2380–95, October 2009.

[103] E. G. Jones. Thalamic circuitry and thalamocortical synchrony. *Philosophical Transactions of the Royal Society of London. Series B, Biological sciences*, 357 (1428):1659–73, December 2002.

[104] Y. Lam and S. M. Sherman. Functional organization of the somatosensory cortical layer 6 feedback to the thalamus. *Cerebral Cortex*, 20(1):13–24, January 2010.

[105] S. R. Olsen, D. S. Bortone, H. Adesnik, and M. Scanziani. Gain control by layer six in cortical circuits of vision. *Nature*, 1, February 2012.

[106] K. Zilles. *The Cortex of the Rat: A Stereotaxic Atlas*. Springer-Verlag, Berlin, 1st edition, 1985.

[107] W. J. S. Krieg. Connections of the cerebral cortex: I the albino rat. b structure of the cortical atlas. *The Journal of Comparative Neurology*, 84(3):277–323, 1946.

[108] R. W. Dykes and Y. Lamour. An electrophysiological study of single somatosensory neurons in rat granular cortex serving the limbs: a laminar analysis. *Journal of Neurophysiology*, 60(2):703–24, August 1988.

[109] D. J. Simons. Response properties of vibrissa units in rat si somatosensory neocortex. *Journal of Neurophysiology*, 41(3):798–820, May 1978.

[110] M. Armstrong-James, K. Fox, and A. Das-Gupta. Flow of excitation within rat barrel cortex on striking a single vibrissa. *Journal of Neurophysiology*, 68(4):1345–58, October 1992.

[111] A. Peters, D. A. Kara, and K. M. Harriman. The neuronal composition of area 17 of rat visual cortex. iii. numerical considerations. *The Journal of Comparative Neurology*, 238(3):263–274, August 1985.

[112] G. Kenan-Vaknin and T. Teyler. Laminar pattern of synaptic activity in rat primary visual cortex: comparison of in vivo and in vitro studies employing the current source density analysis. *Brain Research*, 635(1-2):37–48, January 1994.

[113] R. B. Langdon and M. Sur. Components of field potentials evoked by white matter stimulation in isolated slices of primary visual cortex: Spatial distributions and synaptic order. *Journal of Neurophysiology*, 64(5):1484–1501, November 1990.

[114] V. Mountcastle. Modality and topographic properties of single neurons of cat's somatic sensory cortex. *Journal of Neurophysiology*, 20(4):408–434, 1957.

[115] D. Hubel and T. Wiesel. Receptive fields, binocular interaction and functional architecture in the cat's visual cortex. *The Journal of Physiology*, 160(1):106–154, 1962.

[116] D. H. Hubel and T. N. Wiesel. Shape and arrangement of columns in cat's striate cortex. *The Journal of Physiology*, 165(3):559–568, 1963.

[117] J. Y. Wu, L. Guan, and Y. Tsau. Propagating activation during oscillations and evoked responses in neocortical slices. *The Journal of Neuroscience*, 19(12):5005–15, June 1999.

[118] V. B. Mountcastle. The columnar organization of the neocortex. *Brain*, 120(4): 701–22, April 1997.

[119] R. J. Nelson and Y. Liu. Somatosensory cortex : Functional architecture. In L. R. Squire, editor, *Encyclopedia of Neuroscience*, pages 79–84. Elsevier, Amsterdam, 1st edition, 2009.

[120] J. C. Horton and D. L. Adams. The cortical column: a structure without a function. *Philosophical Transactions of the Royal Society of London. Series B, Biological sciences*, 360(1456):837–62, April 2005.

[121] S. Freeman and H. Sohmer. A comparison of forepaw and vibrissae somatosensory cortical evoked potentials in the rat. *Electroencephalography and Clinical Neurophysiology*, 100(4):362–9, July 1996.

[122] D. Tracey. Somatosensory system. In G. Paxinos, editor, *The Rat Nervous System*, chapter 25, pages 797–815. Academic Press, 3rd edition, 2004.

[123] A. M. Benison, D. M. Rector, and D. S. Barth. Hemispheric mapping of secondary somatosensory cortex in the rat. *Journal of Neurophysiology*, 97(1):200–7, January 2007.

[124] B. Brett-Green, M. Paulsen, R. J. Staba, E. Fifková, and D. S. Barth. Two distinct regions of secondary somatosensory cortex in the rat: topographical organization and multisensory responses. *Journal of Neurophysiology*, 91(3):1327–36, March 2004.

[125] K. Sakatani, H. Iizuka, and W. Young. Somatosensory evoked potentials in rat cerebral cortex before and after middle cerebral artery occlusion. *Stroke*, 21(1): 124–132, January 1990.

[126] T. Jellema, C. H. M. Brunia, and W. J. Wadman. Sequential activation of microcircuits underlying somatosensory-evoked potentials in rat neocortex. *Neuroscience*, 129(2):283–95, January 2004.

[127] T. Jellema and J. a. Weijnen. A slim needle-shaped multiwire microelectrode for intracerebral recording. *Journal of Neuroscience Methods*, 40(2-3):203–9, December 1991.

[128] R. C. Sotero, A. Bortel, R. Martínez-Cancino, S. Neupane, P. O'Connor, F. Carbonell, and A. Shmuel. Anatomically-constrained effective connectivity among layers in a cortical column modeled and estimated from local field potentials. *Journal of Integrative Neuroscience*, 9(4):355–379, 2010.

[129] J. J. Sun, J. W. Yang, and B. C. Shyu. Current source density analysis of laser heat-evoked intra-cortical field potentials in the primary somatosensory cortex of rats. *Neuroscience*, 140(4):1321–36, July 2006.

[130] M. E. Diamond, M. von Heimendahl, P. M. Knutsen, D. Kleinfeld, and E. Ahissar. 'where' and 'what' in the whisker sensorimotor system. *Nature Reviews. Neuroscience*, 9(8):601–12, August 2008.

[131] K. Fox. Introduction to the barrel cortex. In *Barrel Cortex*, chapter 1, pages 1–13. Cambridge University Press, Cambridge, 1st edition, 2008.

[132] C. C. H. Petersen. The functional organization of the barrel cortex. *Neuron*, 56 (2):339–55, October 2007.

[133] P. M. E. Waite. Trigeminal sensory system. In G. Paxinos, editor, *The Rat Nervous System*, chapter 26, pages 817–851. Academic Press, 3rd edition, 2004.

[134] C. C. H. Petersen. Barrel cortex circuits. In L. R. Squire, editor, *Encyclopedia of Neuroscience*, pages 41–45. Elsevier, Amsterdam, 1st edition, 2009.

[135] M. E. Diamond, M. Armstrong-James, F. F. Ebner, and M. J. Budway. Somatic sensory responses in the rostral sector of the posterior group (pom) and in the ventral posterior medial nucleus (vpm) of the rat thalamus: dependence on the barrel field cortex. *The Journal of Comparative Neurology*, 318(1):462–476, May 1992.

[136] V. Ego-Stengel, J. Le Cam, and D. E. Shulz. Coding of apparent motion in the thalamic nucleus of the rat vibrissal somatosensory system. *Journal of Neuroscience*, 32(10):3339–3351, March 2012.

[137] J. Lübke and D. Feldmeyer. Excitatory signal flow and connectivity in a cortical column: focus on barrel cortex. *Brain Structure & Function*, 212(1):3–17, July 2007.

[138] M. Armstrong-James, C. A. Callahan, and M. A. Friedman. Thalamo-cortical processing of vibrissal information in the rat. i. intracortical origins of surround but not centre-receptive fields of layer iv neurones in the rat s1 barrel. *The Journal of Comparative Neurology*, 303(2):193–210, 1991.

[139] C. C. H. Petersen, A. Grinvald, and B. Sakmann. Spatiotemporal dynamics of sensory responses in layer 2/3 of rat barrel cortex measured in vivo by voltage-sensitive dye imaging combined with whole-cell voltage recordings and neuron reconstructions. *The Journal of Neuroscience*, 23(4):1298–1309, February 2003.

[140] C. C. H. Petersen and B. Sakmann. Functionally independent columns of rat somatosensory barrel cortex revealed with voltage-sensitive dye imaging. *The Journal of Neuroscience*, 21(21):8435–8446, November 2001.

[141] F. Matyas, V. Sreenivasan, F. Marbach, C. Wacongne, B. Barsy, C. Mateo, R. Aronoff, and C. C. H. Petersen. Motor control by sensory cortex. *Science*, 330(6008):1240–1243, November 2010.

[142] C. I. Moore, S. B. Nelson, and M. Sur. Dynamics of neuronal processing in rat somatosensory cortex. *Trends in Neurosciences*, 22(11):513–20, November 1999.

[143] I. Ferezou, S. Bolea, and C. C. H. Petersen. Visualizing the cortical representation of whisker touch: voltage-sensitive dye imaging in freely moving mice. *Neuron*, 50 (4):617–29, May 2006.

[144] D. S. Barth, J. Kithas, and S. Di. Anatomic organization of evoked potentials in rat parietotemporal cortex: somatosensory and auditory responses. *Journal of Neurophysiology*, 69(6):1837–1849, 1993.

[145] M. L. Seo. Effect of environmental complexity on the latency of cortical vibrissa potentials. *Developmental Psychobiology*, 25(1):67–76, January 1992.

[146] S. Di and D. S. Barth. Topographic analysis of field potentials in rat vibrissa/barrel cortex. *Brain Research*, 546(1):106–12, April 1991.

[147] Y. Shiraki and T. Satoh. Modulation of vibrissa-evoked cortical potentials after infraorbital nerve crush in rats. *Electroencephalography and Clinical Neurophysiology*, 77(5):376–81, 1990.

[148] R. S. Petersen and M. E. Diamond. Spatial-temporal distribution of whisker-evoked activity in rat somatosensory cortex and the coding of stimulus location. *The Journal of Neuroscience*, 20(16):6135–43, August 2000.

[149] N. C. Roy, T. Bessaih, and D. Contreras. Comprehensive mapping of whisker-evoked responses reveals broad, sharply tuned thalamocortical input to layer 4 of barrel cortex. *Journal of Neurophysiology*, 105(5):2421–37, May 2011.

[150] E. E. Kwegyir-Afful and A. Keller. Response properties of whisker-related neurons in rat second somatosensory cortex. *Journal of Neurophysiology*, 92(4):2083–92, October 2004.

[151] J. Wu, Xiaoying Huang, and Chuan Zhang. Propagating waves of activity in the neocortex: what they are, what they do. *The Neuroscientist*, 14(5):487–502, October 2008.

[152] G. H. Jacobs. The distribution and nature of colour vision among the mammals. *Biological Reviews*, 68(3):413–471, 1993.

[153] A. J. Sefton, B. Dreher, and A. Harvey. Visual system. In G. Paxinos, editor, *The Rat Nervous System*, chapter 32, pages 1083–1165. Academic Press, 3rd edition, 2004.

[154] G. T. Prusky, K. T. Harker, R. M. Douglas, and I. Q. Whishaw. Variation in visual acuity within pigmented, and between pigmented and albino rat strains. *Behavioural Brain Research*, 136(2):339–48, November 2002.

[155] S. G. Espinoza and H. C. Thomas. Retinotopic organization of striate and extrastriate visual cortex in the hooded rat. *Brain Research*, 272(1):137–44, August 1983.

[156] B. M. Kampa, M. M. Roth, W. Göbel, and F. Helmchen. Representation of visual scenes by local neuronal populations in layer 2/3 of mouse visual cortex. *Frontiers in Neural Circuits*, 5(December):18, January 2011.

[157] C. E. Schroeder, A. D. Mehta, and S. J. Givre. A spatiotemporal profile of visual system activation revealed by current source density analysis in the awake macaque. *Cerebral Cortex*, 8(7):575–592, 1998.

[158] D. Barth, N. Goldberg, B. Brett, and S. Di. The spatiotemporal organization of auditory, visual, and auditory-visual evoked potentials in rat cortex. *Brain Research*, 678(1):177–190, 1995.

[159] K. M. Bode-Greuel, W. Singer, and J. B. Aldenhoff. A current source density analysis of field potentials evoked in slices of visual cortex. *Experimental Brain Research*, 69(1):213–219, 1987.

[160] C. D. Aizenman, A. Kirkwood, and M. F. Bear. A current source density analysis of evoked responses in slices of adult rat visual cortex: implications for the regulation of long-term potentiation. *Cerebral Cortex*, 6(6):751–758, 1996.

[161] M. Osanai, S. Tanaka, Y. Takeno, S. Takimoto, and T. Yagi. Spatiotemporal properties of the action potential propagation in the mouse visual cortical slice analyzed by calcium imaging. *PloS one*, 5(10):e13738, January 2010.

[162] L. Domenici, G. W. Harding, and A. Burkhalter. Patterns of synaptic activity in forward and feedback pathways within rat visual cortex. *Journal of Neurophysiology*, 74(6):2649–2664, 1995.

[163] W. Xu, X. Huang, K. Takagaki, and J.-y. Wu. Compression and reflection of visually evoked cortical waves. *Neuron*, 55(1):119–29, July 2007.

[164] L. Horesh. *Some novel approaches in modelling and image reconstruction for multi-frequency electrical impedance tomography of the human brain.* PhD thesis, University College London, 2006.

[165] C. Cronin. Intravenous tissue plasminogen activator for stroke: a review of the ecass iii results in relation to prior clinical trials. *The Journal of Emergency Medicine*, 38(1):99–105, January 2010.

[166] T. Thom, N. Haase, W. Rosamond, V. J. Howard, J. Rumsfeld, T. Manolio, Z. Zheng, K. Flegal, C. O'Donnell, S. Kittner, D. Lloyd-Jones, D. C. Goff, Y. Hong, R. Adams, G. Friday, K. Furie, P. Gorelick, B. Kissela, J. Marler, J. Meigs, V. Roger, S. Sidney, P. Sorlie, J. Steinberger, S. Wasserthiel-Smoller, M. Wilson, and P. Wolf. Heart disease and stroke statistics–2006 update: a report from the american heart association statistics committee and stroke statistics subcommittee. *Circulation*, 113(6):e85–e151, February 2006.

[167] Department of Health. Reducing brain damage: Faster access to better stroke care. National Audit Office Report 52, 2005.

[168] National Institute of Neurological Disorders and Stroke (NINDS). Tissue plasminogen activator for acute ischemic stroke. *The New England Journal of Medicine*, 333 (24):1581–7, December 1995.

[169] S. C. Patel and A. Mody. Cerebral hemorrhagic complications of thrombolytic therapy. *Progress in Cardiovascular Diseases*, 42(3):217–33, 1999.

[170] J. A. Sattin, S. E. Olson, L. Liu, R. Raman, and P. Lyden. An expedited code stroke protocol is feasible and safe. *Stroke*, 37(12):2935–9, December 2006.

[171] M. J. Reeves, S. Arora, J. P. Broderick, M. Frankel, J. P. Heinrich, S. Hickenbottom, H. Karp, K. A. LaBresh, A. Malarcher, G. Mensah, C. J. Moomaw, L. Schwamm, and P. Weiss. Acute stroke care in the us: results from 4 pilot prototypes of the paul coverdell national acute stroke registry. *Stroke*, 36(6):1232–40, June 2005.

[172] A. Romsauerova, A. McEwan, L. Horesh, R. Yerworth, R. H. Bayford, and D. S. Holder. Multi-frequency electrical impedance tomography (eit) of the adult human head: initial findings in brain tumours, arteriovenous malformations and chronic stroke, development of an analysis method and calibration. *Physiological Measurement*, 27(5):S147–61, May 2006.

[173] C. F. Dalziel. Electric shock hazard. *IEEE Spectrum*, 9(2):41–50, January 1972.

[174] A. McEwan, A. Romsauerova, R. Yerworth, L. Horesh, R. Bayford, and D. Holder. Design and calibration of a compact multi-frequency eit system for acute stroke imaging. *Physiological Measurement*, 27(5):S199–210, May 2006.

[175] A. J. Wilson, P. Milnes, A. R. Waterworth, R. H. Smallwood, and B. H. Brown. Mk3.5: a modular, multi-frequency successor to the mk3a eis/eit system. *Physiological Measurement*, 22(1):49–54, February 2001.

[176] L. Fabrizi, A. McEwan, T. Oh, E. J. Woo, and D. S. Holder. An electrode addressing protocol for imaging brain function with electrical impedance tomography using a 16-channel semi-parallel system. *Physiological Measurement*, 30(6):S85–101, June 2009.

[177] H. Koo. *Advances in Instrumentation for Electrical Impedance Tomography of Brain Function*. PhD thesis, University College London, 2013.

[178] L. Fabrizi, A. McEwan, T. Oh, E. J. Woo, and D. S. Holder. A comparison of two eit systems suitable for imaging impedance changes in epilepsy. *Physiological Measurement*, 30(6):S103–20, June 2009.

[179] W. R. B. Lionheart, N. Polydorides, and A. Borsic. The reconstruction problem. In D. S. Holder, editor, *Electrical Impedance Tomography: Methods, History and Applications*, chapter 1, pages 3–64. Cambridge University Press, Cambridge, 1 edition, 2005.

[180] J. K. Seo, J. Lee, S. W. Kim, H. Zribi, and E. J. Woo. Frequency-difference electrical impedance tomography (fdeit): algorithm development and feasibility study. *Physiological Measurement*, 29(8):929–44, August 2008.

[181] S. C. Jun, J. Kuen, J. Lee, E. J. Woo, D. Holder, and J. K. Seo. Frequency-difference eit (fdeit) using weighted difference and equivalent homogeneous admittivity: validation by simulation and tank experiment. *Physiological Measurement*, 30(10): 1087–99, October 2009.

[182] S. Ahn, T. I. Oh, S. C. Jun, J. K. Seo, and E. J. Woo. Validation of weighted frequency-difference eit using a three-dimensional hemisphere model and phantom. *Physiological Measurement*, 32(10):1663–80, October 2011.

[183] A. T. Tidswell, A. Gibson, R. H. Bayford, and D. S. Holder. Validation of a 3d reconstruction algorithm for eit of human brain function in a realistic head-shaped tank. *Physiological Measurement*, 22(1):177–85, February 2001.

[184] A. P. Bagshaw, A. D. Liston, R. H. Bayford, A. Tizzard, A. P. Gibson, A. T. Tidswell, M. K. Sparkes, H. Dehghani, C. D. Binnie, and D. S. Holder. Electrical impedance tomography of human brain function using reconstruction algorithms based on the finite element method. *NeuroImage*, 20(2):752–64, October 2003.

[185] D. Gisser, D. Isaacson, and J. C. Newell. Theory and performance of an adaptive current tomography system. *Clinical Physics and Physiological Measurement*, 9 (A):35, 1988.

[186] O. Gilad, L. Horesh, G. Ahadzi, R. Bayford, and D. Holder. Could synchronized neuronal activity be imaged using low frequency electrical impedance tomography (lfeit)? In *11th Conference on Biomdeical Applications of EIT*, number Table 1, pages 1–4. Citeseer, 2005.

[187] A. Adler and W. R. B. Lionheart. Uses and abuses of eidors: an extensible software base for eit. *Physiological Measurement*, 27(5):S25–42, May 2006.

[188] K. Friston. Statistical parametric mapping. In K. J. Friston, J. T. Ashburner, S. J. Kiebel, T. E. Nichols, and W. D. Penny, editors, *Statistical Parametric Mapping: The Analysis of Brain Images*, chapter 2, pages 10–31. Academic Press, Amsterdam, 1st edition, 2006.

[189] K. Friston and K. Stephan. Modelling brain responses. In K. J. Friston, J. T. Ashburner, S. J. Kiebel, T. E. Nichols, and W. D. Penny, editors, *Statistical Parametric Mapping: The Analysis of Brain Images*, chapter 3, pages 32–45. Academic Press, Amsterdam, 1st edition, 2006.

[190] S. J. Kiebel and A. P. Holmes. The general linear model. In K. J. Friston, J. T. Ashburner, S. J. Kiebel, T. E. Nichols, and W. D. Penny, editors, *Statistical Parametric Mapping: The Analysis of Brain Images*, chapter 8, pages 101–125. Academic Press, Amsterdam, 1st edition, 2006.

[191] W. D. Penny and A. J. Holmes. Random effects analysis. In K. J. Friston, J. T. Ashburner, S. J. Kiebel, T. E. Nichols, and W. D. Penny, editors, *Statistical Parametric Mapping: The Analysis of Brain Images*, chapter 12, pages 156–165. Academic Press, Amsterdam, 1st edition, 2006.

[192] Y. Zhang, P. J. Passmore, R. J. Yerworth, and R. H. Bayford. Statistical analysis for brain eit images using spm. In *Third International Conference on Medical Information Visualisation; BioMedical Visualisation*, pages 60–67. Ieee, 2005.

[193] R. J. Yerworth, Y. Zhang, T. Tidswell, R. H. Bayford, and D. S. Holder. Use of statistical parametric mapping (spm) to enhance electrical impedance tomography (eit) image sets. *Physiological Measurement*, 28(7):S141–51, July 2007.

[194] T. Nichols. False discovery rate procedures. In K. J. Friston, J. T. Ashburner, S. J. Kiebel, T. E. Nichols, and W. D. Penny, editors, *Statistical Parametric Mapping: The Analysis of Brain Images*, chapter 20, pages 246–252. Academic Press, Amsterdam, 1st edition, 2006.

[195] T. Inference and K. J. Friston. Topological inference. In K. J. Friston, J. T. Ashburner, S. J. Kiebel, T. E. Nichols, and W. D. Penny, editors, *Statistical Parametric Mapping: The Analysis of Brain Images*, chapter 19, pages 237–245. Academic Press, Amsterdam, 1st edition, 2006.

[196] M. Brett, W. Penny, and S. Kiebel. Parametric procedures. In K. J. Friston, J. T. Ashburner, S. J. Kiebel, T. E. Nichols, and W. D. Penny, editors, *Statistical Parametric Mapping: The Analysis of Brain Images*, chapter 17, pages 223–231. Academic Press, Amsterdam, 1st edition, 2006.

[197] K. Worsley. Random field theory. In K. J. Friston, J. T. Ashburner, S. J. Kiebel, T. E. Nichols, and W. D. Penny, editors, *Statistical Parametric Mapping: The Analysis of Brain Images*, chapter 18, pages 232–236. Academic Press, Amsterdam, 1st edition, 2006.

[198] T. Nichols and S. Hayasaka. Controlling the familywise error rate in functional neuroimaging: a comparative review. *Statistical methods in medical research*, 12 (5):419–46, October 2003.

[199] J. B. Hopfinger, C. Büchel, a. P. Holmes, and K. J. Friston. A study of analysis parameters that influence the sensitivity of event-related fmri analyses. *NeuroImage*, 11(4):326–33, April 2000.

[200] T. White, D. O'Leary, V. Magnotta, S. Arndt, M. Flaum, and N. C. Andreasen. Anatomic and functional variability: the effects of filter size in group fmri data analysis. *NeuroImage*, 13(4):577–88, April 2001.

[201] M. Mikl, R. Marecek, P. Hlustík, M. Pavlicová, A. Drastich, P. Chlebus, M. Brázdil, and P. Krupa. Effects of spatial smoothing on fmri group inferences. *Magnetic resonance imaging*, 26(4):490–503, May 2008.

[202] K. Worsley, S. Marrett, P. Neelin, and A. Evans. Searching scale space for activation in pet images. *Human Brain Mapping*, 4(1):74–90, January 1996.

[203] P. Skudlarski, R. T. Constable, and J. C. Gore. Roc analysis of statistical methods used in functional mri: Individual subjects. *NeuroImage*, 9(3):311–329, 1999.

[204] J. M. Maisog and J. Chmielowska. An efficient method for correcting the edge artifact due to smoothing. *Human Brain Mapping*, 6(3):128–136, December 1998.

[205] E. Vul, C. Harris, P. Winkielman, and H. Pashler. Puzzlingly high correlations in fmri studies of emotion, personality, and social cognition. *Perspectives on Psychological Science*, 4(3):274–290, May 2009.

[206] C. M. Bennett, A. A. Baird, M. B. Miller, and G. L. Wolford. Neural correlates of interspecies perspective taking in the post-mortem atlantic salmon: An argument for proper multiple comparisons correction. *Journal of Serendipitous and Unexpected Results*, 1(1):1–5, 2011.

[207] J.-B. Poline, K. J. Worsley, A. P. Holmes, R. S. J. Frackowiak, and K. J. Friston. Estimating smoothness in statistical parametric maps: variability of p values. *Journal of Computer Assisted Tomography*, 19(5):788–796, 1995.

[208] T. Nichols and A. Holmes. Non-parametric procedures. In K. J. Friston, J. T. Ashburner, S. J. Kiebel, T. E. Nichols, and W. D. Penny, editors, *Statistical Parametric Mapping: The Analysis of Brain Images*, number 2003, chapter 21, pages 253–272. Amsterdam, 1st edition, 2006.

[209] T. E. Nichols. Multiple testing corrections, nonparametric methods, and random field theory. *NeuroImage*, 62(2):811–5, August 2012.

[210] E. S. Edgington. Approximate randomization tests. *The Journal of Psychology : Interdisciplinary and Applied*, 72(2):143–149, 1969.

[211] K. Jockel. Finite sample properties and asymptotic efficiency of monte carlo tests. *The Annals of Statistics*, 14(1):336–347, 1986.

[212] A. Liu and B. Joe. Relationship between tetrahedron shape measures. *BIT Numerical Mathematics*, 34(2):268–287, 1994.

[213] J. L. Mueller, D. Isaacson, and J. C. Newell. A reconstruction algorithm for electrical impedance tomography data collected on rectangular electrode arrays. *IEEE Transactions on Biomedical Engineering*, 46(11):1379–86, November 1999.

[214] T.-J. Kao, D. Isaacson, J. C. Newell, and G. J. Saulnier. A 3d reconstruction algorithm for eit using a handheld probe for breast cancer detection. *Physiological Measurement*, 27(5):S1–11, May 2006.

[215] G. Sato dos Santos. Personal Communication, 2011.

[216] M. R. Bale and R. S. Petersen. Transformation in the neural code for whisker deflection direction along the lemniscal pathway. *Journal of neurophysiology*, 102 (5):2771–80, November 2009.

[217] J. Hartings. High responsiveness and direction sensitivity of neurons in the rat thalamic reticular nucleus to vibrissa deflections. *Journal of Neurophysiology*, 83 (5):2791–2801, 2000.

[218] S.-H. Lee and D. J. Simons. Angular tuning and velocity sensitivity in different neuron classes within layer 4 of rat barrel cortex. *Journal of neurophysiology*, 91 (1):223–9, January 2004.

[219] W. B. Wilent and D. Contreras. Dynamics of excitation and inhibition underlying stimulus selectivity in rat somatosensory cortex. *Nature neuroscience*, 8(10):1364–70, October 2005.

[220] C. I. Moore. Frequency-dependent processing in the vibrissa sensory system. *Journal of neurophysiology*, 91(6):2390–9, June 2004.

[221] E. Ahissar, R. Sosnik, and S. Haidarliu. Transformation from temporal to rate coding in a somatosensory thalamocortical pathway. *Nature*, 406(6793):302–6, July 2000.

[222] E. Ahissar, R. Sosnik, K. Bagdasarian, and S. Haidarliu. Temporal frequency of whisker movement . ii . laminar organization of cortical representations. *Journal of Neurophysiology*, 86(1):354–367, 2001.

[223] T. a. S. Ewert, C. Vahle-Hinz, and A. K. Engel. High-frequency whisker vibration is encoded by phase-locked responses of neurons in the rat's barrel cortex. *The Journal of neuroscience*, 28(20):5359–68, May 2008.

[224] M. Ito and M. Kato. Analysis of variance study of the rat cortical layer 4 barrel and layer 5b neurones. *The Journal of physiology*, 539(2):511–522, 2002.

[225] G. E. Carvell and D. J. Simons. Biometric analyses of vibrissal tactile discrimination in the rat. *The Journal of Neuroscience*, 10(8):2638–2648, 1990.

[226] J. L. Walker, F. Monjaraz-Fuentes, C. R. Pedrow, and D. M. Rector. Precision rodent whisker stimulator with integrated servo-locked control and displacement measurement. *Journal of Neuroscience Methods*, 196(1):20–30, March 2011.

[227] V. Jacob, L. Estebanez, J. Le Cam, J.-Y. Tiercelin, P. Parra, G. Parésys, and D. E. Shulz. The matrix: a new tool for probing the whisker-to-barrel system with natural stimuli. *Journal of neuroscience methods*, 189(1):65–74, May 2010.

[228] K. Aristovich. Personal Communication, 2012.

[229] M. Schuettler, J. S. Ordonez, C. Henle, D. Oh, O. Gilad, and D. S. Holder. A flexible 29 channel epicortical electrode array. In *13th Annual Conference of the International Functional Electrical Stimulation Society*, pages 1–3. IFESS_2008, 2008.

[230] A. Grinvald, E. Lieke, R. Frostig, C. Gilbert, and T. Wiesel. Functional architecture of cortex revealed by optical imaging of intrinsic signals. *Nature*, 324(6095):361–4, 1986.

[231] R. D. Frostig and C. H. Chen-Bee. Intrinsic signal optical imaging. In R. Brette and A. Destexhe, editors, *Handbook of Neural Activity Measurement*, chapter 8, pages 287–326. Cambridge University Press, Cambridge, 1 edition, 2012.

[232] R. D. Frostig, Y. Xiong, C. H. Chen-Bee, E. Kvasnák, and J. Stehberg. Large-scale organization of rat sensorimotor cortex based on a motif of large activation spreads. *The Journal of neuroscience : the official journal of the Society for Neuroscience*, 28(49):13274–84, December 2008.

[233] J. C. Eccles. Interpretation of action potentials evoked in the cerebral cortex. *Electroencephalography and Clinical Neurophysiology*, 3(4):449–64, 1951.

[234] K. H. Pettersen, H. Linden, A. M. Dale, and G. T. Einevoll. Extracellular spikes and csd. In R. Brette and R. Destexhe, editors, *Handbook of Neural Activity Measurement*, chapter 4, pages 92–135. Cambridge University Press, Cambridge, 1 edition, 2012.

[235] K. H. Pettersen, E. Hagen, and G. T. Einevoll. Estimation of population firing rates and current source densities from laminar electrode recordings. *Journal of computational neuroscience*, 24(3):291–313, June 2008.

[236] Y. Kajikawa and C. E. Schroeder. How local is the local field potential? *Neuron*, 72(5):847–58, December 2011.

[237] T. Goto, R. Hatanaka, T. Ogawa, A. Sumiyoshi, J. Riera, and R. Kawashima. An evaluation of the conductivity profile in the somatosensory barrel cortex of wistar rats. *Journal of neurophysiology*, 104(6):3388–412, December 2010.

[238] K. Pettersen and G. Einevoll. Amplitude variability and extracellular low-pass filtering of neuronal spikes. *Biophysical Journal*, 94(3):784–802, 2008.

[239] G. Buzsáki, C. a. Anastassiou, and C. Koch. The origin of extracellular fields and currents–eeg, ecog, lfp and spikes. *Nature reviews. Neuroscience*, 13(6):407–20, June 2012.

[240] C. Nicholson and R. Llinás. Real time current source-density analysis using multielectrode array in cat cerebellum. *Brain research*, 100(2):418–24, December 1975.

[241] G. Buzsáki. Large-scale recording of neuronal ensembles. *Nature neuroscience*, 7 (5):446–51, May 2004.

[242] K. F. Ahrens and D. Kleinfeld. Current flow in vibrissa motor cortex can phase-lock with exploratory rhythmic whisking in rat. *Journal of neurophysiology*, 92(3): 1700–7, September 2004.

[243] E. Kublik. Contextual impact on sensory processing at the barrel cortex of awake rat. *Acta neurobiologiae experimentalis*, 64(2):229–38, January 2004.

[244] A. Borsic, R. Halter, Y. Wan, A. Hartov, and K. D. Paulsen. Electrical impedance tomography reconstruction for three-dimensional imaging of the prostate. *Physiological measurement*, 31(8):S1–16, August 2010.

[245] K. Aristovich. Personal Communication, 2012.

[246] U. Baysal and G. Sengül. Single camera photogrammetry system for eeg electrode identification and localization. *Annals of biomedical engineering*, 38(4):1539–47, April 2010.

[247] S. A. Masino, M. C. Kwon, Y. Dory, and R. D. Frostig. Characterization of functional organization within rat barrel cortex using intrinsic signal optical imaging through a thinned skull. *Proceedings of the National Academy of Sciences of the United States of America*, 90(21):9998–10002, November 1993.

[248] C. H. Chen-Bee, Y. Zhou, N. S. Jacobs, B. Lim, and R. D. Frostig. Whisker array functional representation in rat barrel cortex: transcendence of one-to-one topography and its underlying mechanism. *Frontiers in neural circuits*, 6(November):93, January 2012.

[249] A. Adler, J. H. Arnold, R. Bayford, A. Borsic, B. Brown, P. Dixon, T. J. C. Faes, I. Frerichs, H. Gagnon, Y. Gärber, B. Grychtol, G. Hahn, W. R. B. Lionheart, A. Malik, R. P. Patterson, J. Stocks, A. Tizzard, N. Weiler, and G. K. Wolf. Greit: a unified approach to 2d linear eit reconstruction of lung images. *Physiological measurement*, 30(6):S35–55, June 2009.